IRON-CONTAINING PEROVSKITE MATERIALS FOR STABLE HYDROGEN PRODUCTION BY CHEMICAL LOOPING WATER SPLITTING

ARUL MURUGAN

A thesis submitted for the degree of Doctor of Philosophy (PhD) in Chemical Engineering at Newcastle University

SCHOOL OF CHEMICAL ENGINEERING AND ADVANCED MATERIALS

October 2011

Abstract

The purpose of this thesis is to investigate 'chemical looping water splitting' processes for hydrogen production which involves reducing a solid oxygen carrier material (such as iron oxide) by a reducing agent such as carbon monoxide, syngas or methane. Following this, a second step can be performed where water is used to oxidise the metal, thereby producing free hydrogen (without requiring any separation steps). These two steps (reduction and oxidation) can be repeated to perform redox cycles which would continuously utilise the solid oxygen carrier material.

Initial experiments were performed using temperature programmed redox cycles to perform chemical looping water-gas shift and compare the performance of two perovskites ($La_{0.6}Sr_{0.4}Co_{0.2}Fe_{0.8}O_{3-\delta}$ and $La_{0.7}Sr_{0.3}FeO_{3-\delta}$) against two supported metal oxides (60% Fe_2O_3/Al_2O_3 and 20% NiO/Al_2O_3). The best performing materials of the perovskites ($La_{0.7}Sr_{0.3}FeO_{3-\delta}$) and support metal oxides (60% Fe_2O_3/Al_2O_3) were further tested in isothermal chemical looping water-gas shift cycles over 150 redox cycles to assess material lifetime. The results showed that 60% Fe_2O_3/Al_2O_3 under these conditions had deactivated due to the formation of $FeAl_2O_4$ which led to lower hydrogen production. $La_{0.7}Sr_{0.3}FeO_{3-\delta}$ gave high material stability and steady hydrogen production over more than 100 redox cycles. A nickel-containing perovskite $La_{0.7}Sr_{0.3}Fe_{0.9}Ni_{0.1}O_{3-\delta}$ was synthesised and subjected to the same experimental conditions but this material showed no improvement compared to $La_{0.7}Sr_{0.3}FeO_{3-\delta}$ in terms of hydrogen production, hydrogen purity and material stability.

In an additional experiment 60% Fe_2O_3/Al_2O_3 and $La_{0.7}Sr_{0.3}FeO_{3-\delta}$ were used as oxygen carrier materials in a three-step chemical looping process involving reduction by methane (to form syngas), water oxidation and air oxidation (to provide heat). 60% Fe_2O_3/Al_2O_3 gave good hydrogen purities during water oxidation but showed low material stability, whereas $La_{0.7}Sr_{0.3}FeO_{3-\delta}$ showed no loss in material stability but gave low hydrogen purity, possibly due to carbon deposition during the reduction step.

Acknowledgements

I would first of all like to thank my supervisor, Prof. Ian Metcalfe, for his outstanding support and guidance during my three years at Newcastle University. He always had the time to discuss new ideas, theories and possible future experiments with me and worked tirelessly to help me as much as he could. I have thoroughly enjoyed working with him and believe that he brought out the best in me, both through my experimental work and as an academic researcher.

I would like to thank Dr Alan Thursfield for his support in the laboratory and for his tremendous assistance in guiding my PhD. I have learnt a lot of my research skills from him which will no doubt be invaluable to me in my future career.

My research group recently became populated with new PhD students, but when I started there was only myself, Francesco Dal Grande and Rafael Vilar Franca. I would like to thank Francesco (our PhD role model) for showing me how a good PhD student should behave and for putting up with being my flatmate for a year. I wish to give a massive thanks to Rafael for being my PhD buddy for the last three years as we have been through everything together. I am grateful that he has always been there for me and I would especially like to thank him for his immense support during the more difficult times of the PhD, I could not imagine what it would have been like without him. I would like to thank the members of my group; Danai Poulidi, Maria Elena Rivas, Naimah Ibrahim, Mas Jalil, Sureena Abdullah and Hang Qi for their various forms of support to me and for being great fun at the Poland conference. Many thanks go to Claire Thompson and Callum Campbell, who only joined the group a year ago but have both become my great friends and made my last year very entertaining. I would further like to thank Callum for being a brilliant flatmate in my last year and for keeping my spirits high towards the final and crucial months of the PhD. Outside of my group, I would like to thank my friends in the Chemical Engineering Department not only for their assistance to my project work but also for being a great laugh.

During my PhD I have had much technical help from the staff of Newcastle University. I would like to give a huge thanks to Simon Daley for all the time he spent

repairing my reactor, and to the rest of the team for their help with equipment repairs and reactor modifications. I wish to thank Pauline Carrick and Maggie White for their endless assistance with material characterisation of my materials. Outside of Newcastle University I would like to thank Supergen XIV and the EPSRC who have funded and supported this research. I am also grateful to Ahmed Rawaz and Maria Olea (Teesside University, UK) for the nickel oxide sample, and Wen Liu and John Dennis (Cambridge University, UK) for the iron oxide sample.

I would like to give a heartfelt thanks to Helen for always being there for me and for making my last two years much happier ones. Finally, I wish to give a massive thank you to my family - Nithya, Mum and Dad for their unconditional support not just during my PhD, but during all of the years leading up to it. I am especially grateful for the help they have given me during the toughest moments of my three years at Newcastle and for making me feel that I was never alone.

Contents

List of Figures

List of Tables

Nomenclature

BET	*Brunauer-Emmett-Teller*	
CCS	*Carbon capture and storage*	
CMH	*Chilled mirror hygrometer*	
COSHH	*Control of substances hazardous to health*	
e^-	*Electron*	
Fe60	*60% wt. Fe_2O_3/Al_2O_3*	
ICP-OES	*Inductively coupled plasma optical emission spectrometry*	
IEA	*International Energy Agency*	
IGCC	*Integrated gasification combined cycle*	
K_{eq}	*Equilibrium constant*	
LSCF6428	*$La_{0.6}Sr_{0.4}Co_{0.2}Fe_{0.8}O_{3-\delta}$*	
LSF731	*$La_{0.7}Sr_{0.3}FeO_{3-\delta}$*	
LSFN7391	*$La_{0.7}Sr_{0.3}Fe_{0.9}Ni_{0.1}O_{3-\delta}$*	
m/z	*mass-to-charge ratio*	
MFC	*Mass flow controller*	
MIEC	*Mixed ionic-electronic conductivity*	
Ni20	*20% wt. NiO/Al_2O_3*	
OCM	*Oxygen carrier material*	
O_{exch}	*Oxygen exchange*	
O_{fin}	*Absolute final oxygen content*	[µmol]
O_{init}	*Absolute initial oxygen content*	[µmol]
$O_{ox(max)}$	*Maximum oxygen capacity*	[µmol]
$O_{ox(min)}$	*Minimum oxygen capacity*	[µmol]
OTM	*Oxygen transport membrane*	
p	*Photon*	
PEM	*Proton exchange membrane*	
PSA	*Pressure swing adsorption*	
QMS	*Quadrapole mass spectrometer*	
R	*Gas constant (8.314 $J\ K^{-1}\ mol^{-1}$)*	
r	*Ionic radius*	
SEM	*Scanning electron microscopy*	
SEM-EDS	*Scanning electron microscopy energy dispersive spectroscopy*	
SMR	*Steam methane reforming*	
SOFC	*Solid oxide fuel cell*	
STP	*Standard temperature and pressure*	
T	*Temperature*	[°C]

t	*Tolerance factor*	
TGA	*Thermogravimetric analysis*	
TPD	*Temperature programmed desorption*	
TPO	*Temperature programmed oxidation*	
TPR	*Temperature programmed reduction*	
$V_o^{\cdot\cdot}$	*Oxygen vacancy*	
WGS	*Water-gas shift*	
XRD	*X-ray diffraction*	
δ	*Oxygen deficiency (in perovskites)*	
ΔG	*Gibbs free energy change*	[kJ mol^{-1}]
ΔH	*Enthalpy change*	[kJ mol^{-1}]
ΔO_{max}	*Maximum oxygen exchange*	[µmol]
ΔS	*Entropy change*	[kJ mol^{-1} K^{-1}]

Chapter 1

1. Introduction

1.1 Hydrogen Production

There are several methods and energy sources that can be used to produce hydrogen and an overview of these methods is shown in Figure 1.1. It should be noted that an important factor for determining the feasibility of each process is the primary source of energy that is used, which at present can be nuclear energy, renewable energy or energy derived from fossil fuels. Currently, there is a high dependence on fossil fuels to obtain hydrogen, but alternative strategies such as using nuclear or renewable energy are also possible.

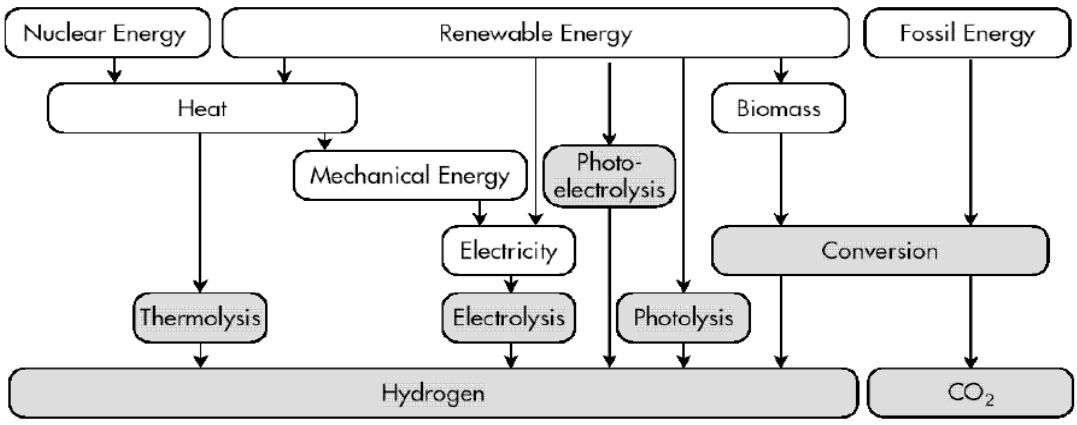

Figure 1.1 Overview of hydrogen production methods[1]

There are currently many options available for producing hydrogen, and a compilation of the costs and efficiencies of these methods was listed by Ali T-Rassi. and is reproduced in Table 1.1. The status of technology describes how well

researched the process is; a process that is well-studied is beneficial as it suggests that a lot of experience has been gained, which could allow for a smoother transition of the process into industry. High efficiencies and lower process costs are favoured in order to make the processes competitive with steam methane reforming.

Table 1.1 Comparison of current hydrogen production processes[2]

Process	Status of Technology	Efficiency [%]	Operating Costs Relative to SMR
Steam methane reforming (SMR)	Mature	70-80	1
Methane/ NG pyrolysis	R&D to mature	72-54	0.9
H_2S methane reforming	R&D	50	<1
Landfill gas dry reformation	R&D	47-58	~1
Partial oxidation of heavy oil	Mature	70	1.8
Naphtha reforming	Mature		
Steam reforming of waste oil	R&D	75	<1
Coal gasification	Mature	60	1.4-2.6
Partial oxidation of coal	Mature	55	
Steam-iron process	R&D	46	1.9
Chloralkali electrolysis	Mature		by-product
Grid electrolysis of water	R&D	27	3-10
Solar & PV-electrolysis of water	R&D to mature	10	>3
High-temp. electrolysis of water	R&D	48	2.2
Thermochemical water splitting	early R&D	35-45	6
Biomass gasification	R&D	45-50	2.0-2.4
Photobiological	early R&D	<1	
Photolysis of water	early R&D	<10	
Photoelectrochemical decomp. of water	early R&D		
Photocatalytic decomp. of water	early R&D		

Table 1.1 shows that steam methane reforming is an efficient, relatively inexpensive and well-studied process, and for these reasons it is currently the leading method for hydrogen production, used to produce 48% of hydrogen worldwide. Figure 1.2 gives a representation of the current sources that are utilised to derive hydrogen; 96% of sources are based on fossil fuels.

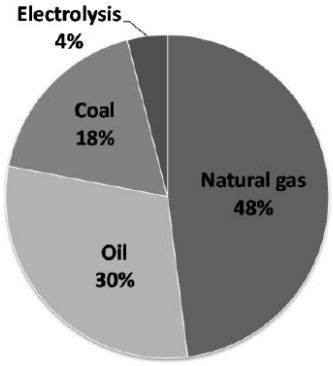

Figure 1.2: Current sources for worldwide hydrogen production[1]

There are other potential options for hydrogen production which are currently under research and the most promising methods are discussed further in this section.

1.1.1 Steam methane reforming

The conventional method for hydrogen production is by steam methane reforming.[3] The International Energy Agency (IEA) predicts that in 2030, compared to other hydrogen processes (such as electrolysis, nuclear, solar and biomass gasification), steam methane reforming (SMR) will still be one of the most economical methods for producing hydrogen,[4] even when incorporating costs for carbon capture and storage (CCS) as shown in Figure 1.3.

Steam methane reforming usually involves two chemical reaction steps:

$$CH_4 + H_2O \rightarrow CO + 3H_2 \qquad \Delta H^0_{298K} = +205\ kJ/mol \qquad (1.1)$$

$$CO + H_2O \rightarrow CO_2 + H_2 \qquad \Delta H^0_{298K} = -41\ kJ/mol \qquad (1.2)$$

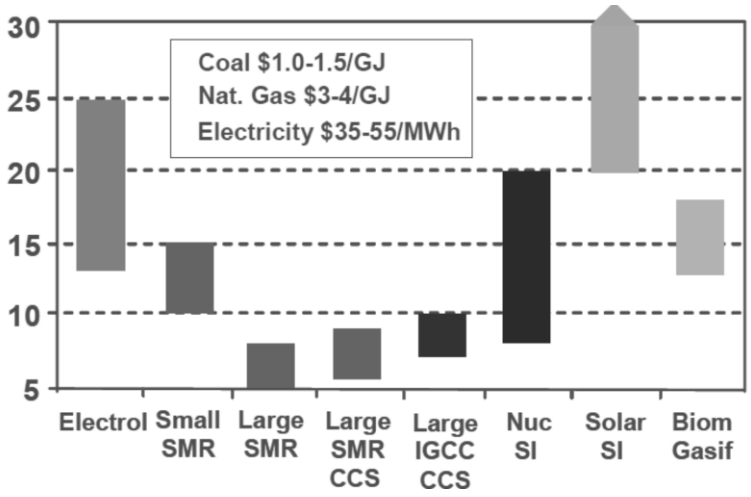

Figure 1.3 Projected hydrogen production cost (US$/GJ) for 2020-2030 (IGCC is integrated gasification combined cycle).

As the overall process is endothermic, a source of heat is required and is usually provided by combusting a quantity of the methane feed in a separate reactor:

$$CH_4 + 2O_2 \rightarrow CO_2 + 2H_2O \qquad \Delta H^0_{298K} = -802\ kJ/mol \qquad (1.3)$$

Equation (1.1) takes place in the presence of a nickel-based catalyst at high temperatures (700-850^{o}C) and pressures of 3-25 bar. This step produces syngas, a mixture of hydrogen and carbon monoxide. In order to improve hydrogen yields, a water-gas shift (WGS) step (Equation (1.2)) is used. WGS is usually carried out in two stages at high (350^{o}C) and low (200^{o}C) temperatures using different catalysts.[5] The first high temperature step completes most of the reaction, and the second low temperature step is performed over a more active catalyst to minimise the remaining carbon monoxide. The final product is a mixture of carbon dioxide and hydrogen, which needs to be separated to provide pure hydrogen. The technique that is usually adopted for this separation step is pressure swing adsorption (PSA), a process that involves adsorption of gaseous molecules onto a molecular sieve at very high pressures to obtain hydrogen purities of ~99.9%.[6] However, this separation technique is very expensive and can contribute to 22% of the total cost of the steam reforming process.[7]

1.1.2 Hydrocarbon decomposition

Carbon and hydrogen can be produced by the decomposition of hydrocarbons, which can range from methane to longer chained species (Equation (1.4)).[8] The reaction can be operated either thermally or by use of plasma. Both methods require a metal catalyst such as nickel or iron.[9]

$$C_xH_{2x+2} \rightarrow xC + (x+1)H_2 \qquad (1.4)$$

An advantage of this system is that it is possible to produce the solid carbon in the form of carbon nanotubes, which are currently used in nanotechnology research.[10] Also, the process is simple and flexible in terms of the types of hydrocarbons that can be used.[9] As no water or air is used in the reaction, there is no formation of carbon monoxide or carbon dioxide, removing the need for a further reaction or separation step. A disadvantage of the system is that the formation of carbon causes deactivation of the metal catalyst, which would therefore require regular replacement.[11] If catalyst deactivation could be avoided, this method of hydrogen production may be a feasible option in the future.

1.1.3 Thermal decomposition of water

In the absence of any catalysts water can be dissociated at temperatures above 2000ºC to form hydrogen and oxygen (Equation (1.5)).[11] A nickel or iron-based catalyst can be used to lower the operation temperature, but not to a low enough temperature to make thermal decomposition of water splitting a feasible method for commercial hydrogen production.[12]

$$H_2O \rightarrow H_2 + ½O_2 \qquad \Delta H^0_{298K} = +286\ kJ/mol \qquad (1.5)$$

1.1.4 Electrolysis

A potential method for producing pure hydrogen is by electrolysis of water, which uses an electric current to split water into hydrogen and oxygen (Equation (1.5)). An advantage of electrolysers is that they can be used to produce hydrogen on site which would therefore avoid transporting issues and costs. If the electricity used to power the system originates from a renewable energy source, the process can be considered carbon neutral and it is therefore a promising technology that could be used to produce hydrogen in the future. Furthermore, as natural gas prices increase this process would become more competitive with steam methane reforming.[13] However, if a non-renewable source of energy is used, the process would emit more carbon dioxide per molar amount of hydrogen formed compared to steam methane reforming.[14]

Current limitations of this process are the lifetime, efficiency and cost of the electrolysers in addition to the high dependency on suitable weather conditions to provide renewable energy to the system. Until these research challenges are overcome, hydrogen production by electrolysis will not be feasible in the near future.

1.1.5 Photolysis of water

Photolysis involves the dissociation of water using sunlight through the use of semiconductor materials.[11] By this method, photons in the sunlight directly react with water by the following reaction to produce hydrogen:

$$H_2O \xrightarrow{h\nu} 2e^- + 2H^+ + ½O_2 \qquad (1.6)$$

where hν is the photon. Currently the process can only operate with very low efficiencies (less than 10%).[15] Also, if this method is employed, it will be completely dependent on sunlight conditions, and therefore may not be able to provide a reliable production of hydrogen when required. According to current research, these are the major limitations of the process.[11, 16]

1.1.6 Biological hydrogen production

Certain types of algae and bacteria use the process of photosynthesis to generate energy from sunlight, water and carbon dioxide, and in some cases the excess energy formed is used to produce hydrogen by water splitting.[11, 17] Researchers are currently attempting to engineer these algae and bacteria to produce increased amounts of hydrogen whilst allowing the organisms to generate enough energy to maintain life. Other types of anaerobic bacteria can produce hydrogen from biodegradable biomass such as glucose and lactose, however in these biological systems a separation step would be required as the hydrogen product would be formed in a mixture with methane, carbon monoxide and carbon dioxide (the mechanisms for these processes are dependent on the type of bacteria used).

Limitations of biological hydrogen production are the slow hydrogen production rates[18] and the large areas of land that are required to grow the algae in order to produce a sustainable amount of hydrogen.[11] As an example, to replace petrol in the USA by hydrogen produced through this method, 25,000 square kilometres of land would be required to grow the algae, which is currently unfeasible.[19] In order for biological hydrogen production processes to become competitive with other methods in the future, research must be performed to improve hydrogen production rates and yields.[18]

1.1.7 Chemical looping water splitting

The aim of this thesis is to follow the research route of a hydrogen production method that was used approximately two decades before steam methane reforming became widely employed in industry. This process is called the steam-iron process and uses iron oxide as an oxygen carrier material to produce hydrogen by water splitting.[20] Iron oxide can exist as one or a mixture of four different oxidation states as shown in Table 1.2.

Table 1.2 The oxidation states of iron oxide

Chemical name	Chemical formula	Oxidation state
Iron	Fe	0
Iron (II) oxide, wüstite	FeO	+2
Iron (II,III) oxide, magnetite	Fe_3O_4*	+2,+3
Iron (III) oxide, haematite	Fe_2O_3	+3

*Magnetite exists as a mixture of wüstite and haematite

The steam-iron process was invented in 1903 and involves a water-splitting step over iron to produce pure hydrogen (Equation (1.7)).[20] During this step, the iron is oxidised to magnetite. Magnetite is then reduced by a reducing agent such as carbon monoxide (Equation (1.8)) in a separate reaction to recover iron. This hydrogen cyclic process can be used to produce separate streams of hydrogen and carbon dioxide (Figure 1.4). Any fuel that can reduce iron oxide can be used as the reducing agent in this cyclic system, which can include coal, biomass and syngas (the use of different reducing agents for this process is reviewed later in Section 2.4).

$$3Fe + 4H_2O \rightarrow Fe_3O_4 + 4H_2 \quad (1.7)$$

$$Fe_3O_4 + 4CO \rightarrow 3Fe + 4CO_2 \quad (1.8)$$

The entire process is described as chemical looping, where a solid material is used to exchange a particular gas (such as oxygen) between two or more reactant streams.[21] This process allows the reactions to occur without permitting the reactant streams to mix. In the steam-iron process iron oxide acts as the oxygen carrier material (OCM). As the hydrogen produced by this process is inherently pure (with no contamination of carbon monoxide or carbon dioxide) there is no requirement for an additional separation step. This process is usually operated isothermally at around 850^{o}C, which is a suitable temperature according to thermodynamic analysis and reaction kinetics, and is not so high that it would cause excessive sintering of iron oxide, which would be detrimental to the process.[22]

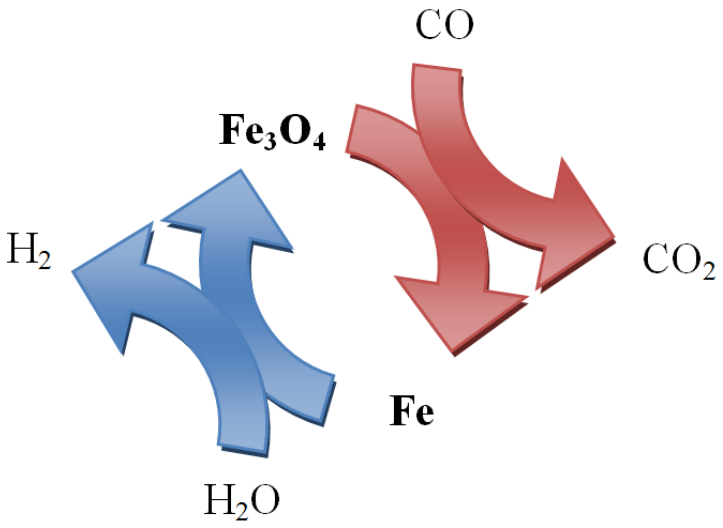

Figure 1.4 The original steam-iron process operated in 1903 (isothermal chemical looping WGS)

Research involving the steam-iron process has so far considered carbon monoxide, syngas (provided by the gasification of coal or biomass) and natural gas as potential reducing agents. In 2003, 96% of world hydrogen production was derived from fossil fuels (as shown in Figure 1.2),[23] and a review by British Petroleum estimates that by the end of 2009 the reserves-to-production ratios of coal and natural gas were 119 and 62.8 years.[24] These are figures that suggest that there are still enough reserves of these fossil fuels for short-term use and at least until research into alternative methods for hydrogen production (such as using electrolysis or by biological processes) are developed enough to provide a solution for the near future.

The original steam-iron process performing the WGS reaction was overall slightly exothermic, but depending on the reducing agent used it can also be endothermic. As an example, if methane is used rather than carbon monoxide as the reducing feed, the overall process is endothermic and therefore some of the reducing gas needs to be combusted in the presence of air in a separate step to provide the required heat for the process.[25] Alternatively, an air reactor could be incorporated into the steam-iron cycling process following the water splitting step to further oxidise the iron oxide to haematite (Equation (1.9)).[26]

$$\frac{1}{2}O_2 + 2Fe_3O_4 \rightarrow 3Fe_2O_3 \qquad \Delta H^0_{298K} = -240\ kJ/mol \quad (1.9)$$

By adding an air reactor to the steam-iron process, additional heat could be provided by this exothermic reaction. Therefore the overall process would operate in a three-step redox cycle as shown in Figure 1.5 (in this example methane is used as the reducing agent). By this method nitrogen formed during the air oxidation step does not mix with any of the other product streams. By adjusting the level of methane oxidation (either partial oxidation of methane to form carbon monoxide and hydrogen, or full oxidation of methane to form carbon dioxide and water) and the amount of iron that is oxidised by air instead of water, the process can be operated autothermal or exothermically (this is discussed in detail in Section 4.8).

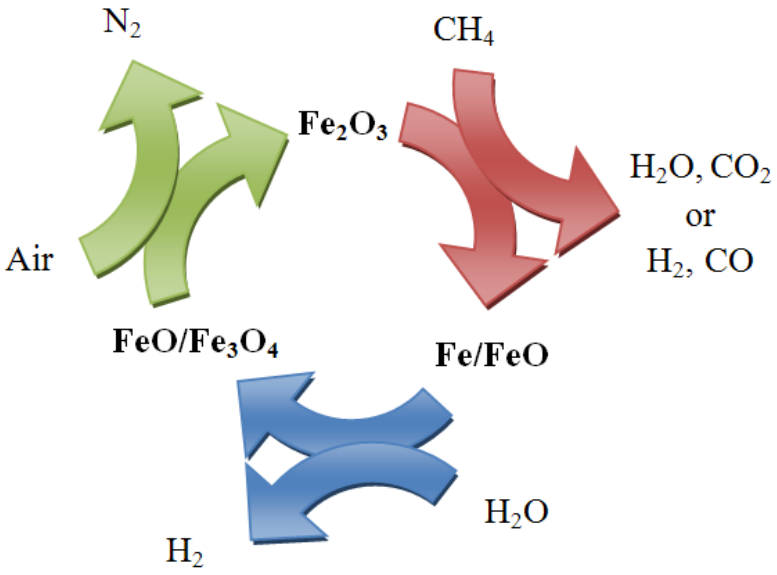

Figure 1.5 The steam-iron cyclic redox process

1.1.8 Summary

Of the hydrogen production methods mentioned in this section, the most widely employed method in industry has been steam methane reforming. It is cheap,

efficient and has been the conventional method for producing hydrogen since 1928 and is therefore well studied. Other promising methods do exist such as the production of hydrogen by electrolysis, photolysis and through the use of biological media but these methods are still under research or are currently not feasible, and therefore are not yet ready for commercialisation.

Hydrogen production by chemical looping water splitting should be acknowledged as a promising practical solution to current hydrogen demand as it could compete with steam methane reforming whilst providing additional benefits. The process can perform the same reaction steps as the steam methane reforming process but without using expensive separation steps such as pressure swing adsorption. As chemical looping water splitting processes can be retrofitted into current steam methane reforming plants, it is a very attractive process for hydrogen production. For these reasons it has recently been claimed to be "the most practical method for hydrogen production in the future" and has received a lot of attention in Europe, USA and Japan.[2]

1.2 Uses of hydrogen

1.2.1 Flight

In 1783 a British scientist by the name of Henry Cavendish discovered that water was not an element, but in fact comprised of two other elements; hydrogen and oxygen.[27] Antoine-Laurent Lavoisier took an interest in this theory and insisted that he would not be satisfied that this was true until he had seen the reverse operation – water splitting to form hydrogen and oxygen. In the autumn of 1783 he planned to carry out experiments to attempt to split water into hydrogen and oxygen, which would achieve two goals. First of all, this would prove that water was actually comprised of hydrogen and oxygen. The second purpose was to produce a buoyant gas that could be used in a hot air balloon; a device that had been invented in Paris within the same year. He passed steam over hot iron at 600^{o}C to produce pure hydrogen[28] and suggested that the process involved two reactions:

$$3Fe + 3H_2O \rightarrow 3FeO + 3H_2 \quad (1.10)$$

$$3FeO + H_2O \rightarrow Fe_3O_4 + H_2 \quad (1.11)$$

He had successfully proven that water was indeed comprised of hydrogen and oxygen, and also used this process to produce pure hydrogen to supply hot air balloons.

Lavoisier was guillotined in 1793 during the 'reign of terror' (which occurred during the French Revolution) and a physicist by the name of Jean-Marie-Joseph Coutelle was put in charge of producing hydrogen gas for military balloons from this date. In March 1794, he successfully operated a 7-pipe hydrogen generating furnace after spending one year realising that the temperature and heating rate of the furnace must be controlled suitably to prevent melting of the reactor and iron inside. Coutelle successfully used this system to supply hydrogen to military hot air balloons between 1794-1797. However, the use of hot air balloons in the military was abandoned soon after for political and military reasons. Commanders of the French army thought of hot air balloons as useless in military combat and unreliable in terms of gas leaks and durability of the balloon itself. It is for this reason that the production of hydrogen by Coutelle's method was also abandoned.

1.2.2 Industrial processes

A large majority of current research concerning the production of hydrogen is focused on using it as a clean source of transportable energy; however, hydrogen is also an important reagent in many chemical processes. In 2003 it was estimated that 80% of worldwide hydrogen production was used in chemical and refinery processes.[29]

Hydrogen and nitrogen are used as reactants to synthesise ammonia in the Haber process, which has uses in the agricultural, petroleum and food industries:

$$3H_2 + N_2 \rightarrow 2NH_3 \quad (1.12)$$

In 2006 alone, 146.5 million tonnes of ammonia were produced.[29] It is also possible to use ammonia as a fuel for internal combustion engines. The combustion products are nitrogen and water and as ammonia can be transported in liquid form, it has a high energy density, compared with gaseous fuels:

$$4NH_3 + 3O_2 \rightarrow 2N_2 + 6H_2O \quad (1.13)$$

Another use of hydrogen is in the food industry. Most vegetable and cooking oils contain a lot of unsaturated fats which are liquid at room temperature. In order to solidify the oil, a hydrogenation reaction must be performed to convert the double bonds contained within the hydrocarbon structure to single bonds by the addition of hydrogen (an example is shown by Equation (1.14)). This hydrogenation reaction can be performed in the presence of a nickel catalyst at temperatures above 150ºC. The result is margarine which is sold worldwide in food retail markets.[30]

$$C_xH_{2x} + H_2 \rightarrow C_xH_{2x+2} \quad (1.14)$$

Hydrogen is commonly used in the petroleum industry for fossil fuel upgrading and processing. It is also used for hydrocracking, where hydrogen reacts with long chained hydrocarbons (such as coal, oil or biomass) to convert them into a useful liquid fuel such as diesel or jet fuel. In addition to cracking the long chained hydrocarbons, a function of the hydrocracking process is to remove impurities such as sulphur and nitrogen species from the liquid fuel.[31]

1.2.3 Source of energy

Recent environmental studies have indicated that the earth is experiencing global climate change, which could be directly related to anthropogenic emissions of greenhouse gases, particularly carbon dioxide into the atmosphere. The Kyoto Protocol, a treaty ratified and signed by members of the United Nations, has set maximum target emission levels for specific greenhouse gases that must not be exceeded by 2012.[32] A high level of carbon dioxide is formed from the combustion of fossil fuels (coal, oil and natural gas):

Coal: $$C + O_2 \rightarrow CO_2 \quad (1.15)$$

Oil: $$C_xH_{2y} + (x + ½y)O_2 \rightarrow xCO_2 + yH_2O \quad (1.16)$$

Natural gas: $$CH_4 + 2O_2 \rightarrow CO_2 + 2H_2O \quad (1.17)$$

It is difficult to simply avoid using these reactions, which are currently employed worldwide to provide energy for industries, homes and transport. Carbon capture and storage (CCS) is a controversial strategy for reducing carbon dioxide emissions. This involves separating carbon dioxide from the combustion process (capture) and injecting it underground or into the deep-sea (storage).[33] Carbon dioxide capture and transport is currently available at a commercial level, however there have not been enough demonstration projects performed to prove that carbon storage is a feasible method for industrial use.[34] There are also other strategies for preventing the emission of carbon dioxide (as shown in Figure 1.6), which can include using captured carbon dioxide for further chemical or biological processing.

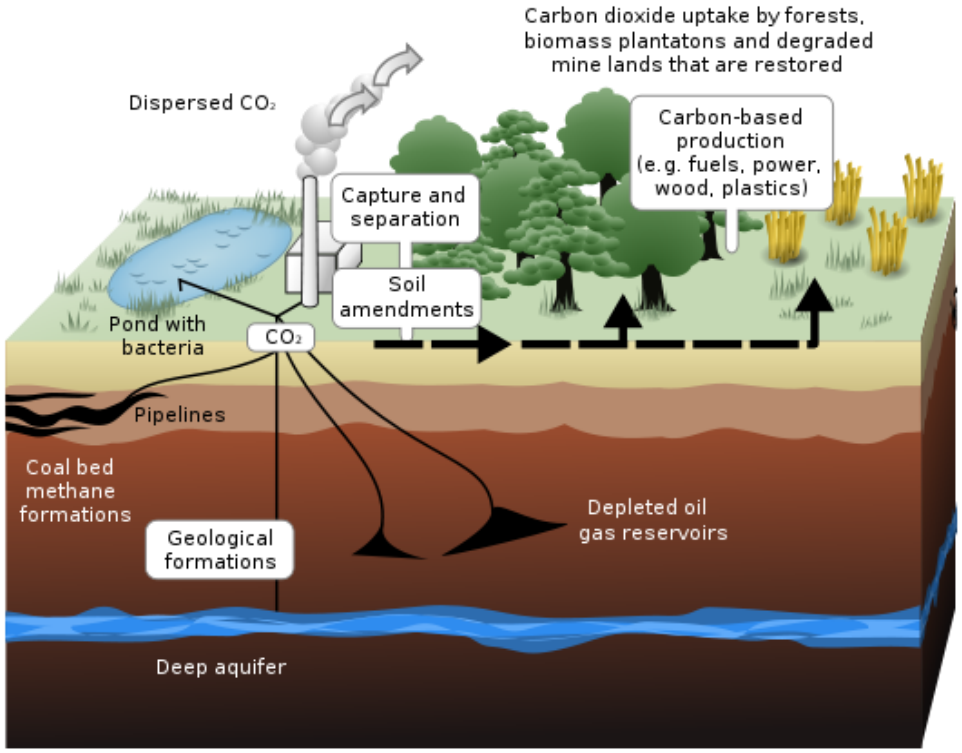

Figure 1.6 Possible strategies for carbon dioxide capture[35]

Vehicles such as cars, ships and planes also use fossil fuels, such as petrol, fuel oil and kerosene as a source of energy. While it is possible for industrial processes to separate carbon dioxide from waste gas streams on site, it is unfeasible to perform a separation step and directly store carbon dioxide on board a vehicle immediately following combustion. An alternative solution for avoiding carbon dioxide emissions from vehicles involves the use of a source of energy that does not produce carbon dioxide when combusted. This source could be hydrogen, which could provide energy to vehicles by oxidation with air whilst only allowing the emission of water as a product (Equation (1.18)). As hydrogen is a secondary energy source derived mainly from fossil fuels it is usually referred to as an energy carrier or energy vector.

Hydrogen can be used to provide clean energy by two methods; the internal combustion engine or a fuel cell. The internal combustion engine involves combustion by the direct oxidation of hydrogen in air to produce only water:

$$H_2 + ½O_2 \rightarrow H_2O \qquad \Delta H^0_{298K} = -286\ kJ/mol \qquad (1.18)$$

This reaction is highly exothermic and therefore heat is released. The water vapour produced by this reaction along with unreacted nitrogen can be emitted as clean exhaust gases. The earliest hydrogen internal combustion engine was developed in 1820 by Reverend W. Cecil, which operated by reacting hydrogen with air. A diagram of the engine is shown in Figure 1.7a. When hydrogen is combusted it expands within the combustion chamber. Following expansion, the piston moves out and the combustion chamber comes into contact with a surface which is cooled by water or air, and this contracts the piston back to its original position. This cyclic action is used to operate a crankshaft, which subsequently provides mechanical energy to operate the vehicle. An advantage of the internal combustion engine is that it can be implemented into existing automobiles easily and can be used in cold weather conditions (unlike fuel cells, which only function under a narrow temperature range). Recently the automobile company BMW have developed the BMW Hydrogen 7, a vehicle that can run on a mixture of hydrogen and petrol by the use of an internal combustion engine (Figure 1.7b).

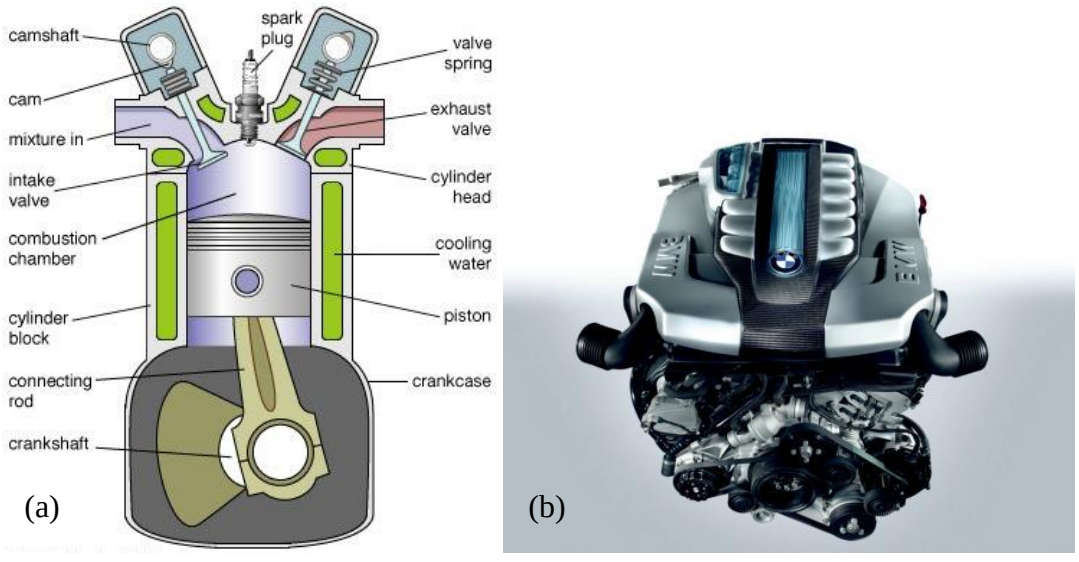

Figure 1.7 (a) Operation of an internal combustion engine[36] (b) The hydrogen internal combustion engine of a BMW Hydrogen 7[37]

A fuel cell is a more complicated system compared to the internal combustion engine, where air and a fuel mix across an anode-electrolyte-cathode interface to produce electricity (and small amounts of heat). Hydrogen is the most common fuel used in this device, but in other types of fuel cells, sources such as methanol, natural gas and other hydrocarbons can be used. The first hydrogen fuel cell was developed by William Grove in 1839.[38] There are different types of hydrogen fuel cells that can be used, which are defined by the type of electrolyte used. The two most common hydrogen fuel cells are proton exchange membrane (PEM) fuel cells and solid oxide fuel cells (SOFC) as shown in Figure 1.8. Both of these fuel cells operate by introducing hydrogen gas at the anode and air at the cathode, but in a PEM fuel cell hydrogen ions are transported through the electrolyte whereas for an SOFC it is oxygen ions that are transported through the electrolyte.

The following reactions take place in a PEM fuel cell:

Anode: $$H_2 \rightarrow 2H^+ + 2e^- \quad (1.19)$$

Cathode: $$½O_2 + 2H^+ + 2e^- \rightarrow H_2O \quad (1.20)$$

where e^- represents an electron. The following reactions take place in an SOFC fuel cell:

Anode: $$H_2 + O^{2-} \rightarrow H_2O + 2e^- \quad (1.21)$$

Cathode: $$½O_2 + 2e^- \rightarrow O^{2-} \quad (1.22)$$

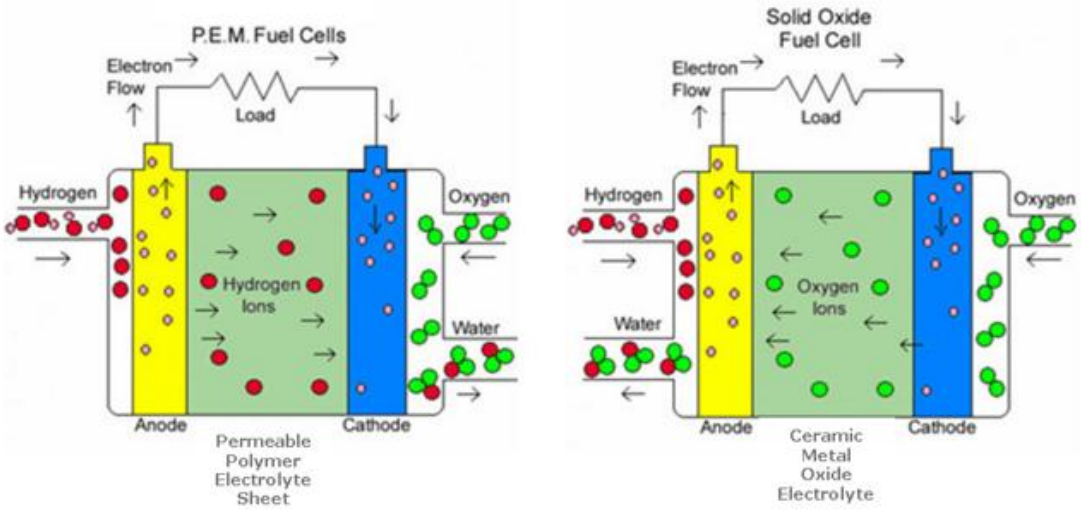

Figure 1.8 Diagram showing the operation of a PEM fuel cell and SOFC[39]

The overall process for both fuel cells is shown by Equation (1.18). The electricity produced by a fuel cell (which is created by the movement of electrons to form an electric circuit as shown in Figure 1.8) can be integrated and used directly in an electronic system. This is an advantage over an internal combustion engine which would lose efficiency if the heat is required to be converted into electricity (perhaps by the use of a turbine). A major disadvantage of PEM fuel cells is that these types of systems generally utilise a catalyst such as platinum, which can become deactivated due to the presence of contaminants. As an example, PEM fuel cells can become poisoned by 50 ppm of carbon monoxide. Purity is therefore a very important consideration when producing hydrogen for use in PEM fuel cells, as opposed to SOFCs which are less sensitive to contaminants. However, compared to SOFCs which operate at temperatures as high as 1000^{o}C, PEM fuel cells can operate at much lower temperatures such as 80^{o}C.[40]

A major issue of utilising hydrogen as an energy vector is transport and storage. Hydrogen exists in the gaseous form at atmospheric pressure and room temperature and has a very low energy density. In comparison, hydrogen is 14 times lighter and has quarter the energy density of petrol. Therefore a very large storage tank would be required if it was to be used as an energy vector on board vehicles.

This also causes problems for transporting hydrogen from the hydrogen production plant to the supplier. Simple solutions to tackle this issue exist which can include pressurising hydrogen (138 bar) or cryogenically cooling it to -253ºC. Both of these methods would increase the energy density of hydrogen, allowing lower volume storage. A major disadvantage of pressurising or cryogenically cooling hydrogen for transportation is the cost required. In addition to this, an added cost would be required to obtain a suitable mode of transport that can either withstand high pressures or maintain low temperatures during delivery.[41]

Hydrogen is naturally a colourless gas, which can potentially cause safety issues if a leak occurs; in a small room it could displace oxygen and act as an asphyxiant. Therefore, hydrogen must be stored in a well-ventilated surrounding. As hydrogen is more buoyant than air, it would tend to rise and pool at the ceiling of a room. Some of the most dangerous properties of hydrogen are the flammability range, which is between 4 and 74 vol. % in air and the explosive range which is between 18 and 59 vol. % in air. These are very large ranges of volume percentages in which hydrogen remains flammable and explosive, and therefore it is very likely that during a hydrogen leak a harmful incident could occur in the presence of an ignition spark. These safety issues have being extensively investigated and according to Ng and Lee (2008)[42] the two most dangerous scenarios regarding hydrogen storage involve rapid release of hydrogen from the storage tank and introduction of air into the tank itself. One solution to avoid these issues has been to use pressure relief devices which allows the safe evacuation of hydrogen from the vehicle during an incident, however, in order for this system to be truly safe the vehicle must always be situated in a well-ventilated or open area.[43]

Another potential solution for safe hydrogen storage and delivery is through the use of metal hydrides. Metal hydrides can be hydrogenated on site, transported into the vehicle and then dehydrogenated during vehicle operation to provide pure hydrogen. This method can be operated at low temperatures (of less than 200^{o}C)[44] and ambient pressures; however the process can be expensive and produce a large additional weight on board a vehicle. An advantage of using metal hydrides is the high energy density that can be achieved by using this system and since hydrogen is not stored in gaseous form this avoids a lot of safety issues.[41] There are many other methods for hydrogen storage through chemicals, which so far include

carbohydrates, ammonia and formic acid that are currently under research but have not been commercialised yet.[45] All of these methods use the same principle of a cyclic storage system which releases hydrogen at the source (in the vehicle) and absorbs hydrogen at a refuelling site.

Currently there is a developing hydrogen infrastructure, especially in the northern parts of Europe, which will be able to provide hydrogen to fuel cell vehicles through hydrogen refuelling stations. Figure 1.9 indicates the number of hydrogen refuelling stations that are currently in operation across Europe.

Figure 1.9 Hydrogen refuelling stations operating in Europe in 2011[46]

The IEA estimates that by 2050 pure hydrogen will be required to power 700 million fuel cell vehicles.[4] These are figures that suggest that the production of pure hydrogen will become an even more important process in the upcoming decades and

this is a major motivation for research into chemical looping water splitting processes for hydrogen production.

.

1.3 Objectives

The first aim of this thesis is to review the thermodynamics and experimental work that have been performed in previous literature on chemical looping water splitting processes to develop an understanding of the current limitations of the process (it appears that a review of the process has not yet been performed in the literature).

The main focus of this thesis is to improve stability and reactivity of the OCM in chemical looping water splitting process by assessing the feasibility of using perovskite-type materials instead of iron oxide based materials. Perovskite-type materials, such as $La_{0.6}Sr_{0.4}Co_{0.2}Fe_{0.8}O_{3-\delta}$ and $La_{0.7}Sr_{0.3}FeO_{3-\delta}$ have previously been used as oxygen conducting membranes and have been shown to have high material stability at high temperatures ($900^{o}C$) whilst performing water splitting reactions to produce pure hydrogen.[47] They are therefore proposed in this thesis as potential OCMs for chemical looping processes involving hydrogen production by water splitting.

It should be noted that although hydrogen produced by this process is expected to be suitable for fuel cells (due to the low carbon monoxide contamination), it would also be a beneficial process for producing hydrogen to be used as a reagent in general industrial processes, due to the expected lowered process costs compared to steam methane reforming and high purity of hydrogen formed without using a downstream separation step.

Chapter 2

2. The Steam-Iron Process

2.1 Introduction

The steam-iron process was invented in 1903 and therefore this literature review comprises of research spanning over a century (although most of the comprehensive thermodynamic and experimental work was performed in the last few decades). In addition to academic papers, there are several patents describing modifications to the original steam-iron process. An initial obstacle for writing this review included the identification of various alternative names that were given to the process such as cyclic water gas shift process and sponge-iron process. Although these processes are in principle the same, they are not referred to as a steam-iron process in the literature.

In addition to steam-iron processes, there have been attempts to produce pure hydrogen by a combined chemical looping and calcium looping process. In this process, methane (with water) and air are used as the reducing and oxidising agents, to form a mixture of hydrogen and carbon dioxide in the reduction step. A calcium oxide carrier material is added to react with the carbon dioxide and remove it from the system to form calcium carbonate. This process is reviewed in Section 2.7.

2.2 Reactor systems

2.2.1 Packed bed

The original steam-iron process was operated using a packed bed reactor, where the iron oxide OCM was subjected to periodic redox cycling by repeated reduction and

oxidation. In this system, the iron OCM was fixed in place whilst the reducing gas and oxidising gas was flowed alternately. This allowed alternate formation of the products from the reducing and oxidising steps, and did not allow continuous production of hydrogen. Furthermore, as the mole fraction of hydrogen depended on the oxidation state of iron oxide, such a system was likely to have a dynamic hydrogen production profile, where the hydrogen mole fraction would change as the oxidation step continued.

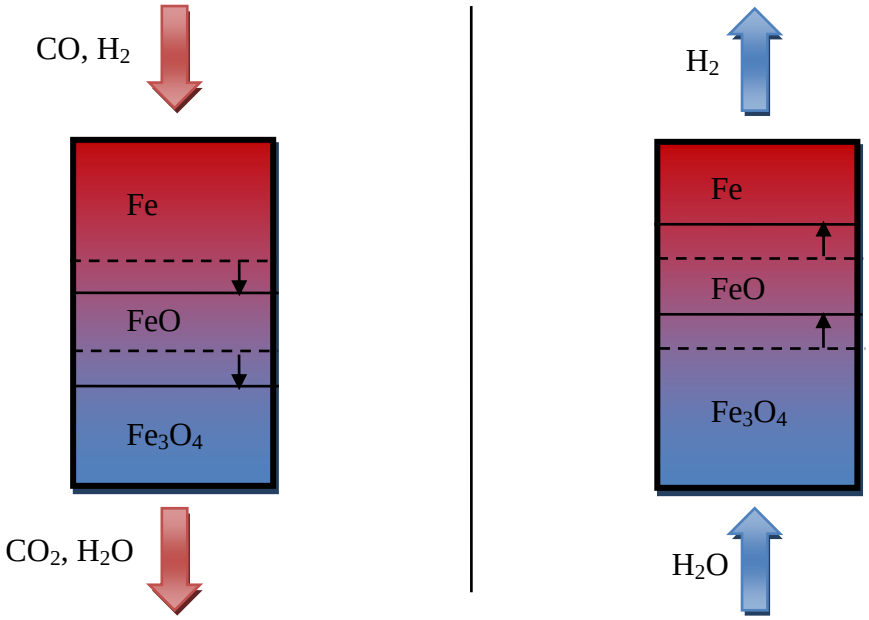

Figure 2.1 Heidebrecht and Sundmacher's proposed moving front model

The behaviour of iron oxide in periodic fixed bed systems was analysed by Heidebrecht and Sundmacher[48] who suggested that reduction and oxidation of the OCM would lead to moving reaction fronts. In a previous study, they suggest that due to the unique thermodynamic limitations of the separate iron oxide phases, hydrogen productivity could be improved by operating the reducing and oxidation steps in counter-current flow.[49] Counter-current operation of the steam-iron process is illustrated in Figure 2.1. By operating the steam-iron process using counter-current operation, during the water oxidation step both iron and wüstite can be oxidised simultaneously (in co-current operation the wüstite would not become oxidised until all of the iron had converted to wüstite).

In order to allow continuous production of hydrogen, counter-current operation could be utilised in a dual-reactor system, which would allow the reducing and oxidising agents to flow continuously to two separate reactors containing the same type of OCM (Figure 2.2). In this system, reduction and oxidation can occur as separate reactions in each reactor, and as soon as hydrogen production becomes too low, the gases can switch to the alternate reactors, to allow hydrogen production to continue (this can be performed by switching both valves in Figure 2.2 simultaneously).

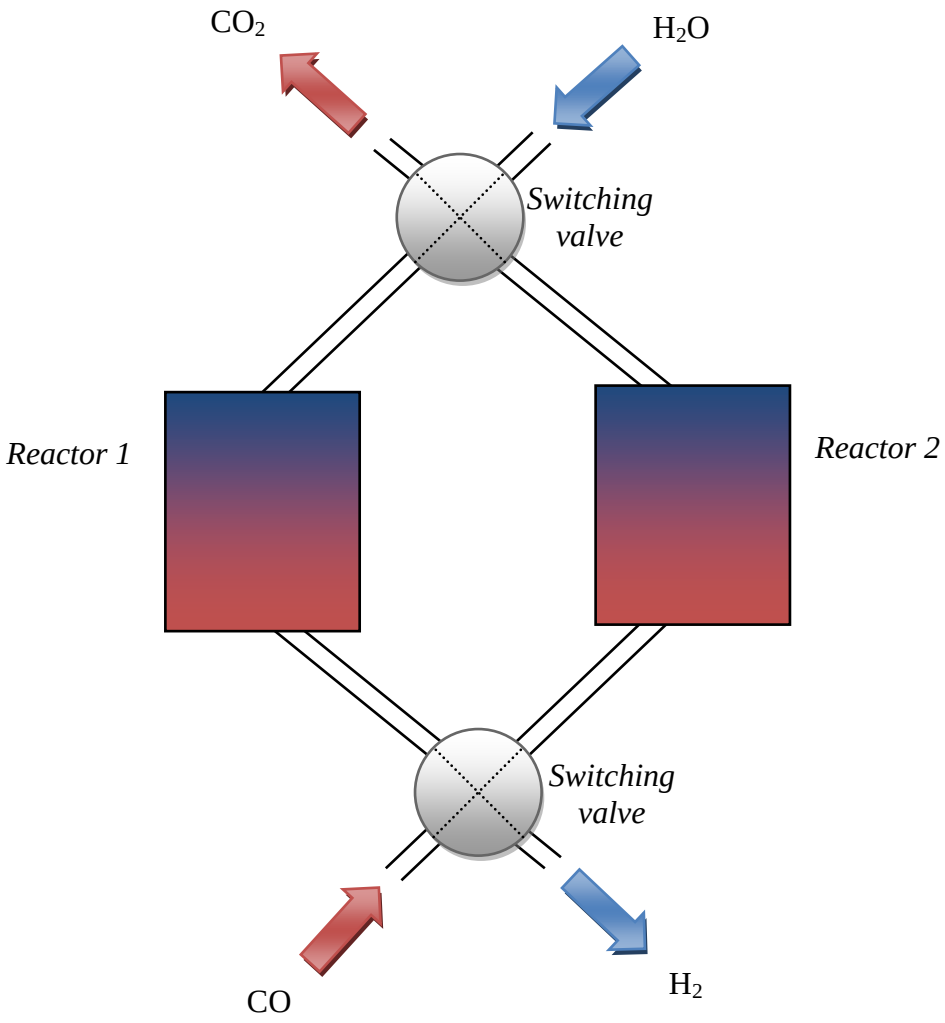

Figure 2.2 Dual fixed bed reactor used to operate the steam-iron process for continuous hydrogen production

2.2.2 Circulating fluidised bed

The circulating fluidised bed is a more complicated reactor system used in chemical looping processes, but holds some advantages over periodic operation in a packed bed reactor. A circulating fluidised bed system uses separate reactors for each of the reduction and oxidation steps. The reactant and product gases remain within each unique reactor, and it is the solid OCM that is fluidised and circulated between the reactors. A simplified diagram of a circulating fluidised bed used to operate an autothermal steam-iron process (where carbon monoxide is the reducing agent) is illustrated in Figure 2.3.

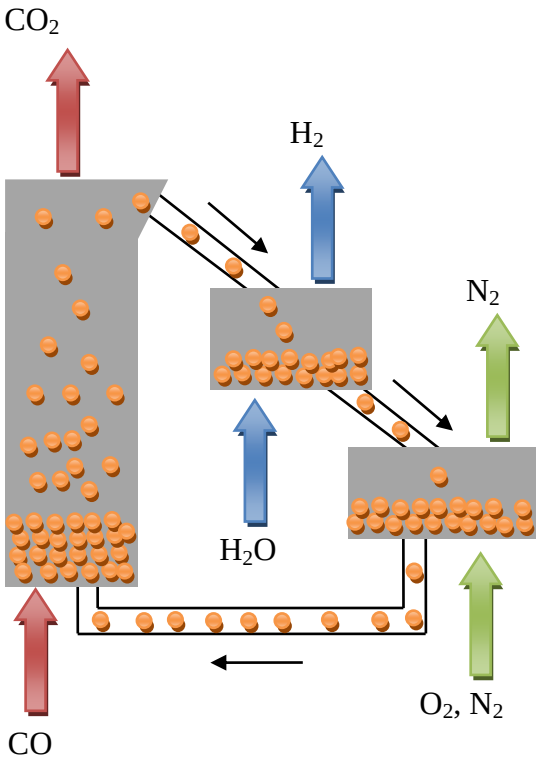

Figure 2.3 Illustration of the movement of fluidised iron oxide OCM particles (orange) in a circulating fluidised bed used to operate the steam-iron process

As shown in Figure 2.3, the OCM particles move downwards through the water oxidation and air oxidation reactors by gravity, and the reducing reactor intentionally

has a low radial area (and usually uses a high flowrate of reactant gas) so that there is enough force to fluidise and carry the particles upwards. Towards the top of the reactor, the area of the column gradually increases until the particles cannot be carried upwards any further, resulting in the particles dropping downwards and eventually into the next reactor. The circulating fluidised bed system usually requires the use of cyclone separators and loop seals to ensure a good separation between the reactors, and additional flushing with inert gas between each stage is usually required.[50]

An advantage of the circulating fluidised bed system over periodic operation in a packed bed is that providing all solid circulation and gas flows are at steady state, the products from the three reactors would be produced continuously and simultaneously with no significant change in product mole fractions during operation. Disadvantages of the periodic packed bed reactor are that the products would be formed in alternate steps and the mole fraction of products would change with time as the steps progress. However, the periodic packed bed reactor is simpler to use and easier to implement.

2.3 Earlier work

2.3.1 Patents

Many papers refer to Howard Lane, an engineer from Birmingham, as the first inventor of a chemical looping process for producing hydrogen. In 1903, he invented the Lane Hydrogen Producer which was the first process that alternately reduced and oxidised iron oxide using the gasified products of coal and water to form pure streams of carbon dioxide and hydrogen.[51] In his article, Lane stated that this process was much more favourable over the other possible processes for obtaining pure hydrogen (by reacting sulphuric acid with zinc/iron or by electrolysis of water).[20] The sulphuric acid process gave low hydrogen purity, and the electrolysis process was very costly.

It was Messerschmitt in 1911 who patented and gave the name steam-iron process to Howard Lane's invention. He defined a steam-iron process as one which

alternately used steam and a reducing gas such as carbon monoxide, syngas or methane to continually oxidise and reduce iron oxide in a chemical looping process. Pure hydrogen product is formed when water splits to oxidise the iron oxide.

After Messerschmitt's steam-iron process patent in 1911, there was very little research on the process until the 1990s. The most likely reason could be the invention of the steam reforming process, which was industrialised as a cheap method for hydrogen production in 1928.[52] Many patents (shown in Appendix A) in addition to a pilot plant study of a fluidised bed reactor for the steam-iron process by Gasior *et al.*[22] in 1961 appear to be the only recorded documents of such research.

Parsons[53] in 1928 proposed a steam-iron process system by carbon monoxide reduction and water oxidation whereby the iron oxide material drops downwards by gravity first through the reduction chamber then through the oxidation chamber, and is carried back to the top of the reactor by a mechanical elevator. By this operation, hydrogen is produced continuously. This is the first design of a steam-iron process where solid is continuously circulated.

Marshall[54] in 1939 proposed a steam-iron system where iron is dropped through a water splitting reactor by gravity (to produce hydrogen). Magnetite at the bottom of the water splitting reactor is transported horizontally (by a conveyor belt) to the reducing furnace where it is reduced to iron by a mixture of methane and air to produce carbon dioxide and water. The reduced iron is then recycled back to the top of the water splitting reactor by the use of another conveyor.

Reed *et al.*[55] in 1953 devised a three reactor circulating fluidised system utilising iron oxide as the OCM comprising of reduction by hydrocarbon, air oxidation and water splitting (in this order). By this method, carbon deposited on the OCM during the reduction step can be removed by the subsequent air oxidation step. The iron oxide would then be free of carbon deposits and can be introduced into the water splitting reactor to allow the production of pure hydrogen. As a separate claim they state that carbon-laden magnetite can be reduced to wüstite by using a mixture of oxygen and carbon monoxide, thus providing wüstite free of carbon.

Gasior *et al.*[22] attempted to improve contact between the gas and solid phases in a steam-iron process that alternated steam and syngas as the oxidising and

reducing agents (methane as a potential reducing agent was also investigated). This study focused on simple fluidised (not circulating) and free-falling bed reactors. They successfully demonstrated hydrogen production at pilot plant scale using both natural and synthetic magnetite (magnetite with magnesia principally). Hydrogen mole fractions on a dry basis of 98% were achieved; the balance being carbon monoxide and carbon dioxide. Reaction rates were found to be first order in pressure for both the oxidation and reduction reactions. Most of their work was performed in the range of 4-14 bar, however, they recommended operation at 20 bar based on thermodynamic and economic considerations. They found that there were problems of using temperatures above 800^{o}C as this caused agglomeration of the iron particles. At temperatures below 700^{o}C, they found that carbon laydown occurred due to the Boudouard reaction.

$$2CO \rightarrow C + CO_2 \qquad (2.1)$$

This carbon was found to react with water during the oxidation step to form the unwanted oxides of carbon alongside hydrogen.

$$C + H_2O \rightarrow CO + H_2 \qquad (2.2)$$

$$C + 2H_2O \rightarrow CO_2 + 2H_2 \qquad (2.3)$$

Watkins[56] devised a system in 1962 that was comprised of two separate steam-iron processes. Each system was comprised of a reduction and oxidation reactor, which circulated iron oxide between them. Note that iron oxide for each system was kept separately and did not mix. For the OCM a metal oxide such as iron, nickel or cobalt supported on a base such as alumina or/and silica was suggested. In the first system, a reduction reactor (which allowed carbon deposition on the OCM to occur) was used to produce syngas by reducing methane, and this was coupled with an air oxidation reactor. The syngas formed by the reduction

reactor in the first steam-iron system, was then used as the reducing agent for the second steam-iron system. In the second system, the reduction reactor (which did not produce carbon) was used to produce carbon dioxide and water (therefore additionally producing heat) and the unit was coupled with a water splitting reactor which could produce hydrogen. It should be noted that in this process, the flue gas following air oxidation would contain carbonaceous gaseous products such as carbon monoxide and carbon dioxide. Oxidation states of the metals and degradation issues are not mentioned.

Benson[57] devised a system in 1969 that could produce separate streams of methane and hydrogen from carbonaceous fuel, steam and air (using iron oxide as the OCM). The carbonaceous fuel is initially gasified by a mixture of steam/hydrogen and the solid char formed is used in the steam-iron process whereas the gaseous products (mainly carbon monoxide) are cleaned to remove sulphur, carbon dioxide and hydrogen sulphide. This gas is then used for a separate methane synthesis step. The system additionally involves a step that upgrades carbon dioxide and water (following reduction of iron oxide) back to syngas by reacting it with char and air. The syngas formed by this step is then used in a second steam-iron cycle to produce further hydrogen from water.

Huebler *et al.*[58] devised a system in 1969 which overall produces separate streams of hydrogen and carbon dioxide/water from water and syngas. In this system there are two reduction reactors, and steam is used to recirculate the iron oxide solid back to the top of the reactors (this is when oxidation of the OCM to provide hydrogen occurs). Syngas is passed through the first reactor, and then through the second, whereas steam flows firstly through the second reactor then the first. This counter-current flow system is performed to maximise hydrogen production.

Johnson[59] devised a continuous steam-iron process in 1971 where carbonaceous solids are used as the reducing agent and steam as the oxidising agent. In this system, the carbonaceous solids are finely divided and flow upwards in counter-current flow against the solid iron oxide.

2.4 Reducing gases

Carbon monoxide is not naturally a primary fuel source and is usually obtained in pure form by separating it from syngas (a mixture of carbon monoxide and hydrogen). Therefore the reduction step for steam-iron processes usually involves syngas derived from coal or biomass gasification, or by partial oxidation of natural gas. Alternatively these fuels (coal, biomass and natural gas) can be used as the reducing agent, and can be fed directly into the reduction stage of the process.

2.4.1 Syngas

Syngas can be derived from any hydrocarbon source including from coal or biomass by an energy intensive gasification step.[60, 61] Coal and biomass can contain many impurities such as sulphur, chlorine and tar. Although the deactivation of the OCM is clearly in general a disadvantage, the fact that the material only survives a limited number of redox cycles means that the presence of poisons in the feed stream is not critical to the process as long as they do not transfer into the gaseous product streams. An investigation by Hacker *et al.*[62] used syngas containing hydrogen chloride as the reducing agent to carry out five steam-iron cycles at 800-900^{o}C. They found that the hydrogen chloride does transfer from the reducing agent into the oxidisation stream, but ends up dissolved in the unreacted water rather than as a contaminant of the product hydrogen stream. A similar test was done for hydrogen sulphide impurities, but no measurement of hydrogen sulphide was detected in the hydrogen product stream after five redox cycles.

2.4.2 Direct Feed Coal

A benefit of using coal as the reducing agent is that it is relatively cheap and, compared to natural gas or crude oil, is more abundant.[63] Coal can be used directly in the steam-iron process to reduce iron oxide by a solid-solid reaction, the advantage of this being the removal of the gasification step and a disadvantage being the difficulties of solid-solid mixing.[64]

Yang *et al.*[65] performed a study to determine the feasibility of introducing coal as a reducing agent into the steam-iron process. Different coal chars were used to directly reduce iron oxide by a solid-solid reaction (without an initial gasification step). Five samples of char were tested; all of these chars were derived from Baorixile Lignite (a Chinese low-rank coal), by devolatisation and impregnation with different weight percentages of potassium and calcium.

Table 2.1 Coal samples used in the study performed by Yang *et al.*

Sample*	C	H	N	O and S (by diff.)
Raw-char	74.87	0.42	0.65	24.06
K-2-char	77.54	0	0.84	21.62
K-5-char	68.19	0.19	0.52	31.10
K-10-char	62.57	0	1.07	36.36
Ca-10-char	60.62	0	1.19	38.19

*K is potassium and Ca is calcium (numbers represent weight percentage of these elements in the sample)

The process they used was typical of a steam-iron process whereby steam and air were used to oxidise iron oxide to magnetite and haematite respectively. Their reduction step used the coal to directly reduce haematite to form iron/wüstite. High potassium (10% wt.) chars were found to be more attractive as they react at lower temperatures and give higher conversions; however they explain that the cost of adding potassium to char would currently be too expensive for commercial application.

2.4.3 Direct Feed Biomass

A concept study modelling a steam-iron process using direct feed biomass has suggested that the process would be carbon negative (if the pure carbon dioxide produced by the cyclic process is captured and stored).[66] This in simple terms means that overall carbon dioxide would be removed from the atmosphere and because of

this, the authors state that this method of hydrogen production would be competitive against conventional methods. As an enhancement, biomass can be converted into pyrolysis oil by rapidly heating the solid biomass in the absence of air.[67, 68] Pyrolysis oil exists in liquid form, which is easier to transfer compared to solid biomass.

2.4.4 Natural gas

Reaction of methane with haematite can be carried out in a step-wise process as shown below. Methane can be selected to either be fully oxidised or partially oxidised by iron oxide. This can be controlled in a circulating fluidised bed reactor by changing the methane-to-iron oxide ratio.[69] A lower ratio of methane-to-iron oxide would induce full oxidation of methane, whereas a higher methane-to-iron oxide ratio would more likely stimulate partial oxidation of methane. This will determine whether a mixture of carbon dioxide and water, or whether syngas will be formed. Methane in the presence of a low oxygen content iron oxide (or iron) can also allow methane decomposition to occur as shown by Equation (2.10).[70]

Full oxidation of methane:

$$CH_4 + 12Fe_2O_3 \rightarrow CO_2 + 2H_2O + 8Fe_3O_4 \quad (2.4)$$

$$2CH_4 + 8Fe_3O_4 \rightarrow 2CO_2 + 4H_2O + 24FeO \quad (2.5)$$

$$6CH_4 + 24FeO \rightarrow 6CO_2 + 12H_2O + 24Fe \quad (2.6)$$

Partial oxidation of methane:

$$CH_4 + 3Fe_2O_3 \rightarrow CO + 2H_2 + 2Fe_3O_4 \quad (2.7)$$

$$2CH_4 + 2Fe_3O_4 \rightarrow 2CO + 4H_2 + 6FeO \quad (2.8)$$

$$6CH_4 + 6FeO \rightarrow 6CO + 12H_2 + 6Fe \quad (2.9)$$

Methane decomposition:

$$CH_4 \rightarrow C + 2H_2 \quad (2.10)$$

In a circulating fluidised bed reactor, the methane-to-iron oxide ratio can be maintained at a continuous value during the process, whereas in a periodic reactor iron oxidation state of the OCM will change as the reaction progresses (therefore in a periodic reactor the products formed could change between carbon dioxide and water, hydrogen and carbon monoxide, and carbon with hydrogen as the step progresses and the oxygen capacity of the OCM lowers). It would therefore probably be more feasible to use a circulating fluidised bed reactor to perform methane-to-syngas conversion in a steam-iron process to allow the mole fractions of products formed to be constant.

There are important considerations for selecting either full oxidation or partial oxidation. It could be argued that the products formed by partial oxidation of methane are much more useful than carbon dioxide and water. Syngas is a useful reactant especially in the form of a hydrogen-to-carbon monoxide ratio of 2:1. This ratio is suitable for Fischer-Tropsch reactions and methanol synthesis.[70] However, the formation of syngas by partial oxidation is a much more endothermic reaction compared to full oxidation, and would therefore require higher energy input.

Go *et al.*[70] recognised that there existed a conceptual design for the steam-iron process using methane as the reducing agent, but that no experimental work had been carried out. Their investigation examined the feasibility of such a process and determined suitable conditions for operation. Experiments were carried out using

thermogravimetric analysis (TGA) to perform redox cycles with iron oxide using methane as the reducing agent. They state that a reduction temperature above 1073K (800^{o}C) and oxidation at 1173K (900^{o}C) should be used to cycle the OCM between wüstite and magnetite. It was also stated that the reduction temperature should not increase above 1148K (875^{o}C) as this would lead to carbon deposition on the OCM due to methane decomposition.

2.4.5 Hydrocarbons

Hydrocarbon fuels other than coal and biomass have been tested as potential reducing feeds in the steam-iron process, where the hydrocarbon is either initially gasified into syngas which is used for the reduction step or hydrocarbon in the solid form is used.

Residual oil (an unwanted product from petroleum refinery) was used as the reducing agent in a steam-iron process, where coke was intentionally deposited on magnetite by thermal cracking.[71] It was stated that theoretically additional oil and gas would be formed during the cracking process, but they were not characterised during the investigation. The coke deposited magnetite was transferred to an air oxidation chamber, where air was used to convert the coke to carbon monoxide, which subsequently reduced the magnetite to wüstite. The wüstite was then transferred to the steam oxidation reactor to perform water splitting. It was found that hydrogen production declined as the process continued and although material sintering was explained as the cause, it was stated that further testing was required to confirm this.

2.5 Autothermal chemical looping process for hydrogen and methanol production

In addition to using water as the oxidising agent in the steam-iron process, an air oxidation step can also be implemented to provide additional energy into the system by further oxidising iron oxide in an exothermic reaction (Equation (2.22)). Using

carbon monoxide as the reducing agent in this example, a three-step steam-iron cycle can be operated at 850^{o}C by performing the following reactions:

$$3Fe_2O_3 + 9CO \rightarrow 6Fe + 9CO_2 \qquad \Delta H^0_{1023K} = -130.6\ kJ/mol \quad (2.11)$$

$$6Fe + 8H_2O \rightarrow 2Fe_3O_4 + 8H_2 \qquad \Delta H^0_{1023K} = -190.5\ kJ/mol \quad (2.12)$$

$$\frac{1}{2}O_2 + 2Fe_3O_4 \rightarrow 3Fe_2O_3 \qquad \Delta H^0_{1023K} = -240\ kJ/mol \quad (2.13)$$

The overall process will therefore provide pure hydrogen in an exothermic reaction:

$$9CO + 8H_2O + \frac{1}{2}O_2 \rightarrow 9CO_2 + 8H_2 \qquad \Delta H^0_{1023K} = -561.1\ kJ/mol \quad (2.14)$$

An additional feature of this system is that the air-to-water ratio can be increased to provide additional energy into the system (at the cost of lower hydrogen production). This feature is particularly advantageous for a system which is slightly endothermic, such as one involving partial oxidation of methane to form syngas as the reducing step (note that in this example iron is only reduced as far as wüstite):

$$3CH_4 + 3Fe_2O_3 \rightarrow 3CO + 6H_2 + 6FeO \qquad \Delta H^0_{1023K} = 760\ kJ/mol \quad (2.15)$$

Clearly this step is highly endothermic requiring additional heat to operate. Additional heat can be generated in this system by selecting a higher air-to-water ratio. By lowering the amount of wüstite that is converted to magnetite by water oxidation, further oxidation in the air step can occur to provide additional energy

whilst converting wüstite to magnetite. The oxidation steps therefore can be represented by Equation (2.13) in addition to the following two reaction steps:

$$3FeO + H_2O \rightarrow Fe_3O_4 + H_2 \qquad \Delta H^0_{1023K} = -61 kJ/mol \quad (2.16)$$

$$\frac{1}{2}O_2 + 3FeO \rightarrow Fe_3O_4 \qquad \Delta H^0_{1023K} = -305\ kJ/mol \quad (2.17)$$

As a further modification to the process, the syngas that is formed during the reduction step can be converted to methanol (this is usually performed at 250^{o}C)[72] as an additional step in a separate reactor:

$$3CO + 6H_2 \rightarrow 3CH_3OH \qquad \Delta H^0_{523K} = -271\ kJ/mol \quad (2.18)$$

The advantage of such a step is that methanol is a useful product and can be sold in addition to the pure hydrogen obtained during the water oxidation step.[73] As the methanol synthesis reaction is exothermic, the addition of this step to the process can also provide heat to the system. The overall cyclic system is illustrated in Figure 2.4 and represented in a chemical equation by:

$$3CH_4 + H_2O + O_2 \rightarrow 3CH_3OH + H_2 \qquad \Delta H^0_{1023K} = -117\ kJ/mol \quad (2.19)$$

The process can be operated to produce pure streams of hydrogen and methanol, with no requirement of a downstream separation step to obtain these products in a pure form, and in addition to this, the process can be performed exothermically to produce heat. By further increasing the air-to-water ratio, the process could provide more energy, and depending on the importance of energy production against hydrogen production, this ratio can be adjusted. This is a practical feature that is not present in

steam methane reforming processes (which usually requires heat from an external source such as by the combustion of natural gas).

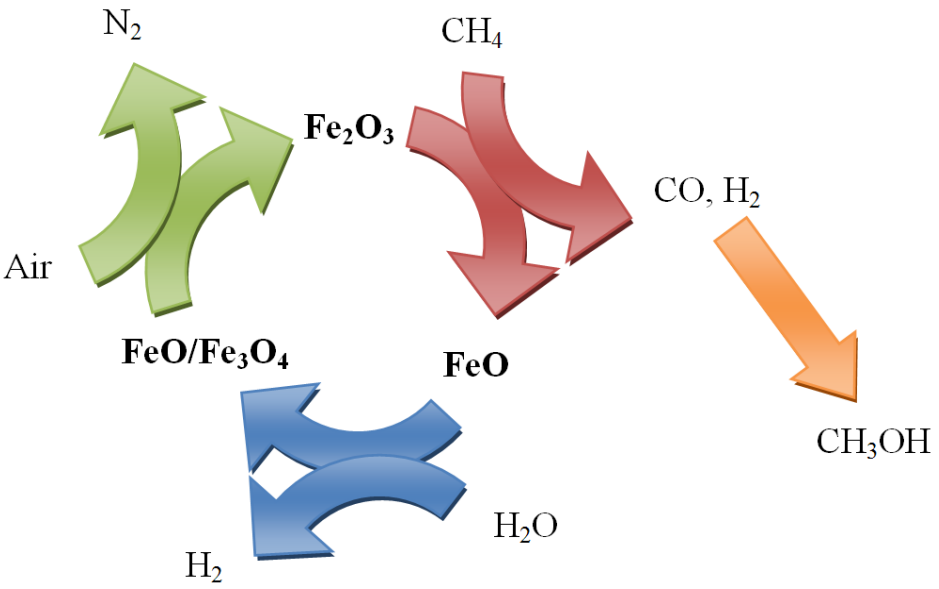

Figure 2.4 Autothermal chemical looping operation to produce inherently separate streams of hydrogen and methanol

Each individual step of this autothermal chemical looping process, such as methanol conversion from syngas and the use of an air oxidation step, has been extensively researched in the literature in separate investigations. However, it would appear that such a process as shown in Figure 2.4 has not yet been mentioned, even though it provides many practical and valuable features. A more detailed thermodynamic analysis of this process is discussed in Section 4.8.

2.6 Other uses

The steam-iron process is usually considered in the literature as a method for producing hydrogen at a localised site, but it can also be used for hydrogen production on board vehicles or in remote locations (Figure 2.5).[74, 75] It should be

noted that in the literature this process is usually called 'hydrogen storage', however it is actually the chemical potential of the reduced iron (which drives the water splitting reaction to form hydrogen) that is stored in the reduced iron and not hydrogen.[76] This method can be performed by reducing iron oxide to iron, transporting the iron to the required location, and finally oxidising the iron with water to produce hydrogen. Therefore, hydrogen is not present in the vehicle until the reduced iron is in contact with water which makes this process much safer compared to other hydrogen storage methods such as by pressurising or cryogenically cooling hydrogen (the problems of storing gaseous hydrogen has been discussed in Section 1.2.3).. Another advantage of using this method rather than transporting hydrogen includes the larger hydrogen storage capacity that it can provide.

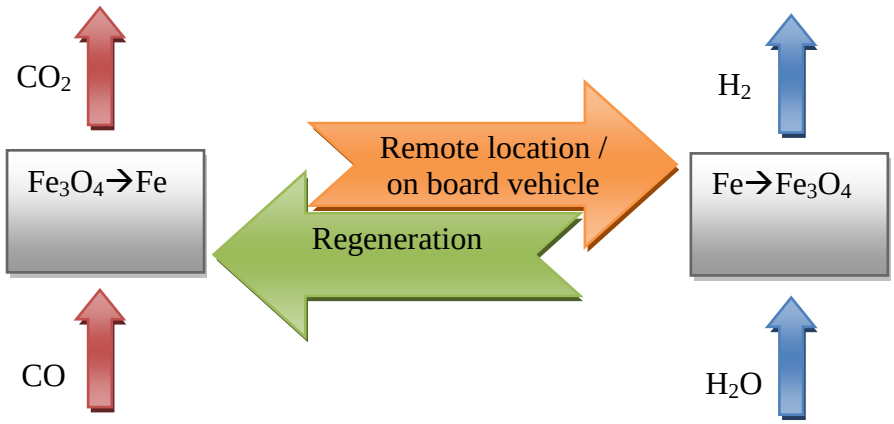

Figure 2.5 Transfer of iron to a remote location or on board a vehicle in a steam-iron hydrogen storage process

Another use of the steam-iron process is to carry out hydrogen separation from a mixture of hydrogen with other components (Figure 2.6).[77] By this method, the hydrogen mixture will reduce the oxygen carrier material, and water will be used in the subsequent oxidation step to produce very pure hydrogen. If any reducing gas such as carbon monoxide is also present in the hydrogen mixture, this may add

additional heat into the system by an additional reaction (Equation (2.11)) which would be beneficial to the process.

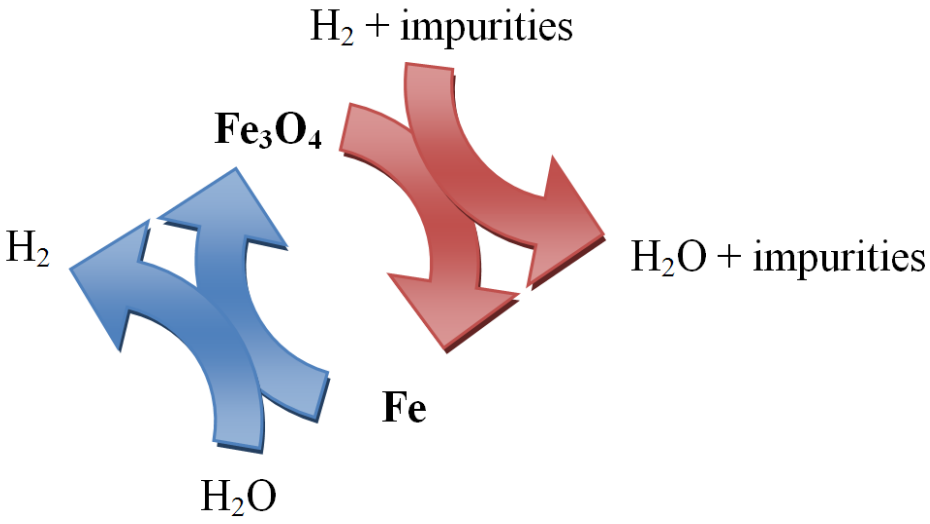

Figure 2.6 Schematic of a steam-iron process used to separate hydrogen from a stream containing impurities and other products

2.7 Other chemical looping processes for pure hydrogen production

The steam-iron process was developed and patented in the early 1900s. Chemical looping for syngas production on the other hand is a fairly recent technology and was most likely derived from chemical looping combustion (Figure 2.7), which uses a hydrocarbon fuel to reduce metal oxide, and air to oxidise the metal back to its original state. The overall reaction is a combustion reaction, however, unlike conventional combustion, the carbon dioxide formed during the fuel reduction step and unreacted nitrogen of the air oxidation step is inherently separated in chemical looping, and therefore additional treatments of the gases such as pressure swing adsorption are not required.

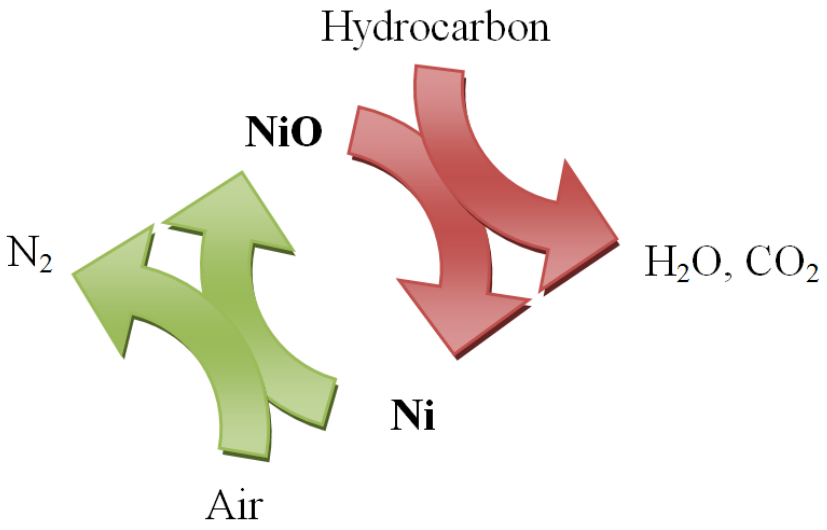

Figure 2.7 Schematic of a chemical looping combustion process using hydrocarbon as the reducing agent

The overall reaction of chemical looping combustion using methane as the fuel is shown in Equation (1.3), although any hydrocarbon could potentially be used. Instead of allowing full oxidation of the methane to occur, partial oxidation can be induced by ensuring that the oxidation of methane is restricted to only allow carbon monoxide and hydrogen production. This can be performed by increasing the methane-to-oxygen feed ratio:

$$CH_4 + \frac{1}{2}O_2 \rightarrow CO + 2H_2 \qquad (2.20)$$

This overall reaction can be performed in a chemical looping process using methane as the reducing agent and air as the oxidising agent by ensuring that a high methane feed is in contact with the OCM. In the literature this process is more commonly known as chemical looping reforming and the individual steps are shown below (this example uses nickel oxide as the OCM):

Fuel step: $$NiO + CH_4 \rightarrow Ni + CO + 2H_2 \quad (2.21)$$

Air step: $$Ni + \frac{1}{2}O_2 \rightarrow NiO \quad (2.22)$$

Syngas can be used as a reactant to synthesise many useful products such as methanol, ethylene and long chained hydrocarbons including diesel, the latter is synthesised using Fischer-Tropsch reactions. Since chemical looping reforming processes produce syngas during the chemical looping step (and not pure hydrogen), this work has not been reviewed further (although a table summarising this work has been provided in Appendix B).

Chemical looping reforming processes can be coupled with calcium looping so that both oxygen (by chemical looping) and carbon dioxide (by calcium looping) can be exchanged between separate reactant streams using solid carrier materials. This system can be represented by the schematic shown in Figure 2.8. The material used in calcium looping is often referred to as the carbon dioxide sorbent. An extensive review on carbon dioxide sorption for enhanced hydrogen production has recently been published.[78] Alternatives to calcia as the carbon dioxide sorbent have been investigated, such as magnesium oxide, barium oxide and strontium oxide, but calcia and dolomite (a natural ore composed of mainly calcia and magnesia with small amounts of silica, haematite and alumina) are the most attractive with regards to thermodynamics, cost and natural abundance.[79, 80] However, a disadvantage of this system is the high temperature required for material regeneration.

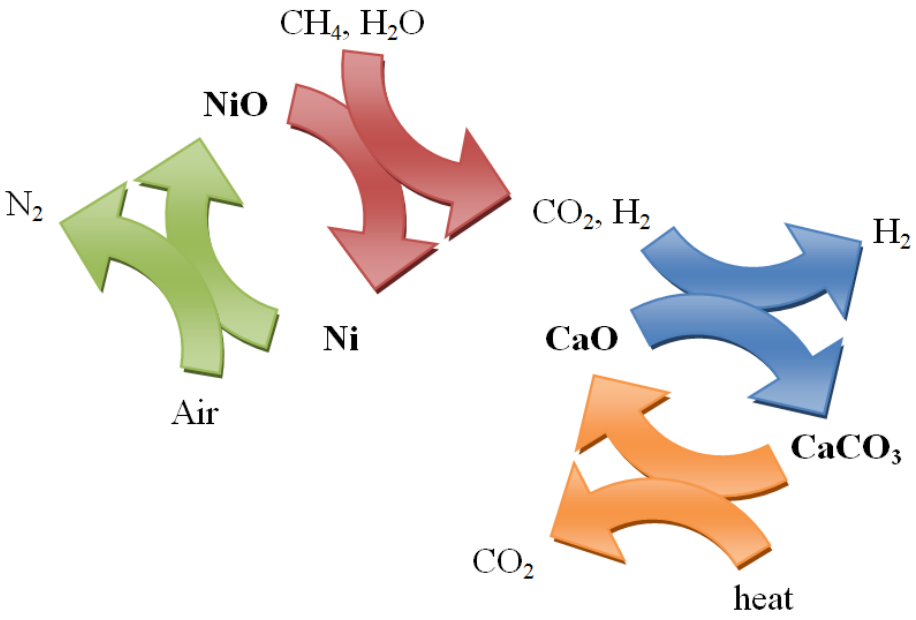

Figure 2.8 Schematic of a combined chemical looping and calcium looping process for pure hydrogen production

The combined process of chemical looping reforming and calcium looping can be used to produce pure hydrogen from a fuel such as methane by a three-step reactor system which continuously circulates nickel oxide and calcia as the solid carrier materials.[81] An air reactor can be used to oxidise nickel as shown by Equation (2.22). Calcia present in the air reactor would remain unchanged during this air oxidation step. The oxidised nickel and calcia can then be transferred to the fuel reactor where methane is added to reduce nickel oxide (Equation (2.21)). Additional water can be added to the fuel reactor to allow the WGS reaction to occur which converts carbon monoxide and water into carbon dioxide and additional hydrogen:

$$CO + H_2O \rightarrow CO_2 + H_2 \qquad (2.23)$$

The calcia present in the fuel reactor can capture the carbon dioxide to form calcium carbonate by the following reaction, leaving only pure hydrogen as the gaseous product from the fuel reactor:

$$CaO + CO_2 \rightarrow CaCO_3 \quad (2.24)$$

Removal of carbon dioxide from the fuel reactor can shift equilibrium of the WGS reaction to allow higher hydrogen production.[82] The nickel and calcium carbonate solids from the fuel reactor can then pass to a carbon dioxide desorption unit where at high temperature (above 900^{o}C) calcia is regenerated by the following thermal desorption:

$$CaCO_3 \rightarrow CaO + CO_2 \quad (2.25)$$

The overall process allows pure hydrogen production with power generation, and by altering the reactant feed ratios it is possible to optimise the process for either increased hydrogen production or increased power production.[81]

An investigation by Dupont *et al.*[80] into suitable OCMs for the process determined that nickel supported on alumina withstands the high temperatures required by the steam reforming process. In particular, low nickel loadings of around 27.5 wt. % were recommended to obtain suitable rates of reduction, which was noted as an important factor for attaining high process efficiency.

Hydrocarbons can be used instead of methane as the reducing feed for combined chemical looping reforming with calcium looping processes. Instead of fully combusting the hydrocarbon to carbon dioxide and water, it can be partially oxidised to syngas, and water can then be added to perform the WGS reaction. Following this, the carbon dioxide can be removed from the process by a calcium looping cycle. Dupont *et al.*[80] performed this process using sunflower oil as the reducing feed (using a reducing temperature of 600ºC) and dolomite as the carbon dioxide absorber, which gave 93% purity hydrogen. They state that more work is required for this process in terms of achieving autothermal operation, avoiding coking and testing for effects of impurities in the hydrocarbon source. They also suggest that other hydrocarbons such as biomass pyrolysis oils and waste (industrial and cooking) oils could be investigated as potential reducing agents.

Pimenidou *et al.*[82] used waste vegetable oil as the reducing agent, nickel supported on alumina as the OCM and dolomite as the carbon dioxide sorbent to perform six redox cycles at 600^{o}C where the main aim was to produce syngas with high hydrogen content. They carried out the redox cycles successfully with no signs of a drop in hydrogen production and recommended that further tests investigating the lifetime of the solid carriers should be performed.

2.8 Summary

Since its invention in 1903, the steam-iron process has been subjected to many modifications and improvements. The main feature of the process is the use of solid material to exchange oxygen between two or more gaseous reactant streams, and this can be performed either by keeping the solid carrier material in a fixed bed (where the redox reactions are dynamically controlled by alternative reducing and oxidising feeds) or by circulating the solids through separate reactors (where each reactor receives continuous flow of reactant gas). A further modification has been the use of different reducing agents instead of carbon monoxide (which was initially used), which can include natural gas, coal and biomass.

The overall cyclic process can be endothermic, and in these cases an external source of energy would be required. To manage this, an additional air step can be implemented into the system to further oxidise the OCM material by an exothermic reaction. It is possible to further increase energy production by reducing the water feed and increasing the air feed (although this would decrease hydrogen production).

Chapter 3

3. Oxygen Carrier Materials

3.1 Introduction

3.1.1 Properties of oxygen carrier materials

Rydén *et al.*[83] proposed the following five characteristics that indicate a suitable OCM for chemical looping:

- High reactivity with the reducing and oxidising agent
- High ratio of oxygen in the sample that can react compared to the total oxygen in the sample
- Low production of solid carbon on the material surface
- Low cost
- Low probability of fragmenting or undergoing any mechanical or thermal change that will hinder performance

All of these factors are important considerations for determining a suitable OCM for chemical looping processes. Iron oxide is a cheap material and was originally selected for the steam-iron process through thermodynamic analysis, reactivity studies and carbon deposition tests; however, material stability is still an issue that needs to be addressed and is therefore the main focus of this thesis. A material with high stability would allow the OCM to be used for many redox cycles whilst still maintaining reactivity and would therefore allow steady hydrogen production as the cycles progress.

The steam-iron process is aptly named because of the steam-iron reaction that occurs during the water oxidation step. However, in this section alternative OCMs to iron oxide are proposed (including OCMs not containing iron) and therefore this process will henceforth be referred to as chemical looping water splitting. This terminology describes a cyclic process whereby water reacts with a reduced metal or metal oxide composite to form hydrogen and the metal is then regenerated through a following reduction step with a suitable agent such as hydrogen, carbon monoxide or methane.

In this section, the properties that define a suitable OCM for chemical looping water splitting are discussed. Previous investigations have involved improving material stability and enhancing reactivity of iron oxide and this work is reviewed in detail. Iron-containing perovskite materials are also introduced as potential OCMs for chemical looping water splitting processes. The beneficial properties of perovskites that may allow these materials to undergo redox reactions without losing material stability are discussed.

3.1.2 Oxygen content

In chemical looping processes, the amount of oxygen that can be released or taken up by the OCM will influence the amount of hydrogen that can be produced during each water oxidation step. Therefore oxygen content is an important factor. The theoretical maximum amount of oxygen (of a specified weight of OCM sample) that can be exchanged during reduction and oxidation is defined as ΔO_{max}, which is expressed as:

$$\Delta O_{max} = O_{ox(max)} - O_{red(min)} \quad (3.1)$$

where $O_{ox(max)}$ and $O_{red(min)}$ are determined at a selected isothermal temperature and are the amounts of oxygen contained in the OCM following full oxidation with a specific oxidising agent (maximum oxygen capacity) and full reduction with a specific reduction agent (minimum oxygen capacity), respectively. It is important to

note that ΔO_{max} is dependent on the temperature used during isothermal operation and the reducing and oxidising feeds employed. Therefore it will vary if using different reactant feeds and operating temperatures. As an example, chemical looping using air instead of water as the oxidising feed would most likely allow a higher $O_{ox(max)}$.

It is well documented that following iron oxide reduction, water can only oxidise the metal back to magnetite, and not haematite at 850°C.[84] ΔO_{max} for iron oxide at 850°C is therefore calculated by assuming that the lowest oxygen capacity ($O_{red(min)}$) and highest oxygen capacity ($O_{ox(max)}$) are when the OCM exists as iron and magnetite respectively. ΔO_{max} in this case equals the difference in molar oxygen capacity between these two iron oxide states. For other metal oxides, such as nickel oxide, the calculation may be more straightforward as nickel can only exist as nickel or nickel oxide at 850°C.

The expression oxygen exchange, O_{exch}, is used throughout this thesis to indicate the fraction of available oxygen that the OCM exchanges during redox cycling, which is expressed as:

$$O_{exch} = \frac{|(O_{init} - O_{fin})|}{\Delta O_{max}} \tag{3.2}$$

where O_{init} and O_{fin} are the absolute initial and final oxygen contents of the OCM during a reduction or oxidation step. To provide an example of how O_{exch} is calculated, Table 3.1 provides the different molar oxygen capacities of 1 g of haematite at different oxidation states (assuming that oxygen is removed from 1 g of haematite by a reduction step to form the other oxidation states).

Table 3.1 Oxygen molar content of iron oxide following reduction of 1 g of haematite

Iron oxide composition	Total weight (g)	Oxygen molar content (mmol)
Haematite (Fe_2O_3)	1	18.75
Magnetite (Fe_3O_4)	0.967	16.67
Wüstite (FeO)	0.9	12.5
Iron (Fe)	0.7	0

If carbon monoxide and water are used as the reducing and oxidising agents to perform redox cycling at 850^{o}C, reduction of 1 g of iron oxide from magnetite to iron would result in a loss of 16.67 mmol of oxygen. Since this is the maximum amount of oxygen that can be removed from the sample under the imposed conditions (haematite cannot be formed during water oxidation), O_{exch} would be equal to one in this case. However, if air was used as the oxidising agent instead of water for the same process, and during oxidation iron was converted only to magnetite (and not haematite), O_{exch} in this case would be 0.89. This is because using air as the oxidising agent, iron oxide could theoretically be oxidised to haematite, and therefore if only magnetite had been formed following oxidation the full oxygen capacity would not have been utilised. It should be noted that whilst ΔO_{max} is a function of the OCM weight, O_{exch} has been normalised.

3.1.3 Hydrogen Purity

Carbon deposition can occur when a carbonaceous reducing agent is used in a chemical looping process (Figure 3.1). This can include carbon monoxide, methane or any other hydrocarbon source. In the reducing step, carbon deposition can occur in the presence of carbon monoxide (by the Boudouard reaction) or methane (by methane decomposition):

$$2CO \rightarrow C + CO_2 \quad (3.3)$$

$$CH_4 \rightarrow C + 2H_2 \quad (3.4)$$

These reactions usually occur in an environment low in oxygen partial pressure. The carbon can solidify and deposit on the OCM, thereby blocking active sites and lowering the activity of the OCM during the reducing step. The solid carbon formed on the OCM will then be transferred into the oxidation step, where water can react with the solid carbon to form carbon monoxide or carbon dioxide by the following reactions:

$$C + H_2O \rightarrow CO + H_2 \quad (3.5)$$

$$C + 2H_2O \rightarrow CO_2 + 2H_2 \quad (3.6)$$

Although additional hydrogen may be produced due to these reactions, carbon monoxide and carbon dioxide will also be produced during the water oxidation step.

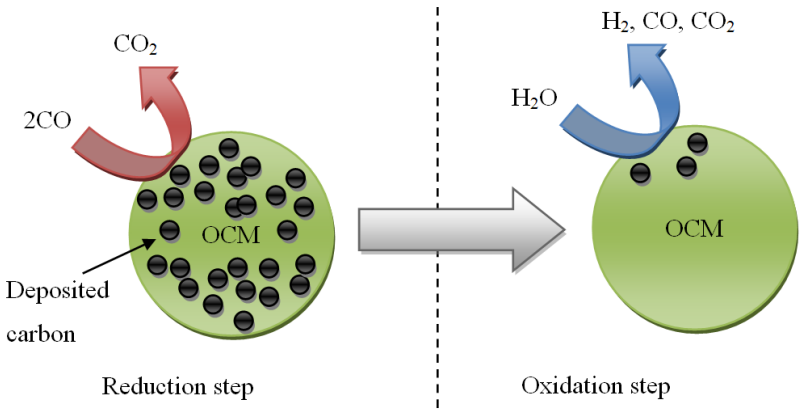

Figure 3.1 Diagram representing the mechanism for carbon deposition by the Boudouard reaction

For chemical looping processes involving pure hydrogen production, carbon deposition is undesired as it would lead to low purity hydrogen. Carbon deposition can be controlled by thermodynamics and kinetic analysis and it also greatly depends on the OCM used. As an example, iron oxide can allow the Boudouard reaction to occur above 500^{o}C in the presence of carbon monoxide, but above ~900^{o}C, the reaction is thermodynamically limited and therefore carbon deposition does not occur.[85]

Hydrogen purity is calculated using the following equation:

$$H_2\ purity = \frac{pH_2}{pH_2 + pCO + pCO_2 + pCH_4} \quad (3.7)$$

This definition is used throughout this thesis, and measures the product concentration of hydrogen during the water oxidation step (excluding the carrier gas which does not take part in the reaction steps). This calculation assumes that carbon monoxide, carbon dioxide and methane are the only species that could contaminate the hydrogen formed in the water oxidation step.

3.2 Iron oxide

3.2.1 Introduction

Iron oxide does not exist naturally in a pure form on the surface of the earth and is generally formed from iron ore. Iron ore contains principally iron oxide, but also other compounds such as silica, calcia and alumina (previous research has indicated that these additional compounds may have a positive effect on material stability of the OCM and this is reviewed later in Section 3.2.4). Iron oxide is very attractive from an economic point of view in addition to environmental and health perspectives.[86] Compared to other common OCMs used in chemical looping processes such as nickel, copper and manganese, it is much cheaper.[87]

3.2.2 Thermodynamics

Oxides of iron, nickel, cobalt, chromium and manganese have been compared thermodynamically for pure hydrogen production *via* chemical looping. The reoxidation step in water vapour for many of these oxides results in a low equilibrium hydrogen mole fraction with iron oxide appearing to be the best system from a thermodynamic point of view, the thermodynamics of this system having been investigated in detail but only at temperatures up to 900K (627^{o}C).[88-90]

Iron in the iron oxides used in the steam-iron process usually exists in one of the four oxidation states shown in Table 3.2 (repeated here for convenience).

Table 3.2 The oxidation states of iron oxide

Chemical name	Chemical formula	Oxidation state
Iron	Fe	0
Iron (II) oxide, wüstite	FeO	+2
Iron (II,III) oxide, magnetite	Fe_3O_4*	+2,+3
Iron (III) oxide, haematite	Fe_2O_3	+3

*Magnetite exists as a mixture of wüstite and haematite

Iron oxide exists as different phases depending on temperature and gas phase conditions. Wüstite is known to be iron-deficient when the iron/oxygen ratio is actually within the range of 0.83-0.95.[84, 91] Workers have either chosen a particular iron/oxygen ratio within this range or assumed that the iron oxide is not iron-deficient and this leads to, as Hacker *et al.*[84] explain, a discrepancy in data obtained during thermodynamic analysis. To avoid discrepancies and complications with thermodynamic analysis, wüstite will be assumed to be in the form of FeO unless otherwise stated in this thesis.

Thermodynamic analysis can indicate the maximum yield of products for reactions; however rate of reactions are also important, because, depending on the

enthalpy of the reaction, additional heat may be required to perform the reaction at a suitable rate. The calculation of Gibbs free energy change (*dG*) is used to determine the feasibility of a reaction occurring. The Gibbs-Duhem equation states that:

$$dG = Vdp - SdT + \sum_{i=1}^{I} \mu_i dN_i \tag{3.8}$$

where dG is the change in Gibbs free energy, *V* is volume, *p* is pressure, *S* is entropy, T is reaction temperature, μ is chemical potential of component *i* and *N* is the number of moles of component *i*. At constant temperature and pressure:

$$dG = \sum_{i=1}^{I} \mu_i dN_i = \sum_{i=1}^{I} \mu_i v_i dX \tag{3.9}$$

where v_i is the stoichiometric coefficient and dX is the change in extent of reaction. By rearranging Equation (3.9):

$$\left(\frac{dG}{dX}\right)_{T,P} = 0 = \sum_{i=1}^{I} \mu_i v_i \tag{3.10}$$

The chemical potential of component *i* is calculated by:

$$\mu_i = \mu_i^o + RT \ln a_i \tag{3.11}$$

where μ_i^o is μ_i at standard conditions, *R* is the gas constant (8.314 J mol^{-1} K^{-1}) and a_i is activity of component *i*. Therefore by combining Equations (3.10) and (3.11), the following can be derived:

$$\sum v_i \mu_i^o + \sum RT \ln {a_i}^{v_i} = 0 \quad (3.12)$$

therefore:

$$\Delta G_R^0 + \sum RT \ln {a_i}^{v_i} = 0 \quad (3.13)$$

and therefore:

$$\Delta G_R^0 = -RT \ln K_p \quad (3.14)$$

where K_p is the gas constant at a constant pressure. Of particular importance is the use of dG to derive phase-diagrams. When the reaction is in equilibrium, Gibbs free energy can be expressed as:

$$\Delta G = -RT ln K_{eq} \quad (3.15)$$

where K_{eq} is the equilibrium constant. Hence, for reactions taking place between a gas and a solid, a phase diagram can be derived by plotting K_{eq} against temperature. The Baur-Glaessner phase diagram (which indicates the oxidation states of iron oxide at different temperatures in the presence of either a mixture of carbon monoxide and carbon dioxide or a mixture of hydrogen and water) was used by Bleeker *et al.*[67] to thermodynamically analyse iron oxide and is shown in Figure 3.2. This is a very useful plot as it can be used to determine the oxidation state of the iron oxide under different feeds (carbon monoxide/carbon dioxide or hydrogen/water) at different temperatures ranging from 400-1000^{o}C. Also, it can be used to determine the expected gaseous product yield. As an example at 800^{o}C, iron (Fe) in the presence of water will oxidise to wüstite ($Fe_{0.945}O$) whilst providing a maximum

hydrogen yield of ~65%, whereas wüstite ($Fe_{0.945}O$) in the presence of water will oxidise to magnetite (Fe_3O_4) whilst providing a maximum hydrogen yield of ~40%. These calculations are indicated by dashed lines in Figure 3.2.

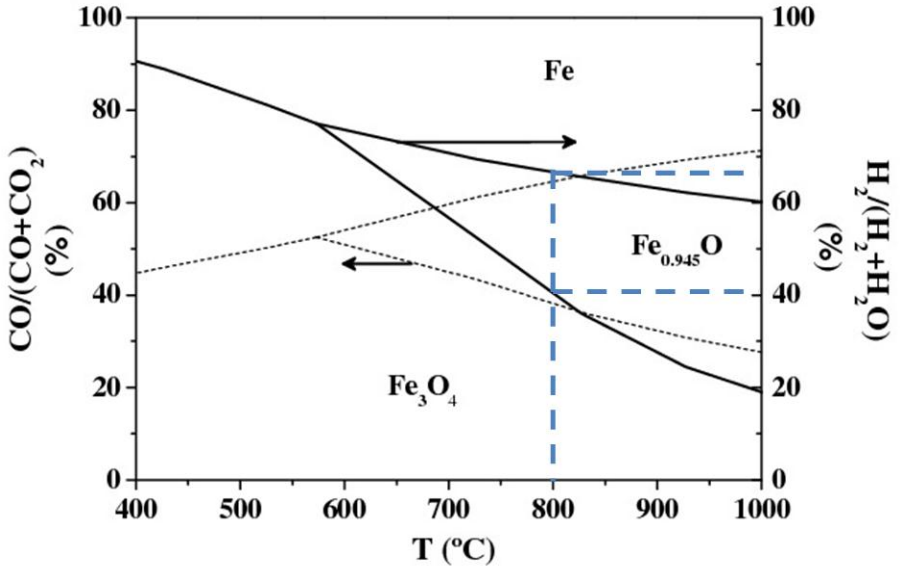

Figure 3.2 Baur-Glaessner phase diagram depicting these different phases taken from Bleeker *et al.*[67]

Figure 3.2 indicates that wüstite only exists at temperatures above ~565°C, which is in agreement with other thermodynamic studies which state that temperatures below 567°C causes instability of wüstite and that only iron-magnetite would be thermodynamically stable.[90, 92, 93] Haematite cannot exist in the presence of a water/hydrogen ratio less than 10^5, however in the presence of air or oxygen it can exist.[94]

The reactions that can occur between water and iron/iron oxide are shown below. These reactions would occur in a step-wise process:

$$H_2O + Fe \rightarrow H_2 + FeO \qquad (3.16)$$

$$\frac{1}{3}H_2O + FeO \rightarrow \frac{1}{3}H_2 + \frac{1}{3}Fe_3O_4 \quad (3.17)$$

In early steam-iron processes, carbon monoxide obtained by the gasification of coal was used as the reducing agent:

$$CO + Fe_3O_4 \rightarrow 3FeO + CO_2 \quad (3.18)$$

$$CO + FeO \rightarrow Fe + CO_2 \quad (3.19)$$

Using a carbonaceous reducing agent can be detrimental to the overall chemical looping process, as carbon can usually form a solid layer upon the surface of the OCM. Reducing agents used in early steam-iron processes have been 'producing gas' (products from gasification of coal), carbon monoxide or syngas. These reducing agents contain carbon monoxide which could potentially cause carbon deposition *via* the Boudouard reaction:

$$2CO \rightarrow C + CO_2 \quad (3.20)$$

The reaction of iron oxide with carbon monoxide has been studied by Mondal *et al.* who produced a plot (Figure 3.3) presenting the Gibbs free energy of the reactions shown.

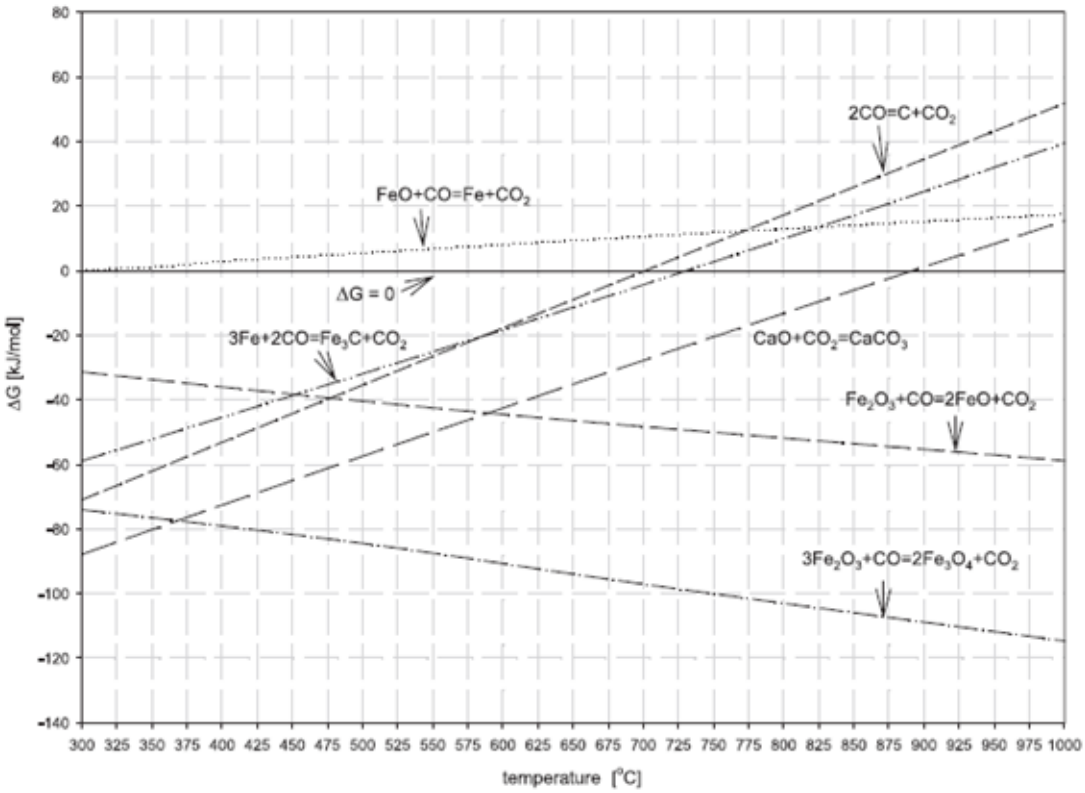

Figure 3.3 Phase diagram showing Gibbs free energy for iron oxide reactions with carbon monoxide taken from Mondal *et al.*[85]

As ΔG from the Boudouard reaction in Figure 3.3 shows, the production of solid carbon by this reaction can be lowered by an increase in temperature. This finding agrees with the work of Gasior *et al.*[22] which proved that increasing temperature above a certain point reduces carbon deposition. According to Figure 3.3, lowering temperature should theoretically produce more carbon from a thermodynamic point of view. However due to kinetic limitations, the rate of reaction for the Boudouard reaction would decrease as the temperature is lowered and this would lead to lower carbon deposition. Hence, there would be a particular temperature associated with maximum carbon deposition.

Sulphur and sulphur-containing species such as hydrogen sulphide can be present in coal, biomass and natural gas, and unless the feeds are cleaned by a desulphurisation step before use, sulphur will also be present in the chemical looping process. Wang *et al.*[95] have investigated the effects of sulphur on iron oxide in

chemical looping processes using thermodynamic analysis. They suggest that at higher temperatures and in an oxygen enriched environment, hydrogen sulphide compounds present in the reducing feed would convert to sulphur dioxide and hydrogen sulphide, whereas at lower temperatures and in an oxygen-deficient environment sulphur may react with the iron oxide. A study by Huebler *et al.*[58] proved that a small amount of sulphur in the form of hydrogen sulphide (0.1-0.5%) in the reducing feed can actually improve the overall process by minimising carbon monoxide production in the water oxidation stage by inhibiting carbon formation, although in their paper an explanation for this phenomenon is not provided.

3.2.3 Kinetic models

Before the reactant gases can react with the solid OCM during the reduction and oxidation steps, they must transfer from the gas phase to the surface of the OCM and diffuse through the porous layers of the OCM. The gas is then adsorbed onto the active sites of the unreacted OCM layer where finally the gas-solid reaction occurs. The gaseous product formed then returns to the bulk gaseous stream by desorption and diffusion back through the porous layer out of the OCM.[96] This is the general description of a gas-solid interaction, but the actual gaseous reaction is not this simple and in most cases the steps that occur can be more complicated. There are two simple kinetic models that can be used to describe the gas-solid interactions in chemical looping processes, and these are the shrinking core model and crackling core model.

The shrinking core model was considered by Alamsari *et al.*[97] and is shown in Figure 3.4: in this example iron oxide is used as the OCM and syngas as the reducing agent. In this model, all of the oxidation states of iron oxide are assumed to be porous and have the same porosity.

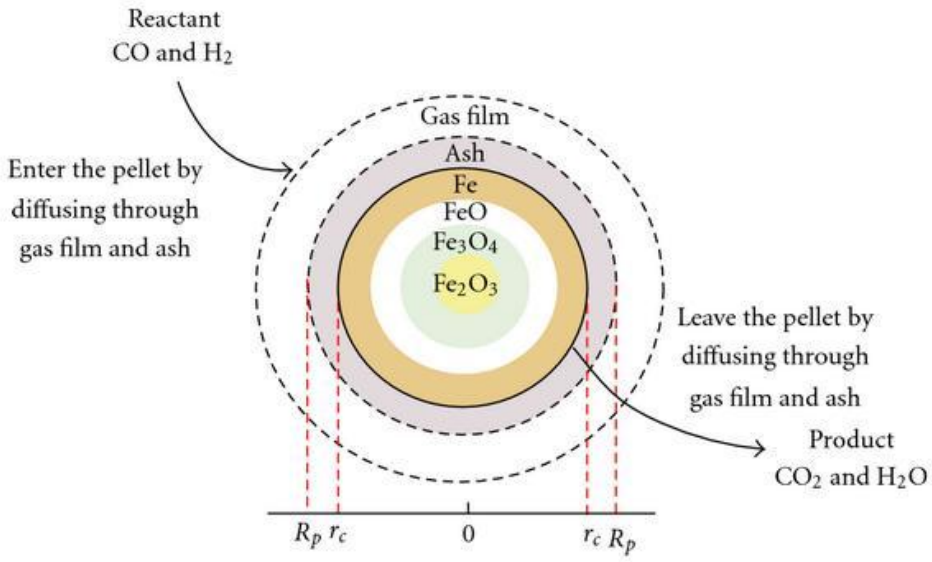

Figure 3.4 Diagram of the shrinking core model of an iron oxide pellet in a chemical looping process taken from Alamsari *et al.*[97]

This model considers the formation of different iron oxide compositions as layers within the pellet where the boundaries are sharply defined. Figure 3.4 shows at the centre of the pellet the most oxidised form of iron oxide (haematite) and gradually the oxidation states of iron oxide decreases progressively away from the centre. The steps of the kinetic model involve firstly diffusion of the syngas through the gas film and ash (deposited carbon) surrounding the pellet. Assuming that the entire OCM initially exists as fully oxidised (haematite), the gas reduces the OCM at the surface (haematite to magnetite) but also permeates through the OCM starting from the outside of the pellet through to the core. The thickness of each oxidation layer is therefore dependent on the gas diffusivity of the OCM. Faster diffusion allows quicker reduction of the entire OCM.

An alternative approach to modelling these interactions is by the crackling core model which assumes that the gas diffusivities for the four different states of iron oxides are not the same. This would suggest that as haematite is reduced to magnetite, and so forth, the gas diffusivity through the layers would also change. It is assumed that as iron oxide is reduced it becomes more porous and therefore allows higher gas diffusivity. Out of these two models, the shrinking core model is simpler

to use but less accurate (as only three different diffusion modes, through the gas film, ash and bulk OCM, are considered in this case).[76] Both models can also be used to describe oxidations of the OCM with water or carbon dioxide.

The shrinking core and crackling core models are two of the simpler kinetic models that have been applied to chemical looping processes. More detailed models can consider the nucleation of active sites (Figure 3.5), which has been used to kinetically model the oxidation step in steam-iron processes using the Johnson-Mehl-Avrami-Kolmogorov (JMAK) equation.[98] This model assumes that grain size impacts on the overall rate of reaction.

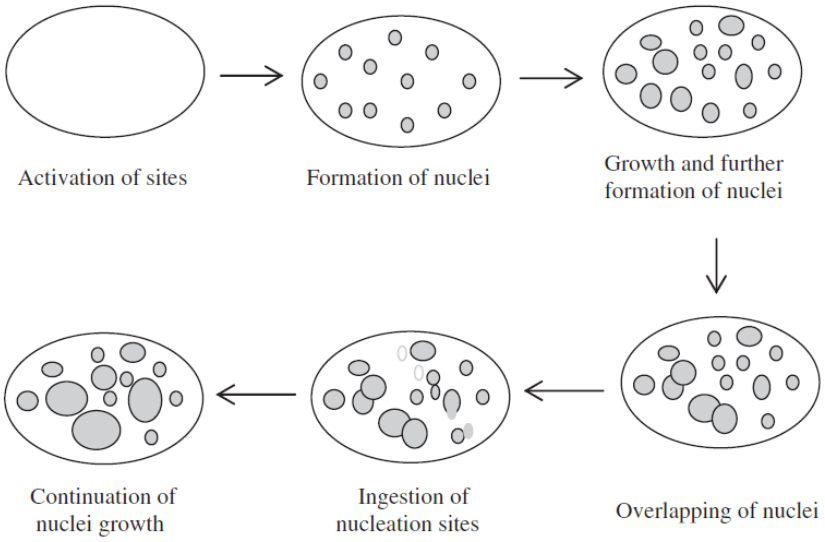

Figure 3.5 Nucleation process to form active sites on an OCM

Nucleation initiates by the formation of active sites upon the OCM surface. These active sites allow the reduction to occur rapidly, and this leads to the quick growth of reduced regions known as nuclei. As the nuclei grows, the reduced regions overlap and merge together as shown in Figure 3.5.

In a previous study, to maintain accuracy of the kinetic models, the three models shown above (shrinking core, crackling core and nucleation) have been used in combination to derive an accurate kinetic model of the reduction of iron oxide.[77]

As the main focus of this thesis is the stability of OCMs during chemical looping processes these kinetic models will not be used for further analysis of the process but it has been outlined here for the purpose of illustrating the reduction and oxidation mechanisms.

3.2.4 Stability

Cyclability of iron oxide is a major issue during the steam-iron process. Poor cyclability leads to reduced hydrogen production to the point at which the iron oxide needs to be replaced.

A recent investigation by Bohn *et al.*[94] tested the cyclability of iron oxide. The aim of the study was to see if reduction to iron resulted in excessive loss of surface area and a decrease in carrier performance. They carried out 10 cycles of reduction and water oxidation at three different temperatures (600, 750 and 900^{o}C). In one set of experimental runs the iron oxide was reduced using carbon monoxide as the reducing agent (this was expected to produce iron) and in another run the iron oxide was reduced in an equimolar mixture of carbon monoxide and carbon dioxide (this was expected to produce wüstite). Note that the reductions to iron and wüstite are controlled thermodynamically through use of a carbon monoxide/carbon dioxide mixture. In the case of iron formation the reactions would be:

Reduction: $$Fe_3O_4 + 4CO \rightarrow 3Fe + 4CO_2 \quad (3.21)$$

Oxidation: $$3Fe + 4H_2O \rightarrow Fe_3O_4 + 4H_2 \quad (3.22)$$

In the case of wüstite formation the reactions would be:

Reduction: $$Fe_3O_4 + CO \rightarrow 3FeO + CO_2 \quad (3.23)$$

Oxidation: $3FeO + H_2O \rightarrow Fe_3O_4 + H_2$ (3.24)

From these reactions it is clear that the oxidation of iron to magnetite would produce four times the molar amount of hydrogen per redox cycle than oxidising from only wüstite.

The results from their study indicated that each reduction in carbon monoxide/carbon dioxide produced a small but constant amount of hydrogen over the 10 cycles for all three temperatures. However, for the runs involving reductions in carbon monoxide, initially higher amounts of hydrogen were produced but this dropped to very low amounts as the cycles progressed. The results confirmed that reduction to iron instead of wüstite does indeed allow the production of larger amounts of hydrogen initially, but at the cost of a drop in hydrogen production as the cycles progress. In a redox cycle where stability of the material is important, it would be preferred to produce slightly lower amounts of hydrogen but at a constant level over a larger number of cycles. Useful material characterisation, which may have determined the cause for deterioration of the OCM such as sintering, was not performed in this study.

The experiment was then repeated with fresh material but this time including an additional air oxidation step for every cycle. This step would convert magnetite to haematite:

$$\frac{1}{2}O_2 + 2Fe_3O_4 \rightarrow 3Fe_2O_3 \quad (3.25)$$

Using an air oxidation step showed marginal difference in hydrogen production levels, but it was noted that the benefits of adding the step would be heat production and removal of carbon impurities from the OCM.

An alternative approach to improving stability rather than introducing carbon dioxide into the reducing feed is to add a support material to the iron oxide.[99, 100] The concept of this method is to construct a material that inhibits surface area loss even

when the carrier is reduced to iron (the reduction to iron allowing greater hydrogen production per cycle than reduction to wüstite). The use of iron oxide composites, by the co-precipitation of iron oxide with additional oxides has been attempted. Bohn *et al.*[99] modified iron oxide by impregnation with salts of aluminium, chromium, magnesium and silicon by a co-precipitation method. Steam-iron cycles were carried out using carbon monoxide or hydrogen as the reducing agent at 1123K (850^{o}C) both with and without air addition. Out of the different salts tested, the addition of aluminium gave the greatest improvement in cyclability compared to unsupported iron oxide.

Kierzkowska *et al.*[100] compared four samples of composite iron oxide and alumina synthesised by the sol-gel method with different iron oxide-to-alumina mass ratios. These four ratios were 60:40, 80:20, 90:10 and 100:0. From performing 40 redox cycles using carbon monoxide as the reducing agent and water as the oxidising agent, oxygen carriers with a loading of 10-20% of alumina gave a small drop in activity and hydrogen conversion, whereas the sample with a loading of 40% alumina gave no drop in performance over all 40 cycles. They explain that during the initial cycles, the iron oxide reacts with alumina to form the spinel ($FeO.Al_2O_3$) and this stabilises the OCM, leading to steady hydrogen production. For this reason, they select 60% haematite supported on alumina (60% Fe_2O_3/Al_2O_3) as the best candidate oxygen carrier material for the steam-iron process over 40 cycles.

Sponge iron, also known as direct reduced iron, has also been used as an OCM for the steam-iron process. It is described as an iron-containing metal oxide that is formed by reducing iron ore with either natural gas or coal.[101] Some researchers have attempted to simulate direct reduced iron by reacting haematite with carbon to form iron oxide-carbon composite pellets.[102] Sponge iron produced by the first method usually contains other minerals such as silica, quicklime and alumina[103] whereas the second method would form material containing only carbon and iron oxide. Sponge iron used in experiments are obtained either by purchasing the material in the form of commercial iron ore pellets or by synthesising it in the laboratory by adding alumina, silica and quicklime to pure iron oxide. It appears that no direct comparison was made between these materials and pure iron oxide and so the benefits of the additives cannot be concluded explicitly from these results. Two

particular forms of iron ores have been under investigation, which are the commercial iron ore pellets SEK and Malmberget (the compositions of these materials are shown in Table 3.3).[103]

Table 3.3 Compositions of Sek and Malmerget Pellets as a percentage of total weight used in the study performed by Selan *et al.*

	Sek	Malmberget
Fe	57.83	66.70
SiO_2	7.96	1.16
Mn	0.03	0.06
CaO	3.91	1.21
O	1.04	0.81
Al_2O_3	0.39	0.33
P	0.01	0.033
S	0.024	0.001
Na	0.075	0.045
Ti	0.025	0.10
K	0.094	0.03
Zn	0.025	0.0038
Pb	0.001	0.0002

These commercial iron ore pellets were tested as potential oxygen carrier materials for the sponge-iron process by Selan *et al.*[103] who carried out two sets of experiments by performing 20 cycles of reduction and water oxidation using hydrogen and carbon monoxide as the reducing agents. For both experiments, a gas chromatograph was used to measure gas concentrations, but the results were converted into and presented as weights of oxygen uptake and release from the material during oxidation and reduction. For the hydrogen reduction experiments, they also presented the weight of water formed. Additional results (not provided in the paper) apparently showed that using carbon monoxide as the reducing agent allowed the production of very

pure hydrogen with trace amounts of carbon monoxide and carbon dioxide in the hydrogen product stream. However, the term 'trace' is fairly vague and does not give the reader an idea of the actual amount produced. Low levels of 50 ppm carbon monoxide could be considered by some as 'trace' amounts, but even these levels could poison a PEM fuel cell. In terms of stability, both materials were able to perform 20 cycles of reduction and oxidation with only a small decrease in performance. Using hydrogen as the reducing gas allowed 20 redox cycles using the Sek pellets without any decrease in performance. This is explained briefly by the fact that the Sek pellets contain a higher percentage of inert components which would stabilise the material.

Further experiments with Sek iron ore pellets were carried out by Hacker *et al.*[84] using gas mixtures representing 'syngas derived from biomass' as the reducing agent. In their paper they named these iron pellets as 'SEK new pellets'. Although they mention that they carried out experiments using many iron ore pellets, they only mention SEK new pellets in the paper and present data for only that one material. SEK new pellets were not characterised in terms of composition or properties. Hacker *et al.*[84] tested the compressive strength of SEK new pellets for all four possible oxidation states of iron oxide. Their study found that out of the four possible iron oxide phases wüstite had the lowest compressive strength, followed by iron, magnetite and haematite, however they state that these compressive strengths were all high enough to withstand pressure in a steam-iron process.

Kindermann *et al.*[104] investigated how haematite content affects performance in steam iron processes using hydrogen and carbon monoxide as reducing agents and sponge iron as the OCM. Two different haematite weight contents of 85% and 88% were tested with additional compositions of silica (0-10%), alumina (2-5%) and calcia (0-10%) and the results showed that the samples with 88% haematite were more stable, as the 85% haematite samples were more likely to deactivate by losing oxygen capacity or fragmenting. However, the mean pore radius for samples containing 88% haematite was found to increase during operation, whereas the mean pore radius for 85% haematite samples decreased. Previous studies have shown that alumina, which is an unreactive species in this process, reduces sintering of the

material and so performance would be improved by increasing alumina composition.[105]

Concerning silica content, a higher content of silica proved to give better results in terms of improved porosity and reduced deactivation.[104] From performing tests using various samples containing 0-10% silica, 10% silica gave the best results by showing least reduction in surface area over 5 redox cycles. Scanning electron microscopy (SEM), X-ray diffraction (XRD) and mercury intrusion porosimetry analysis all confirmed that a higher silica content would avoid sintering and increase the lifetime of the material. TGA studies of the sponge-iron process using hydrogen and water as the reducing and oxidising agents saw a large improvement when using a sponge iron material with a higher composition of silica, which gave a higher rate of reaction and larger degree of material oxidation. The presence of calcia in the sample caused production of calcium ferrite ($Ca_2Fe_2O_5$).

So far only a small combination of sponge iron composites have been tested, but the results have shown that increased silica improves porosity and stability of the material with reduced sintering. However, results have also shown that the addition of alumina can improve performance by reducing sintering.

Further tests using different reducing agents and operating temperatures show that changing experimental conditions can effect which compositions of the sponge iron material would give the best performance. Hacker *et al.*[106] suggest that the acidity or alkalinity of the sponge iron pellet is a determining factor. Alkalinity was calculated by:

$$Alkalinity = \frac{\%\, CaO + \%\, MgO}{\%\, SiO_2 + \%\, Al_2O_3} \qquad (3.26)$$

Their results indicated that a higher alkalinity above an operating temperature of 600^{o}C gave higher reaction rates, whereas below this temperature a higher alkalinity gave lower rates.

Hacker *et al.*[104] looked at different compositions of iron oxide pellets with alumina, silica and calcia. TGA, SEM, XRD and mercury-porosimetry were used for characterisation of the fresh and used pellets. Different oxidisation states of iron oxide were seen in the catalyst and the pellets were described as either compact, porous or whisker like. The porous pellets appeared to be most beneficial for cycling. Silica appeared to have some beneficial structural affects in maintaining pore volume. However, during this experiment, the sum weight percent of silica and calcia were always equal to 10%, which means that the benefits seen by adding silica may actually be due to the absence of calcia.

Galvita *et al.*[107-109] performed stability studies for iron oxide using cerium, lanthanum and zirconium as promoters. 80% Fe_2O_3-$Ce_{0.5}Zr_{0.5}O_2$ was used to perform 100 redox cycles using syngas reduction and water oxidation steps but showed a considerable drop in hydrogen production (~50% drop). By additionally doping 2% molybdenum onto the structure to form 2% Mo- 80% Fe_2O_3-$Ce_{0.5}Zr_{0.5}O_2$ steady hydrogen production over 100 redox cycles was recorded.[110] Adding zirconia and ceria-zirconia oxide to iron to form Zr_2O_3-Fe_3O_4-$CeZrO_2$ also allowed steady hydrogen production over 100 cycles (using syngas as the reducing agent and steam as the oxidising agent).[111]

It is clear that although iron oxide is thermodynamically suitable for the steam-iron process, there are issues with material stability that could arise during operation. Loss of activation can be caused by either material sintering or carbon deposition (during the reduction step) and also by loss of material in the reactor due to material fragmentation. The formation of iron was found to elevate material instability, and attempts have been made to avoid iron formation through the addition of carbon dioxide or water to the reducing feed. This would alter the thermodynamics of the system to prevent the formation of iron. However, avoiding the formation of iron gives a reduction in the total amount of hydrogen that can be produced during the water oxidation step, which is a disadvantage.

It appears that 100 cycles are the most that have been performed in a chemical looping water splitting process where the OCM remained stable and allowed steady hydrogen production.[111] This process utilised iron composites as the OCM where other metal oxides such as ceria oxide would take part in the redox

cycles. Out of the materials tested where only iron oxide took part in the redox cycles, 60% Fe_2O_3/Al_2O_3 appears to be the best performing OCM in terms of material stability.

3.2.5 Reactivity

A catalyst is defined as a substance which enhances the rate of a reaction without being consumed by the reaction itself.[112] From an overall perspective, an OCM utilised in chemical looping processes behaves like a catalyst as it allows the reduction and oxidation reactions to occur but following each redox cycle remains unchanged. In order for the OCM to be suitable for a chemical looping process, it should allow the reactions to occur rapidly thereby lowering the reduction and oxidation cycle times and this is controlled by thermodynamics and kinetics. Generally, in chemical looping processes the rate of a reaction can be increased by raising temperature, which provides a larger amount of kinetic energy to the process. However, thermodynamics may be favoured by an increase in temperature if the reaction is endothermic or by a decrease in temperature if the reaction is exothermic (in accordance to Le Chatelier's principle).

Recently, the use of iron oxide doped with transition metals have been used to improve reaction rates of the steam-iron process. Otsuka *et al.*[74] added various metals (less than 3 mol. %) to iron oxide by co-precipitation. In particular the focus was to accelerate rates of reactions so that lower operating temperatures could be used. Experiments were performed at 330^{o}C and hydrogen was always used as the reducing agent (oxidation was performed with water). XRD analysis was only carried out on iron oxide samples with gadolinium and zirconium additives and the results indicated that there was no interaction between the additives and iron oxide to form new compound oxides). Since phase composition and surface area characterisation was only performed for those additives, the work is of limited direct value for understanding the role of the additives. In terms of reactivity during water splitting, aluminium, chromium, molybdenum, gadolinium and vanadium gave the best performance (Figure 3.6) although BET analysis before and after redox cycles indicated that severe sintering had occurred in each case.

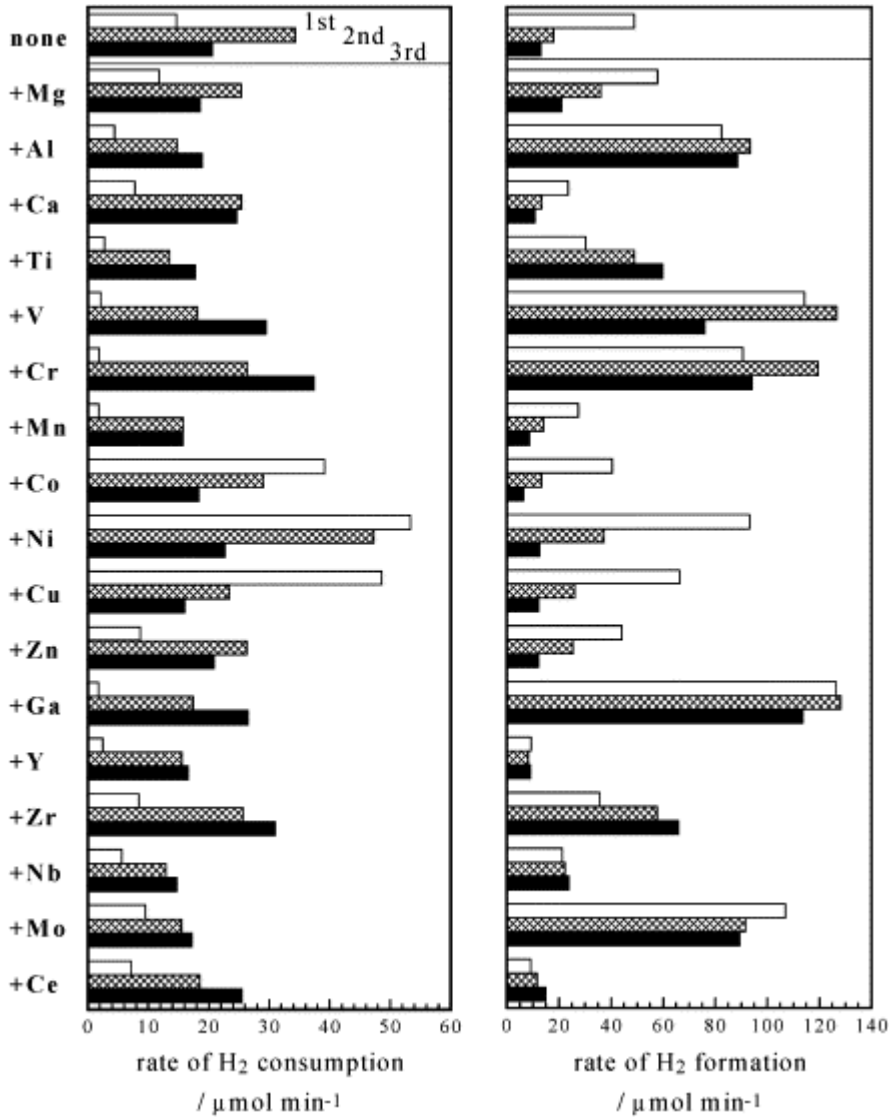

Figure 3.6 Average rates of redox reactions for iron oxides with and without additives taken from Otsuka *et al*.[74] Rates for first, second and third cycles

A following study (comparing 26 different metal additives) indicated that aluminium, molybdenum and cerium additives gave the largest improvement for stability and increased hydrogen production, although it was stated that scandium, titanium, vanadium, chromium, yttrium and zirconium also showed improvements of stability compared to pure iron oxide. Additionally, the noble metals ruthenium, rhodium, palladium, silver, iridium and platinum enhanced water splitting (with rhodium showing the largest improvement).[75] None of the noble metal additives

could suppress sintering. It was therefore suggested that a combination of rhodium (which improved water splitting) and molybdenum (which improved stability) could together improve performance further. Carrying out five redox cycles using iron oxide containing both rhodium and molybdenum (Rh:Mo:Fe = 3:3:94), showed high stability and constant high hydrogen production over five cycles. These results were confirmed by Takenaka *et al.*[113] who further tested molybdenum and rhodium additives by comparing iron oxide samples containing only molybdenum, only rhodium and a mixture of both. SEM analysis showed that the addition of molybdenum prevented sintering.

Urasaki *et al.*[114] tested the additives palladium and zirconium on iron oxide as an alternative steam-iron oxygen carrier material. In both cases, only small amounts (0.23 mol%) were added to iron oxide, and the reduction and oxidation rates were measured with a tapered element oscillating microbalance (TEOM) during cycles of reduction by hydrogen and oxidation by water at 723K (450^{o}C). Zirconium had little effect on the reduction step, however, palladium addition increased the reduction rate by 21% compared to unmodified iron oxide. Both palladium and zirconium improved oxidation rates, but palladium gave the biggest improvement of a 55% increase in oxidation rate compared to zirconium, which only gave a 26% increase.

For high temperature (800-900^{o}C) steam-iron processes with methane as the reducing agent, Komada *et al.*[115] considered the mixed metal oxides of iron oxide with the general formula $M_{0.39}Fe_{2.61}O_4$, where M represents either nickel, cobalt or zirconium, as alternative modified carriers (prepared by the "oxidation method of aqueous suspensions"). XRD analysis was performed to verify the synthesis of these mixed metal oxides. $Ni_{0.39}Fe_{2.61}O_4$ produced a much larger yield of syngas compared to the same composition with cobalt or zirconium in place of nickel. In an additional test, zirconia was used as a support material to reduce sintering in further tests using $Ni_{0.39}Fe_{2.61}O_4$. Post operation XRD analysis of $Ni_{0.39}Fe_{2.61}O_4/ZrO_2$ showed no evidence of change to the original sample, indicating excellent stability following redox cycling. Hydrogen yields of ~20% were obtained, however carbon deposition was noted. In a further test, $Ni_{0.39}Fe_{2.61}O_4/ZrO_2$ was successfully used as the oxygen carrier material in a steam-iron process with solar energy being used to provide the heat.

Peña *et al.*[77] carried out tests to compare the performance of $NiFe_2O_4$ and $CuFe_2O_4$ compared to pure iron oxide. This investigation only studied the reduction step and showed that for both cases where methane and hydrogen were used as the reducing agents, $CuFe_2O_4$ allowed the reduction to start at a lower temperature compared to $NiFe_2O_4$ which in turn was an improvement over iron oxide. The performance of these mixed metal oxides during the oxidation step was not tested in the investigation. Due to its attractiveness $CuFe_2O_4$ was used to carry out cycles of methane reduction (900^{o}C) and water splitting (800^{o}C) by Kang *et al.*[116] and the results showed faster reduction kinetics, lower carbon deposition and higher selectivity for partial oxidation when using this material instead of iron oxide. However, there were no experiments involving the oxidation step (which may have showed a reduction in performance compared to using iron oxide). Further tests were carried out using zirconia and ceria as a support material to $CuFe_2O_4$ and the results showed that both supports improved methane conversion and material stability.[117] After 11 redox cycles using methane reduction and water oxidation, the ceria-supported material gave a high reactivity compared to the zirconia-supported material. Although water oxidation was performed, these studies only focused on methane-to-syngas conversion during the reduction steps, and therefore hydrogen production during the water oxidation steps was not mentioned. To determine whether these materials could be used in a chemical looping process to produce pure hydrogen, the oxidation step would require further investigation.

3.2.6 Alternative oxygen carrier materials

Chemical looping processes using water oxidation have previously been investigated using OCMs that do not contain iron. Miyamoto *et al.*[118] in 1984 tested germanium oxide supported on alumina as a possible OCM and directly compared it to iron oxide (hydrogen was used as the reducing agent). The results showed that the germanium oxide only provided higher yields of hydrogen during water splitting compared to iron oxide when it was supported with alumina (in these tests the iron oxide was only used without a support). This result was consistent over the temperature range 300-700^{o}C. Results from XRD analysis suggested that the germanium oxide had spread over the alumina support, which was used to explain

the increase in hydrogen yield compared to using no support. The effect of further modifying the OCM using additives was tested at 700^{o}C, and the results showed that yields of hydrogen during water splitting could be increased by using nickel additives. These candidate materials were never compared to supported iron oxide.

A two-step chemical looping water splitting process using methane as the reducing agent was tested by Kodama *et al.*[119] using various metal oxides including tungsten oxide, which gave the best reactions rates for the reduction step even when compared to iron oxide. However, there appears to be no comparison between the different materials for the water splitting step. In a further test, tungsten oxide supported of silica, alumina and zirconia was used to perform one redox cycle of methane reduction and water oxidation, and the support of zirconia gave the most improvement in reactivity for both the reduction and oxidation steps. It was concluded that tungsten oxide could perform redox cycling to produce syngas and hydrogen from methane reduction and water oxidation at 1273K (1000^{o}C) without allowing carbide formation.

Otsuka *et al.*[120] performed redox cycles using ceria as the OCM (using hydrogen or carbon monoxide as the reducing agent and water as the oxidising agent) but iron oxide was not used as a comparison material in this study. By performing cycles of reduction in hydrogen at 873K (600^{o}C) and water oxidation at 573K (300^{o}C), a decrease in surface area of the material was seen over seven cycles, although this did not seem to reduce rates of reactions. The addition of palladium, platinum and nickel oxide gave a very small increase in rates of reduction, but significantly improved water oxidation rates. However, the effects of the additives upon material surface area or cyclability was never tested.

3.3 Iron-containing perovskite-type materials

3.3.1 Introduction

Of particular interest to this investigation are perovskite-type mixed metal oxides, which have previously been utilised as oxygen exchanging membranes and for OCMs in chemical looping combustion. Unlike simple metal oxides, these materials

can exchange oxygen without undergoing a phase change due to the ability to easily form and deplete oxygen vacancies within the lattice structure. This function allows these materials to carry out oxygen exchange without suffering material degradation.

Perovskite materials are complex metal oxides that hold multi-functional properties suitable for capacitors, metallic conductors, catalysts and superconductors.[121] A perovskite structure is defined as a material with an ABO_3 crystal structure and is named after the mineral 'perovskite', also known as calcium titanate ($CaTiO_3$). Within the ABO_3 structure, A ions can be an alkali, rare earth or alkaline earth metal ion and B ions can be a transition metal. The A ions exist in the dodecahedral site and B ions in the octahedral sites as shown in Figure 3.7.[122] The overall structure is cubic and closely-packed. Their potential advantages are derived from the ability of the cubic ABO_3 structure to incorporate a great range of metal cations at different valence states within the size constraints of the A- and B-sites.[123] This allows for materials engineering of the required properties through controlled point defect chemistry.[124-127]

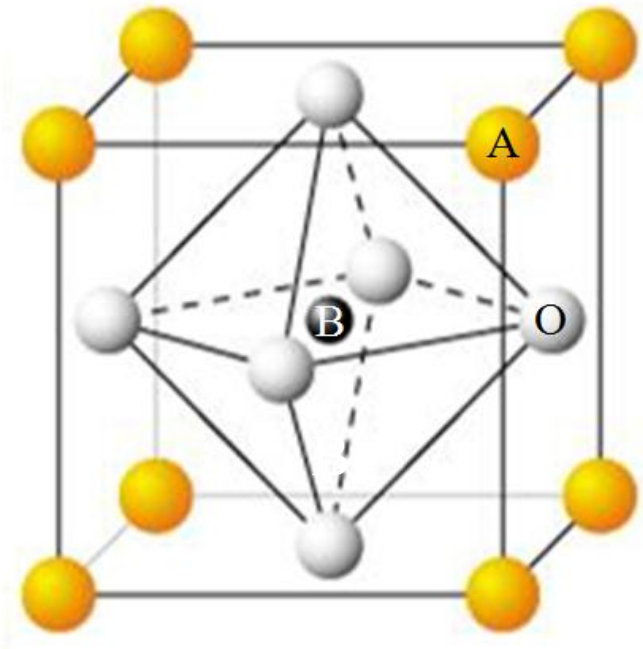

Figure 3.7 Ball and stick diagram depicting the ABO_3 structure of a perovskite material

The total charge on the A- and B-site must total +6 to keep charge neutrality but doping in a metal cation of lower valence e.g., Sr^{2+} for La^{3+} at the A-site creates oxygen vacancies ($V_{\ddot{O}}$ in Kröger-Vink notation) to compensate for the lower charge. The aim is to facilitate reversible oxygen transport into and out of the bulk of the material in a system that exhibits significant oxygen storage capacity. These vacancies facilitate oxygen ion mobility at elevated temperature allowing the transport of oxygen ions from deeper within the crystallites so that more oxygen becomes accessible for use.[128-130] The B-site cation is usually a transition metal that can exist in variable valence states giving rise to electronic conductivity and hence these materials demonstrate mixed ionic-electronic conductivity (MIEC).[131] Thus oxygen transport through the lattice is the result of an equal and opposite oxygen-ion current and electron current.

The creation and removal of oxygen vacancies in a perovskite-type structure is usually depicted by Kröger-Vink notation.[132] To describe a La-atom placed in a Sr-site of a perovskite-type material, the term would be written, La_{Sr}. This type of notation can also be used to describe a vacancy, which is represented by V, so for example a vacancy in a Fe-site would be written, V_{Fe}. Furthermore, a dot (positive), forward slash (negative) or cross (neutral) after the atom can be used to depict atomic charge. As an example, a double-positive charged Cl-atom in a Na-site would be written, $Na_{Cl}^{\bullet\bullet}$. Hence, using Kröger-Vink notation, oxidation of a perovskite-type material using gaseous oxygen to eliminate an oxygen vacancy can be expressed by:

$$½O_2 + V_O^{\bullet\bullet} + 2e^- \Leftrightarrow O_O^x \qquad (3.27)$$

From this expression we can see that oxygen uptake by the material depends on both oxygen and electronic conductivity making them ideal for oxygen exchanging membranes; hence synthesis of perovskite-type hollow fibre membranes is of major interest in current research, in particular to perform reactions between fuel and either air or water without allowing the reactant streams to mix. As an example, the combustion of methane with air using MIEC membranes can be performed to produce separate streams of carbon dioxide and water on the reduction side

(Equation (3.28)) and nitrogen on the oxidation side. Since the carbon dioxide is inherently separate from the nitrogen during operation this eliminates the requirement of an additional expensive separation step to obtain pure carbon dioxide, therefore only a condensation step to remove water is needed.

$$CH_4 + 4O_O^x \Leftrightarrow CO_2 + 2H_2O + 4V_O^{\bullet\bullet} + 8e^- \quad (3.28)$$

MIEC membranes have also been used to perform water splitting reactions using perovskite materials.[133-147] This can be performed by using water as the oxidising feed rather than air (Equation (3.29)). Water splits on the surface of the perovskite material, producing free hydrogen, and the oxygen ions pass through the membrane to oxidise the reducing feed.

$$H_2O + V_O^{\bullet\bullet} + 2e^- \Leftrightarrow H_2 + O_O^x \quad (3.29)$$

High strontium and cobalt concentrations on the A- and B-sites respectively give rise to impressive oxygen transport performance under chemical potential gradients but also make these materials prone to degradation over time, particularly under reducing atmospheres.[148] Due to a good compromise between stability and oxygen conductivity under operating conditions, the MIEC family $La_{1-x}Sr_xCo_{1-y}Fe_yO_{3-\delta}$ has been much studied as suitable materials for fuel cell cathodes and oxygen conducting membranes.[149-158] Recently, $La_{0.8}Sr_{0.2}Co_{0.2}Fe_{0.8}O_{3-\delta}$ has been put forward as a candidate material for chemical looping combustion using only air (and not water) as the oxidising feed.[159] Indeed complete removal of cobalt, producing the $La_{1-x}Sr_xFeO_{3-\delta}$ family results in a more stable system.[160-165]

Currently, membrane modules are time-consuming and cumbersome to build; each membrane needs to be tightly sealed and during operation the membranes can experience thermal expansion under high temperature leading to stresses and strains. This could lead to the formation of cracks which would allow the reactant streams to mix, impairing the process. The analogue system to oxygen permeable perovskite

membranes (Figure 3.8b) in the field of chemical looping is the circulating fluidised bed reactor system using perovskite materials as the OCM (Figure 3.8a).

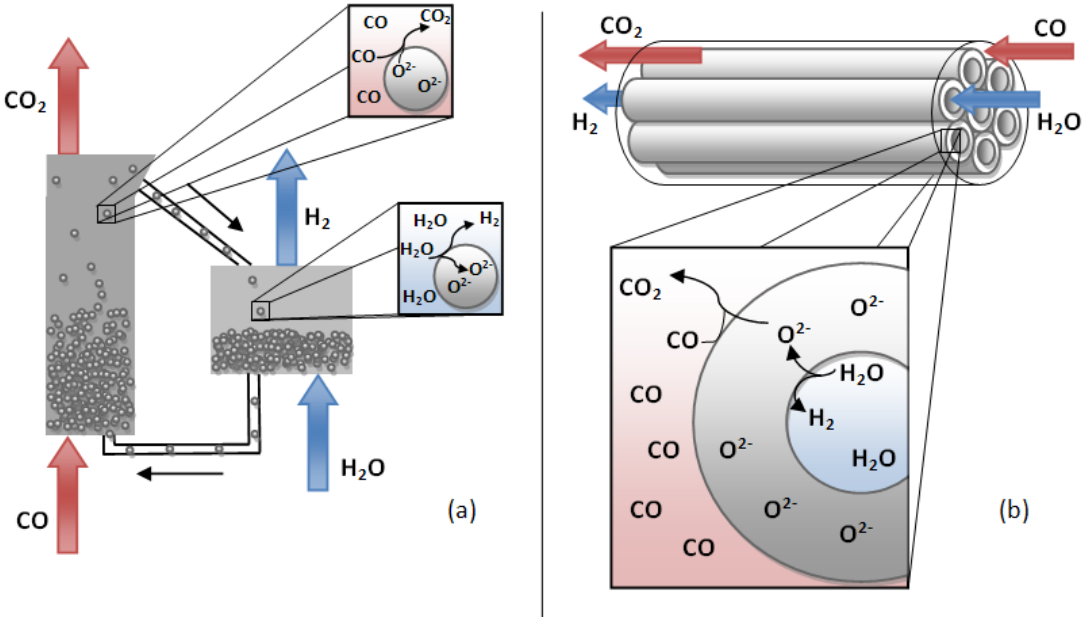

Figure 3.8 The use of oxygen deficient perovskite materials in (a) a circulating fluidised bed using chemical looping and (b) a membrane system; both systems can be used to perform water splitting (note that in both examples electron transfer would occur in the opposite direction to oxygen conductance across the perovskite)

In this thesis the use of perovskite powders, rather than membranes, are used to perform the redox process in a chemical looping system (by alternating the reduction and oxidation steps). Operation by this method prevents problems from thermal expansion, sealing and leaks which could easily occur through the use of membranes.

Rather than using methane, other reducing agents such as carbon monoxide or hydrogen can be used to create oxygen vacancies within the perovskite structure. Carbon monoxide reduction and water oxidation cycles can be performed on powdered perovskite material in a periodic reactor to produce pure streams of carbon dioxide and hydrogen in a chemical looping process:

$$CO + O_O^x \Leftrightarrow CO_2 + V_O^{\bullet\bullet} + 2e^- \quad (3.30)$$

$$H_2O + V_O^{\bullet\bullet} + 2e^- \Leftrightarrow H_2 + O_O^x \quad (3.31)$$

Carbon deposition on perovskites during carbon monoxide reduction has been investigated by Scott *et al.*[166] which indicate that for the $La_{1-x}Sr_xCo_{1-y}Fe_yO_{3-\delta}$ family, higher strontium content would be expected to lower carbon deposition by the Boudouard reaction:

$$CO + V_O^{\bullet\bullet} + 2e^- \Leftrightarrow O_O^x + C_{(s)} \quad (3.32)$$

From these studies, $La_{0.7}Sr_{0.3}FeO_{3-\delta}$ (LSF731) and $La_{0.6}Sr_{0.4}Co_{0.2}Fe_{0.8}O_{3-\delta}$ (LSCF6428) are selected as potential oxygen carrier materials and used in this thesis to perform isothermal chemical looping WGS cycles for hydrogen production, which involves reduction and oxidation of the OCM by carbon monoxide and water in separate steps. The overall reaction is the WGS:

$$CO + H_2O \rightarrow CO_2 + H_2 \quad (3.33)$$

LSF731 and LSCF6428 were expected to show low susceptibility to carbon deposition and retain high material stability under cycling.

3.3.2 Thermodynamics

In order to understand the behaviour of LSF731 during chemical looping WGS operation, the thermodynamics of iron-containing perovskite materials under these conditions were analysed. For this analysis, the chemical looping process was selected to be isothermal and performed at 850^{o}C (this temperature was selected

based on previous isothermal chemical looping WGS studies involving iron oxide).[26] For iron oxide, there is a thermodynamic limitation which prevents the formation of haematite by iron oxide oxidation with water. In this section, the thermodynamic limitations of LSF731 are studied. Kröger-Vink notation is used throughout this analysis to illustrate the reactions that take place between gas reactants and oxygen vacancies within the perovskite lattice structure. For the LSF731 perovskite, where there are no A- or B-site vacancies, there exists the site restriction:

$$[La_{La}^{\times}] + [Sr_{La}'] = 1 \tag{3.34}$$

$$[Fe_{Fe}'] + [Fe_{Fe}^{\times}] + [Fe_{Fe}^{\bullet}] = 1 \tag{3.35}$$

$La_{La}^{\times}$ represents a La(III) cation at a La-site and $Sr_{La}^{'}$ represents a Sr(II) cation at a La-site.[167, 168] Fe_{Fe} represents an Fe cation at an Fe-site which may possess an oxidation state of Fe(II) ($Fe_{Fe}^{'}$), Fe (III) ($Fe_{Fe}^{\times}$) or Fe(IV) ($Fe_{Fe}^{\bullet}$); the square brackets signify average number of the species per unit cell. Essentially, these equations lead to the assumptions that on the A-site, there can only exist a lanthanum or strontium atom (it cannot be vacant), and similarly on the B-site there can only exist iron and that no vacancy can be formed. The oxygen sites can only hold lattice oxygen or oxygen vacancies which give the restriction:

$$[O_O^{\times}] + [V_O^{\bullet\bullet}] = 3 \tag{3.36}$$

where:

$$[V_O^{\bullet\bullet}] = \delta \tag{3.37}$$

To maintain overall charge neutrality, the oxidation states of the transition metals must adjust to accommodate O^{2-} or $V_O^{\bullet\bullet}$.

$$[Sr'_{La}] + [Fe'_{Fe}] = 2[V_O^{\bullet\bullet}] + [Fe^{\bullet}_{Fe}] \quad (3.38)$$

where for LSF731:

$$[Sr'_{La}] = 0.3 \quad (3.39)$$

During oxidation and reduction of LSF731, the two dominant reactions that occur are oxidation (here expressed in terms of oxidation by gaseous oxygen) and disproportionation of Fe(III) to Fe(II) and Fe(IV):

$$V_O^{\bullet\bullet} + 2Fe^{\times}_{Fe} + ½O_2 \Leftrightarrow O_O^{\times} + 2Fe^{\bullet}_{Fe} \quad (3.40)$$

$$2Fe^{\times}_{Fe} \Leftrightarrow Fe^{\bullet}_{Fe} + Fe'_{Fe} \quad (3.41)$$

The equilibrium constants for these reactions are therefore defined as:

$$K_{Ox} = \frac{[O_O^{\times}][Fe^{\bullet}_{Fe}]^2}{p_{O_2}^{½}[Fe^{\times}_{Fe}]^2\delta} \quad (3.42)$$

$$K_{Fe} = \frac{[Fe^{\bullet}_{Fe}][Fe'_{Fe}]}{[Fe^{\times}_{Fe}]^2} \quad (3.43)$$

K_{Ox} can be adapted to relate to pH_2O/pH_2 instead of pO_2 by substituting in the following expression:

$$pO_2^{½} = \mathrm{K_{wat}} \frac{pH_2O}{pH_2} \tag{3.44}$$

where K_{wat} is the equilibrium constant for water dissociation:

$$H_2O \rightarrow \frac{1}{2} O_2 + H_2 \tag{3.45}$$

For the perovskite structure, oxygen in the unit cell is related to δ by:

$$[O_O^X] = 3 - \delta \tag{3.46}$$

Combining Equations (3.42), (3.44) and (3.46) gives:

$$K_{Ox} = \frac{p_{H_2}}{K_{wat}\, p_{H_2O}} \frac{(3-\delta)[Fe_{Fe}^{\bullet}]^2}{\delta [Fe_{Fe}^{\times}]^2} \tag{3.47}$$

By further combining Equations (3.34)-(3.47) to eliminate $[Fe_{Fe}]$, the following expression is derived (it should be noted that a similar derivation of this equation has been attempted in previous literature[167] but the final expression appears to be incorrect):

$$\frac{\delta^{\frac{1}{2}}(2\delta - x + 1)}{(3-\delta)^{\frac{1}{2}}(2\delta - x)} \frac{K_{wat}^{½} pH_2O^{½}}{pH_2^{½}} = \frac{K_{Fe}}{K_{ox}} \frac{(1 + x - 2\delta)(3-\delta)^{\frac{1}{2}}}{\delta^{\frac{1}{2}}(2\delta - x)} \frac{pH_2^{½}}{K_{wat}^{½} pH_2O^{½}} - K_{ox}^{-\frac{1}{2}} \tag{3.48}$$

Equation (3.48) is plotted to show δ vs. pH_2O/pH_2 for LSF731 at 850°C:

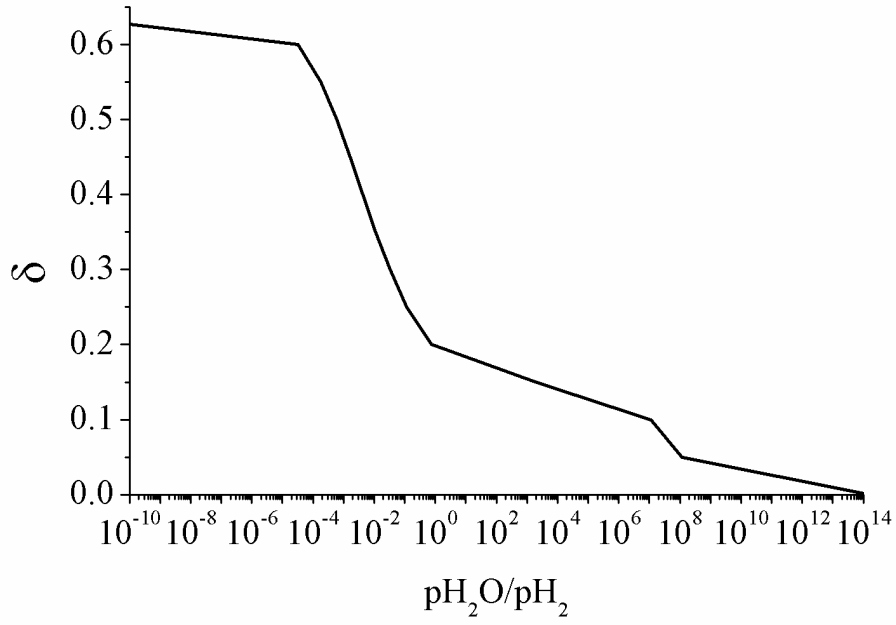

Figure 3.9 $La_{0.7}Sr_{0.3}FeO_{3-\delta}$ oxygen deficiency (δ) in relation to pH_2O/pH_2 at 850°C

From this plot it is clear that it is not feasible to reach a value of zero for δ by oxidation with water at 850°C, which would require a very high H_2O/H_2 ratio of above 10^{10}. Thermodynamically, reduction of $La_{0.7}Sr_{0.3}FeO_{3-\delta}$ should occur in two stages with $0 < \delta < 0.15$ (Fe(IV) conversion to Fe(III)) and $0.15 < \delta < 0.65$ (Fe(III) to Fe(II)). This plot is used throughout this thesis to determine expected hydrogen partial pressures during water oxidation for a range of δ.

An attempt to model the defect chemistry in LSCF6428 type perovskites proposed three models of increasing complexity where; (i) Fe and Co are not distinguished (ii) Fe and Co are distinguished and (iii) Fe and Co are distinguished including Co as Co(II), Co'_{Fe}.[169] The latter two models assume that Co replaces Fe at the Fe-site. The study focused on coulimetric titration and thermogravimetric analysis. Model (iii) gave the best fit to the δ *vs* pO_2 experimental data over 727 to 1027°C but the oxidation states of Co and Fe could not be determined. This complication in the thermodynamics means that application of a model to derive δ *vs*.

pH_2O/pH_2 for LSCF6428 is not attempted here. However, it is assumed that the thermodynamic behaviour of LSCF6428 at 850^oC in the presence of carbon monoxide and water would be similar to LSF731.

3.3.3 Kinetic models

A previous study has investigated the kinetic models of oxygen-deficient perovskites (including $La_{0.9}Sr_{0.1}FeO_3$ and $La_{0.9}Sr_{0.1}CoO_3$) under oxidising conditions.[170] The models was applied to a mixed metal oxide membrane (where each side of the membrane was subjected to high and low oxygen partial pressures); but the same theory can be applied to perovskite materials present in a periodic reactor. In a periodic reactor under oxidising conditions (assuming the perovskite starts in a reduced state), oxygen ions would permeate from the oxidising environment into the bulk of the material due to a chemical potential difference. An illustration of this step is shown in Figure 3.10 (note that in this particular example the metal ion exists as M^+ or M^{2+} but in a perovskite structure many different oxidation states are possible depending on the elements used as the B-site metals). The A-site metal is assumed not to change oxidisation state during oxidation or reduction as long as the structure remains in a perovskite phase.

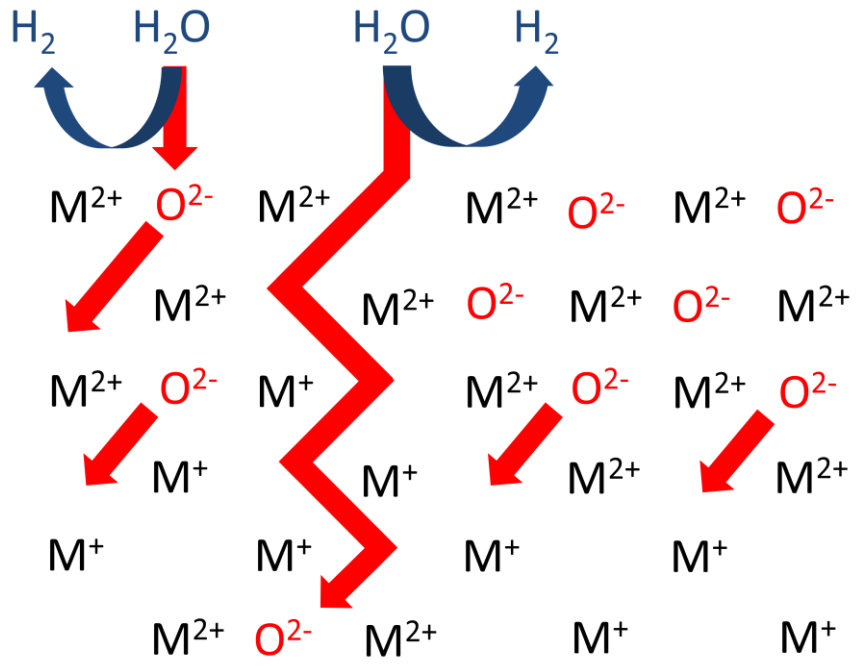

Figure 3.10 Diagram representing oxygen ion transfer within the perovskite lattice during water oxidation (M represents a metal on the B-site)

Electrons would migrate out of the perovskite in the opposite direction to movement of the oxygen ions to balance the overall charge. The oxygen ions are free to move and fill oxygen vacancies (as shown by the red arrows in Figure 3.10) in a process known as 'oxygen vacancy hopping'.[171] The kinetics of oxygen uptake by the bulk of the perovskite depends on the electronic conductivity and ionic conductivity properties of the material. It is also possible for rate of oxidation to be limited at the surface boundary of the perovskite (this is more probable for smaller sized particles).[170]

3.3.4 Stability

The stability of perovskite-type materials is measured by the tolerance factor, a concept introduced by V. M. Goldschmidt, one of the first scientists working with crystal chemistry:

$$t = \frac{(r_A + r_O)}{\sqrt{2} \bullet (r_B + r_O)} \tag{3.49}$$

where *t* is the tolerance factor and r is the ionic radius of the A, B or O (oxide) ion.

The perovskite will generally exist when t is in the range of 0.8-1. The tolerance factor ideally suggests how much the ionic radius can change before the structure becomes a non-perovskite. A great advantage of perovskites is the variety of different composites that can be formed by utilising different A or B metal ions which can lead to a range of structures possessing different properties. In addition to this, non-stoichiometric compositions can be formed through ionic substitution, addition or elimination whilst still maintaining a perovskite structure. This area of research is known as defect chemistry.

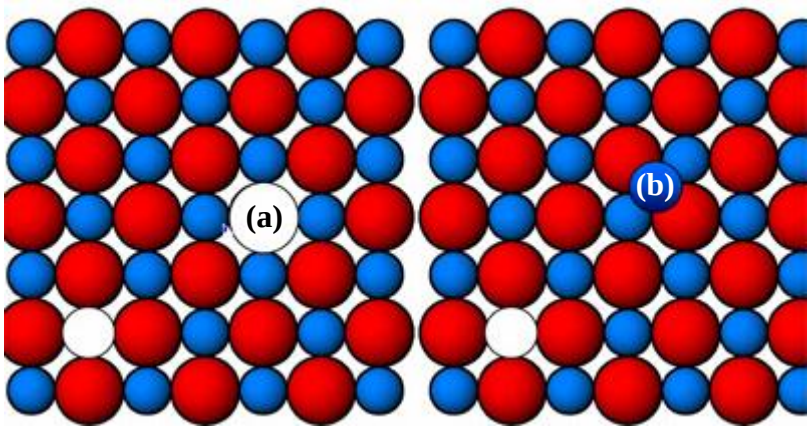

Figure 3.11 (a) Schottky Defect (b) Frenkel Defect

Defect chemistry suggests that all ionic crystal structures digress from the perfect atomic arrangements represented by the ideal ionic crystal and this is due to atomic defects.[172] An example of this is wüstite, a form of the simple iron oxide, which possesses a chemical formula similar to $Fe_{0.95}O$. These defects can exist in different forms such as nonstoichiometry and point defects. Point defects occur when a cation

or anion relocates to the surface of the material (Schottky defect) or displaces onto an interstitial site (Frenkel defect). Both types of point defects leave ionic vacancies where the ions have been displaced (Figure 3.11).[173]

Nonstoichiometry defects occur from cation deficiencies in either the A- or B-site or by oxygen deficiency or excess. Nonstoichiometry of the perovskite-type material can be influenced by temperature and oxygen partial pressure, and it is this property of perovskites that can be employed in chemical looping processes. By performing a reduction (lowering oxygen partial pressure), oxygen is drawn out of the lattice structure leaving oxygen vacancies. Following this by an oxidation step (increasing oxygen partial pressure), the oxygen vacancies can be replenished with oxygen ions (Figure 3.10).

The perovskite phase is stable over a very large range of oxygen partial pressures. In addition, the crystal lattice can accommodate significant changes in oxygen content through the generation and consumption of oxygen vacancies. The process of lattice oxygen removal to form an oxygen vacancy, gaseous oxygen and electrons can be described in Kröger-Vink notation (Equation (3.27)). These properties of good oxygen transport and oxygen exchange without undergoing crystal phase changes are not possessed by transition metal oxides, such as iron oxide, to an appreciable degree. However, it should be noted if the perovskite material is reduced as far as $ABO_{2.5}$, there may possibly be a change in phase to form a brownmillerite structure.[174, 175]

3.4 Objectives

In this chapter a full literature review has been performed for iron oxide OCMs used in chemical looping processes for water splitting to produced pure hydrogen. In addition, iron-containing perovskites have been introduced and the key properties that may allow these materials to be superior to simple metal oxides in terms of material stability are discussed.

In this thesis, two iron-containing perovskite materials, $La_{0.6}Sr_{0.4}Co_{0.2}Fe_{0.8}O_{3-\delta}$ (LSCF6428) and $La_{0.7}Sr_{0.3}FeO_{3-\delta}$ (LSF731), are nominated as potential candidate

OCMs in a chemical looping process for hydrogen production and are compared against 60% Fe_2O_3/Al_2O_3 (Fe60), which has been used in previous literature to provide pure hydrogen in a chemical looping water splitting process over 40 cycles with no recorded drop in performance.[100] Due to the nonstoichiometric properties of the iron-containing perovskite-type materials, it is possible that they could show good material stability under redox cycling by not allowing a change in phase to occur (provided that δ does not exceed 0.5). They are also catalytically active to induce the water-splitting reaction, thereby producing free hydrogen from water.[176] Previous work involving combined chemical looping and calcium looping to produce pure hydrogen has been reviewed in section 2.7, and from this work 20% NiO/Al_2O_3 (Ni20) was determined as a suitable OCM for the process. According to thermodynamic analysis nickel oxide is not thermodynamically active to induce the water splitting reaction in a chemical looping water splitting process, but despite this Ni20 was selected as an additional fourth OCM to be tested in this experiment as an additional comparison material and to experimentally assess the feasibility of using nickel oxide materials.

Initial screening of all four OCMs was performed by a temperature programmed method where five chemical looping WGS cycles were completed for each OCM. This procedure allowed a quick assessment of water splitting activity, susceptibility to carbon deposition (under carbon monoxide reducing feed) and material stability under fairly reducing conditions and high temperatures. Whereas a conventional steam-iron process would operate isothermally at 850^{o}C, the temperature programmed cycles were operated up to 1000^{o}C.

Following the temperature programmed experiment, the best performing materials out of the metal oxides and perovskite materials (in terms of material stability, activity and hydrogen purity were selected) to perform further isothermal chemical looping redox cycles at 850^{o}C. In one experiment a chemical looping process involving WGS redox cycles was used and in a second experiment a three-step chemical looping cycle involving methane reduction, water oxidation and air oxidation was used. In both cases, a high number of cycles were performed (150 cycles for WGS and 50 cycles for autothermal chemical looping) to thoroughly test the material stability of both OCMs under the imposed cycle treatments.

One feature of perovskite materials is the wide range of possible compositions that can be produced simply by adjusting the amount of metals situated on the A- and B-site of the perovskite structure. Previous literature has shown that the addition of a small amount of nickel doped on to iron oxide can enhance OCM activity, therefore speeding up rates of reaction and lowering the time required to perform each reduction and oxidation step (this is discussed in Section 3.2.5). Therefore, in an additional test, LSF731 was doped with 10% nickel on the B-site, thus forming $La_{0.7}Sr_{0.3}Fe_{0.9}Ni_{0.1}O_{3-\delta}$ (LSFN7391) to perform 65 cycles of isothermal chemical looping WGS redox cycles at 850^{o}C. Whereas the addition of nickel to iron oxide OCMs caused a reduction in material stability in previous studies, addition of nickel to LSF731 is still expected to give high material stability of the cycles performed whilst allowing enhanced rates of reactions.

Chapter 4

4. Experimental

4.1 Introduction

This chapter details the methods used for synthesising the OCMs used in the experimental work of this thesis (these are outlined in Section 4.2), in addition to the equipment that was used for all of the experiments (Section 4.3). A combined microreactor and mass spectrometer unit (Hiden CATlab) was used to perform periodic chemical looping cycles using the OCMs; an advantage of the system was the automation function which allowed programmable sequences to be used (this is detailed in Section 4.4). The material characterisation techniques used are also detailed (Section 4.5). An outline of the methodologies used for the chemical looping experiments is discussed in Sections 4.6, 4.7 and 4.8. Possible experimental errors, reactor downtime and safety considerations are discussed in Sections 4.9, 4.10 and 4.11.

4.2 Material synthesis

4.2.1 Methods

Commercial $La_{0.6}Sr_{0.4}Co_{0.2}Fe_{0.8}O_{3-\delta}$ (LSCF6428) and $La_{0.7}Sr_{0.3}FeO_{3-\delta}$ (LSF731) powders were purchased from Praxair Specialty Ceramics and used without further processing.

60% Fe_2O_3/Al_2O_3 (Fe60) was produced by dissolving iron nitrate and aluminium nitrate (in a mass ratio of 60:40) in water purified by reverse osmosis. An

aqueous solution of 1M Na_2CO_3 was gradually added into the nitrate solution and stirred vigorously at room temperature and atmospheric pressure until the pH of the solution had reached 9.5. The precipitated mixture was left to stand without stirring for two hours. The precipitate was washed with large volumes of water purified by reverse osmosis repeatedly to remove the Na^+ ions. Sufficient washing was indicated by an ionic conductance of ~120 μS. The washed precipitate was filtered and dried at 80°C in air to remove most of the moisture. The product was calcined at 950°C in air for three hours and then crushed and sieved.

20% NiO/Al_2O_3 (Ni20) was produced by a combined deposition-precipitation method; 1.5 g of $Ni(NO_3)_2.6H_2O$ was dissolved in 10 g of deionised water and the pH adjusted to 9-11 with an ammonia solution. To this, 1 g of γ-Al_2O_3 nano powder (average particle size 50 nm) was added and left under stirring for five hours. The product was then filtered and washed with deionised water and dried at 120°C for 17 hours followed by calcination at 650°C for three hours.

$La_{0.7}Sr_{0.3}Fe_{0.9}Ni_{0.1}$ (LSFN7391) was synthesised using a modification of the procedure outlined in Rivas *et al.*[177] where stoichiometric amounts of $La(NO_3)_3$, $Sr(NO_3)$, $Fe(NO_3)_2$ and $Ni(NO_3)_2$ were dissolved in distilled water and added to equimolar amounts of citric acid and ethylene glycol. The excess water was slowly removed from the sample using a heating plate. Following this, the sample was placed in a furnace and slowly heated in air (using a temperature ramp of 0.5°C min^{-1}) up to 850°C and left at this temperature for six hours.

4.2.2 Oxygen content (ΔO_{max})

The amounts of active molar oxygen (not including oxygen in the supports) present in the OCMs are tabulated in Table 4.1.

Table 4.1 Material characterisation of fresh OCM samples

OCM	Abbreviation	Oxygen content* / µmoles
$La_{0.6}Sr_{0.4}Co_{0.2}Fe_{0.8}O_{3-\delta}$	LSCF6428	675
$La_{0.7}Sr_{0.3}FeO_{3-\delta}$	LSF731	663
60% Fe_2O_3/Al_2O_3	Fe60	563
20% NiO/Al_2O_3	Ni20	375
$La_{0.7}Sr_{0.3}Fe_{0.9}Ni_{0.1}O_{3-\delta}$	LSFN7391	663

*based on 50 mg of sample

Oxygen content of the materials is defined by ΔO_{max}, which takes into account oxygen availability of the OCMs in terms of present active material (not support) and thermodynamic limitations by carbon monoxide reduction and water oxidation at 850^{o}C. It should be noted that the definition of ΔO_{max} has only been applied to analysis in Sections 5, 6 and 8, where the cyclic redox processes used reduction and oxidation by carbon monoxide and water. It has not been used in Section 7 where the feeds were methane, water and air. In Section 5, temperature programmed redox operation is performed (to a final set-point temperature of 1000^{o}C) and it is assumed that there would not be a significant change in ΔO_{max} between 850^{o}C and 1000^{o}C.[94, 168]

ΔO_{max} for the two iron-containing perovskite-type materials have been calculated using the thermodynamic analysis shown in Section 3.3.2. LSFN7391 was assumed to have a similar ΔO_{max} as LSF731 due to the very small difference in elemental composition. The iron oxide present in Fe60 was assumed to only exist as iron, wüstite or magnetite (not haematite) during redox cycling with carbon monoxide reduction and water oxidation at 850ºC, therefore ΔO_{max} for the material is calculated by the difference in oxygen capacity between magnetite and iron. Ni20 was assumed to exist as nickel or nickel oxide. The calculated ΔO_{max} for 50 mg of LSCF6428, LSF631, Fe60, Ni20 and LSFN7391 are shown in Table 4.2.

Table 4.2: Oxygen contents of the OCMs in terms of ΔO_{max}

OCM	ΔO_{max}* / µmoles
LSCF6428	113
LSF731	111
Fe60	500
Ni20	375
LSFN7391	111

*based on 50 mg

4.3 Equipment

4.3.1 CATlab microreactor system

All of the chemical looping experiments for this thesis were performed using a fully automated and programmable microreactor-gas analysis system (CATlab, Hiden Analytical, UK) at 1 atm. This system consists of two modules; the microreactor (a plug flow reactor) and soft ionisation quadrupole mass spectrometer (QMS). A diagram of the system used to perform the chemical looping experiments is illustrated in Figure 4.1. The microreactor module comprises of a furnace, quartz microreactor, sampling tube (quartz tube containing the catalyst) and ports to allow for gas inlet and outlet flow. Four mass flow controllers (MFCs) external to the microreactor allows flow of four different dry gases, either individually or blended. These mass flow controllers were connected to four different gas cylinders at a single time. All gases are quoted as volume percentages. All flow rates are quoted at standard temperature and pressure, and all gases used were 99.9995 vol. % pure (BOC, UK):

- MFC 1: Calibration Gas (2 vol. % of H_2, O_2, CO, CO_2, CH_4 in He)
- MFC 2: 5 vol. % H_2 in He, 5 vol. % CO in He or 10 vol. % CH_4 in He
- MFC 3: 5 vol. % O_2 in He
- MFC 4: 100 vol. % He carrier gas

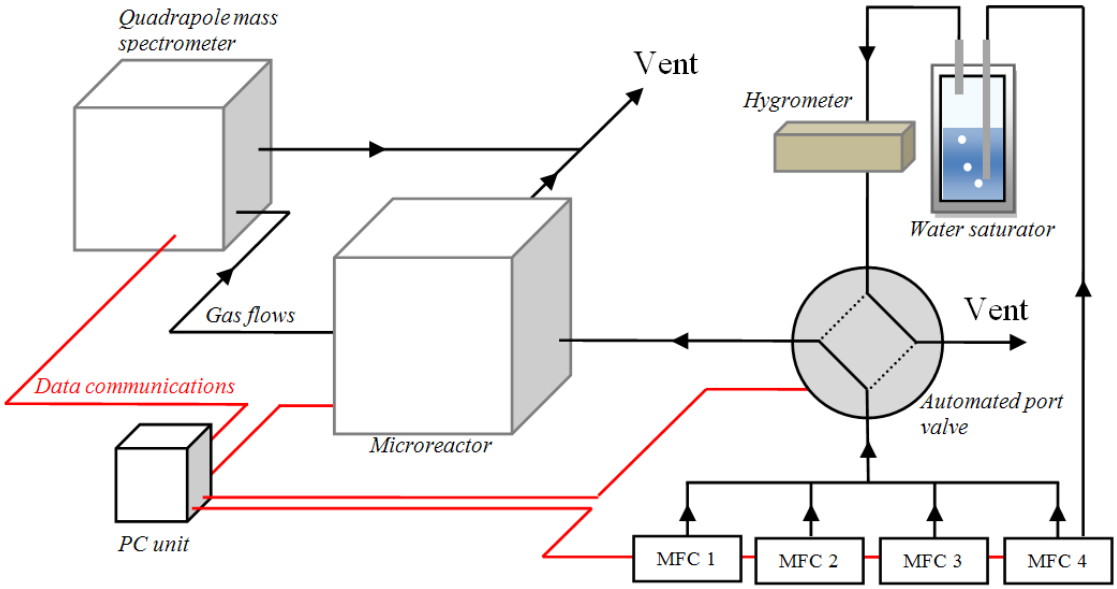

Figure 4.1 Schematic of the system used to perform experimental work involving chemical looping operation

MFC 2 was used to control the reducing gas, which was connected to either a hydrogen, carbon monoxide or methane cylinder (all in inert helium gas). For experiments involving oxidation by air, a gas cylinder comprising of 5 vol. % O_2 in helium was used which was controlled by MFC 3. The outlet from the microreactor was fed *via* a heated capillary line to the QMS (QIC-20, Hiden Analytical, UK) for continuous online analysis. By coupling the modules close together, maximum sensitivity by minimal response time was achieved.

The microreactor and soft ionisation QMS units are shown in Figure 4.2. The microreactor contains an inert quartz sampling tube, which can hold between 25-250 mg of catalyst sample. To avoid solid material dispersion downstream of the microreactor, silica wool was present to allow only gas throughput (Figure 4.3). For all of the experiments in this investigation, typically ~50 mg of sample was used. The sample volume was typically ~0.04 ml. Inlet gas was introduced to the top of the sampling tube which passed downwards through the plug of catalyst sample and silica wool. Reduction and oxidation of the sample was performed periodically by

alternating the flow of reducing and oxidising agents. The products in addition to unreacted gases were sent to the QMS for gas analysis.

Figure 4.2 (a) QIC-20 QMS (b) CATlab microreactor

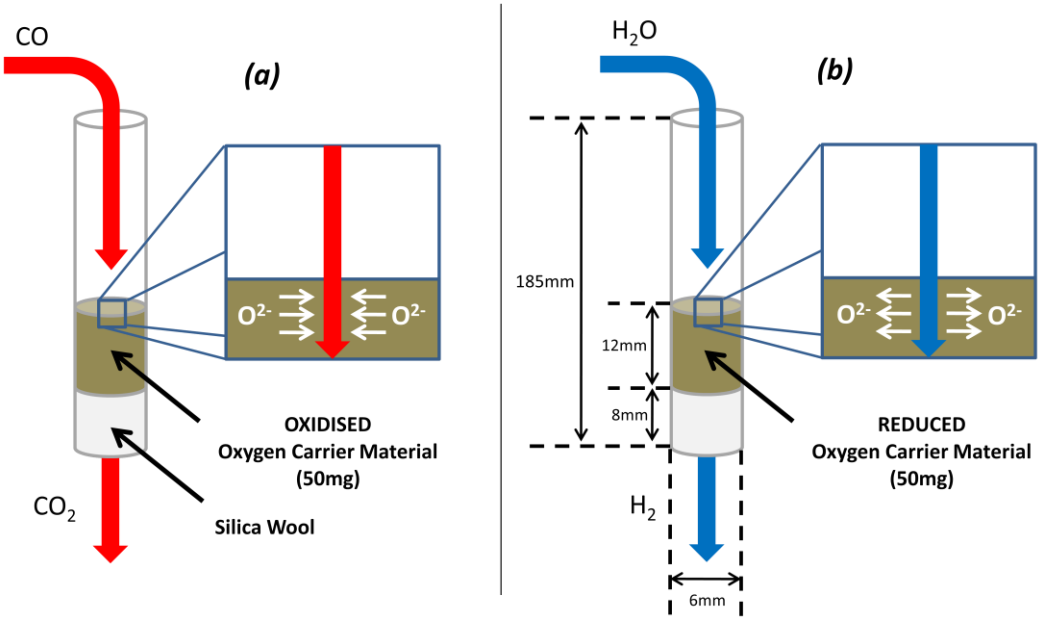

Figure 4.3 Diagram representing (a) reduction by carbon monoxide and (b) oxidation by water of 50 mg of OCM inside the sampling tube in the CATlab microreactor

An internal K-type thermocouple (sample thermocouple) inserted into the top of the sampling tube was used to monitor and control the temperature at the top of the sample layer through the use of a computer software and furnace system. The thermocouple was inserted into an inert alumina sleeve to prevent possible contribution to the observed catalytic activity. Using the complimentary computer software, the sample temperature could be set between furnace ambient (this was usually ~40^{o}C depending on laboratory temperature) and 1000^{o}C using temperature heating/cooling rates of 0.1 – 20^{o}C min^{-1}. In addition to the sample thermocouple, the microreactor system consisted of two other thermocouples (sentry and furnace) which were present in the furnace block. These thermocouples measured the temperature directly at the furnace. If any of the three thermocouples (sample, sentry or furnace) were to reach 1100^{o}C or became faulty, the furnace would shut down as a safety precaution.

The four MFCs were used to allow flow of 2-100 ml (STP) min^{-1} of the different gases. These MFCs were all controlled by computer software. All gas cylinders were firmly attached into place using bench clamps. Gas regulators were used to allow the individual gas outlet flow from the cylinders to reach 5 bar before reaching the MFCs. All gas connections to and from the mass flow controllers were made using 1/8 inch Swagelok fittings.

4.3.2 Water saturator

Water was delivered into the microreactor by a water saturator system where helium was used as the carrier gas (Grant Scientific, UK).[178] A schematic of the water saturation unit is shown in Figure 4.4. Flow of helium into the water saturator was controlled manually by an individual mass flow controller (Aalborg Instruments & Controls, Inc.).

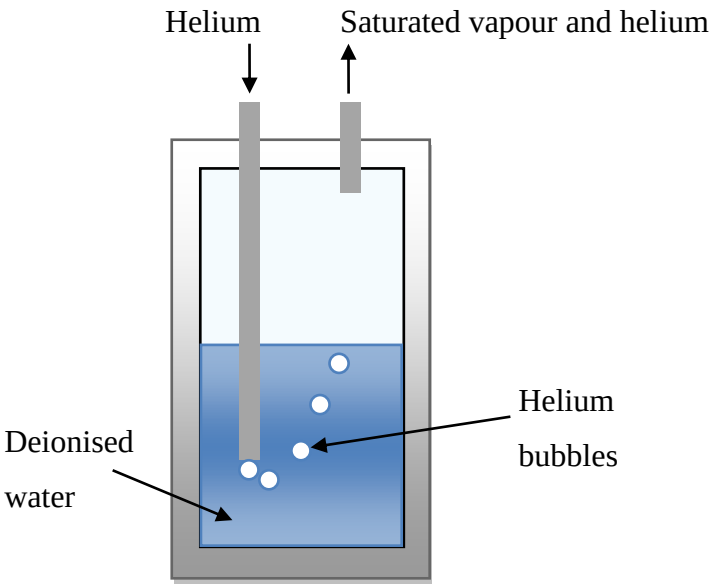

Figure 4.4 Illustration to show operation of the water saturator unit to produce water vapour

The saturation of water into the helium gas was controlled by varying the temperature of the water bath. The concentration of water leaving the water saturator could be increased by increasing the water bath temperature according to the pressure curve graph shown in Figure 4.5.

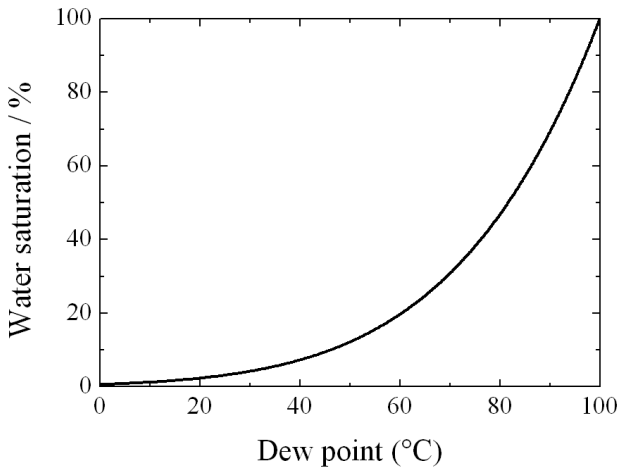

Figure 4.5 Water saturation curve (level of water saturation against temperature)

A preliminary test was performed, which indicated that an increase in the water bath temperature also caused a small increase in the measured concentrations of oxygen and hydrogen (whereas nitrogen remained relatively stable). The results from this test are shown in Appendix C1. The result from this test indicates that the deionised water stored within the saturators reservoir contained absorbed hydrogen and oxygen, however at concentrations less than 1% of the water feed concentration, these small amounts of saturated oxygen and hydrogen are negligible.

Condensation is usually a problem within reactor systems that use water vapour as a reactant feed. Areas within the reactor system known as 'cold-spots' may exist, which generally have lower temperatures compared to the initial water feed temperature and therefore allow condensation to occur resulting in the pooling of water. These areas can be located at cold Swagelok fittings, metal pipelines and in other cold areas within the reactor. For this reason, a water bath temperature below room temperature (20^{o}C) was used during all experiments to minimise condensation. Additionally, heating lines were used between the water saturator and the hygrometer in an attempt to keep all gases travelling between the water saturator and microreactor at a temperature of around 70^{o}C.

The water content of the stream leaving the water saturator was monitored by a chilled mirror hygrometer (CMH-1, Alpha Moisture Systems, UK). This unit was also used to calibrate the water signal for the QMS. To ensure that the hygrometer was working efficiently it was regularly calibrated by Alpha Moisture Systems, UK.

4.3.3 Quadrapole mass spectrometer (QMS)

In order to identify gaseous products leaving the microreactor, a gas analysis technique such as gas chromatography or mass spectrometry must be utilised. For this investigation, mass spectrometry analysis was selected as the appropriate technique due to the suitable speed at which accurate data could be produced. The QMS unit was used to carry out online analysis of the gaseous outlet from the microreactor. Standard features of the unit include less than 500 ms response time to changes in gas composition and the ability to detect less than 100 ppb of a species.

The QMS used throughout this project was HAL 201 RC, with dual faraday/electron multiplier detector. This unit has the capacity to detect gaseous molecules of atomic mass units up to 200. Before gaseous sample reaches the QMS, it is sent through a heated capillary line (containing a silica liner to disperse the heat efficiently). This heated inlet system was controlled manually by arbitrary settings of 0-9 corresponding to temperatures between ambient and 200^{o}C. In an initial test with the heater operating at setting 4, the QMS mass spectrometer received outlet gas from the microreactor at 16 ml min^{-1} through the heated capillary line. To investigate the effects of inlet capillary heating, the inlet flowrate into the QMS was measured at each temperature setting and the results are shown in Appendix C2.

It was concluded that an increase of temperature in the heating line lowers the flowrate intake of the QMS. Following the change in heater setting, there were no observed fluctuations in flowrate once a set point temperature had been reached. Following this test, heater setting 4 was used for all following experiments, which was hot enough to ensure that condensation would not occur during passage to the QMS. The QMS inlet flowrate was regularly measured to ensure that it was constantly at 16 ml min^{-1}. The remaining gas was diverted safely towards the vent.

In order to obtain a low enough pressure for the sample to be analysed by the mass spectrometer (usually pressures as low as 1 x 10^{-9} atm), the pressure of gaseous sample is lowered in two stages. In the first stage, operation of the bypass pump draws gaseous sample down the capillary line, which would consequently exit at a low pressure and high velocity. The gaseous sample then passes firstly through a platinum orifice, which would cause a further reduction in pressure, and then into an ultrahigh vacuum chamber to be evacuated by a turbomolecular pump operating at 70 L s^{-1}.

A residual gas analyser probe is situated inside the ultrahigh vacuum chamber. The probe contains an electron-impact ion source mounted on a quadrapole mass analyser, which ionises neutral particles entering from the sampling line:

$$M + e^- \rightarrow M^{\bullet +} + 2e^- \qquad (4.1)$$

where M is the molecular species, e^- is the electron and M is the radical form of the molecular species. Fragmentation of the molecular ions was expected, which would lead to the formation of radicals and neutral molecules:

$$M^{\bullet+} \rightarrow EE^+ + R^\bullet \quad (4.2)$$

$$M^{\bullet+} \rightarrow OE^{\bullet+} + N \quad (4.3)$$

where EE^+ is an even ion, $OE^{\bullet+}$ is an odd ion, $R^\bullet$ is a radical and N is a neutral molecule. Further fragmentation of the new species would also be expected to occur. A QMS system detects species by the mass-to-charge ratio (m/z), rather than their mass alone and comprises of four rods (either circular or hyperbolic), which must be perfectly parallel to each other. Of these four rods, two are positively charged and two are negatively charged (Figure 4.6).

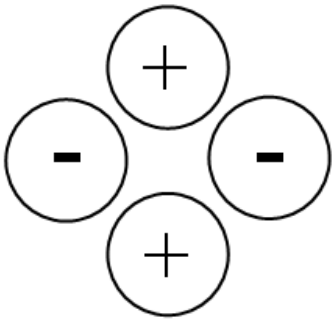

Figure 4.6 Arrangement of quadrapole rods in the QMS

Ions pass in between the rods, and depending on the voltage applied to each pair of charge rods, ions will either have the correct mass-to-charge ratio to pass straight through to the detector, or will become unstable and collide with the charged rods. By continuously varying the applied voltage to the charged rods, a range of mass-to-charge ratios can be scanned and the signal (in Torr) is measured. The data recorded by the QMS can then be converted into gaseous mole fractions by calibrating the

system. Numerical conversion of product mole fraction to product molar flow rate for a gaseous species was performed using the following equation (*x* represents the gaseous species):

$$\dot{n}_x = \frac{y_x F}{60} \frac{1}{22400} \tag{4.4}$$

where $\dot{n}_x$ is outlet molar flow rate of *x* (mol s^{-1}), y_x is product mole fraction of *x* and *F* is total inlet volumetric flow rate including carrier gas (ml (STP) min^{-1}). To convert volumetric flowrate to molar flowrate, the ideal gas law stating that 22400 ml of gas is equivalent to 1 mole at standard conditions was used.

The mass-to-charge ratios of the gaseous species used in the following investigations are shown in Table 4.3.

Table 4.3: Mass-to-charge ratios of gaseous species used

Gaseous species	Mass-to-charge ratio
H_2	2
CH_4	16
H_2O	18
CO	28
N_2	28
O_2	32

From Table 4.3 it is apparent that carbon monoxide and nitrogen have the same mass-to-charge ratio of 28, and therefore the QMS would not be able to distinguish between them. For this reason, nitrogen was not used as a carrier gas for any of the experiments. Instead, helium (with a mass-to-charge ratio of 4) was used as the carrier gas. However, it was still possible that nitrogen could have entered the

system due to an air leak. To avoid this issue, leaks into the system were minimised by leaving the system under constant helium flush prior to experiments.

As a preliminary test to measure background levels caused by leaks, each gas cylinder was flowed into the microreactor for two hours (to reach steady state) and then measured by the QMS for five minutes. This was performed for helium (Appendix D1), 5% CO in helium (Appendix D2), 10% CH_4 in helium (Appendix D3), 1% H_2O in helium (Appendix D4) and 5% O_2 in helium (Appendix D5). For these preliminary studies, the signal corresponding to nitrogen and carbon monoxide is labelled as 'm/z = 28' as shown in Appendix D. All of the five minute tests showed signals corresponding to residual water, which was seen to fluctuate depending on the laboratory temperature and the amount of time that the microreactor had been previously open to the atmosphere.

The five minute flush using helium (Appendix D1) showed that there was a small mass-to-charge of 28 signal present (300 ppm), which was most likely caused by a leak of nitrogen. This leak of nitrogen, although very low, would make it unfeasible to calculate carbon monoxide mole fractions at 100 ppm levels. The same mass-to-charge signal of 28 was seen during the five minute flush using 5% O_2 in helium (Appendix D5). The five minute flush using carbon monoxide (Appendix D2) appeared to show almost no leaks (although residual water was measured) during the five minute flush. Before supplying carbon monoxide to the microreactor, it was always calibrated on the basis that the mass-to-charge signal of 28 should be at 5% and therefore any interference of a nitrogen signal would add an experimental error. However, as the five minute helium flush shown in Appendix D2 indicates, this nitrogen signal would only contribute to ~0.03% of the mole fraction measured, which is a relatively small experimental error.

The methane flush (Appendix D3) shows signals corresponding to hydrogen and mass-to-charge of 28. It is likely that this hydrogen may have originated from the methane gas cylinder. The mass-to-charge signal of 28 is more likely to have been caused by nitrogen from an air leak; however this is measured as a small signal (400 ppm).

The water flush (Appendix D4) shows high levels of oxygen that was not exclusively caused by an air leak (as the oxygen signal is much higher than the mass-to-charge signal of 28). According to Henry's Law, oxygen is more soluble in water than nitrogen.[179] This would suggest that the large majority of the oxygen measured was contributed to oxygen that had dissolved into the water rather than being formed from an air leak.

Leak prevention steps were taken which included the use of Viton rubber o-rings to tightly clamp in place the sampling tube and microreactor. Temperature resistant ferrules were also used at all connections (these were regularly replaced to ensure a low level of leak in the microreactor). The microreactor system has a bypass/analysis switch which allows the inlet gas from the mass flow controllers to pass either through the microreactor (during analysis) and to the QMS or straight to the QMS without passing through the microreactor. By measuring 100% helium gas after passing through both modes, the quick detection of leaks within the microreactor can be made (indicated by the presence of air). If air was measured by the QMS during both analysis and bypass modes, this would indicate that the leak was outside of the microreactor.

4.3.4 Calibration

Calibration (not including water) was performed using a mixture of; 2 vol. % H_2 (m/z = 2), 2 vol. % O_2 (m/z = 32), 2 vol. % CO (m/z = 28), and 2 vol. % CO_2 (m/z = 44), balanced in helium (STGases, UK) and individual components of; 5 vol. % O_2, 10 vol. % CH_4 and 5 vol. % CO, all balanced by helium. The calibration for each gas was performed at the same flow rate used during the experiments and for longer than a typical cycle to verify that signal drift was negligible (Figure 4.7).

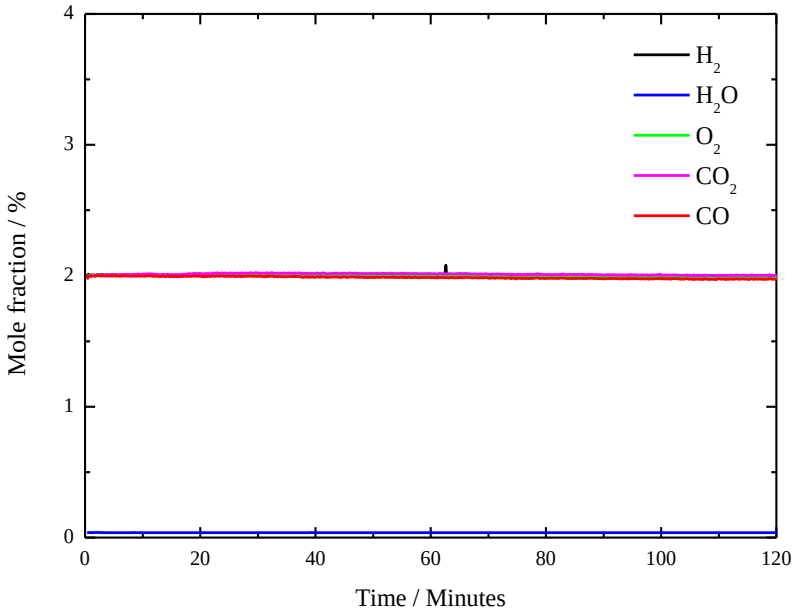

Figure 4.7 Calibration test operated at room temperature for two hours indicating no signal drift from QMS

Water was calibrated by flowing water directly from the water saturator firstly through the hygrometer unit and finally through the microreactor sampling tube and into the QMS. The water signal of the QMS was then adjusted to match the reading from the hygrometer.

4.4 Automation

4.4.1 Automated Sequencing

A significant advantage of using the CATlab microreactor system is the automation function, which allows the operation of programmable sequences involving temperature, flow rates and data acquisition. The four CATlab mass flow controllers, temperature of the microreactor furnace and QMS were all automatically controlled *via* the computer software and could be automated by running sequences. Through this function, experiments were set up to run automatically for long periods of time permitting more efficient use of the microreactor system. Another benefit of

automation is during multi-cyclic operation where experimental parameters are required to be repeated accurately.

4.4.2 Water inlet

The CATlab mass flow controllers are not designed to control the flow of water vapour from the water saturator as they were only intended for use with dry gases. Additionally, they cannot be used to control the dry helium inlet flow into the water saturator as setting the flow rate to zero during operation (for example during the reduction steps) can produce back pressure and back-flow of water into the mass flow controller which would most likely perform damage to the unit. For these reasons, the initial experimental set-up did not allow automated control of water vapour. A large part of the work performed for this thesis involved modification of the CATlab microreactor to allow the use of an automated water inlet system that could be incorporated into automation sequences.

A 6-port valve injector (originally used for CATlab pulsing experiments) was utilised to allow automated switching between gases from the CATlab mass flow controllers and water vapour feed from the water saturator (Figure 4.8). The valve injector was modified so that only two inlets (CATlab mass flow controllers and water vapour) and two outlets (QMS and vent) were open. This ensured that the water vapour was continuously flowing (either to QMS or the vent), which prevented the build up of pressure which would have caused safety issues. As shown in Figure 4.8, by rotating the valve by 60º (either clockwise or anti-clockwise), each of the inlets could be directed to either QMS for gas analysis or towards the vent.

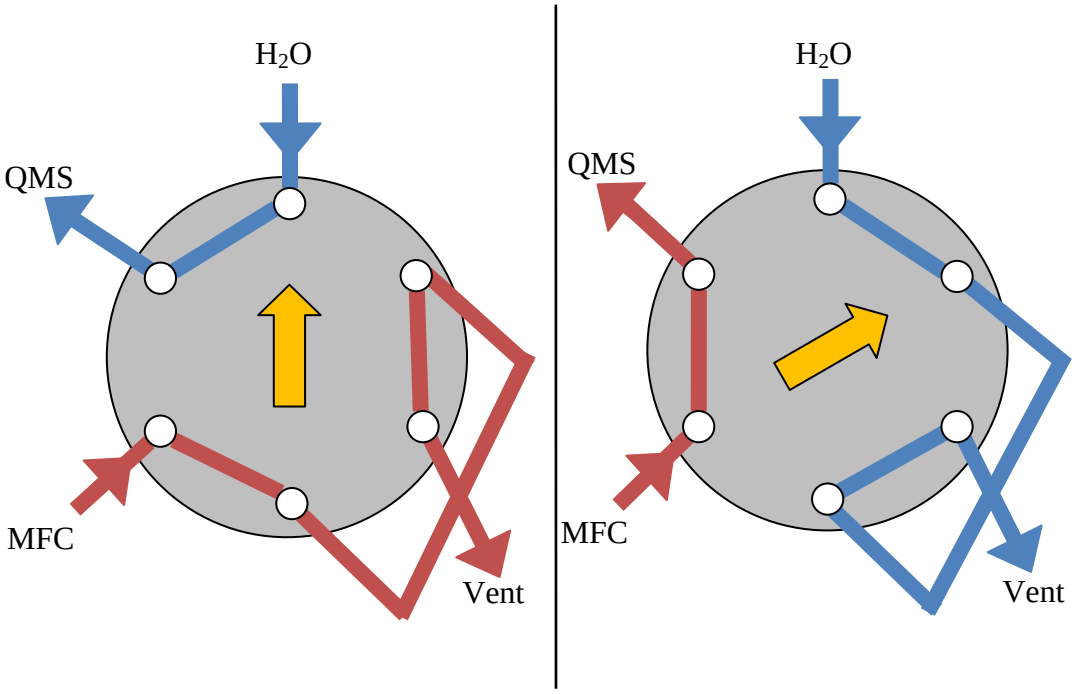

Figure 4.8 Operation of the 6-port valve to direct flow of CATlab MFC gases (MFC) and water vapour (H_2O) to either QMS or vent (the orange arrow has been added to indicate valve rotation of 60º)

Control of the electronic 6-port valve switch (allowing rotation of the valve by 60º) was incorporated into the computer software allowing the CATlab microreactor to automatically switch between flow from either the four CATlab mass flow controllers or the water saturator. This modification significantly improved the efficient use of the CATlab system as it allowed automated experiments involving water feeds, which was previously not possible with the initial set-up.

4.5 Analytical techniques

4.5.1 Scanning Electron Microscopy (SEM)

SEM analysis was used (JEOL 65 JSM5300LV and XL30 ESEM-FEG) to optically analyse the OCMs to provide magnified images of the material surface. Four different magnifications were used (x100, x500, x3500 and x15000) as a standard

procedure for inspecting all of the materials. All of the OCMs used in the investigations were characterised using this technique to analyse particle size, surface topography and particle geometry. Figure 4.9 shows a typical SEM image of fresh LSF731 powder at magnification of x15000.

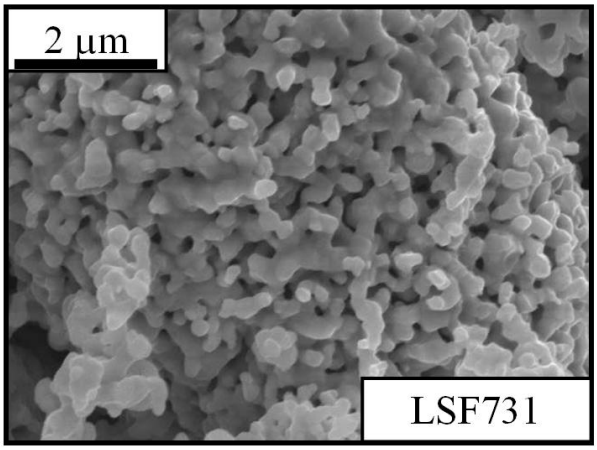

Figure 4.9 SEM image of fresh LSF731 at magnification x15000

SEM operates by shooting an electron beam on to the surface of the specimen from a powerful electron gun located at the top of the machine (Figure 4.10). The beam systematically scans across a specified area of the OCM and the electrons that reflect off the surface (secondary electrons) are captured by a detector, which collects the data to form the SEM image.

SEM analysis has been used in this investigation to compare the OCMs before and after chemical looping operation. An increase in average particle size during operation in the chemical looping process (which might be evident from comparing the lower magnification SEM images) could indicate material sintering or agglomeration. Loss of features to form a smoother surface (which might be evident from comparing higher magnification SEM images) may indicate a loss in surface area.

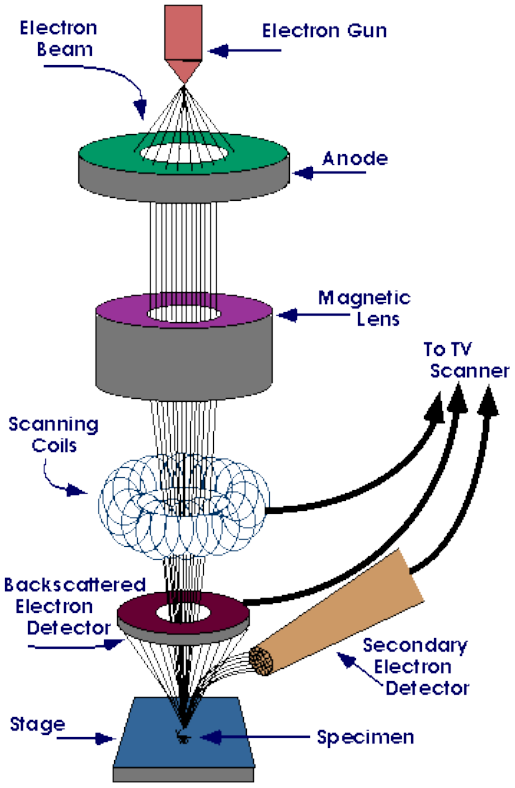

Figure 4.10 Diagram of a scanning electron microscope in operation[180]

4.5.2 Scanning Electron Microscopy Energy Dispersive Spectroscopy (SEM-EDS) and Inductively Coupled Plasma Optical Emission Spectrometry (ICP-OES)

SEM-EDS was performed on all samples to characterise the OCMs by measuring the elemental balance. For this technique, a high-energy beam of X-rays is focussed into the sample material and due to electron excitement (where electrons jump between electron shells), an additional X-ray is emitted from the sample. The energy of the X-ray emitted is unique to each element, and by measuring the energy and number of X-rays emitted by the sample (using an energy-dispersive spectrometer), an approximate elemental composition of the sample can be measured.[181] SEM-EDS confirmed that all of the samples were correctly labelled apart from one which was labelled as 56% NiO/Al_2O_3 by the OCM supplier. The results from SEM-EDS indicated that the nickel oxide content of this sample was a lot lower than 56%, and closer to 20%. ICP-OES was therefore used as an additional material

characterisation technique to accurately determine the correct elemental balance of the sample (the method of ICP-OES is illustrated in Figure 4.11).

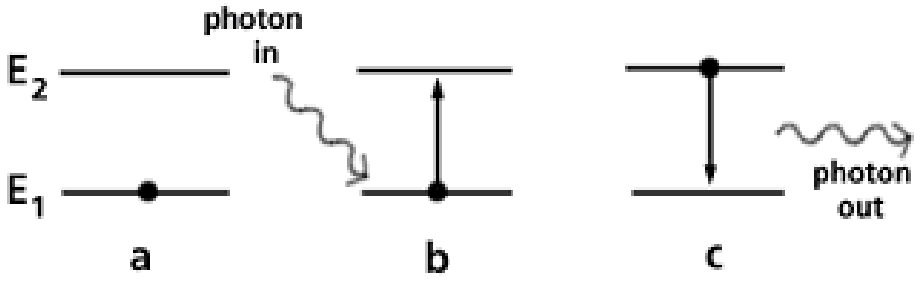

Figure 4.11 Plasma used to raise electron to a higher electron level in ICP-OES analysis (E_1 is lower electron level and E_2 is higher electron level)[182]

In this analytical technique, a very small amount of the sample is dissolved in acid. High energy plasma is exposed to the sample to raise electrons within the elements to a higher electron level, thus producing photons. Each element produces a unique wavelength of light, which is picked up by a detector. Through this method, the elemental composition of the OCM can be measured. The results indicated that the nickel oxide sample was 20% NiO/Al_2O_3, rather than 56% NiO/Al_2O_3 as labelled by the supplier. The supplier later confirmed that the sample was indeed 20% NiO/Al_2O_3 and that the mistake was due to a labelling error.

4.5.3 X-Ray Diffraction (XRD)

XRD analysis was used (60 PANalytical X'Pert Pro diffractometer fitted with an X'Celerator) to determine the chemical composition of the OCMs. Rather than detect elements, XRD can detect crystal phases which is particularly useful as it can determine the oxidation state of the OCM. To perform XRD analysis, the sample powder is placed in a small crucible, and X-rays are employed by Cu K-α radiation, λ=1.54180, or Cu K-α1, λ=1.54059. In this technique, the X-rays reflect off the atoms within the crystal structure (Figure 4.12),[183] and this causes the formation of secondary waves. In most cases, the waves are cancelled out through destructive

interference, but in a few directions constructive interference occurs which is determined by Bragg's Law:

$$n\lambda = 2dsin\theta \quad (4.5)$$

where d is spacing between diffracting planes, θ is the incident angle, n is an integer and λ is the beam wavelength. A nominal step size of 0.033 degrees 2-theta with a step time of 100 seconds in continuous mode was routinely used for XRD analysis in this thesis to scan through $0 < \theta < 90$. The secondary waves are measured by a detector. Each reflection is characteristic to a specific phase or crystal structure, and by comparing the peaks formed from XRD analysis to a database, the crystal structure of the material can be determined.

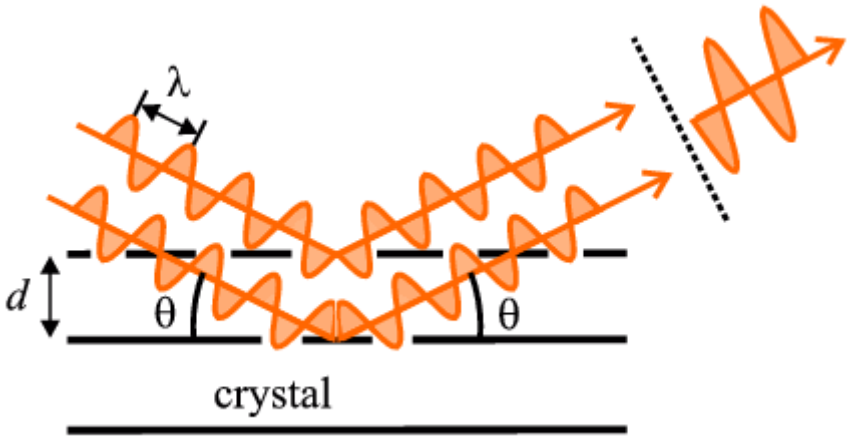

Figure 4.12 Bragg's Law used to perform x-ray diffraction analysis

4.5.4 Brunauer-Emmer-Teller (BET) Analysis

BET analysis was used to determine the surface area of the fresh OCM samples. BET is performed using modified Langmuir theory to measure the physical adsorption of gas molecules (in this case nitrogen) to the solid surface of the

OCM.[184] BET theory is different to Langmuir theory as it takes into account the fact that adsorbed gas upon the material surface may form multilayers, whereas Langmuir theory assumes that the gas would be in the form of a monolayer and uniform at all adsorption sites. The adsorption mechanism for BET theory can be described by:

$$A_{(g)} + S \leftrightarrow AS \tag{4.6}$$

$$A_{(g)} + AS \leftrightarrow A_2S \tag{4.7}$$

$$A_{(g)} + A_2S \leftrightarrow A_3S \tag{4.8}$$

$$A_{(g)} + A_xS \leftrightarrow A_{x+1}S \tag{4.9}$$

where A is the gas molecule (such as nitrogen) and S is the adsorption site on the OCM. The surface area of the OCM is determined by calculating the amount of gas that has adsorbed onto the surface.

4.6 Temperature programmed redox cycling

4.6.1 Pretreatment

After weighing and placing 50 mg of fresh OCM into the Hiden CATlab microreactor, the sample was flushed under helium at 20 ml (STP) min^{-1} prior to testing to evacuate the sampling tube of air. The sample was then pretreated by heating to 1000ºC (using a temperature ramp of 10ºC min^{-1}) under the flow of 20 (STP) ml min^{-1} of 5% vol. O_2 in helium. Once the temperature of the sampling tube had reached 1000ºC, it was left at this temperature for one hour before lowering the temperature back to ambient using the same temperature ramp of 10ºC min^{-1} (all under 5% O_2 in He). This preoxidation procedure was performed to fully oxidise the OCMs to a known oxidation state, which would allow accurate oxygen molar balances to be performed during the following temperature programmed reduction and oxidation experiments.

4.6.2 Procedure

Following the pretreatment step, the sample was immediately flushed with helium at 20 ml min^{-1} to evacuate the sampling tube. Temperature programmed reduction (TPR) was initiated by flowing 20 ml min^{-1} of 5% CO in helium and increasing the furnace temperature to 1000ºC using a temperature ramp of 10ºC min^{-1}. Upon reaching the final set-point temperature of 1000ºC, the 5% CO was switched off and helium at 20 ml min^{-1} was used to evacuate the sampling tube. Under the flow of helium, the furnace temperature was lowered back to ambient (using a temperature ramp of 10ºC min^{-1}), which completed the TPR cycle. Temperature programmed oxidation (TPO) was performed using the same procedure as for the TPR step, except using 20 ml min^{-1} 1% H_2O in helium provided by the water saturator rather than 5% CO in helium. Five cycles of TPR and TPO were performed for all four of the OCMs.

Following the experiment, the OCMs were left at room temperature under the flow of 20 ml min^{-1} helium for at least one hour to evacuate the sampling tube of remaining reactant and product gases. They were then removed from the microreactor for weighing, and characterisation by SEM and XRD analysis.

4.7 Isothermal chemical looping water-gas shift (WGS) process at 850°C

4.7.1 Procedure

After weighing and placing 50 mg of fresh OCM into the Hiden CATlab microreactor, the sample was flushed under helium at 20 ml min^{-1} prior to testing to evacuate the sampling tube of air. Under helium, the furnace temperature was raised to 850°C using a temperature ramp of 10°C min^{-1}. Each sample was subjected to multi-cycle isothermal reduction under 5% CO in helium and isothermal oxidation under 1% H_2O in helium at 850°C with inlet flow rates of 20 ml min^{-1}. Reduction and oxidation steps were performed for 30 minutes each, which was selected as a compromise between allowing sufficient reduction and oxidation of the OCMs

during redox cycling and operating a high number of cycles within a feasible time frame. Helium flushes of 7 minutes after reduction and 13 minutes after oxidation were carried out to evacuate the reactor of feed and products and to avoid mixing of the reducing and oxidising feeds.

Following 150 redox cycles, the furnace temperature was lowered back to ambient under the flow of helium. Following the experiment, the OCMs were left at room temperature under the flow of 20 ml min^{-1} helium for at least one hour to evacuate the sampling tube of remaining reactant and product gases. They were then removed from the microreactor for weighing, and characterisation by SEM and XRD analysis. For clarity only every fifth data point over the 150 cycles performed is shown in the figures. It should be noted that preoxidation treatment of the samples was not performed before carrying out isothermal cycling as the intention was to perform a very large number of cycles. As the samples were not fully oxidised before operation, the initial oxygen content of the samples was not determined.

A mass-to-charge ratio of 28 signal was observed after 7 minutes post-reduction flushing in helium. Assuming this signal is due to carbon monoxide would indicate that a mole fraction of 100 ppm carbon monoxide remained (increasing the flush to one hour still left an observable signal corresponding to about 50 ppm carbon monoxide). It is possible that nitrogen (from the air) was leaking into the system and therefore an additional five-cycle chemical looping WGS test at 850^{o}C was performed using 50 mg of alumina (γ-Al_2O_3). Alumina is frequently used as a support material for OCMs in chemical looping processes and is expected to be relatively inert.[100]

The blank run using γ-Al_2O_3 indicated that ~4 µmol of carbon monoxide was produced per cycle (Figure 4.13). The QMS operates by detecting species according to the mass-to-charge ratio and as nitrogen and carbon monoxide have the same mass-to-charge ratio of 28, it cannot distinguish between these gaseous species. A nitrogen leak resulting in 100 ppm in the product stream over a 30 minute water oxidation step corresponds to a total of 4 µmol. During the water oxidation step of isothermal chemical looping WGS (Section 6.2) with LSF731 and Fe60 the product at mass-to-charge ratio of 28 approximately matched the levels produced during the γ -Al_2O_3 blank run consistent with such a leak of nitrogen. This is consistent with low

rates of carbon monoxide production (and certainly significantly less than 100 ppm). However, the presence of this trace of nitrogen did not allow the accurate measurement of carbon monoxide concentration. The nitrogen in the product stream is too low to have any impact on the carbon balance and any oxygen leak would introduce an insignificant amount of oxygen, some two orders of magnitude lower than in the water feed.

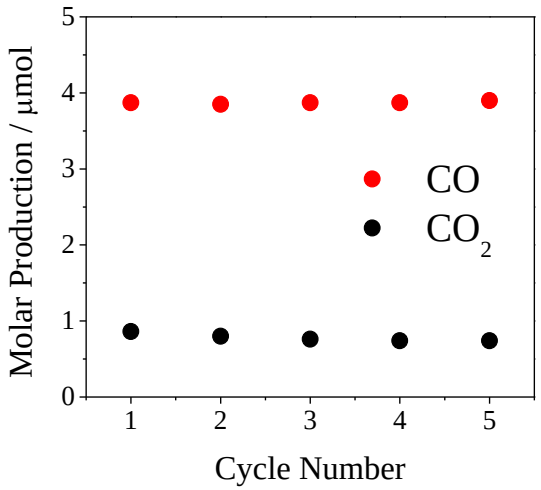

Figure 4.13 Five cycle blank run using 50 mg γ-Al_2O_3 showing carbon monoxide and carbon dioxide produced during the water oxidation steps

4.8 Autothermal chemical looping operation using methane, water and air at 850°C

4.8.1 Procedure

After weighing and placing 50 mg of fresh OCM into the Hiden CATlab microreactor, the sample was flushed under helium at 20 ml min^{-1} prior to testing to evacuate the sampling tube. Each sample was subjected to isothermal multi-cycle reduction under 10% CH_4 in helium, oxidation under 1% H_2O in helium and oxidation under 5% O_2 in helium at 850°C with inlet flow rates of 20 ml min^{-1}. Each reduction and oxidation step was performed for 10 minutes and followed by a helium

flush of 5 minutes to evacuate the reactor of feed and products and to avoid mixing of the feeds. For clarity only every fifth data point is shown in the figures.

It should be noted that preoxidation treatment of the samples was not performed before carrying out isothermal cycling as the intention was to perform a very large number of cycles. As the samples were not fully oxidised before operation, the initial oxygen content of the samples was not determined.

4.9 Experimental errors

Experimental errors can occur due to uncertainties with the measurements made by the equipment used. This would affect accuracy of the results recorded. Table 4.4 shows the equipment used in this work that may have produced experimental errors and the maximum experimental error that may have occurred for each.

Table 4.4 Experimental errors calculated for equipment used

Equipment	Routine set point*	Maximum experimental error	
		Absolute	% (of set point)
Water saturator	1 mol. % H_2O	± 0.1% H_2O	± 10
Mass flow controllers	20 ml min^{-1}	± 0.5 ml min^{-1}	± 2.5
Mole fraction reading by QMS	0-10 mol. %	± 0.05 mol. %	± 0.5
Weighing scales	50 mg	± 0.05 mg	± 0.1
Mass loss		± 9 mg	± 18

* All percentages (%) for routine set point are molar based

At a set point of 1% H_2O in helium, readings from the hygrometer generally fluctuated between 0.9 and 1.1% (this was due to variation of the laboratory temperature and due to mirror balance corrections that were automatically performed

by the hygrometer for efficient feedback control). This experimental error of ± 0.1% H_2O is relatively small, but considering that the hygrometer is used to calibrate the water signal of the QMS, this could lead to larger experimental errors for measuring high water partial pressures (as an example, if 5% H_2O is produced during a reduction step, the absolute error for this measurement could be ± 0.5%). However, this experimental error would have little effect on the results obtained during hydrogen production as the hydrogen mole fraction is calibrated using the calibration gas. Also, over a long water oxidation step a variance of ± 0.1 H_2O in the feed would make little difference to the total hydrogen production formed during the step provided that towards the end of the step the OCM is close to being fully oxidised.

All of the mass flow controllers used for the reactant gases were controlled by computer software, which required an integer value for the flowrate. To ensure that the mass flow controllers were accurate, a flow meter (Varian, UK) was used. Since only integer values can be inputted into the computer software, an experimental+ absolute error of ± 0.5 ml min^{-1} for all flowrates was recorded. Although this error would make insignificant difference for mole fraction measurements by the QMS, during the calculation of the product molar flowrate (Equation (4.4)) this would lead to an error of ± 2.5% of the calculated molar flowrate.

Preliminary experiments were performed to detect the effects of air leaks to the QMS system, and it was noted that at a flow of 20 ml min^{-1} a maximum air leak of 0.04 mol. % was recorded (Section 4.3.3). In addition to this, it was noted in Section 4.3.1 that the purity of all gases used for the experiment was 99.9995% (which could add an addition experimental error of 0.0005%). Therefore, an approximate total error of ± 0.05 mol. % was assumed for measurement by the QMS.

The mass scales used to weigh the samples were accurate to 0.0001 g, which would give an experimental error of ± 0.00005 g for all samples measured. Loss of sample mass occurred as measured by the difference in weight of the sampling tube before and after operation was also recorded which would affect the accuracy of the results. As it was not possible to determine whether mass loss had occurred during operation or following operation (and during removal of the sample from the reactor system), this experimental error was incorporated into all of the results.

Of the experimental errors recorded, it would appear that the mole fraction of water recorded by the QMS was the largest, giving ± 10% experimental error. However, as the mole fraction of water used in the experiments were so low (~1% H_2O), the absolute error was calculated at ± 0.1% H_2O. To check the consequence of this error (in addition to errors by the QMS mole fraction readings), molar balances were performed for water oxidation steps from the temperature programmed studies. The maximum error (assuming 1% H_2O was used as the inlet water oxidation flow) from closure of the hydrogen molar balance was calculated at ~10% (Appendix E1). For the carbon monoxide reduction steps, molar balances could not be performed (due to carbon deposition and OCM reduction allowing loss of carbon and addition of oxygen to the balance). Throughout this thesis the experimental errors calculated in this section have been incorporated into the data involving cyclic molar production.

All of the experiments performed were repeated as cycles (five cycles for temperature programmed operation and over 50 cycles for isothermal chemical looping operation). For this reason, they were not repeated to obtain averaged results as this was unfeasible according to the project timeline provided. To ensure accurate results, calibration of the QMS and flowrate checks were performed on a weekly basis.

4.10 Reactor downtime

Due to the high temperatures exposed to the microreactor and the large amount of electronic equipment used within the CATlab microreactor and QMS system, there were many system faults and equipment breakages encountered during operation of the investigations (including quartz microreactor, microreactor furnace, QMS capillary line heater, QMS bypass vacuum pump and water saturator heating lines as some of the major faults). To minimise downtime, each of the units were quickly sent out for repair as soon as a fault occurred and in some cases replacement units were taken on loan.

4.11 Safety considerations

As the experimental work performed for this thesis involved exothermic reactions, flammable gases and high temperatures, before performing any work in the laboratory the safety risks were assessed. To reduce the risk of explosions and flames in the laboratory, all of the reactant gases used were diluted in helium to below (or close to) the lower flammability/explosive limits. Additionally, carbon monoxide, hydrogen and hydrocarbon detectors were present in the laboratory, which were set to sound an alarm if small levels of these gases (50 – 125 ppm) were detected. All gases were secured in place with a bench clamp and in case of an electrical fault, the CATlab microreactor and QMS system contained three separate thermocouples within the furnace which were set to automatically power down the furnace if a temperature above 1100^{o}C was measured.

Control of substances hazardous health (COSHH) and risk assessment forms were written and inspected by the safety officers of the department and laboratory supervisors to ensure that all of the experiments performed were according to safety regulations. All of the equipment was fully inspected and earthed safely by the department's electronic technician.

Chapter 5

5. Improving the stability of OCM using iron-containing perovskites

5.1 Introduction

The work detailed in this chapter has been published in the Journal of Energy & Environmental Science and the following sections have been adapted from this paper.[185]

The purpose of this study was to perform experiments to determine the feasibility of using iron-containing perovskites as OCMs in a chemical looping process. In such a process, OCMs need to be constantly reduced and oxidised at high temperature, and this can lead to material instability (causing a reduction in activity as the cycles progress). In a previous study, Fe60 was shown to give good material stability and steady hydrogen production over 40 redox cycles in an isothermal chemical looping WGS process at 850^{o}C (Section 3.2.4). Iron-containing perovskites are complex metal oxide materials that are both conductors of ions and electrons (Section 3.3), and have been extensively used as oxygen permeable membranes for continuous production of hydrogen by water splitting. This study compares the iron-containing perovskites LSCF6428 and LSF731 against Fe60. Ni20, which was shown to be a suitable material for combined chemical looping reforming and calcium looping processes for hydrogen production (Section 2.7), is also tested as an additional comparison material. Nickel oxide materials were shown to be suitable for chemical looping combustion processes involving oxidation by air,[186] but in this study the ability to split water at high temperature is assessed.

Temperature programmed operation can be performed by exposing a reactive gas to a catalyst or active material as the temperature is slowly increased using a constant temperature ramp. It is an ideal method to investigate the general catalytic properties of a material and to quickly screen the temperature ranges of reactions that occur due to solid-gas interactions. As an example, iron oxide can exist in four different phases (Fe, FeO, Fe_3O_4 and Fe_2O_3) and by performing TPR using hydrogen, carbon monoxide or methane, the temperatures at which these phase changes occur in the presence of these reducing feeds can be determined. Similarly, the same principle can be applied to perform TPO, where an oxidising agent such as water or air is used instead of a reducing agent. In this investigation, one complete cycle of TPR and TPO represents one temperature programmed redox cycle.

Temperature programmed operation was employed to perform cycles of TPR using carbon monoxide as the reducing agent and TPO using water as the oxidising agent. The overall reaction is the WGS reaction (repeated here for convenience):

$$CO + H_2O \rightarrow CO_2 + H_2 \qquad \Delta H^0_{298K} = -41\ kJ/mol \qquad (5.1)$$

Carbon monoxide was selected (instead of hydrogen or methane) as a suitable reducing agent for this experiment for the following reasons. During the reduction steps, carbon monoxide could allow the Boudouard reaction (Equation (5.2)) to occur and therefore the OCMs could be tested for susceptibility to carbon deposition.

$$2CO \rightarrow C + CO_2 \qquad (5.2)$$

Additionally, during reduction of the OCM with carbon monoxide, only one gaseous product would be formed (carbon dioxide), allowing straightforward analysis of reduction peaks. For simple analysis of the reduction properties of the samples, using carbon monoxide would be advantageous over other carbonaceous reducing agents, for example methane, which can form many different products (carbon monoxide, carbon dioxide, water and hydrogen) during the reduction step.

Five cycles of TPR and TPO using the WGS chemical looping process were performed to analyse the suitability of the four selected OCMs (LSF731, LSCF6428, Fe60 and Ni20). The experimental method for this investigation is described in Section 4.6. Suitability of an OCM was determined by high material stability (no drop in hydrogen production over the five cycles), high hydrogen purity (low levels of carbon monoxide and carbon dioxide during the water oxidation step) and high utilisation of available oxygen in the OCM (this is defined as O_{exch} in Section 3.1.2).

5.2 Results

5.2.1 Material characterisation

A summary of the fresh OCMs is shown in Table 5.1. BET analysis of the materials showed that Ni20 had the highest surface area per mass of sample at 130 m^2 g^{-1}. In terms of rates of reaction, this sample would be expected to show good kinetics due to the high surface area subjected to the reactant gas. The perovskites and Fe60 showed a similar surface area of 6-13 m^2 g^{-1}. Due to the presence of oxygen vacancies within the perovskite structure, oxygen transfer to the bulk of the material was expected to be high, whereas for the Fe60 material kinetic transfer was expected to be limited by the surface reaction (this is discussed in Sections 3.2.3 and 3.3.3).

XRD analysis was performed for all fresh OCM samples and is shown in Figure 5.1. From this analysis LSCF6428, LSF731 and Fe60 showed the correct compositions, whereas Ni20 showed an additional reflection assigned to nickel aluminate ($NiAl_2O_4$) which is usually formed during synthesis of nickel supported on alumina using low nickel loadings.[187] Nickel aluminate would not be expected to participate in redox reactions, but previous studies have shown that it may give benefits such as suppressing sintering of nickel oxide and alumina, and enhancing material stability.[187]

SEM images were taken of the fresh OCMs and are shown in Figure 5.2. LSCF6428 mainly consists of small particles in the micrometer range. LSF731 shows agglomerates up to 200 μm in size composed of crystallites smaller than 2 μm. Fe60 shows particles up to 200 μm in size and the particle surfaces appear to be

rough. Ni20 shows a great range of agglomerated particles up to ~200 μm; the surface of a typical particle is relatively featureless.

Table 5.1 Material characterisation of fresh OCM samples

OCM	Abbreviation	BET / $m^2\ g^{-1}$	ΔOmax* / μmoles	Oxygen content / μmoles
$La_{0.6}Sr_{0.4}Co_{0.2}Fe_{0.8}O_{3-\delta}$	LSCF6428	9	113	675
$La_{0.7}Sr_{0.3}FeO_{3-\delta}$	LSF731	6	111	663
60% Fe_2O_3-Al_2O_3	Fe60	13	500	563
20% NiO-Al_2O_3	Ni20	130	375	375

*based on 50 mg of sample

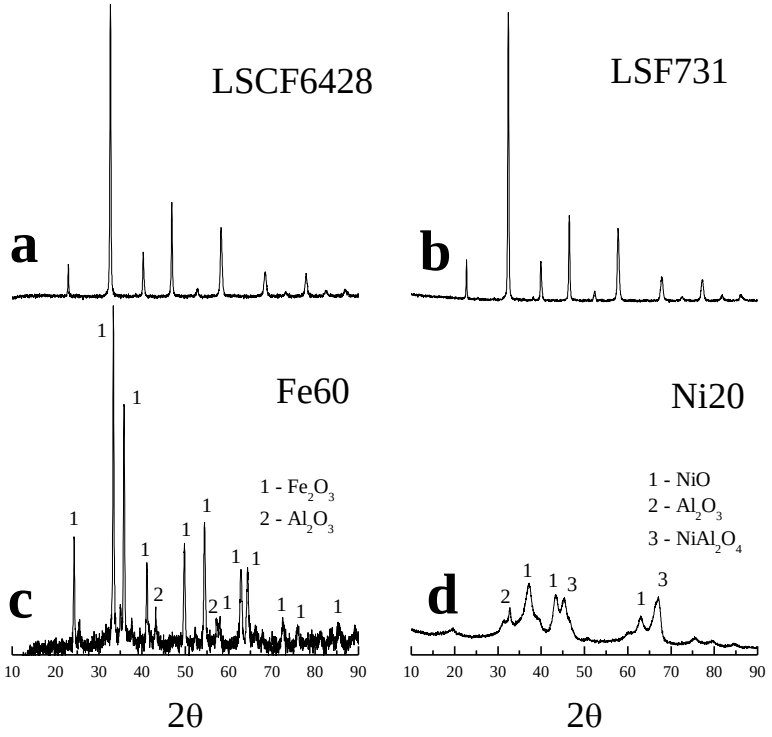

Figure 5.1 XRD analysis of fresh (a) LSCF6428, (b) LSF731, (c) Fe60 and (d) Ni20. Unmarked peaks for (a) and (b) are reflections assigned to the perovskite structure.

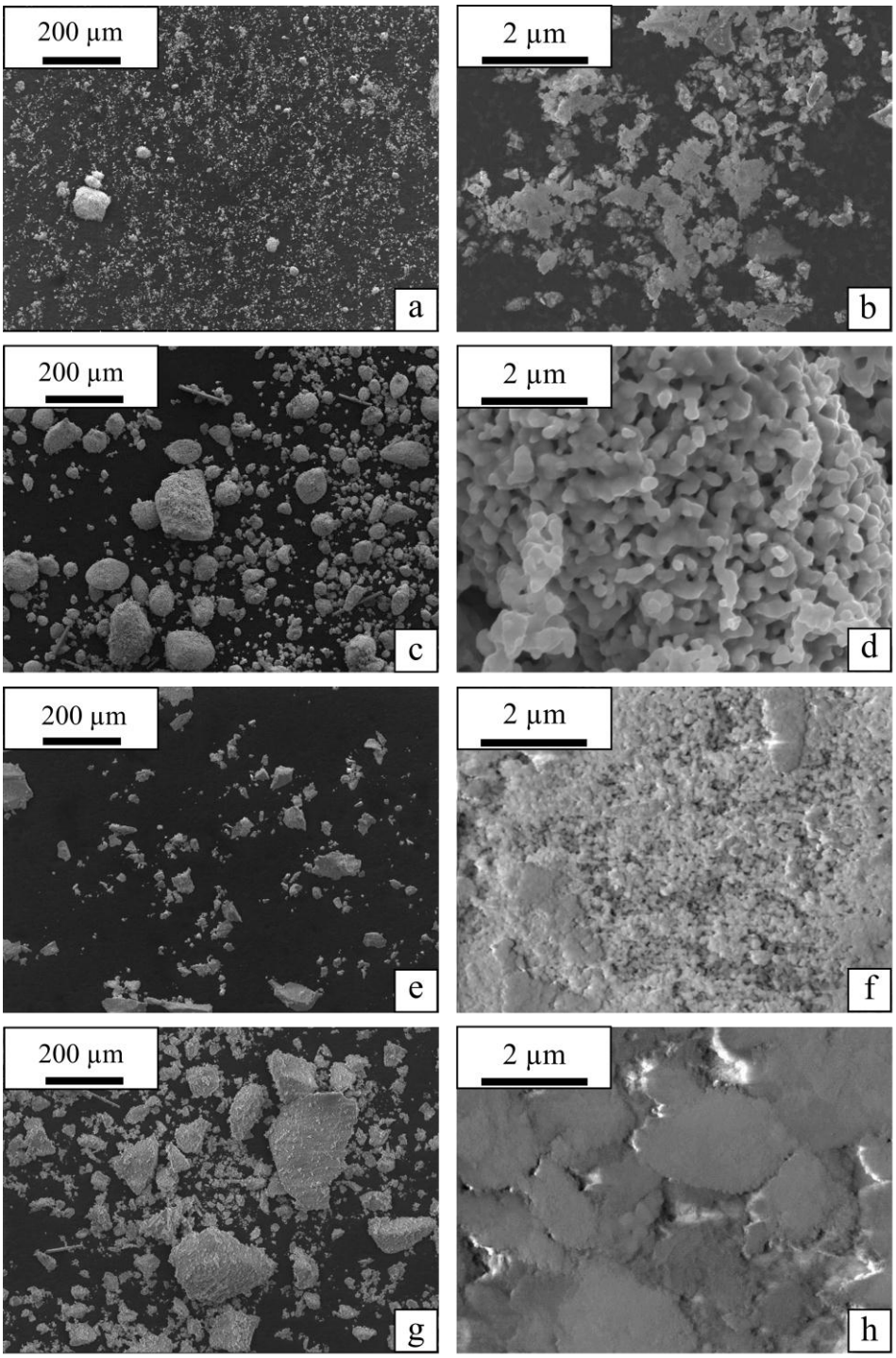

Figure 5.2 SEM images of (a) and (b) fresh LSCF6428, (c) and (d) fresh LSF731, (e) and (f) fresh Fe60 and (g) and (h) fresh Ni20. Images (b), (d), (f) and (h) are magnified images of a typical particle surface.

5.2.2 Survey of activity and deactivation

As mentioned in Section 4.6, the OCMs were preoxidised using 5% O_2 in helium before starting the temperature programmed redox cycles. It was therefore assumed that the four OCMs following pretreatment existed as the following compositions: $La_{0.6}Sr_{0.4}Co_{0.2}Fe_{0.8}O_3$, $La_{0.7}Sr_{0.3}FeO_3$, 60% Fe_2O_3/Al_2O_3 and 20% NiO/Al_2O_3. To compare the change in activity over the five cycles, analysis of the 1st and 5th TPR and TPO cycles are shown in Figure 5.3 in terms of mole fraction of product formed against temperature. As a temperature ramp of 10ºC min^{-1} was used for each experiment, it can be assumed that each 10^oC increase along the x-axis corresponds to approximately one minute of operation. As hydrogen purity is important for this study, the mole fractions of carbon monoxide and carbon dioxide produced during the 1^{st} and 5^{th} water TPO steps are shown in Figure 5.4. In this chapter, O_{exch} is used to express the fraction of oxygen capacity of the OCMs that have been utilised during reduction and oxidation. Calculation of O_{exch} has been defined in Section 3.1.2 and the values of ΔO_{max} used in this chapter have been provided in Table 4.2 in Section 4.2.2.

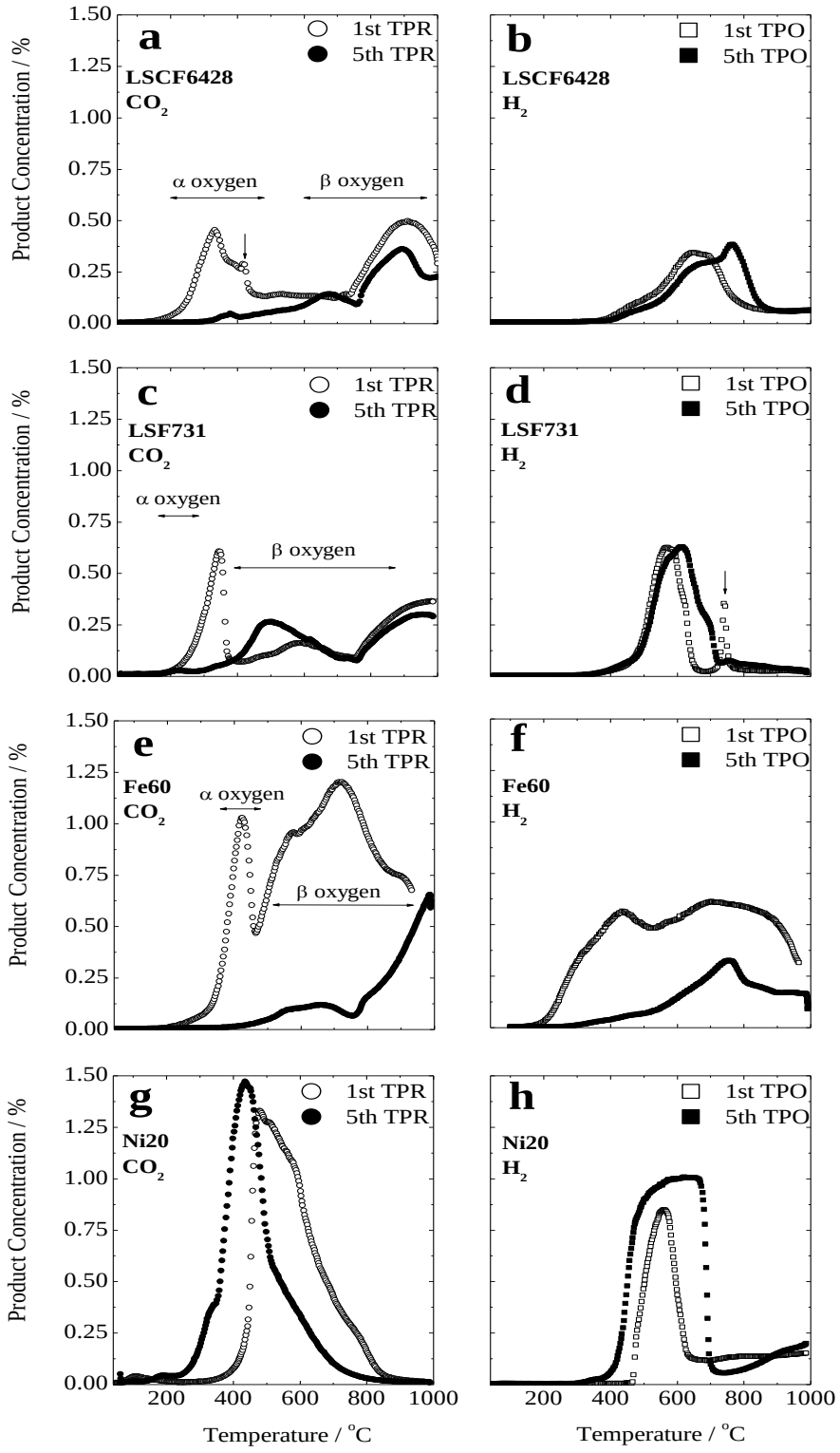

Figure 5.3 Carbon dioxide production during the 1st and 5th TPR and hydrogen production during the 1st and 5th TPO for (a) and (b) LSCF6428; (c) and (d) LSF731; (e) and (f) Fe60 and (g) and (h) Ni20.

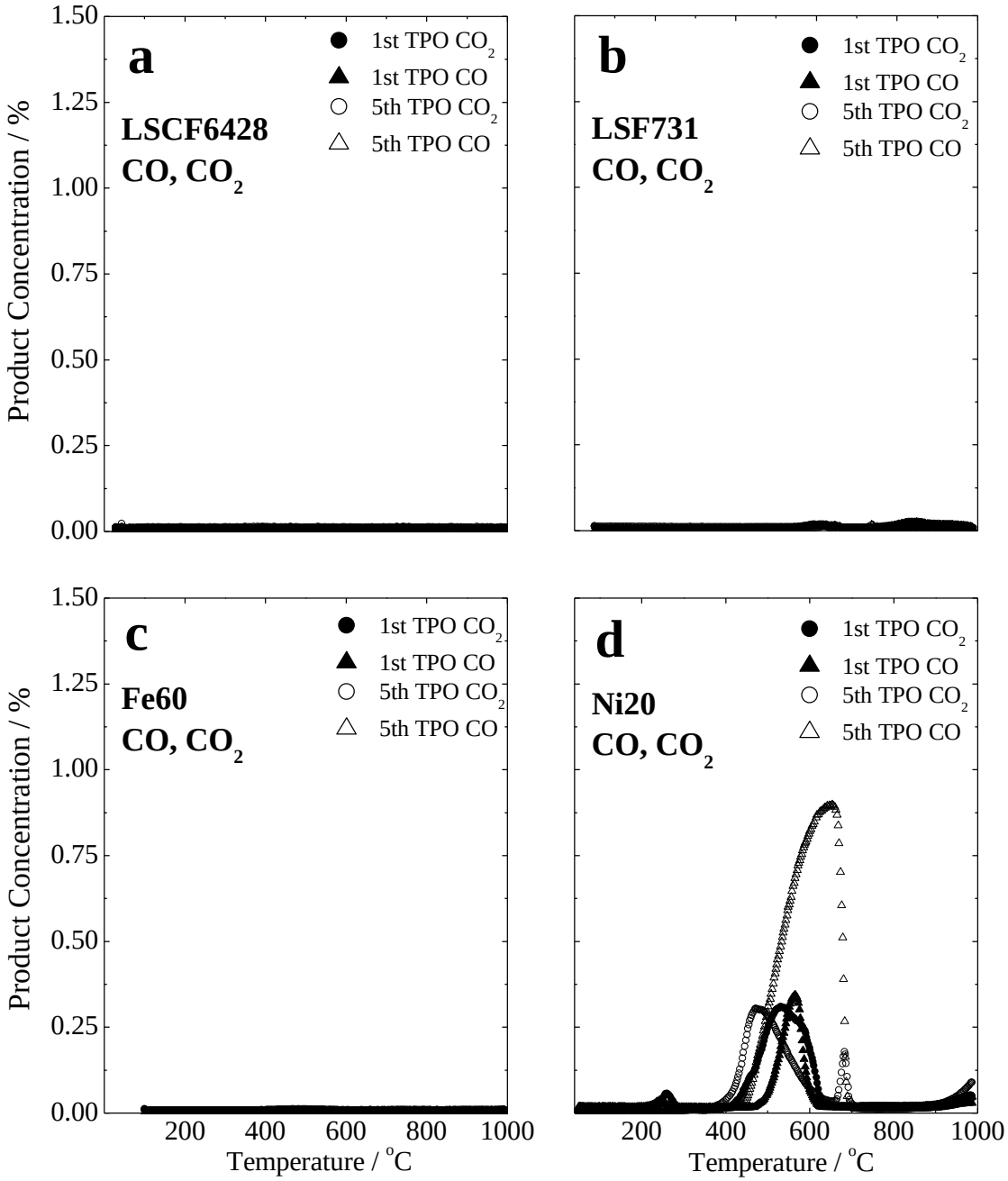

Figure 5.4 Carbon monoxide and carbon dioxide production over the 1st and 5th TPO for (a) LSCF6428; (b) LSF731; (c) Fe60 and (d) Ni20

The two perovskites show a first cycle low temperature carbon dioxide peak (shown as α oxygen in Figure 5.3a and c). This peak does not completely reappear in subsequent reduction cycles. Also present for the perovskites are two asymmetric high temperature carbon dioxide peaks which are assigned to more strongly bound β

oxygen. The β oxygen peaks are rejuvenated after oxidation in water whereas the α oxygen peaks are not to any appreciable extent. The same occurrence is seen for Fe60, which also produces an initial α-peak during the first oxidation which does not reappear in subsequent TPR results (Figure 5.3e). In the literature, experiments performed by water oxidation of Fe60 indicate that water cannot fully oxidise iron oxide back to haematite due to thermodynamic limitations,[100] which would cause the disappearance of the α-peak. However, a similar experiment testing the highest oxidation state possible by water oxidation does not appear to have been performed with the iron-containing perovskite materials. Therefore this additional experiment was performed as part of this study.

In this additional experiment, three samples of 50 mg of fresh LSF731 were firstly reduced by TPR up to 1000^{o}C using 5% CO in helium. Following this, TPO was performed up to 1000^{o}C for each sample but using different methods. One sample was oxidised in 5% O_2 in helium and another sample was oxidised in 5% O_2 in helium and then subjected to a temperature programmed desorption (TPD) step. TPD was performed by flowing helium into the sampling tube whilst raising the temperature from ambient using a temperature ramp of 10^{o}C min^{-1}. The third sample was subjected to TPO up to 1000^{o}C using 1% H_2O in helium and followed by TPD. Following TPO, each of the three samples were subjected to another TPR step in 5% CO in helium up to 300^{o}C (this is the temperature at which the α-peak during the first TPRs for all three samples ended as shown in Figure 5.5).

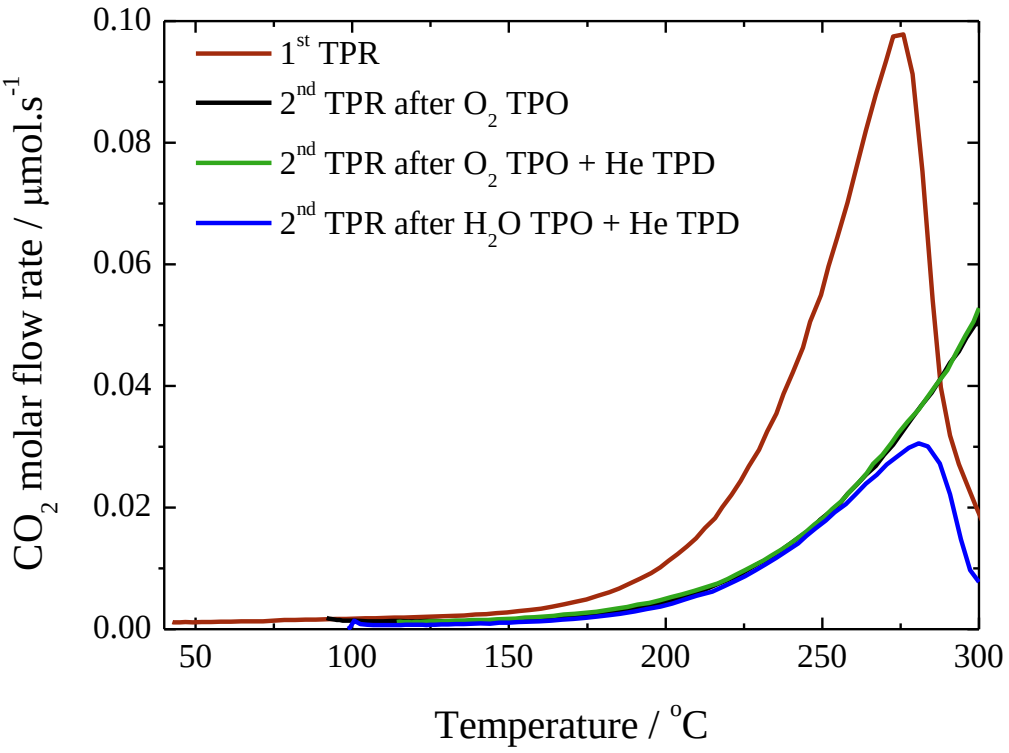

Figure 5.5 Results from the 2nd TPR CO reduction steps following an initial TPR in CO and TPO by either H_2O or O_2

Figure 5.5 shows that a TPO using water or oxygen as the oxidising agent following the initial TPR step cannot fully regenerate the α-peak that is seen in Figure 5.3c. It should be noted however, that the carbon dioxide peak formed seems to be much larger when using a TPO step in oxygen rather than water. It was considered that during oxygen TPO labile oxygen may have adhered to the surface of the OCM, which could have transferred to the reduction step. To eliminate this possibility, a TPO using oxygen was performed immediately followed by a helium TPD step which would remove any labile oxygen. As seen in Figure 5.5 (2nd TPR after O_2 TPO + He TPD), the addition of a helium TPD following oxygen TPO appeared to make no difference to the carbon dioxide peak formed during the 2nd TPR, showing that this peak was not formed due to labile oxygen.

The additional experiment was carried out to reinforce the theory that perhaps there is a thermodynamic limitation that does not allow the iron-containing perovskites to be fully oxidised back to a δ of zero (ie. $La_{0.7}Sr_{0.3}FeO_3$) using water.

A thermodynamic analysis of redox cycling of LSF731 at 850^{o}C using water as the oxidising agent was performed in Section 3.3.2, and this also confirmed that there did exist a thermodynamic limitation (the results showed that during water oxidation of reduced iron oxide at 850^{o}C, δ is not likely to be less than 0.15). This is similar behaviour to iron oxide, which is thermodynamically limited to magnetite (and not haematite) when using water as the oxidising agent at 850^{o}C.

From Figure 5.3a, for LSCF6428 the α oxygen peak is followed by a sharper unresolved peak at higher temperature, indicated by the arrow. The O_{exch} during the first TPR is calculated as 0.29 (Δδ = 0.15) resulting in $La_{0.6}Sr_{0.4}Co_{0.2}Fe_{0.8}O_{2.85}$. Production of carbon dioxide in this step would be formed by the following reaction:

$$CO + O_O^x \Leftrightarrow \ CO_2 \ + V_O^{\bullet\bullet} + \ 2e^- \qquad (5.3)$$

The subsequent β oxygen peak window is ~670-1000°C. According to the oxygen molar balance, LSCF6428 exists as $La_{0.6}Sr_{0.4}Co_{0.2}Fe_{0.8}O_{2.33}$ following the first reduction, which gives an O_{exch} of 1.35 (Δδ = 0.67). O_{exch} is larger than unity in this case as the initial composition of the OCM was $La_{0.6}Sr_{0.4}Co_{0.2}Fe_{0.8}O_3$ due to the preoxidation step in air, (whereas O_{max} is defined on the basis of oxidation in water). The corresponding hydrogen peak from reoxidation with water (Figure 5.3b) is broad and asymmetric. Hydrogen in this step would be produced by Equation (5.4). During the first reoxidation of LSCF6428, O_{exch} = 0.73 (Δδ = 0.37), resulting in $La_{0.6}Sr_{0.4}Co_{0.2}Fe_{0.8}O_{2.7}$.

$$H_2O \ + \ V_O^{\bullet\bullet} + \ 2e^- \ \Leftrightarrow \ H_2 + O_O^x \qquad (5.4)$$

LSF731 shows a low temperature α oxygen peak (Figure 5.3c) which is assigned to the initial reduction step $0 < \delta < 0.15$ and this relates to Fe(IV) conversion to Fe(III) within the perovskite structure. The O_{exch} during the first TPR is calculated at 0.24 (Δδ = 0.12) giving $La_{0.7}Sr_{0.3}FeO_{2.88}$. Carbon dioxide was formed during the step by Equation (5.3). The subsequent β oxygen peak window is 500-

1000ºC. According to the oxygen molar balance, LSF731 exists as $La_{0.7}Sr_{0.3}FeO_{2.35}$ following the first reduction, relating to an O_{exch} of 1.3 ($\Delta\delta$ = 0.65). Again, O_{exch} exceeds unity due to the initial OCM composition existing as $La_{0.7}Sr_{0.3}FeO_3$. For the first reoxidation (Figure 5.3d), which would be performed by Equation (5.4), O_{exch} = 0.73 ($\Delta\delta$ = 0.37), resulting in $La_{0.7}Sr_{0.3}FeO_{2.72}$. LSF731 shows a smaller, sharper high temperature peak at 745ºC indicated by the arrow for the first cycle in addition to the main activity at ~600ºC, this sharp peak reduces greatly in intensity after the first cycle but the feature is not completely removed. It implies that LSF731 initially possesses a well defined reduction site which disappears under cycling. Its position coincides approximately with the strong peak displayed at 770ºC in the 5th cycle for LSCF6428. The entire redox process (Equations (5.3) and (5.4)) shows some irreversibility according to the temperature programmed data which may be manifested in microstructure and crystal structure changes. It is interesting to note that the effect of a small difference in strontium content and the presence of cobalt at the B-site is more apparent in the water oxidation step rather than in the reduction step.

Only one peak can be seen during the first reduction with nickel oxide as the metal oxide can only exist in one of two possible oxidation states at 850ºC (Ni/NiO). During reoxidation of nickel with water, more hydrogen is produced during the 5th TPO compared to the 1st TPO. However, this increase in hydrogen production is due to water oxidation of deposited carbon and results in the production of significant amounts of carbon monoxide and carbon dioxide in the TPO step:

$$C + H_2O \rightarrow CO + H_2 \quad (5.5)$$

$$C + 2H_2O \rightarrow CO_2 + 2H_2 \quad (5.6)$$

The deposited carbon would have been formed by the Boudouard reaction during the reduction step (Equation (5.2)). In comparison, the perovskites and Fe60 exhibit much lower carbon monoxide and carbon dioxide production levels during the oxidation step compared to Ni20.

5.2.3 Oxygen exchange capacity

A comparison of the oxygen exchange capacities (O_{exch}) of the four OCMs over the five redox cycles is shown in Figure 5.6, which have been derived from the TPR and TPO data and normalised to ΔO_{max} (and therefore represented as O_{exch}). Note that the oxygen capacity changes are calculated assuming that carbon dioxide produced during TPR is only formed from reduction of the OCM and hydrogen produced during TPO is only formed from oxidation of the OCM. Therefore, additional carbon dioxide produced by the Boudouard reaction during the TPR is not excluded from the calculation, which results in a very high (above unity) O_{exch} for Ni20 as shown in Figure 5.6b.

The perovskites are fairly stable over the five cycles, giving an O_{exch} of ~0.8-0.9 during each oxidation. This oxygen exchange relates to a $\Delta\delta$ of approximately 0.4-0.45 during redox cycling. This is a remarkable result considering the highly reducing environment and high temperatures subjected to the materials, which suggests that they may be suitable OCMs for long-term isothermal chemical looping cycling.

Fe60 initially had a similar O_{exch} (~0.65) compared to the perovskites as shown in Figure 5.6, however as the cycles progressed the value of O_{exch} reduced for Fe60 whereas for the perovskites O_{exch} remained constant over five cycles. The gradual downwards trend of O_{exch} with increased cycling for Fe60 was possibly due to a loss in surface area of the OCM (this is further discussed in Section 5.2.4).

As explained earlier, Ni20 seemed to cycle with a much higher O_{exch} of above unity due to additional carbon dioxide formed by the Boudouard reaction (Equation (5.2)). This additional carbon would contribute to additional carbon dioxide production during TPR and additional hydrogen production during TPO. Ni20 also shows a reduction in oxygen exchange capacity as the cycles progress, possibly attributable to material sintering or deactivation due to carbon deposition.

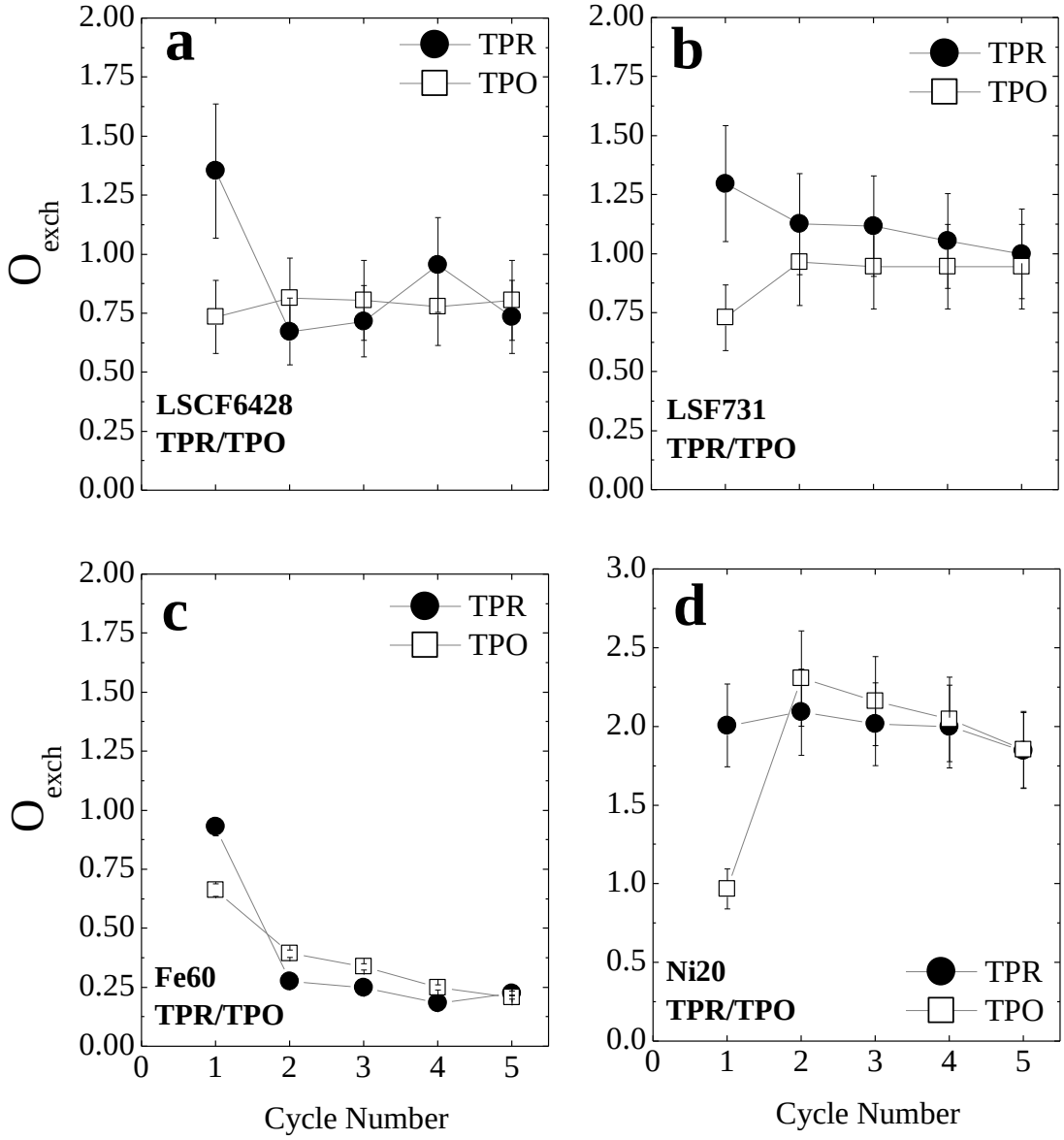

Figure 5.6 Oxygen exchange capacities (with error bars) for (a) LSCF6428 (b) LSF731 (c) Fe60 and (d) Ni20 over five redox cycles integrated over 40-1000°C. The y-axis scale for (d) has been maximised to fit all of the data points.

5.2.4 Post-operation material characterisation

After the five redox cycles were completed, the samples were removed and reweighed. It was clear that sample loss had occurred for all OCMs. The perovskites suffered 18% and 16% loss in mass for LSCF6428 and LSF731, respectively. Fe60 suffered the least severe loss (1%) and Ni20 suffered 10% loss. These mass changes were significant and cannot be explained by irreversible oxygen removal. The most likely explanations are carry-through of the powder past the quartz wool plug and loss of powder during removal of the sampling tube from the microreactor.

All of the samples were characterised by SEM and XRD immediately after performing the experiments to analyse microscopic structural changes and phase changes. Characterisation of fresh OCM has been provided in Section 5.2.1 as a comparison. The results from XRD analysis and SEM analysis following temperature programmed WGS redox cycling are shown in Figure 5.7 and Figure 5.8.

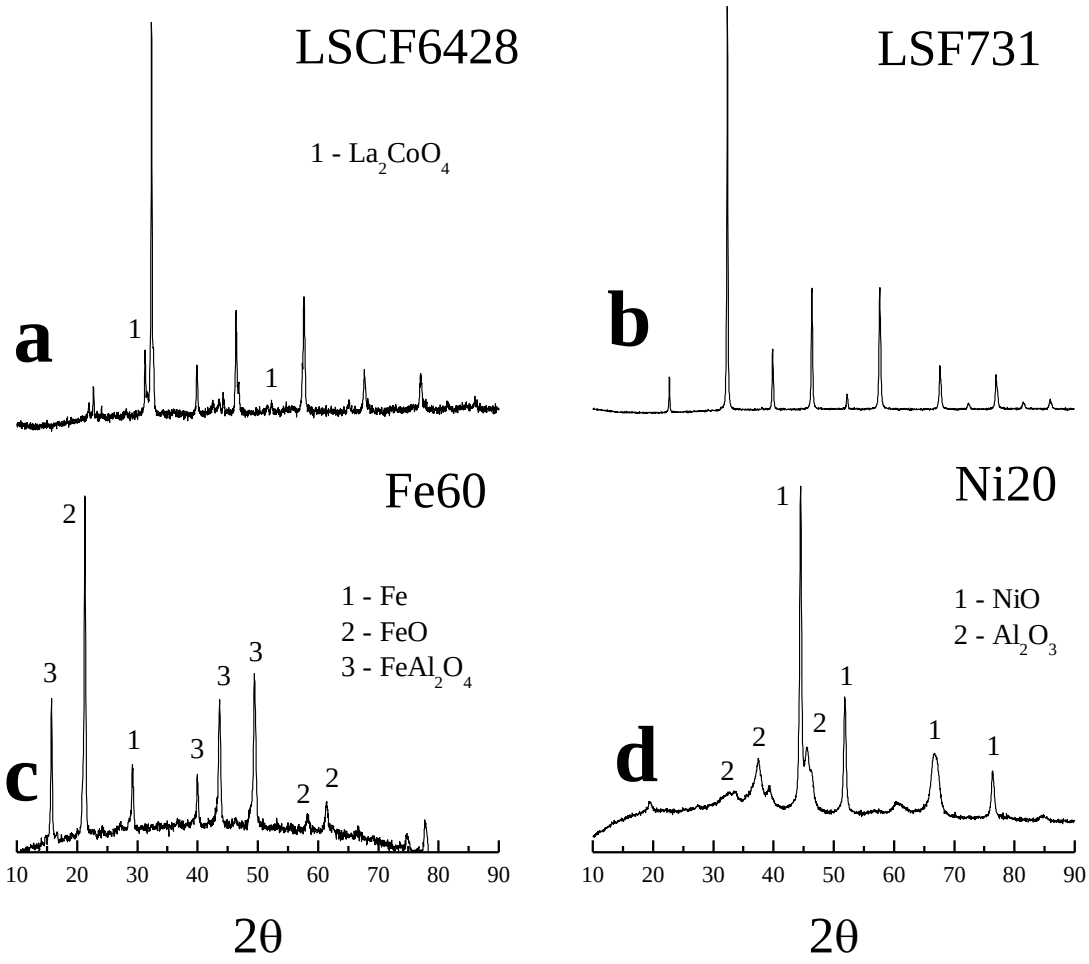

Figure 5.7 XRD analysis of (a) LSCF6428, (b) LSF731, (c) Fe60 and (d) Ni20 following temperature programmed chemical looping WGS operation. Unmarked peaks for (a) and (b) are reflections assigned to the perovskite structure.

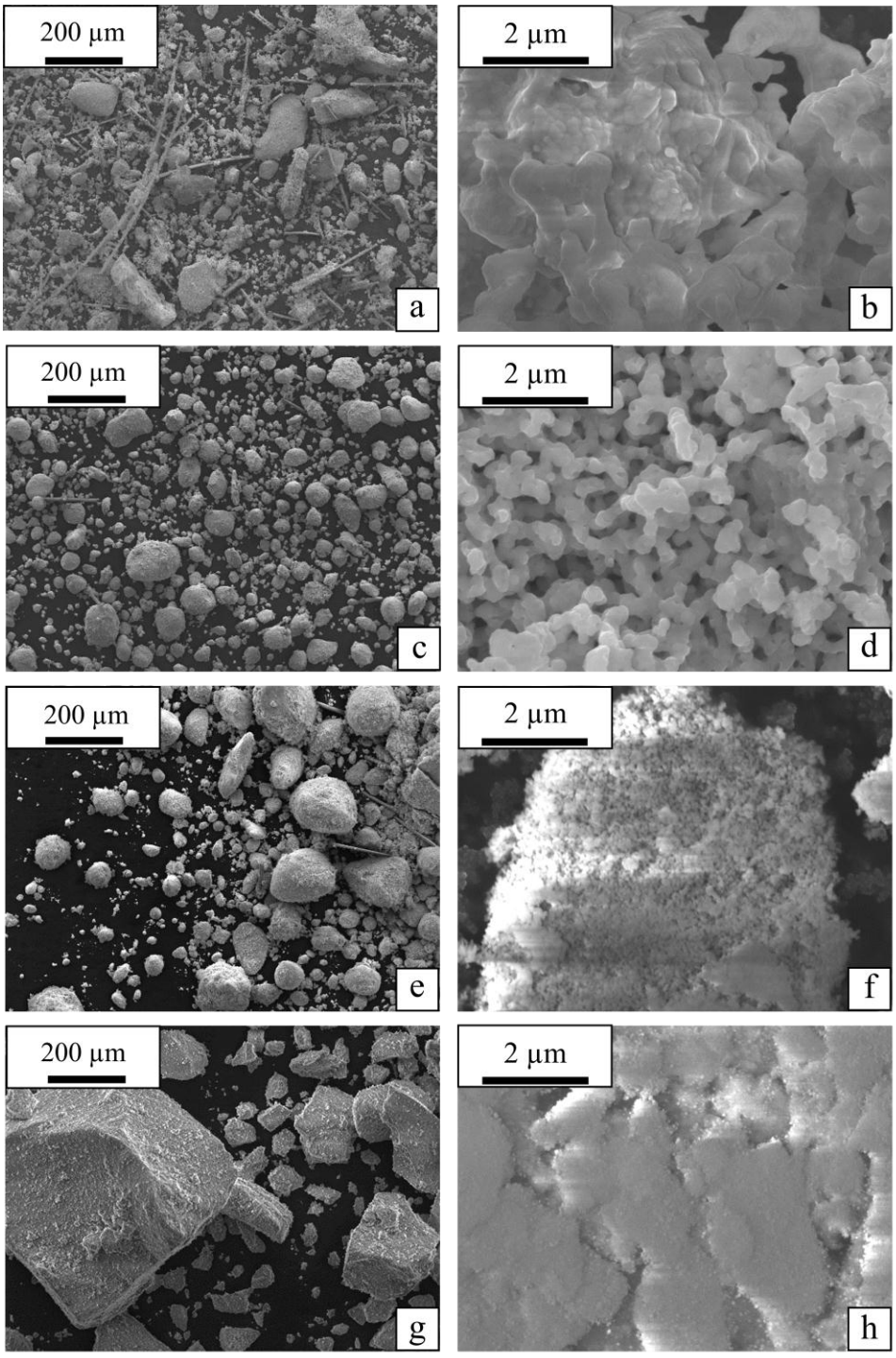

Figure 5.8 SEM images of (a) and (b) LSCF6428, (c) and (d) LSF731, (e) and (f) Fe60 and (g) and (h) Ni20 following temperature programmed WGS operation. Images (b), (d), (f) and (h) are magnified images of a typical particle surface.

The results from XRD show that LSF731 (Figure 5.8b) remained stable during temperature programmed cycling and had not changed phase. This is a remarkable result considering the highly reducing conditions and high temperatures that were repeatedly subjected to the OCM. LSCF6428 formed a secondary phase of La_2CoO_4 indicating slight material instability under temperature programmed cycling. For Fe60 it appears that all of the alumina support has interacted with iron to form the spinel, iron aluminate ($FeAl_2O_4$), which would become an inactive species during cycling under carbon monoxide and water redox cycling.[100] The thermodynamics of iron oxide and alumina has been studied previously by Trumble,[188] who investigated the following reaction:

$$Fe + \frac{1}{2}O_2 + Al_2O_3 \rightarrow FeAl_2O_4 \qquad (5.7)$$

It was noted that high stability of iron oxide on alumina would only exist at high temperatures (above 1600°C).

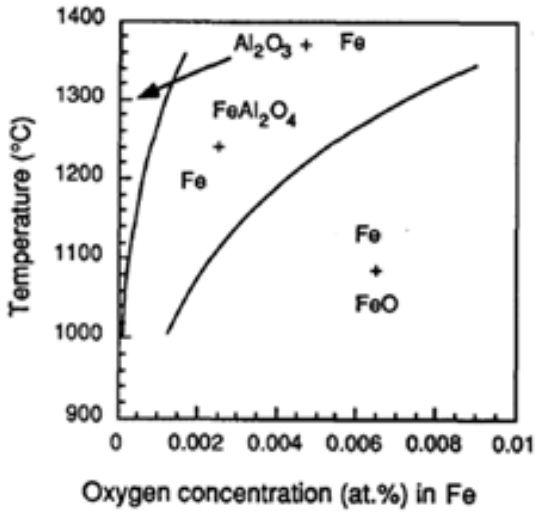

Figure 5.9 Plot taken from Trumble's work showing a thermodynamic phase diagram for Equation (5.7); note that this plot has been simplified for this thesis

Figure 5.9 shows that at high temperatures, an increase in oxygen concentration contained in the iron phase would lead to iron aluminate formation, therefore it is likely that this formation occurs when the iron oxide is in a high oxidation state. This theory is in agreement with a separate study by Tsvigunov *et al.*[189] which states that iron aluminate is formed during oxidation and can be converted back to iron and alumina through carbon monoxide reduction at temperatures in the range of 800-1100^{o}C. This step can be represented by:

$$FeAl_2O_4 + CO \rightarrow Fe + Al_2O_3 + CO_2 \quad (5.8)$$

This argument does not agree with the work of Kierzkowska *et al.*[100] who state that during isothermal chemical looping redox cycling at 850^{o}C using Fe60 as the OCM, it is the carbon monoxide reducing feed which allows formation of iron aluminate, and conversion back to iron oxide and alumina can be performed using only an air oxidation step (and not water). This argument was supported by experimental results. The results from Figure 5.7c can be explained by both arguments, as alumina is not present following the 5th temperature programmed oxidation cycle, indicating that either iron aluminate is formed during water oxidation or that iron aluminate is formed during the carbon monoxide reduction step but not reoxidised during water oxidation.

XRD analysis of fresh Ni20 (Figure 5.1d) shows in addition to nickel oxide and alumina, a secondary phase of nickel aluminate. Figure 5.8d indicates that nickel aluminate had converted back to nickel oxide and alumina after subjecting Ni20 to temperature programmed redox cycling.

SEM images taken of fresh OCMs before performing temperature programmed redox cycling is shown in Figure 5.2 and are compared here against SEM images taken after temperature programmed redox cycling, shown in Figure 5.8. LSCF6428, Fe60 and Ni20 show larger particle sizes following temperature programmed operation, whereas LSF731 seems to have not changed particle size during operation. At high magnification, it would seem that there was no loss of

features for any of the OCMs, apart from for LSCF6428 which had formed agglomerates.

A comparison of pre- and post-operation material characterisation of the OCMs show that out of the materials used in this experiment, only LSF731 had maintained the same material structure in terms of particle size, surface features and phase. As a result, this OCM gives great material stability during redox cycling up to high temperatures.

5.3 Summary

Temperature programmed redox cycling representing an overall WGS reaction was carried out over five cycles to test the ability of the four OCMs to produce pure hydrogen by water splitting and to ascertain susceptibility to sintering. It is clear that both LSCF6428 and LSF731 can produce steady amounts of hydrogen over the five cycles tested, indicating that they do not allow the production of carbon monoxide or carbon dioxide during the TPO step and also do not undergo sintering. This suggests that these materials may perform well as OCMs for isothermal WGS redox cycling under 1000°C. However, from these results it is evident that LSF731 shows slightly better material stability and utilisation of oxygen capacity compared to LSCF6428.

Fe60 gave high hydrogen purity however material stability was an issue as seen by a reduction in hydrogen production as the cycles progressed. Ni20 also showed slight material instability, leading to a slight decrease in hydrogen production as the cycles progressed. Ni20 produced very low purity hydrogen due to carbon deposition, which would make this OCM unsuitable for chemical looping water splitting processes using carbon monoxide as the reducing agent.

Chapter 6

6. Isothermal chemical looping water-gas shift (WGS) operation at 850^{o}C

6.1 Introduction

The work detailed in this chapter has been published in the Journal of Energy & Environmental Science and the following sections have been adapted from this paper.[185]

The results from the previous temperature programmed redox study (Section 5) show that Ni20 is highly susceptible to carbon deposition during reduction with carbon monoxide, whereas Fe60 is not as susceptible and is therefore able to produce pure hydrogen during water oxidation. The results for the two perovskite materials showed that they gave similar performances to each other; however it was evident that LSF731 showed slightly higher hydrogen production per cycle compared to LSCF6428. Therefore LSF731 and Fe60 were selected for further testing by carrying out a large number of isothermal chemical looping WGS cycles at 850^{o}C using carbon monoxide as the reducing agent and water as the oxidising agent. In the literature Fe60 has previously been used to perform isothermal chemical looping water splitting at 850^{o}C in order to produce steady hydrogen production over 40 cycles and it was therefore used as the comparison OCM for this study. The experimental method for this investigation is described in Section 4.6.

In this chapter, O_{exch} is used to express the fraction of oxygen capacity of the OCMs that had been utilised during reduction and oxidation. Calculation of O_{exch} has been defined in Section 3.1.2 and the values of ΔO_{max} used in this chapter have been provided in Table 4.2 in Section 4.2.2.

6.2 Results

6.2.1 Survey of activity and deactivation

Figure 6.1 compares the carbon dioxide and hydrogen production during the 1st and 150th reduction and oxidation steps respectively for both LSF731 and Fe60 as a function of time. The dotted line in Figure 6.1d shows the hydrogen product molar concentration which would indicate the transition of iron to wüstite, and wüstite to magnetite according to thermodynamic analysis.[67] The ratio of water to hydrogen (pH_2O/pH_2) measured during the water oxidation steps for both LSF731 and Fe60 is shown on the y-axis of Figure 6.1b and d. This ratio can be used to approximate the δ of LSF731 according to Figure 3.9 in Section 3.3.2.

During the first reduction of 50 mg of LSF731, 78 μmol of carbon dioxide was formed relating to an O_{exch} of 0.7 and Δδ increase of 0.35 (Figure 6.1a). Reduction of LSF731 would be performed by:

$$CO + O_O^x \Leftrightarrow CO_2 + V_O^{\bullet\bullet} + 2e^- \quad (6.1)$$

Comparing the 1st to the 150th oxidation cycle, it is clear that carbon dioxide production had decreased slightly during the 150th reduction cycle compared to the 1st cycle. It is also interesting to note that the hydrogen peak maxima for LSF731 increases from ~0.9% to ~1.05%, and that the oxidation period is shorter for the latter.

Production of hydrogen during the first oxidation cycle using LSF731 (Figure 6.1b) stops after 12 minutes. Hydrogen would be performed by water oxidation of LSF731 by:

$$H_2O + V_O^{\bullet\bullet} + 2e^- \Leftrightarrow H_2 + O_O^x \quad (6.2)$$

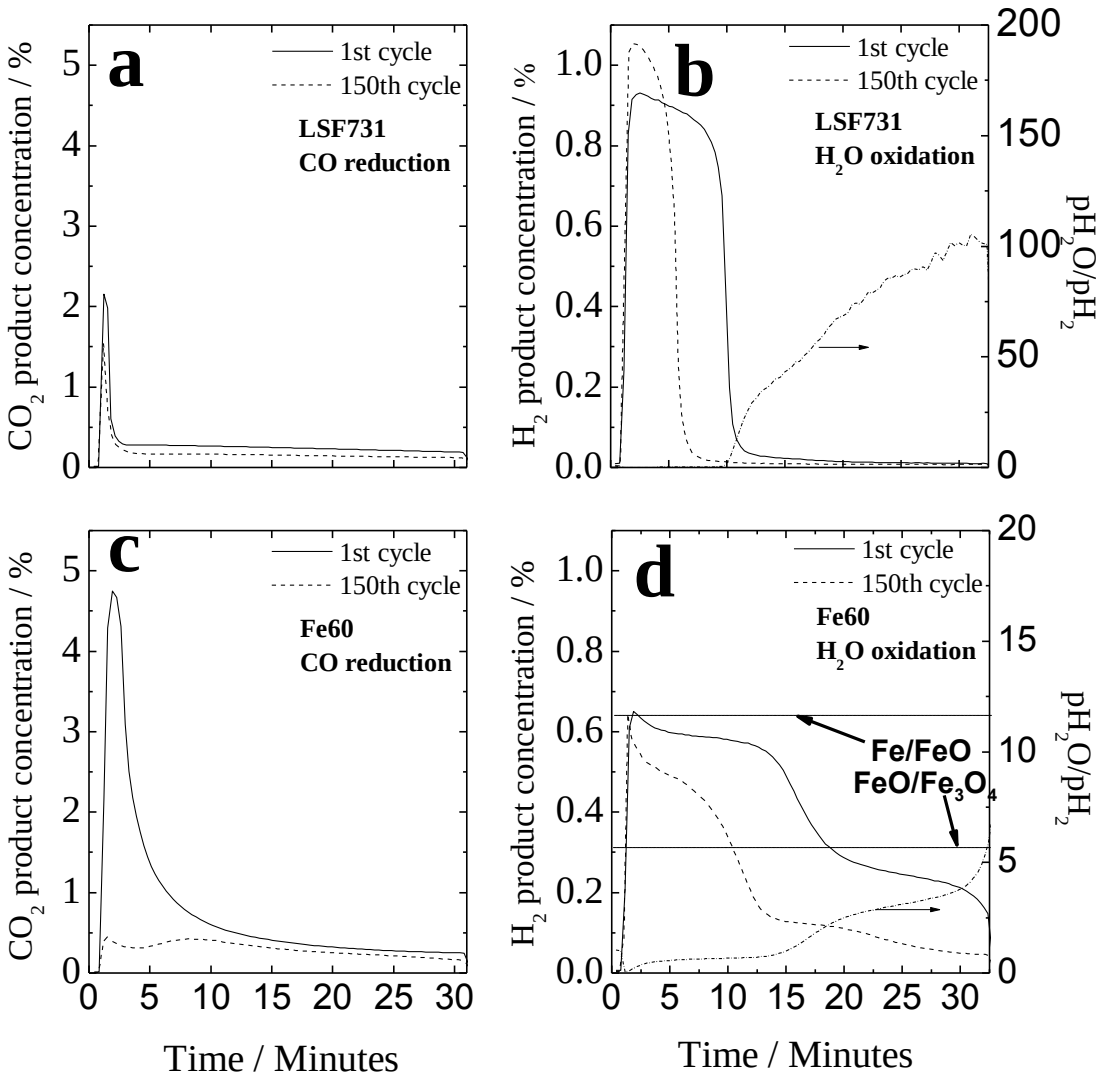

Figure 6.1 1st (solid line) and 150th (dashed line) isothermal chemical looping WGS cycles recorded at 850°C for 50 mg of (a) LSF731, reduction in carbon monoxide (b) LSF731, reoxidation in water (c) Fe60, reduction in carbon monoxide (d) Fe60, reoxidation in water. Arrows indicate oxidation state changes of iron in Fe60 according to thermodynamic studies.

The first water oxidation step causes an O_{exch} of 0.65 (producing 72 µmol of hydrogen for 50 mg of sample) which closely matches the O_{exch} measured during the first reduction step of 0.7 (producing 78 µmol of carbon dioxide for 50 mg of sample). The pH_2O/pH_2 ratio at the end of the first oxidation cycle for LSF731 is close to ~100, which indicates that δ should be 0.15 according to the thermodynamic

plot shown in Figure 3.9. Therefore, it is calculated that following the 1st reduction δ should be 0.48, which indicates that the brownmillerite phase had not been formed.[174, 175]

Comparing the 1st and 150th reduction and oxidation cycles, the Fe60 shows signs of deactivation as indicated by lower levels of production during the 150th cycle, especially with regards to carbon dioxide production during the reduction step (Figure 6.1c, d). The steps that would occur during reduction would be:

$$CO + Fe_3O_4 \rightarrow 3FeO + CO_2 \quad (6.3)$$

$$CO + FeO \rightarrow Fe + CO_2 \quad (6.4)$$

During water oxidation the following reaction steps are possible:

$$H_2O + Fe \rightarrow H_2 + FeO \quad (6.5)$$

$$\frac{1}{3}H_2O + FeO \rightarrow \frac{1}{3}H_2 + \frac{1}{3}Fe_3O_4 \quad (6.6)$$

O_{exch} during the first reduction is ~0.42 (producing 210 µmol of carbon dioxide for 50 mg of sample). Figure 6.1c shows that the initial reduction to magnetite is very quick and occurs within the first five minutes, whereas the following reduction period is much longer. The carbon dioxide mole fraction towards the end of the reduction step is lower than 1.75%, which according to thermodynamics indicates that the Fe60 had been fully reduced to iron.[84]

Comparatively, the following reoxidation step with water (Figure 6.1d) gives an O_{exch} of ~0.23 (115 µmol of hydrogen for 50 mg of sample). It is interesting to note that during water oxidation, there appears to be two oxidation stages. The

hydrogen concentrations during these two steps approximately match the expected levels obtained from thermodynamic analysis assuming that the two separate steps reflect iron-to-wüstite oxidation and wüstite-to-magnetite oxidation.[48] At the end of the oxidation step hydrogen production starts to decline towards zero, indicating that the sample had nearly fully oxidised to magnetite. It is clear that O_{exch} during the first reduction and oxidation steps, which should be equal to unity for redox cycling between iron and magnetite, is much lower than expected and this could be attributed to the loss of active iron in the material to form the spinel, $FeAl_2O_4$.

6.2.2 A comparison between the activity of LSF731 and Fe60 over 150 chemical looping WGS cycles at 850^{o}C

Long term cycling data are presented in Figure 6.2. The plots indicate the absolute molar amount of product(s) and also O_{exch}, both as a function of cycle number.

So far in previous studies, 40 cycles have been reported using Fe60 with carbon monoxide as the reducing agent and full oxidation to haematite using first water and then air.[100] In that investigation the water oxidation step was used to oxidise iron to magnetite and produce hydrogen, and the air oxidation step was subsequently used to oxidise magnetite to haematite. The advantage of incorporating the air step is that the reaction between oxygen and magnetite is exothermic and provides additional heat to the system.

The results of the investigation indicated no loss in activity of Fe60 over the 40 cycles. In comparison, in this work, LSF731 shows stable reduction behaviour over 140 cycles. The corresponding reoxidation to produce hydrogen shows a small decrease over the first 40 cycles, however over the next 100 cycles O_{exch} is stable at ~0.37-0.41 (41-45 μmol of hydrogen for 50 mg of sample).

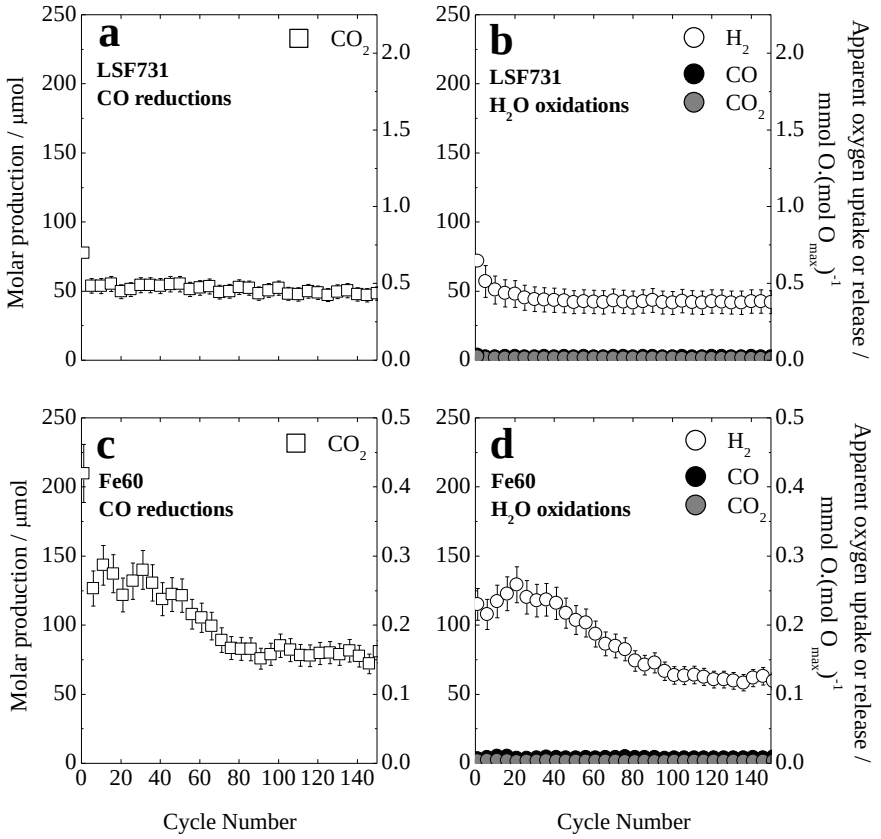

Figure 6.2 Molar production (with error bars) during isothermal cycling at 850°C for 50 mg of (a) LSF731, reduction in carbon monoxide (b) LSF731, reoxidation in water (c) Fe60, reduction in carbon monoxide (d) Fe60, reoxidation in water.

Fe60 is less stable compared to LSF731 but allows a higher reduction activity. Carbon dioxide production appears to decrease with cycling up to cycle number 100; a similar reduction in hydrogen production is also observed during reoxidation. After 16 cycles, O_{exch} reaches ~0.25 (producing 125 µmol of hydrogen for 50 mg of sample). After 100 cycles, this drops to ~ 0.16 (80 µmol of hydrogen for 50 mg of sample).

The calculated carbon dioxide production during the reduction steps is always considerably larger than the hydrogen produced during the oxidation steps, possibly signifying continual deposition of carbon *via* the Boudouard reaction during the reduction cycles which is not removed during reoxidation with water. It is also possible that the reduction step forms an additional phase caused by the reaction of

iron oxide with alumina, which has been observed in previous investigations where a stable phase described as $FeO•Al_2O_3$ was detected by powder XRD.[100] Post-operation analysis, presented later in Section 6.2.3, indicates that this phase is the spinel, $FeAl_2O_4$. A combination of a decrease in surface area caused by sintering, restricted access to the exchangeable oxygen caused by stable carbon deposition and the formation of $FeAl_2O_4$ could explain the progressive decrease in hydrogen and carbon dioxide production in the oxidation and reduction steps.

A drop in hydrogen production as the cycles progress could cause problems in an industrial process if hydrogen levels need to be predictable and constant. This could eliminate Fe60 as the ideal OCM for chemical looping WGS operation at 850^{o}C. The advantage of using LSF731 would be steady hydrogen production per cycle. This would lead to more straight forward process control and design as there would be no fluctuations in hydrogen production per cycle. Also, since LSF731 can withstand long-term redox cycling without losing material stability, if the process is industrialised the OCM would not require regular replacement, which may reduce plant downtime. Additionally, a recent study has shown that if material degradation or formation of secondary phases were to occur, perovskite materials could be regenerated using an in-situ recalcination step[190, 191] and removal of carbon from the OCM could also be performed easily.[192] This could eliminate the requirement of having to replace the OCM due to material deactivation or carbon contamination, and the perovskite OCM could be considered as a capital cost rather than an operation cost.

The amount of hydrogen produced per cycle during isothermal chemical looping WGS operation at 850^{o}C using LSF731 was ~45 μmol. As each redox cycle was performed for one hour and 50 mg of the OCM was used, the molar amount of hydrogen that was produced per mass of OCM is calculated at ~0.9 mol kg^{-1} hr^{-1}. Assuming that the density of LSF731 is 1.26 g cm^{-3} (Pi-Kem Ltd., UK), the annual production of hydrogen that could be produced by this method using a 1 m^3 reactor packed with LSF731 would scale up to produce ~220,000 m^3 (or ~20 tons) of hydrogen per annum (assuming no material deactivation). Considering that one hour was used to perform one redox cycle, a shorter cycling time could be used (according to Figure 6.1 less than 30 minutes may be sufficient) which may give an

improvement in hydrogen production rate. The rate of reduction and oxidation could further be improved by increasing the reduction and oxidation feed flowrates and concentrations. Additionally, instead of performing the process in a periodic reactor, it could be carried out in a circulating fluidised bed reactor to ensure continuously high production of hydrogen.

6.2.3 Post operation analysis

Following operation of the isothermal chemical looping WGS process, the OCM samples were removed and reweighed. It is clear that sample loss had occurred for all OCMs. The losses in mass were 8% for LSF731 and 7% for Fe60. The most likely explanations are carry-through of the powder past the quartz wool plug and loss of powder during removal of the sampling tube from the microreactor.

All of the samples were characterised by SEM and XRD immediately after performing the experiments to analyse microscopic structural changes and phase transitions. Characterisation of fresh OCM has been provided in Section 5.2.1 as a comparison. The results from XRD analysis and SEM analysis following isothermal WGS redox cycling at 850^{o}C compared against fresh OCM are shown in Figure 6.3 and Figure 6.4.

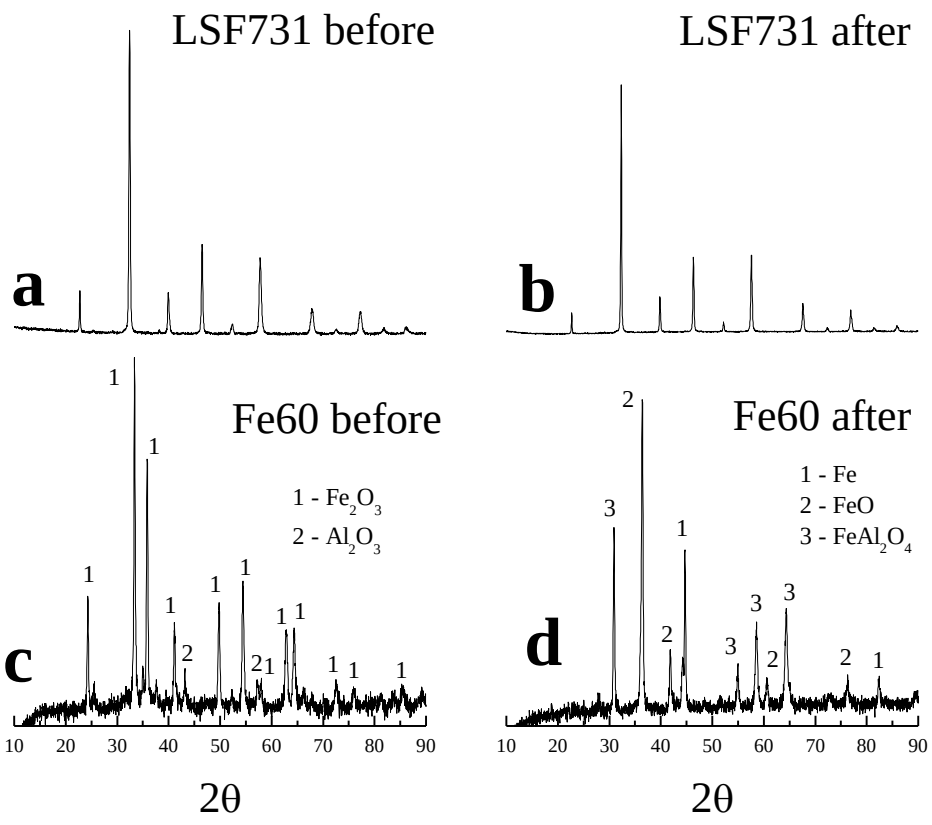

Figure 6.3 XRD analysis of (a) LSF731 fresh, (b) LSF731 following isothermal chemical looping WGS operation at 850^{o}C, (c) Fe60 fresh and (d) Fe60 following isothermal chemical looping WGS operation at 850^{o}C. Unmarked peaks for (a) and (b) are reflections assigned to the perovskite structure.

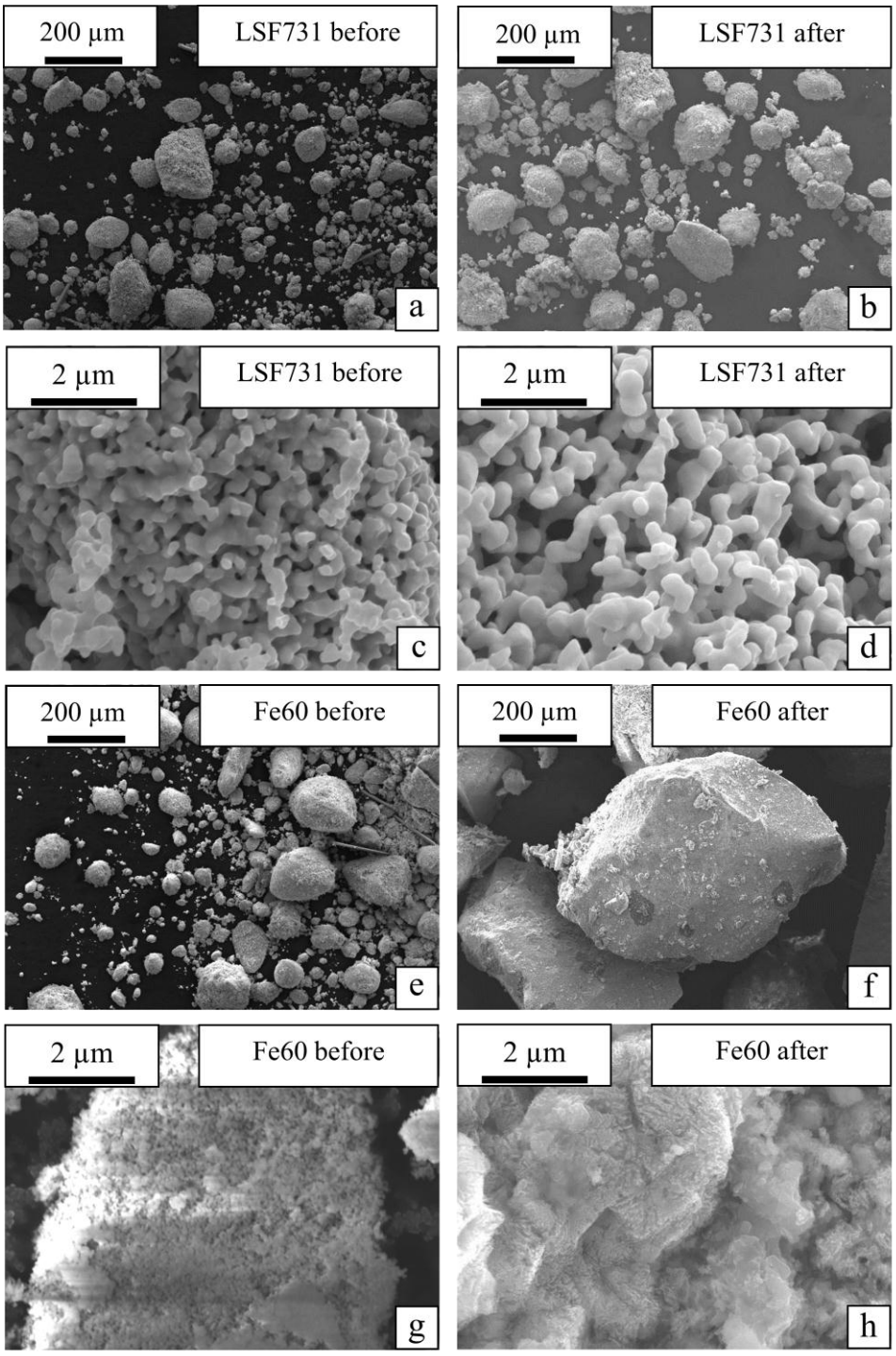

Figure 6.4 SEM images of (a) and (c) fresh LSF731, (e) and (g) fresh Fe60, (b) and (d) LSF731 following isothermal chemical looping WGS operation at 850^{o}C and (f) and (h) Fe60 following isothermal chemical looping WGS operation at 850^{o}C. Images (c), (d), (g) and (h) are magnified images of a typical particle surface.

Following 150 isothermal chemical looping redox cycles performed using carbon monoxide as the reducing agent and water as the oxidising agent, there appears to have been no phase transitions for LSF731 (Figure 6.3b); it has remained entirely in single-phase following operation. In addition to this, SEM analysis (Figure 6.4) shows no signs of sintering or agglomeration by LSF731, and the finger-like features at high magnification of the material surface are still present (Figure 6.4d).

Similar to the results from temperature programmed chemical looping WGS operation (as performed in Section 4.6), XRD analysis of Fe60 has shown the interaction between iron oxide and alumina to form iron aluminate ($FeAl_2O_4$). The formation of this inactive species would explain the continuous reduction in hydrogen production as the isothermal chemical looping WGS cycles progressed as shown in Figure 6.2d. In addition to the transition phase, the Fe60 OCM particles appear to have agglomerated during operation, leading to larger particle sizes (Figure 6.4f).

6.3 Summary

The work performed in this study has shown that if LSF731 is used in the isothermal chemical looping WGS process at 850^{o}C, there would be minimal material stability loss which would lead to less OCM replacement in an industrial process. LSF731 can perform 140 cycles of steady hydrogen production by isothermal chemical WGS at 850^{o}C (this appears to be the highest number of steady hydrogen production cycles performed for a chemical looping WGS process in the literature so far). Fe60 showed high activity at the start of the redox cycles, but as the cycles progressed activity dropped due leading to lowered hydrogen production.

LSF731 was continuously reduced and oxidised in cycles that lasted one hour each, and therefore in total the OCM was under operation for above 150 hours continuously with no signs of deactivation or material change. Previous studies have also shown that if the perovskite does lose activity, a recalcination step could be performed to regenerate the material, making LSF731 a promising candidate OCM for chemical looping water splitting processes.

Chapter 7

7. Autothermal chemical looping water splitting operation

7.1 Introduction

The work in this chapter is based on the conceptual study of the autothermal chemical looping process for hydrogen and methanol production described in Section 2.5. In this process, iron oxide is used as the OCM for a three-step cyclic process using methane, water and air as the feeds. Thermodynamic analysis shows that the process can be operated slightly exothermically whilst producing pure hydrogen and methanol as products.

The feasibility of using iron-containing perovskite materials as OCMs for a chemical looping process involving hydrogen production has been assessed in Section 6. Steady hydrogen production was seen over more than 100 cycles using LSF731 in an isothermal WGS redox cycling process, where carbon monoxide was employed as the reducing agent and water was used as the oxidising agent at 850^{o}C. In an industrial process, it may be difficult to obtain carbon monoxide in a pure form to be used as the reducing feed and therefore in this chapter methane is considered instead. Methane can either be fully or partially oxidised by an OCM which gives two possible groups of products that can form during the reduction step. However, solid carbon can also be formed which would deposit on the OCM if methane decomposition was to occur. The possible reactions that can occur during the methane reduction step using iron oxide as the OCM are repeated here for convenience:

$$CH_4 + 4Fe_3O_4 \rightarrow CO_2 + 2H_2O + 12FeO \quad (7.1)$$

$$3CH_4 + 12FeO \rightarrow 3CO_2 + 6H_2O + 12Fe \quad (7.2)$$

$$4CH_4 + 4Fe_3O_4 \rightarrow 4CO + 8H_2 + 12FeO \quad (7.3)$$

$$12CH_4 + 12FeO \rightarrow 12CO + 24H_2 + 12Fe \quad (7.4)$$

$$CH_4 \rightarrow C + 2H_2 \quad (7.5)$$

It should be noted that according to these reactions, the ratio of water-to-carbon dioxide or hydrogen-to-carbon monoxide produced during the methane reduction of the OCM should be equal to two. A ratio higher than this could indicate that methane pyrolysis is occurring (Equation (7.5)), as the carbon from the methane in this case would be depositing onto the OCM and therefore would not be measured as a gaseous product by the QMS. This solid carbon could then react with water during the water oxidation step to form carbon monoxide and carbon dioxide impurities during hydrogen production, which should be avoided if pure hydrogen is required.

The overall process where methane and water is used as the reducing and oxidising agents would be a steam methane reforming step. In this process, methane can be either fully or partially oxidised and the reactions would be endothermic:

$$CH_4 + H_2O \rightarrow CO + 3H_2 \qquad \Delta H^0_{298K} = 241 kJ/mol \quad (7.6)$$

$$CH_4 + 2H_2O \rightarrow CO_2 + 4H_2 \qquad \Delta H^0_{298K} = 165\ kJ/mol \quad (7.7)$$

If methane is used as the reducing agent, additional heat will be required to operate the process. An additional air oxidation step can be incorporated into the chemical looping cycling process to further oxidise the OCM by an exothermic reaction to provide heat to the system:

$$\frac{1}{2}O_2 + 2Fe_3O_4 \rightarrow 3Fe_2O_3 \qquad \Delta H^0_{298K} = -240\ kJ/mol \qquad (7.8)$$

Since water cannot oxidise magnetite to haematite (due to thermodynamic limitations), the additional air step would not reduce the amount of hydrogen produced per cycle, however more reducing feed would be needed for the additional step required to convert haematite to magnetite. The overall process that is operated in this study is illustrated by Figure 7.1.

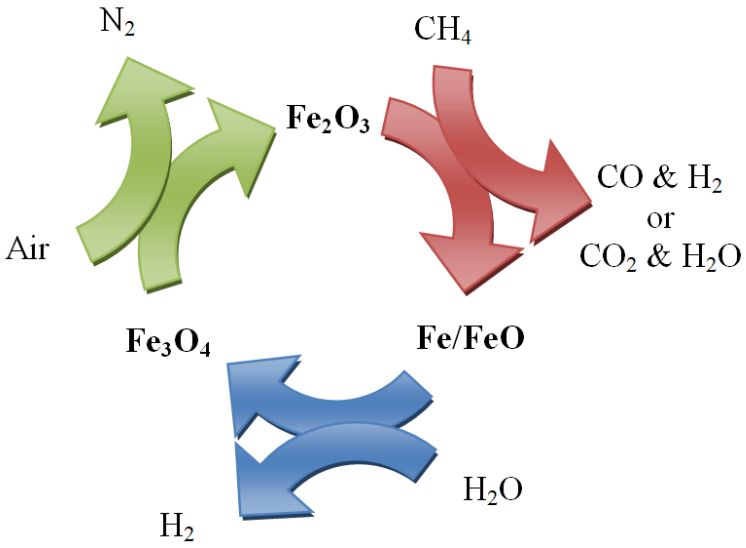

Figure 7.1 Three-step autothermal chemical looping process for pure hydrogen production

This three-step cyclic process is used to assess the performance of LSF731 and Fe60 over 50 cycles, where material stability, hydrogen purity and selectivity towards partial or full oxidation of methane were the main focus of the investigation. For this experiment an isothermal operating temperature of 850°C was used throughout. This temperature was selected based on the work of Go *et al.*[70] who determined that a temperature between 800-900°C should be used for chemical looping processes involving methane reduction and water oxidation (as explained in Section 2.4.4). This temperature was also selected because this work follows on from the

investigation in Section 6, which involved isothermal chemical looping WGS operation at 850^{o}C.

It should be noted that in the following experiments, the air oxidation step uses oxygen balanced in helium (5% O_2 in helium) rather than actual air (oxygen in nitrogen) as the oxidising agent. The use of nitrogen as a carrier gas was avoided because nitrogen and carbon monoxide cannot be distinguished by mass spectrometry (due to these species having the same mass-to-charge ratio).

7.2 Results

7.2.1 Survey of activity and deactivation

Figure 7.2 shows the mole fraction of products formed during the 1st and 50th methane reduction steps for LSF731. Mainly syngas was formed during the 1st reduction step rather than water and carbon dioxide, indicating that methane had only been partially oxidised by LSF731 rather than fully oxidised.

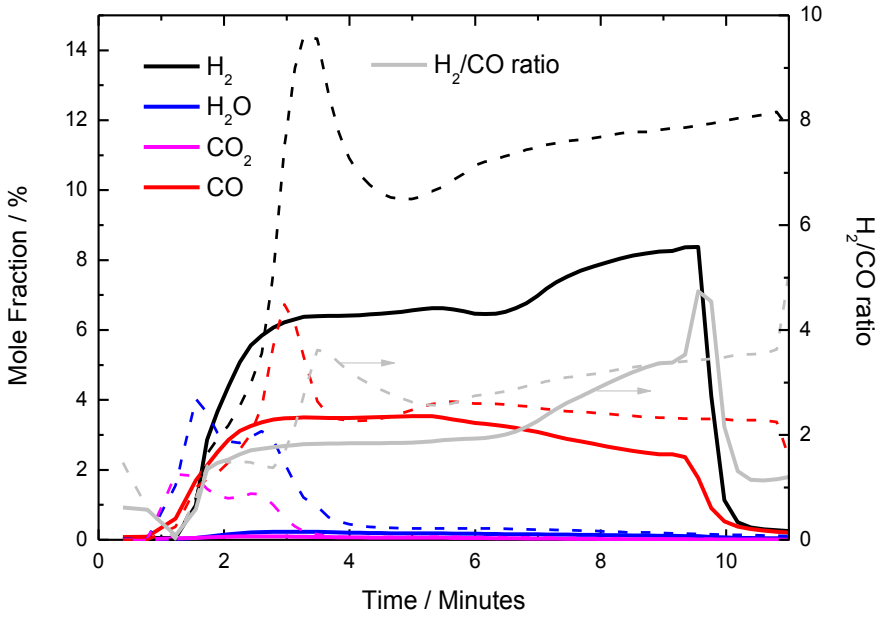

Figure 7.2 Molar fraction of products formed during the 1st (solid line) and 50th (dashed line) methane reduction steps using LSF731

The reactions that could take place during the reduction steps using LSF731 as the OCM are shown below:

$$CH_4 + 4O_O^x \Leftrightarrow CO_2 + 2H_2O + 4V_O^{\bullet\bullet} + 8e^- \quad (7.9)$$

$$CH_4 + O_O^x \Leftrightarrow CO + 2H_2 + V_O^{\bullet\bullet} + 2e^- \quad (7.10)$$

$$CH_4 \rightarrow C + 2H_2 \quad (7.11)$$

For the first seven minutes of the 1st reduction step, syngas was formed by Equation (7.10) as shown in Figure 7.2 and the ratio of hydrogen-to-carbon monoxide during this period was ~2:1. However, as the reduction step continued, it was evident that carbon monoxide production had started to drop whereas hydrogen production continued to increase. This indicates that methane pyrolysis had occurred (Equation (7.11)), which would have led to carbon deposition. As explained earlier, carbon deposition is to be avoided if pure hydrogen is required during the water oxidation step. It is important to note that no carbon dioxide or water is produced during the 1st reduction step (by Equation (7.9)), and this is possibly due to thermodynamic limitations and the restriction of oxygen ions from the lattice structure (as documented in previous work which investigated the use of lanthanum and strontium containing perovskite materials for partial oxidation of methane).[193, 194]

During the 50th methane reduction step, carbon dioxide and water were produced over the initial four minutes of operation, and this was followed by a subsequent production of syngas which lasted for the remainder of the reduction step. The molar ratio of hydrogen-to-carbon monoxide was higher than 2:1, again indicating that methane pyrolysis had occurred. In the subsequent 1st and 50th water oxidation steps, it is clear that both hydrogen and carbon monoxide were produced

(Figure 7.3). The presence of carbon monoxide confirms that carbon deposition had indeed occurred during the methane reduction steps.

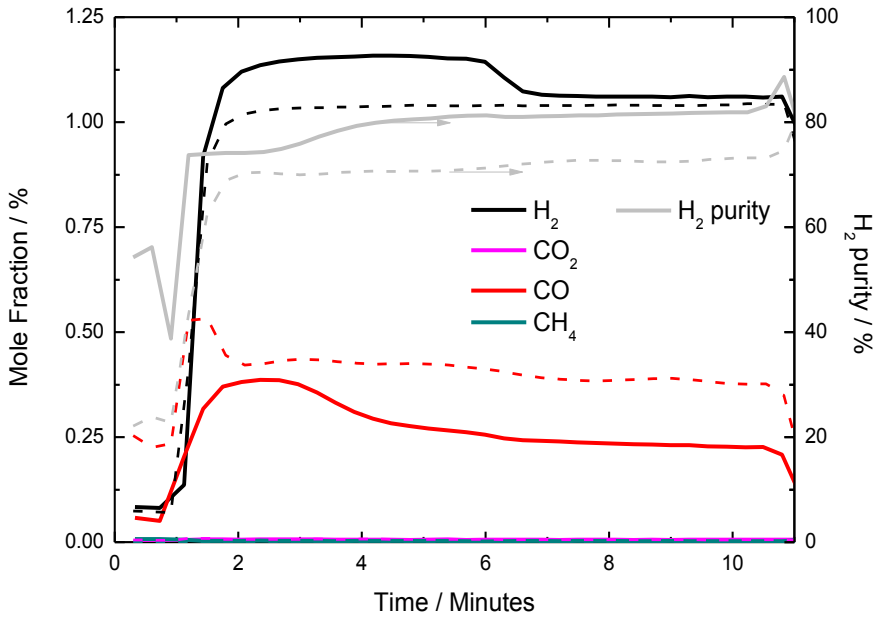

Figure 7.3 Molar fraction of products formed during the 1st (solid line) and 50th (dashed line) water oxidation steps using LSF731

Figure 7.3 shows that following two minutes of the 1st water oxidation, the hydrogen and carbon monoxide mole fractions were ~1.1% and ~0.4%, which indicates high levels of carbon monoxide contamination (low hydrogen-to-carbon monoxide ratios of less than 10). Water reacting with solid carbon would form hydrogen and carbon monoxide in the molar ratio of 1:1.

$$C + H_2O \rightarrow CO + H_2 \qquad (7.12)$$

During the 1st and 50th water oxidation steps, the ratio of hydrogen-to-carbon monoxide was clearly much higher than 1:1, which confirms that in addition to

oxidation of solid carbon, water oxidation of LSF731 had also occurred to provide free hydrogen by water splitting:

$$H_2O + V_O^{\bullet\bullet} + 2e^- \Leftrightarrow H_2 + O_O^x \qquad (7.13)$$

For Fe60, it is evident that for the 1st methane reduction step, carbon dioxide (maximum of ~3 %) and water (maximum of ~6.5 %) was initially produced in a fast reduction step, after which (two minutes into the reduction step) production switched to syngas formation (Figure 7.4).

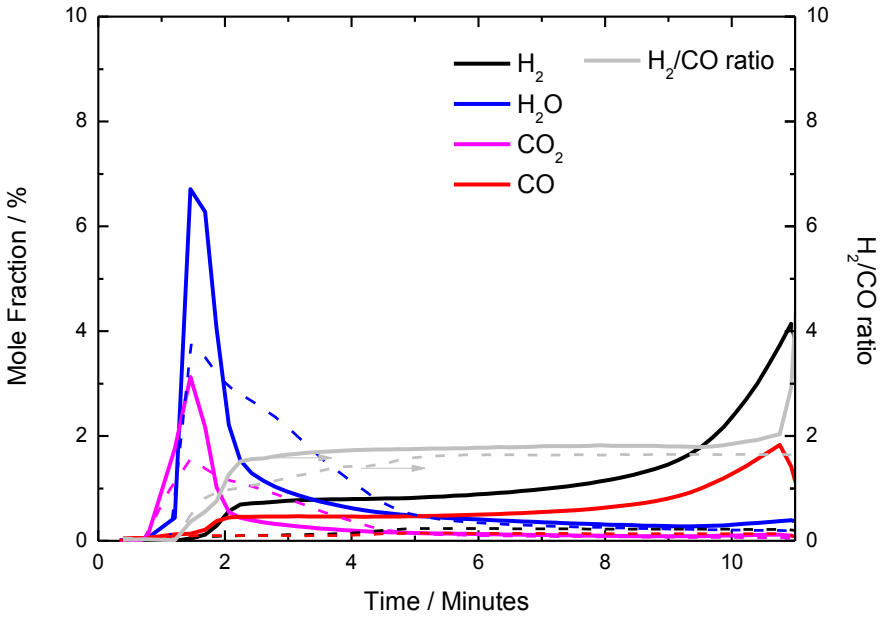

Figure 7.4 Molar fraction of products formed during the 1st (solid line) and 50th (dashed line) methane reduction steps using Fe60

As shown in Figure 7.4, as the 1st reduction step progressed, syngas production increased to ~4% hydrogen and ~2% carbon monoxide before the step was completed. It would appear that the ratio hydrogen-to-carbon monoxide had remained close to ~2, suggesting that carbon deposition by methane pyrolysis may not have occurred. Go *et al.*[70] investigated the use of iron oxide as OCM in a

chemical looping process using methane (as the reducing agent) and water (as the oxidising agent), and found that carbon deposition by methane pyrolysis was only likely to occur in the presence of iron. Following 10 minutes of the 1st reduction step as shown in Figure 7.4, there is evidence of syngas production indicating that Fe60 was still being reduced and that iron had not yet been formed. This would further suggest that methane pyrolysis had not occurred. During the 50th reduction step, a lower production of water and carbon dioxide was measured compared to the 1st reduction step. Syngas production during the 50th reduction step was also very low.

The products formed during the 1st and 50th oxidation steps for Fe60 are shown in Figure 7.5.

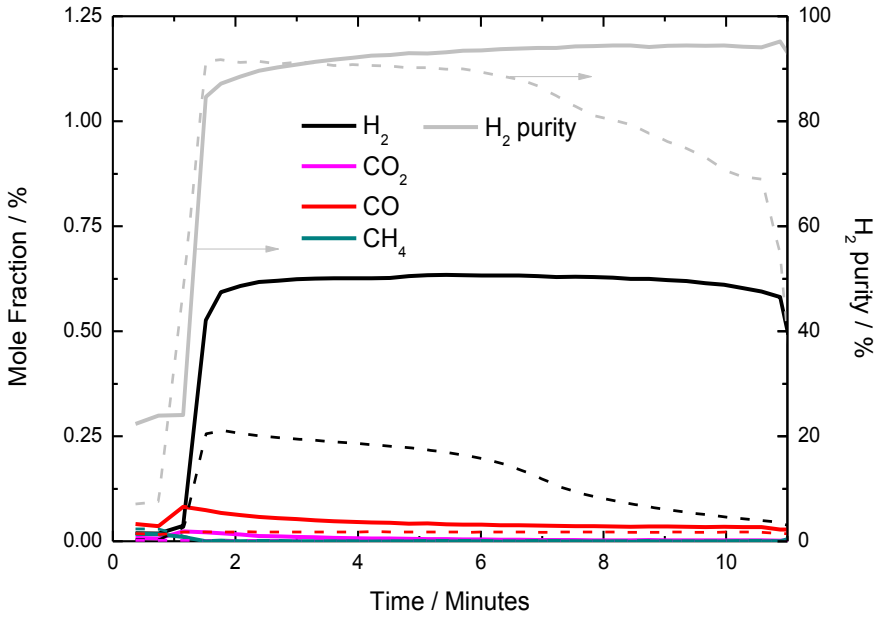

Figure 7.5 Molar fraction of products formed during the 1st (solid line) and 50th (dashed line) water oxidation steps using Fe60

Compared to LSF731, the production of carbon monoxide during water oxidation was much lower for Fe60, which gave higher hydrogen purity during the 1st water oxidation step. However, for the 50th oxidation step there was a lower production of hydrogen compared to the 1st oxidation step, and also lower hydrogen purity (dropping from ~90% to ~70% as the water oxidation step progressed). Lower

hydrogen production could be caused by material sintering or blockage of active sites due to carbon deposition. Lower hydrogen purity may have been measured due to the fact that low mole fractions were being produced, which would lower the accuracy of the hydrogen purity calculation.

According to these results, LSF731 influenced mainly methane pyrolysis and partial oxidation of methane, resulting in the production of carbon monoxide, hydrogen and solid carbon during the reduction steps. Fe60 influenced mainly the production of carbon dioxide and water through full oxidation of methane, and small amounts of syngas through partial oxidation of methane. There appears to be only a small amount of carbon monoxide produced during the water oxidation steps for Fe60, indicating that methane pyrolysis was not a dominant reaction in the reduction step.

In a previous study, a two-step cycle using iron oxide as the OCM was performed using methane as the reducing agent and water as the oxidising agent.[70] Chiesa *et al.*[26] performed thermodynamic analysis of the three-step cycle (involving methane reduction, water oxidation and air oxidation) and found it to be feasible, however no practical work appears to have been performed using this system in the literature and therefore it is not possible to compare the air oxidation results from this chapter to other investigations using the same process.

The 1st and 50th air oxidation steps for LSF731 are shown in Figure 7.6 and confirm that carbon deposition had indeed occurred for LSF731. A large production of carbon monoxide and carbon dioxide were produced in addition to small amounts of hydrogen and methane during the 1st air oxidation step. This is consistent with previous studies involving $La_{0.8}Sr_{0.2}Co_{0.5}Fe_{0.5}O_{3-\delta}$ as OCMs in a chemical looping system involving reduction by methane and oxidation by air, which concluded that during oxidation of solid carbon by air at temperatures above 850^{o}C carbon dioxide would be formed and at temperatures lower than 850^{o}C carbon monoxide would be formed.[195]

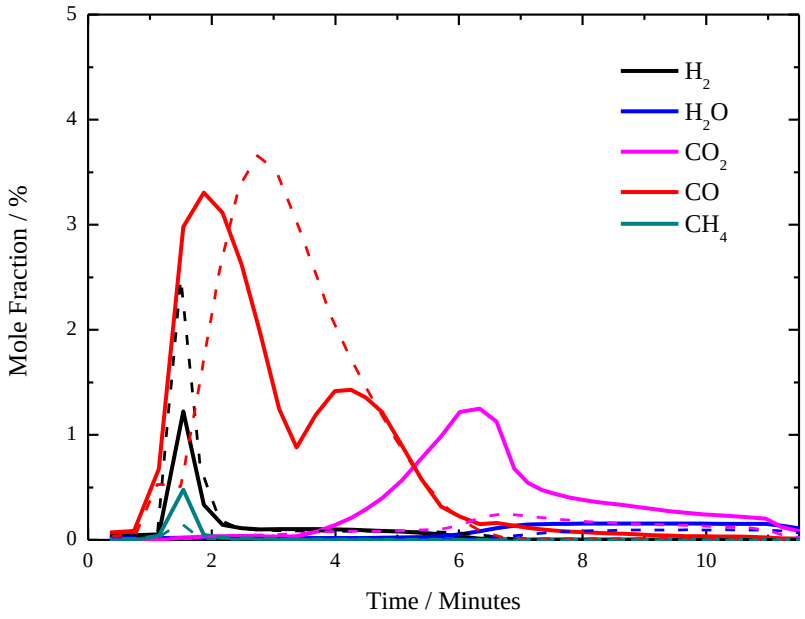

Figure 7.6 Molar fraction of products formed during the 1st (solid line) and 50th (dashed line) air oxidation steps using LSF731

The formation of hydrogen and methane during the air oxidation step suggests that perhaps compounds in the form of CH_x had adsorbed onto the surface of LSF731 during the reduction step. It was also possible that residual methane had remained in the stainless steel pipework following the previous methane reduction step and was released at the start of the air oxidation step.

The formation of hydrogen and carbon monoxide in the air oxidation step could have been produced by partial oxidation of this adsorbed or residual methane:

$$CH_4 + \frac{1}{2}O_2 \rightarrow CO + 2H_2 \qquad (7.14)$$

The formation of additional carbon monoxide and carbon dioxide could have been caused by air oxidation of solid carbon:

$$C + \frac{1}{2}O_2 \rightarrow CO \tag{7.15}$$

$$C + O_2 \rightarrow CO_2 \tag{7.16}$$

The formation of these products in the air oxidation steps suggests that some of the carbon deposited on LSF731 during the methane reduction steps was not removed during water oxidation. There are two possible explanations for this result; either the water oxidation step was not long enough to remove all of the deposited carbon from the OCM or some of the deposited carbon required a very high partial pressure of oxygen to be removed. During the 50th air oxidation step, carbon monoxide and hydrogen were produced, but production of carbon dioxide and methane was much lower than during the 1st air oxidation step.

In comparison to LSF731, Fe60 produces almost no carbon monoxide or carbon dioxide products during the 1st and 50th air oxidation cycles, as shown in Figure 7.7.

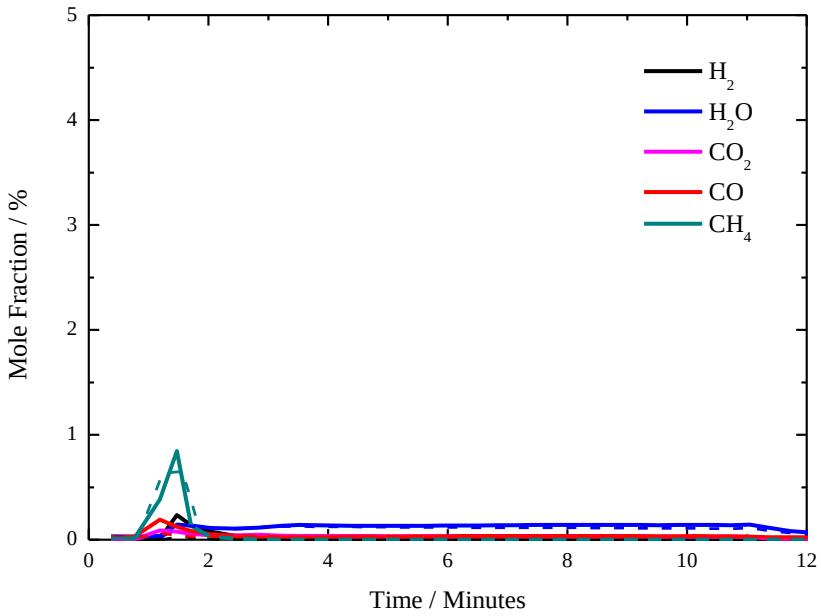

Figure 7.7 Molar fraction of products formed during the 1st (solid line) and 50th (dashed line) air oxidation steps using Fe60

There appears to be an initial peak of methane formation over the first two minutes of both the 1st and 50th air oxidation steps for Fe60, as observed for LSF731. Syngas is also produced during the initial minute of the 1st air oxidation step, possibly by partial oxidation of methane, but these levels are not as high as seen for LSF731. The formation of these products could again be explained by residual methane gas or adsorption of CH_x onto the OCM which may have occurred during the reduction steps. Fe60 appeared to produce purer hydrogen compared to LSF731. The highest hydrogen purity for Fe60 was ~95% (during the 1st water oxidation step) however the true value may have been higher considering that a fraction of the carbon monoxide contaminant level was most likely attributed to background nitrogen (which usually contributes a signal of 0.01-0.04%).

The results from the experiments have been replotted to show the molar amount of products formed during the methane reduction (Figure 7.8) and water oxidation steps (Figure 7.9). For clarity, only results for every five cycles are shown.

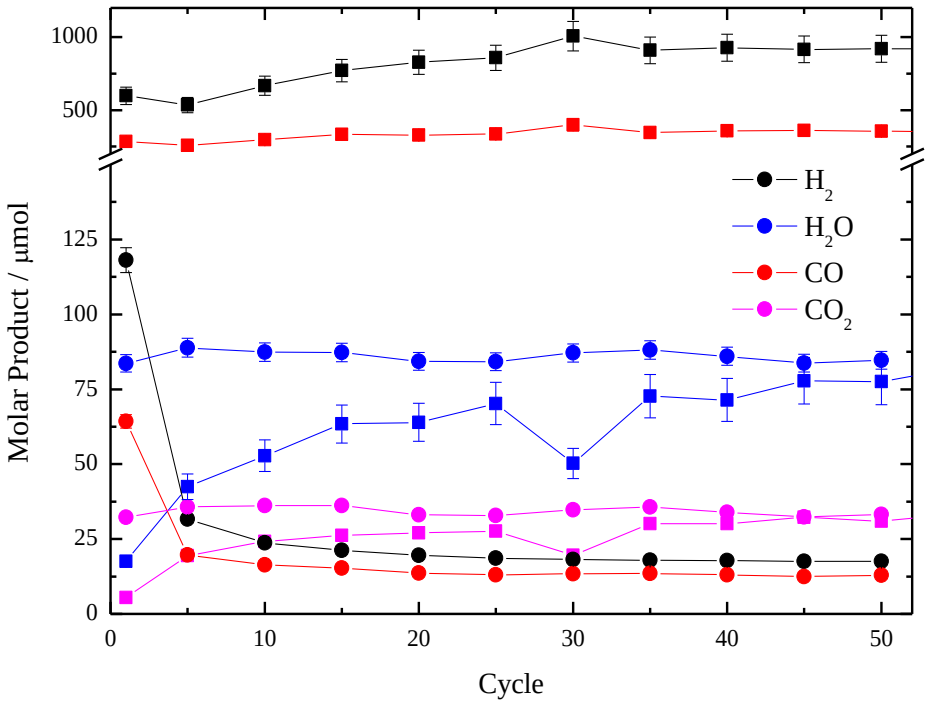

Figure 7.8 Molar production (with error bars) during methane reduction steps in the autothermal chemical looping cycling for hydrogen production process at 850°C performed using 50 mg of Fe60 (●) and LSF731 (■)

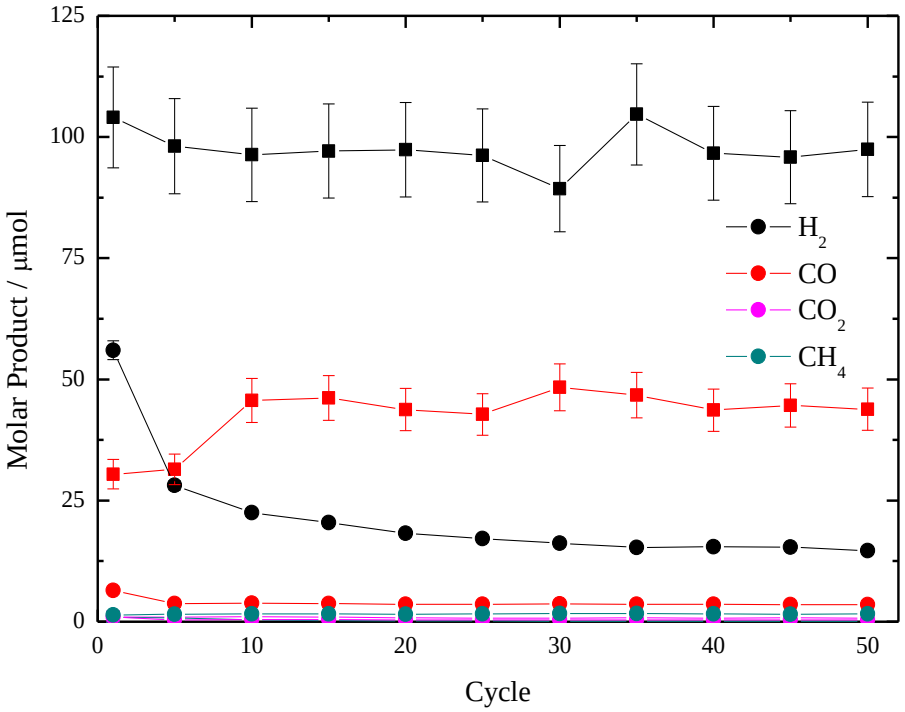

Figure 7.9 Molar production during water oxidation steps in the autothermal chemical looping cycling for hydrogen production process at 850°C performed using 50 mg of Fe60 (●) and LSF731 (■)

In terms of material stability, LSF731 continued to maintain activity over 50 redox cycles as shown by the methane reduction (Figure 7.8) and water oxidation (Figure 7.9) steps. Using Fe60 as the OCM allowed purer production of hydrogen during the water oxidation steps in comparison to LSF731, however activity was shown to decrease as the cycles progressed (this is apparent in both the methane reduction and water oxidation steps).

To ascertain whether the process was autothermal for Fe60, the average molar amounts of products formed during each reduction and oxidation step were calculated and used to generate a representative overall chemical reaction of the process (this calculation was not performed for LSF731 due to the large amount of carbon deposition that had occurred which would affect the overall enthalpy balance). The average molar amounts of products formed for Fe60 were calculated over the 5th to 50th cycles (when the process was generally at steady state) and it was

assumed that the air oxidation steps had fully oxidised the iron oxide back to haematite. These results are shown in Table 7.1.

Table 7.1 Average molar products formed during the 5th to 50th methane reduction, water oxidation and air oxidation steps during autothermal chemical looping operation at 850^{o}C using 50 mg of Fe60

Gaseous product	Average production during CH_4 reductions (µmol)	Average production during H_2O oxidations (µmol)	Average production during air oxidations (µmol)
CO_2	38		
CO	10		
H_2	24		
H_2O	80	20	
Oxygen uptake by OCM	-170	20	150

As shown in the table, during the methane reductions, an average of 170 µmol of oxygen was released from the iron oxide sample. Assuming that at the start of each reduction the OCM existed as haematite and that deactivation of the OCM did not occur, such a reduction would lead to the formation of an iron oxide containing mainly wüstite and a small amount of magnetite. Following water oxidations, the OCM was only slightly oxidised (20 µmol of oxygen incorporation) and following these steps there was still mainly wüstite and only a small amount of magnetite. This result would suggest that the water oxidation steps were too short, and could be extended to longer than 10 minutes to produce significantly more hydrogen. The average amount of oxygen incorporated into the OCM during air oxidation was calculated at 150 µmol based on the oxygen molar balance. Therefore based on these calculations the overall process can be represented by:

$$CH_4 + 0.4H_2O + 1.5O_2 \rightarrow 0.8CO_2 + 1.6H_2O + 0.2CO + 0.8H_2 \quad (7.17)$$

A calculation of the overall enthalpy change for this reaction gives ~-550 kJ per mole of methane feed reacted, which is highly exothermic. This excess energy could be used to produce electricity, but it is also possible to adapt the chemical looping process to produce less heat and form more useful products. This can be performed by either allowing the water oxidation steps to occur for longer to produce more hydrogen or by increasing the methane feed molar flow rate or mole fraction to allow more syngas (and less carbon dioxide and water) to be produced. Both of these modifications would lower the amount of heat formed per cycle.

It can be concluded that LSF731 would have been a suitable OCM for the autothermal chemical looping process if hydrogen purity during the water oxidation steps was higher as it showed good material stability over 50 cycles giving no loss in activity as the cycles progressed. Therefore further tests with LSF731 were performed using different experimental conditions where water was added to the methane reduction feed in an attempt to reduce carbon deposition caused by methane pyrolysis. The results of these experiments are detailed in the next section.

7.2.2 Addition of water to the reduction step for LSF731

The results from the previous section show that Fe60 is not a suitable OCM for performing the three-step autothermal chemical looping process for hydrogen production at 850^{o}C due to loss of material activity that is experienced over a high number of redox cycles. LSF731 on the other hand does show good material stability, but methane pyrolysis occurred during the reduction steps, which caused the production of low purity hydrogen during water oxidation. It is possible to suppress methane pyrolysis by adding an oxidising agent (such as water or air) to the reducing feed. If carbon does form in the reducing feed, the presence of water may immediately oxidise the carbon to form hydrogen with carbon monoxide or carbon dioxide:

$$C + H_2O \rightarrow CO + H_2 \quad (7.18)$$

$$C + 2H_2O \rightarrow CO_2 + 2H_2 \quad (7.19)$$

To assess whether the addition of water in the methane reducing feed could reduce carbon deposition, additional experiments were performed. In these experiments, the same method was used as in Section 7.2.1, but water was added to the methane feed (to perform 50 chemical looping redox cycles using LSF731 as the OCM. Two methane-to-water molar ratios of 4.5:1 and 2.2:1 were tested. The mole fraction of products formed during the 1st and 50th reduction steps using a methane-to-water molar ratio of 4.5:1 (Figure 7.10) and 2.2:1 (Figure 7.11) are shown below.

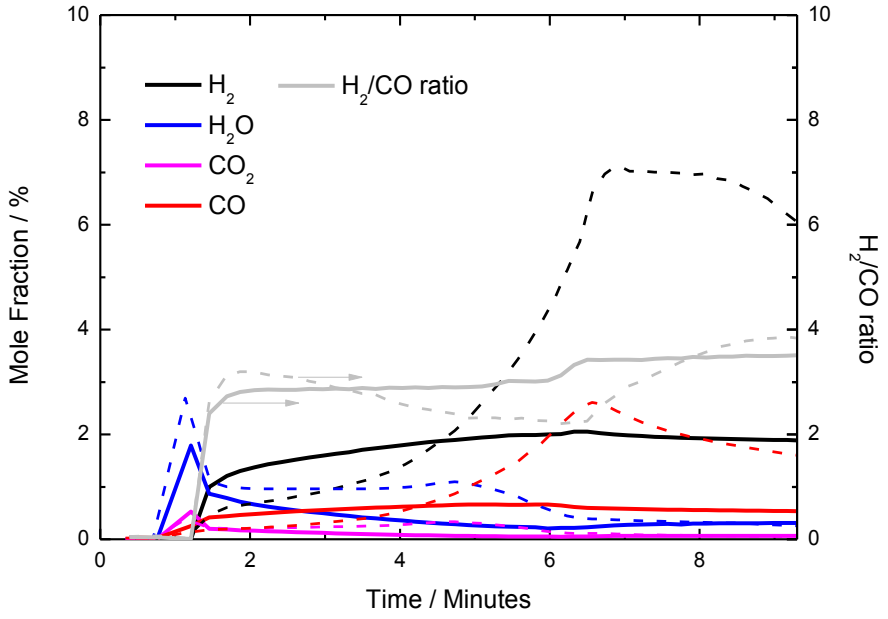

Figure 7.10 Molar fraction of products formed during the 1st (solid line) and 50th (dashed line) methane reduction steps using LSF731 (using a methane-to-water ratio of 4.5:1 in the reducing feed)

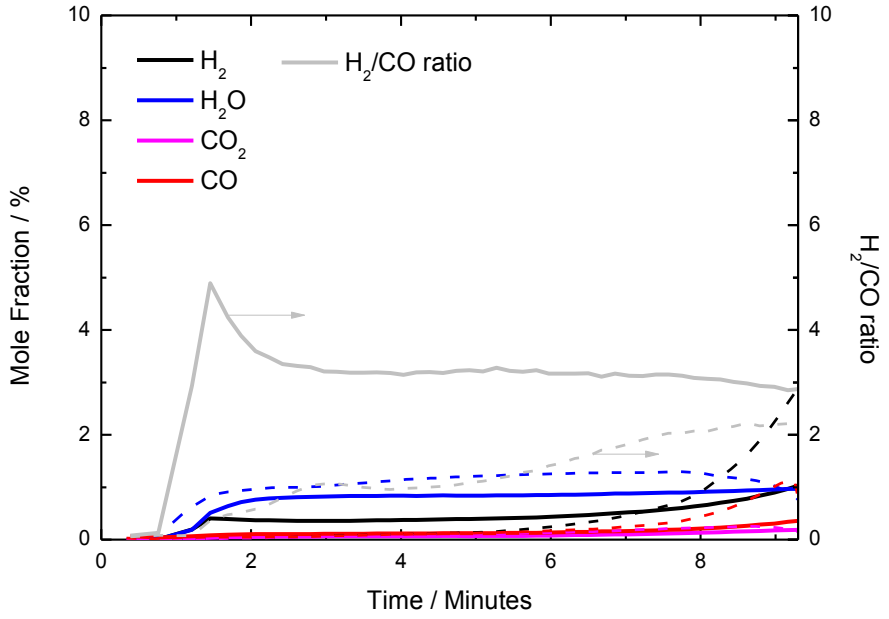

Figure 7.11 Molar fraction of products formed during the 1st (solid line) and 50th (dashed line) methane reduction steps using LSF731 (using a methane-to-water ratio of 2.2:1 in the reducing feed)

The addition of water to the methane feed did not seem to have much effect on the maximum hydrogen-to-carbon monoxide ratio over the 1st reduction step, which were ~3.5 using a methane-to-water ratio of 4.5:1 and ~5 using a methane-to-water ratio of 2.2:1 (a hydrogen-to-carbon monoxide ratio higher than two indicates the formation of carbon by methane pyrolysis). This is no improvement compared to using pure methane as the reducing feed, which for LSF731 gave a maximum hydrogen-to-carbon monoxide ratio of ~5 during the 1st reduction step (as shown in Figure 7.2). However, the levels of syngas formed in the 1st and 50th reduction steps using methane mixed with water as the reducing feed (for both methane-to-water ratios used) were lower compared to using pure methane as the reducing feed, indicating that adding water to the reduction feed had lowered the activity of LSF731.

The corresponding mole fraction of products formed during the 1st and 50th water oxidation steps are shown below in Figure 7.12 and Figure 7.13:

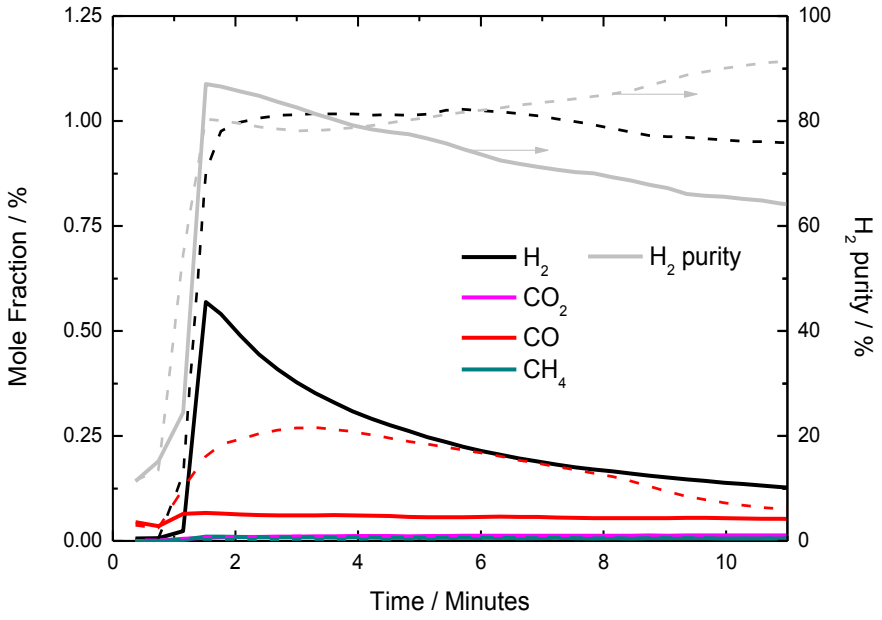

Figure 7.12 Molar fraction of products formed during the 1st (solid line) and 50th (dashed line) water oxidation steps using LSF731 (using a methane-to-water ratio of 4.5:1 in the reducing feed)

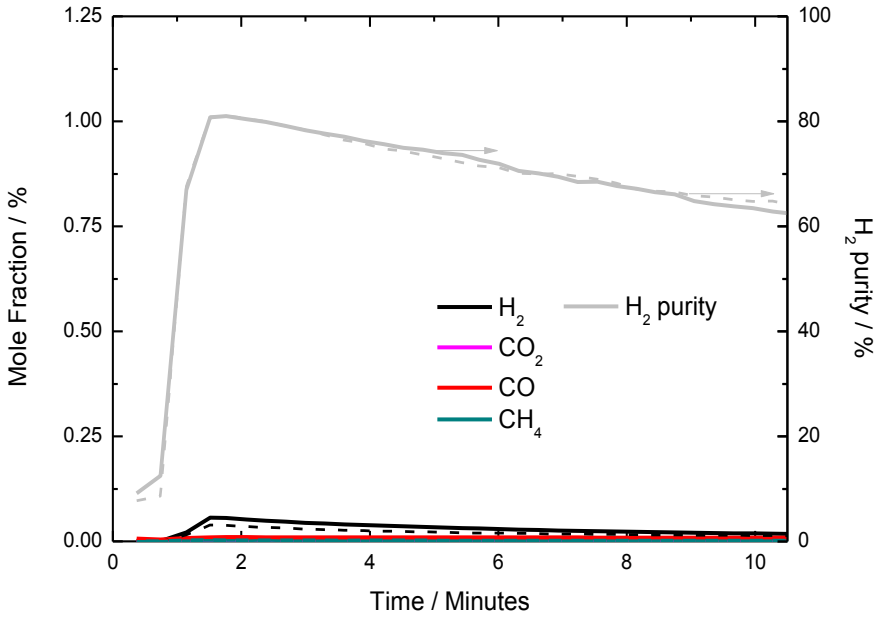

Figure 7.13 Molar fraction of products formed during the 1st (solid line) and 50th (dashed line) water oxidation steps using LSF731 (using a methane-to-water ratio of 2.2:1 in the reducing feed)

The addition of water to the methane feed severely reduced the amount of hydrogen produced during the 1st and 50th water oxidation for the experiment using a methane-to-water ratio of 2.2:1 in the reducing feed (Figure 7.13). For the experiments where pure methane was used as the reducing agent, the initial mole fraction of hydrogen produced in the 1st oxidation step peaked above 1% although hydrogen purity remained between 70-80% (Figure 7.3). The addition of water to the methane feed using a ratio of 4.5:1 of methane-to-water led to a smaller production of hydrogen during the 1st oxidation step (Figure 7.12) compared to using pure methane as the reducing feed, however by the 50th cycle hydrogen production had increased to give a relatively steady hydrogen mole fraction of ~1% during the entire water oxidation step. The hydrogen purity during this oxidation step was also much improved compared to using a pure methane feed as the reducing agent, and steadily increased over the oxidation step from ~80% to ~90% as the step progressed (whereas for operation using pure methane as the reducing feed, hydrogen purity remained close to ~70%).

The results from using a methane-to-water molar ratio of 2.2:1 as the reducing feed show a much lower production of hydrogen for both the 1st and 50th oxidation steps as shown in Figure 7.13. It would seem that hydrogen purity had also decreased, however this may be due to the fact that low mole fractions were being produced which would lower the accuracy of the hydrogen purity calculation.

The amount of hydrogen produced over 50 cycles of operation in the water oxidation steps for both Fe60 and LSF731 are plotted in Figure 7.14. For brevity, only hydrogen molar product and average hydrogen purity per cycle are shown here (all results for carbon monoxide, carbon dioxide and methane molar production during the reduction and oxidation steps over 50 redox cycles are shown in Appendix F).

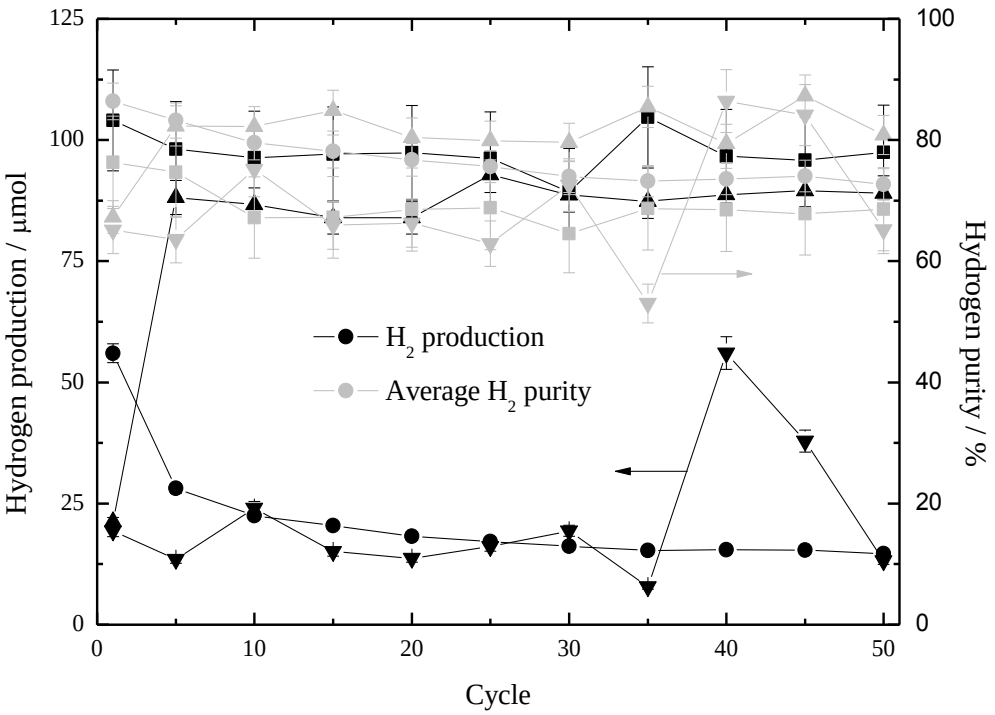

Figure 7.14 Molar production and hydrogen purity during the water oxidation steps of the autothermal chemical looping hydrogen production process performed at 850^{o}C utilising 50 mg of Fe60 (●), 50 mg of LSF731 (■) using pure methane as the reducing feed, 50 mg of LSF731 using a methane-to-water feed of 4.5:1 (▲) and 50 mg of LSF731 using a methane-to-water feed of 2.2:1 (▼)

The results from Figure 7.14 show that by adding water to the methane feed, carbon deposition can be suppressed during the reduction steps in the autothermal chemical looping process, which can allow purer hydrogen to be produced during the water oxidation steps. Initially, Fe60 and LSF731 were utilised as OCMs for the process and pure methane feeds were used as the reducing agents, but for Fe60 material instability occurred as the cycles progressed leading to a diminishing production of hydrogen and for LSF731 hydrogen purity was much lower compared to Fe60. Using a methane-to-water molar feed of 4.5:1 and utilising LSF731 as the OCM, hydrogen production was low for the 1st water oxidation step compared to using pure methane feed, but the following cycles showed similar hydrogen production levels. Additionally, a higher average purity of hydrogen was produced in comparison to

using Fe60 as the OCM for this process. Material stability was also maintained leading to steady hydrogen production over the 50 cycles performed.

An operating temperature of 850^{o}C was used for the experiments performed in this chapter which involved 150 cycles of isothermal WGS chemical looping operation. The intention was to utilise similar conditions to the previous experiment performed in Section 6 but using methane, water and air as the separate reactant feeds rather than carbon monoxide and water. In a previous study using $La_{0.8}Sr_{0.2}Co_{0.5}Fe_{0.5}O_{3-\delta}$ as oxygen permeable membranes for methane partial oxidation (methane as the reducing feed and air as the oxidising feed) it was found that high oxidation of methane during the reduction step occurred at lower temperatures.[195] Also, $La_{1-x}Sr_xFeO_{3-\delta}$ materials have been proven to be reduced at very low temperatures (~400^{o}C) by methane[196] and that the thermodynamics of the methane pyrolysis reaction is such that a lower temperature during the reduction step could lower carbon deposition.[197] Therefore, a lower reduction temperature may show improvements in hydrogen purity during the water oxidation steps. However, it was also noted that a lower temperature could reduce conversion of the OCM during redox cycling (this was found to be more apparent during the reduction step), allowing less hydrogen to be produced during water oxidation.[70]

In addition to changing operating conditions, it should be considered that LSF731 may not contain the suitable A- and B-site metals for this process. A previous study using $LaFeO_3$, $La_{0.8}Sr_{0.2}FeO_3$, and $La_{0.8}Sr_{0.2}Fe_{0.9}Co_{0.1}O_3$ as oxygen carriers for partial oxidation of methane showed that compared to $LaFeO_3$, addition of strontium to form $La_{0.8}Sr_{0.2}FeO_3$ improved catalytic activity of methane oxidation. The addition of cobalt to $La_{0.8}Sr_{0.2}FeO_3$ to form $La_{0.8}Sr_{0.2}Fe_{0.9}Co_{0.1}O_3$ also further improved reactivity and oxygen capacity. The addition of rhodium to oxygen-deficient perovskite materials has also been shown to improve carbon monoxide selectivity.[198] However, for those studies water splitting for hydrogen production was not performed and therefore it should be considered that the addition of metals to the perovskite may have also resulted in a decline in water splitting performance. Since water splitting was not performed for those experiments, the detrimental effects to product purity were not seen.

7.2.3 Post-operation analysis

Following operation of the autothermal chemical looping water splitting, the OCM samples were removed and reweighed. It was clear that sample loss had occurred for all OCMs. The mass losses were 0.4% for Fe60, 7% for LSF731 using pure methane as the reducing feed, 1.6% for LSF731 using a methane-to-water feed of 4.5:1 and 3% for LSF731 using a methane-to-water feed of 2.2:1. The most likely explanations are carry-through of the powder past the quartz wool plug and loss of powder during removal of the sampling tube from the microreactor.

Characterisation by SEM and XRD was performed immediately after the experiments to analyse microscopic structural changes and phase changes for Fe60 and LSF731 (for the experiments using pure methane and a methane-to-water feed ratio of 4.5:1). Characterisation of fresh OCM has been provided in Section 5.2.1 as a comparison. The results from XRD and SEM following operation are shown in Figure 7.15 and Figure 7.16.

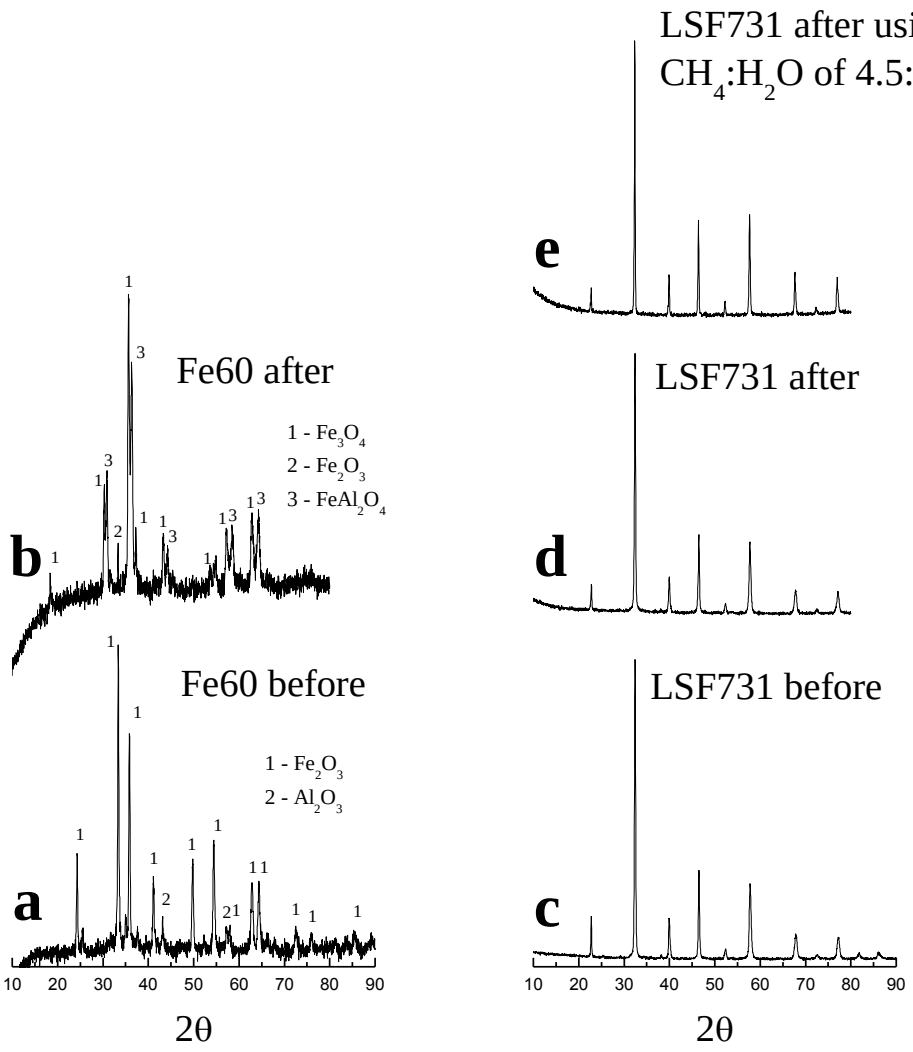

Figure 7.15 XRD analysis of (a) Fe60 fresh, (b) Fe60 following autothermal chemical looping operation, (c) LSF731 fresh, (d) LSF731 following autothermal chemical looping operation and LSF731 following autothermal chemical looping operation using a reducing feed of 4.5:1 CH_4:H_2O, all performed at 850^oC. Unmarked peaks for (c), (d) and (e) are reflections assigned to the perovskite structure.

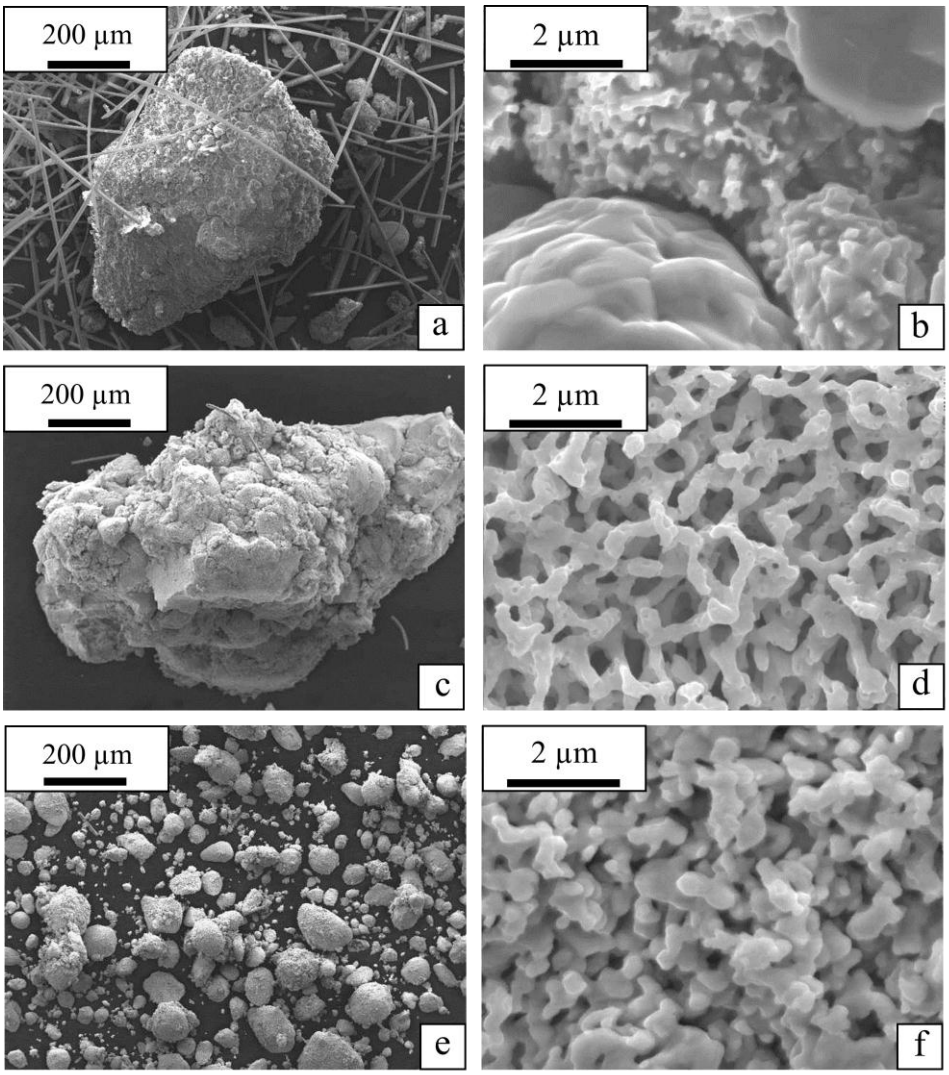

Figure 7.16 SEM images of (a) and (b) Fe60 and (c) and (d) LSF731 following autothermal chemical looping water splitting using pure methane reducing feed, and (e) and (f) LSF731 following autothermal chemical looping water splitting using a methane-to-water reducing feed of 4.5:1. Images (b), (d) and (f) are magnified images of a typical particle surface.

XRD analysis of the OCMs (Figure 7.15) shows that LSF731 following autothermal chemical looping operation both using pure methane and a methane-to-water feed of 4.5:1 did not change phase and remained in a perovskite form. Fe60 following operation using pure methane as the reducing feed formed the spinel, $FeAl_2O_4$. According to the work of Kierzkowska *et al.*[100] $FeAl_2O_4$ is formed during the reduction step, and only oxidation by air (not water) can convert it back to iron oxide

and alumina. However, this theory does not agree with the XRD analysis shown in Figure 7.15b which does not appear to show any reflections corresponding to phases of alumina. Tsvigunov *et al.*[189] proposed the theory that the formation of $FeAl_2O_4$ occurs during the oxidation step, and is then converted back to iron oxide and alumina during the reduction step. This is also confirmed by a thermodynamic study that was performed by Trumble.[188] The theory proposed by Tsvigunov *et al.* does agree with the results shown in Figure 7.15b and is the probable explanation for this occurrence.

SEM analysis of the OCMs following operation (Figure 7.16) show that during operation using pure methane feed, LSF731 and Fe60 both undergo agglomeration or sintering as indicated by larger particle sizes compared to the fresh material. Upon inspecting the material surfaces, there appears to have been no change in surface features, this is more apparent for LSF731 which had maintained the finger-like characteristics. LSF731 following autothermal chemical operation using a reducing feed with methane-to-water ratio of 4.5:1 did not appear to agglomerate or sinter, and also maintained surface features.

7.3 Summary

Fe60 and LSF731 were used as OCMs in a three-step autothermal chemical looping process at 850^{o}C. Fe60 gave better hydrogen purity than LSF731 when using pure methane as the reducing feed, however there were signs of a drop in activity for Fe60 as the cycles progressed. LSF731 allowed carbon deposition to occur due to methane pyrolysis during the reduction step which resulted in carbon monoxide production during the water splitting step. Attempts to prevent carbon deposition by addition of water to the reducing feed (using a methane-to-water molar ratio of 4.5:1) resulted in an improvement in the average hydrogen purity formed during the water oxidation steps (even when compared to using Fe60 as the OCM) but a lower oxygen exchange of LSF731 leading to slightly lower hydrogen production compared to using LSF731 as the OCM and pure methane as the reducing feed. The use of a lower methane-to-water feed of 2.2:1 showed both low hydrogen production and no

improvements in hydrogen purity compared to using pure methane as the reducing feed.

The autothermal chemical looping process proposed in this chapter should be considered as a potential industrial application for hydrogen production. As the overall process can be autothermal (it can also be selected to be exothermic by increasing the air-to-water ratio per cycle), additional energy is not required from an external source. This is a beneficial feature of the process that is not present in conventional methods of hydrogen production such as steam methane reforming. By optimising operating temperatures and considering the addition of water in the methane reducing feed, this process has promising potential for producing pure streams of hydrogen and syngas, from only methane, water and air. The syngas formed can be further processed into useful products by additional exothermic reactions. As an example, methanol[199] and ethylene[200] can be produced from syngas; these hydrocarbons are currently being used as liquid fuels and as reagents for the synthesis of useful polymers and could potentially be sold in the current market.[201, 202]

Chapter 8

8. Improving kinetics by Ni-doping of LSF731 for isothermal water-gas shift (WGS) operation at 850^{o}C

8.1 Introduction

As detailed in Section 3.2.5, previous studies have shown that the reactivity of iron oxide OCMs can be improved through the method of transition metal doping. This can involve adding a small fraction of reactive transition metal (such as nickel or copper) to iron oxide. The addition of nickel to iron oxide to form $NiFe_2O_4$ showed improvements in OCM activity in a chemical looping water splitting process.[77] Perovskite materials can be tailored to contain different metals on the A- and B-site, and therefore it is possible to add a small amount of nickel to the B-site of LSF731. The purpose of this experiment was to investigate whether the addition of nickel to LSF731 on the B-site could improve the kinetics of chemical looping cycling and lower the time required to perform the reducing and oxidation steps.

Previous studies have shown that the doping of nickel to LSF731 can allow a decrease in sintering at high temperatures as the nickel inhibits grain growth.[203] However, in the same study it was also noted that nickel segregation within the material could occur. In other studies it was noted that the substitution of up to 20% of nickel on the B-site would allow the perovskite to remain in a single-phase cubic state, whereas doping of higher amounts of nickel (above 20% on the B-site) could lead to a phase change from cubic to orthorhombic[204] and the formation of additional secondary phases of NiO and $La_{2-x}Sr_xNiO_4$.[205]

The perovskite structure $La_{0.7}Sr_{0.3}Fe_{0.9}Ni_{0.1}$ (LSFN7391) was synthesised and used to perform 65 cycles of isothermal WGS chemical looping at 850°C, using the same procedure as outlined in Section 4.7. The performance of LSFN7391 in this study was compared to the results from LSF731 performed in Section 6.

8.2 Results

8.2.1 Survey of activity

The production of carbon dioxide during the 1st, 5th and 65th reduction steps (using carbon monoxide as the reducing agent) over 30 minutes for LSFN7391 and LSF731 are shown in Figure 8.1.

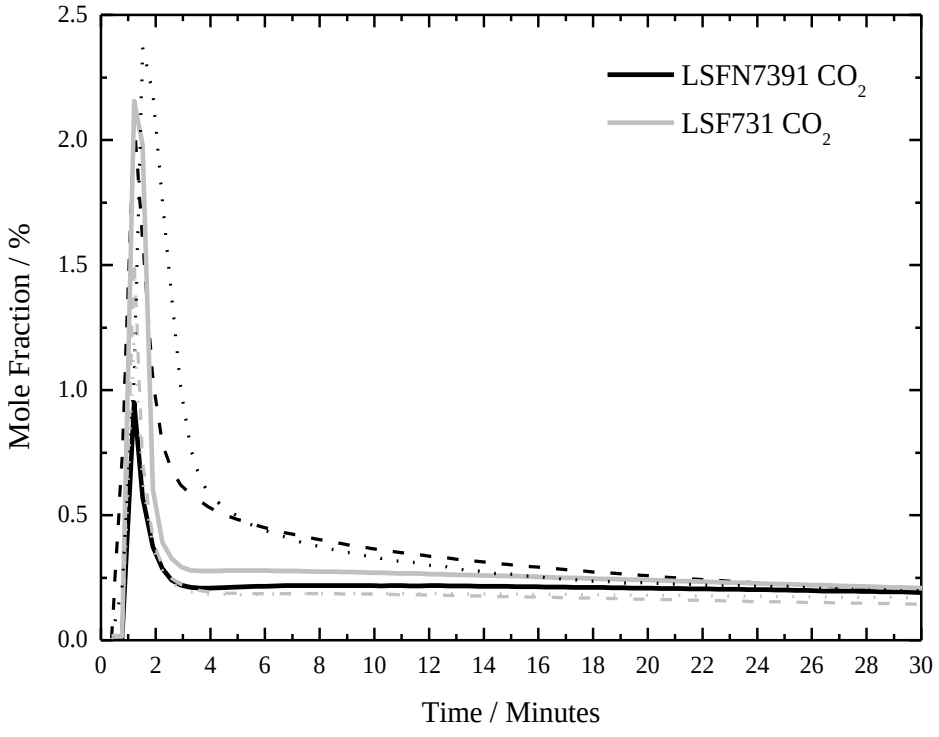

Figure 8.1 Molar fraction of carbon dioxide formed during the 1st (solid line), 5th (dotted line) and 65th (dashed line) carbon monoxide reduction steps using LSFN7391 and LSF731 during isothermal chemical looping WGS at 850°C

It is evident from Figure 8.1 that during the 1st reduction step, the maximum carbon dioxide mole fraction is lower for LSFN7391 (maximum of ~1%) compared to LSF731 (maximum of ~2.2%) but for the 5th and 150th cycle the maximum mole fraction of carbon dioxide produced for LSFN7391 was slightly higher for LSF731 at ~2.4% and ~2% compared to ~1.2% and ~1.5%. This signifies that LSFN7391 was not initially very active in the 1st reduction step but following five cycles activity was improved. The mole fractions of hydrogen produced for LSFN7391 and LSF731 during the 1st, 5th and 65th water oxidation steps are compared in Figure 8.2

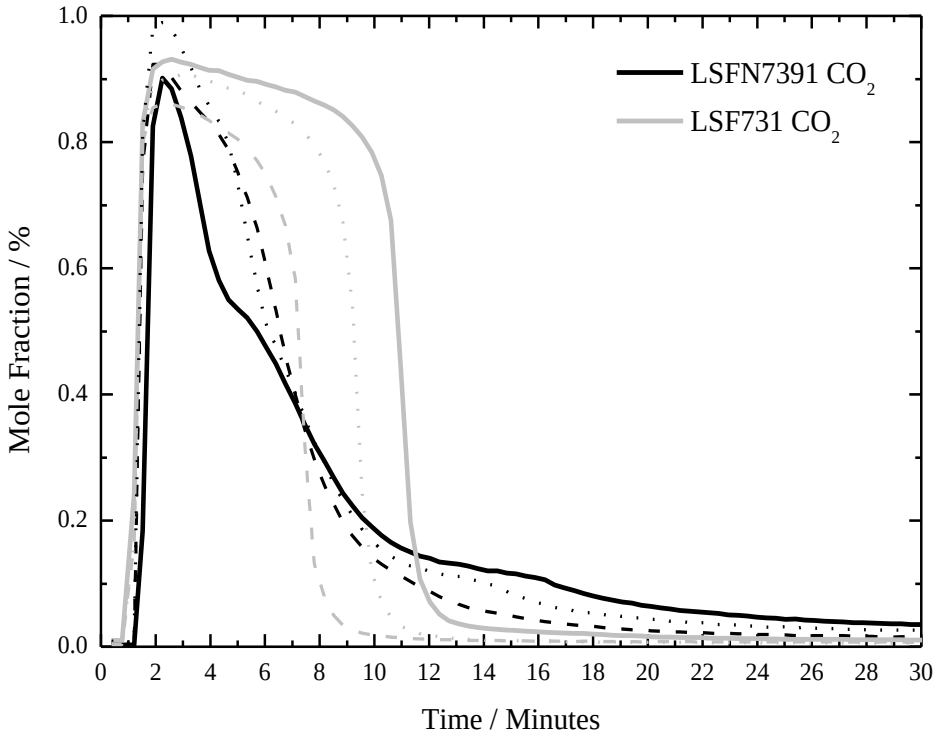

Figure 8.2 Molar fraction of hydrogen formed during the 1st (solid line), 5th (dotted line) and 65th (dashed line) carbon monoxide reduction steps using LSFN7391 and LSF731

For the 1st oxidation step using LSF731, oxidation of the OCM completed after ~12 minutes and produced an almost square-shaped peak (Figure 8.2). Oxidation of

LSFN7391 during the 1st oxidation step did not finish until almost the end of the 30 minute oxidation step, which indicated lowered rates for the water oxidation steps for LSFN7391 compared to LSF731 as shown by the lower levels of hydrogen mole fraction throughout each oxidation step.

8.2.2 Survey of stability over redox cycling

The molar production of carbon dioxide produced during the reduction steps for isothermal WGS chemical looping operation at 850°C using LSFN7391 is shown in Figure 8.3 (and compared against LSF731 over the first 65 cycles).

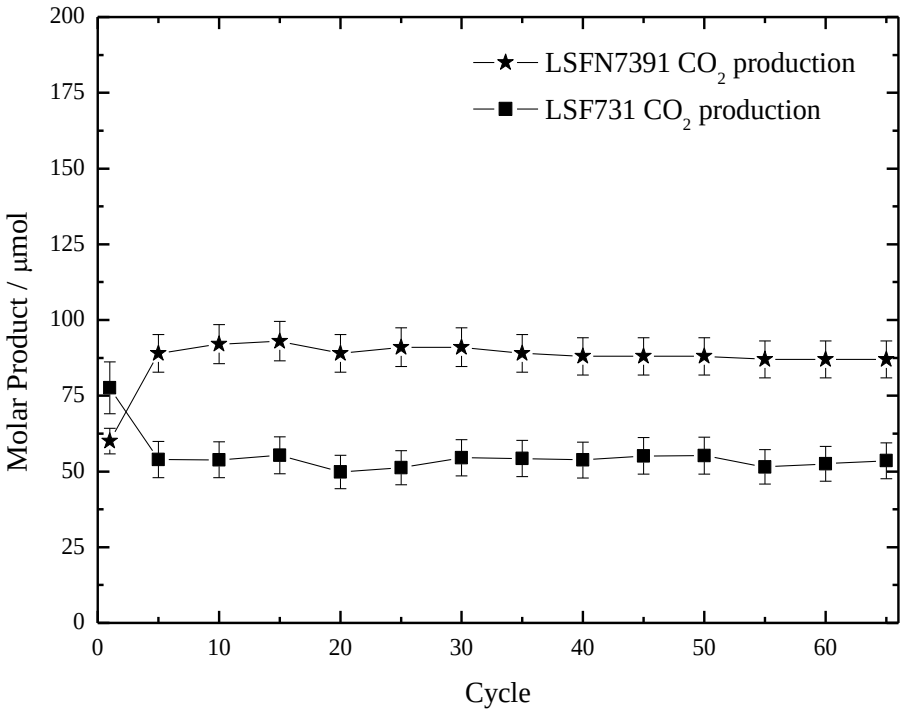

Figure 8.3 Molar production (with error bars) of carbon dioxide formed during reduction steps for isothermal WGS chemical looping performed at 850°C utilising 50 mg of LSFN7391 (★) and LSF731 (■)

Figure 8.3 shows that higher production of carbon dioxide per cycle (after the 1st cycle) can be induced by doping a small amount of nickel to LSF731 and

additionally there were no signs of reduction in material stability (as shown by steady carbon dioxide production. It is possible that this increase in carbon dioxide production was a result of improved kinetics, allowing for faster rates of carbon dioxide production during the 30 minute reduction step (therefore more carbon dioxide would be produced during the cycle). However it is also possible that nickel doping enhanced activity of the Boudouard reaction:

$$2CO \rightarrow C + CO_2 \qquad (8.1)$$

To investigate this theory, the molar production of hydrogen, carbon monoxide and carbon dioxide formed during the water oxidation steps were calculated and are plotted in Figure 8.4 against cycle number.

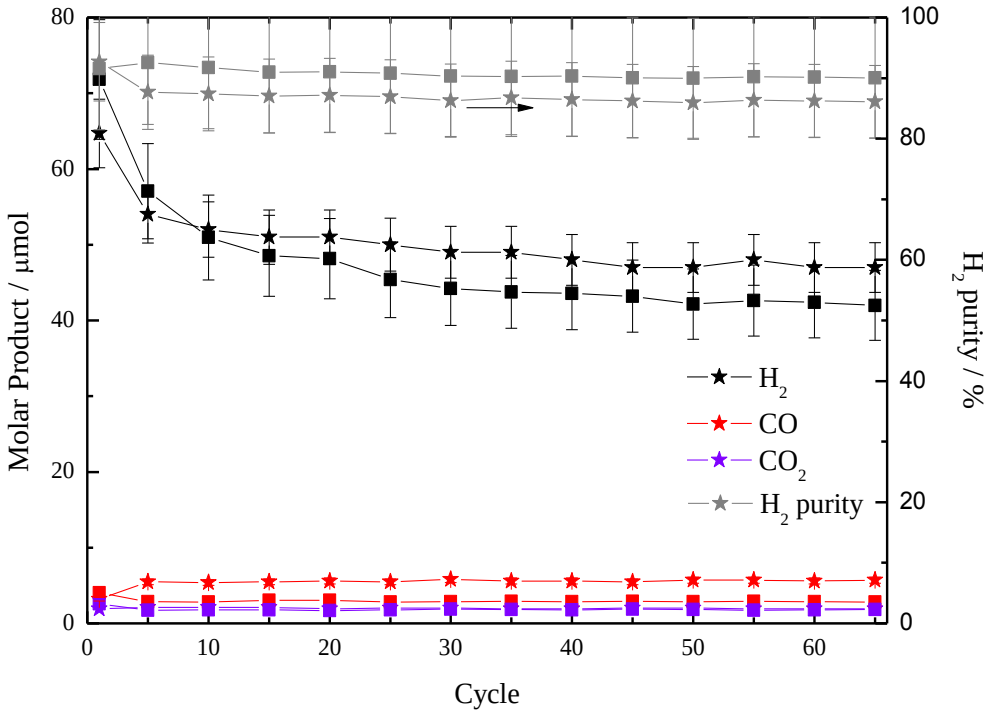

Figure 8.4 Molar production (with error bars) of hydrogen, carbon monoxide and carbon dioxide formed during water oxidation steps for isothermal WGS chemical looping performed at 850°C utilising 50 mg of LSFN7391 (★) and LSF731 (■)

As Figure 8.4 shows, the amounts of carbon monoxide and carbon dioxide produced per cycle in the water oxidation steps were slightly higher for LSFN7391 compared to LSF731, causing a decline in hydrogen purity. Carbon monoxide and carbon dioxide would have been produced during water oxidation by the reaction of water with deposited carbon:

$$C + H_2O \rightarrow CO + H_2 \quad (8.2)$$

$$C + 2H_2O \rightarrow CO_2 + 2H_2 \quad (8.3)$$

There was only an increase in ~3 μmol of carbon monoxide and ~0.2 μmol of carbon dioxide by using LSFN7391 instead of LSF731. However, the amount of carbon dioxide produced during the reduction steps for LSFN7391 was much higher than the amount of hydrogen produced per cycle during the oxidation steps, and as the amounts of carbon monoxide and carbon dioxide did not also increase considerably during oxidation, it appears that there was a loss of carbon and oxygen from the system. By comparing the molar amount of products formed during the 65th reduction step and oxidation step (Table 8.1) it was calculated that ~50 μmol of carbon dioxide was produced during the 65th reduction step which was not accounted for by OCM reduction. This is confirmed by the carbon molar balance performed in Figure 8.5, which shows that during the 65th reduction step, a mole fraction of ~0.25% could be attributed to the formation of carbon.

Note that the 65th reduction step was used for this carbon molar balance and calculation as it represented steady state performance as shown by Figure 8.3. A calculation of the molar amount of solid carbon formed over the 65th reduction step according to the carbon molar balance (as shown in Figure 8.5) indicates that ~55 μmol of carbon was produced, which could account for the high amounts of carbon dioxide produced in Figure 8.3. This carbon, in a solid form, would not be measured by the QMS.

Table 8.1 Molar products formed during 65th reduction and oxidation step during isothermal chemical looping WGS operation at 850°C using LSFN7391

Gaseous product	Production during 65th reduction step (µmol)	Production during 65th oxidation step (µmol)
CO_2	87	1.9
CO		5.7
H_2 (by OCM and carbon oxidation)		47
H_2 (by only OCM oxidation)		37.5

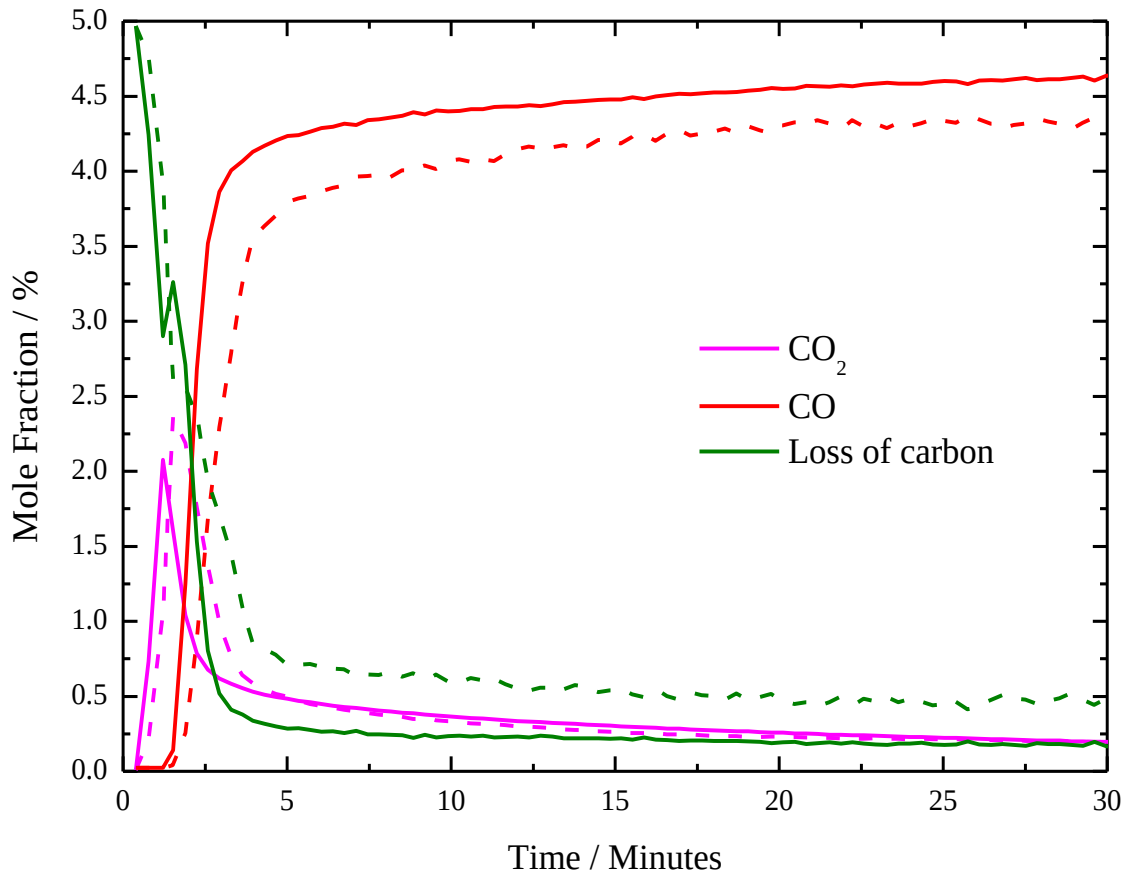

Figure 8.5 Carbon monoxide, carbon dioxide and mole fraction of estimated carbon lost (in accordance to a carbon molar balance) during the 65th (solid line) and 5th (dashed line) carbon monoxide reduction steps for isothermal WGS chemical looping performed at 850°C utilising 50 mg of LSFN7391

Until now, only two reactions were considered during the reduction step, which involved the Boudouard reaction (Equation (8.1)) and the gas-solid reaction between carbon monoxide and lattice oxygen of the perovskite:

$$CO + O_O^x \Leftrightarrow\ CO_2\ + V_O^{\bullet\bullet} +\ 2e^- \tag{8.4}$$

In the oxidation phase only three possible reactions have been considered which were the reactions between water and deposited carbon (Equations (8.2) and (8.3)) and the removal of an oxygen vacancy from the perovskite lattice to form hydrogen:

$$H_2O\ +\ V_O^{\bullet\bullet} +\ 2e^-\ \Leftrightarrow\ H_2 + O_O^x \tag{8.5}$$

Since Figure 8.4 indicates that only a small amount of carbon monoxide and carbon dioxide was produced during water oxidation of LSFN7391 (proving that Equations (8.2) and (8.3) were not significant reaction steps), one would expect a high molar production of hydrogen during the water oxidation steps to correspond (on a molar basis) with the high amounts of carbon dioxide produced during the carbon monoxide reduction steps. However, this was not the case and it appears that there was double the amount of carbon dioxide produced during the reduction steps compared to hydrogen produced during the water oxidation steps.

The unaccountable additional carbon dioxide can only be explained by two theories. One is that the Boudouard was in fact occurring during the reduction steps, but that the carbon formed on the OCM was too strongly bonded to be oxidised by water during the oxidation steps. The second theory is that carbon was being lost by the formation of carbonate species within the perovskite structure. This is further discussed in the next section.

8.2.3 Post-operation analysis

Following operation of the isothermal chemical looping WGS experiment, the weight loss was 4% for LSFN7391. The most likely explanation for this was carry-through of the powder past the quartz wool plug and loss of powder during removal of the sampling tube from the microreactor.

Characterisation by SEM and XRD was performed immediately after the experiments to analyse microscopic structural changes and phase changes. The results from XRD analysis and SEM analysis following operation are shown in Figure 8.6 and Figure 8.7.

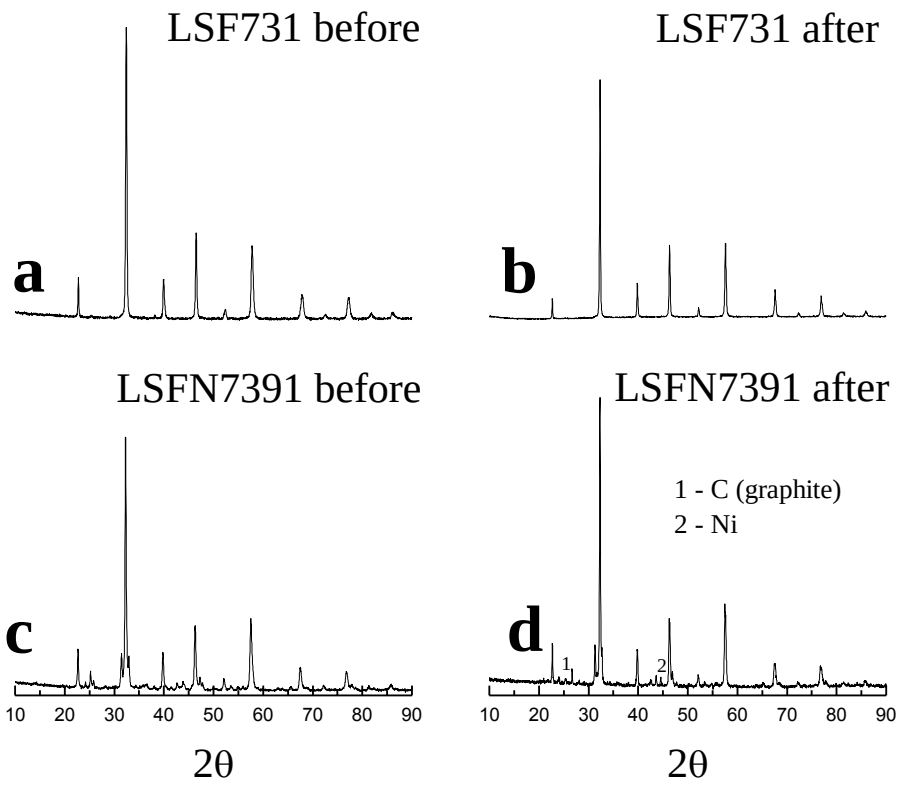

Figure 8.6 XRD analysis of (a) LSF731 fresh, (b) LSF731 following isothermal chemical looping WGS operation at 850^{o}C, (c) LSFN7391 fresh and (d) LSFN7391 following isothermal chemical looping WGS operation at 850^{o}C. Unmarked peaks are reflections assigned to the perovskite structure.

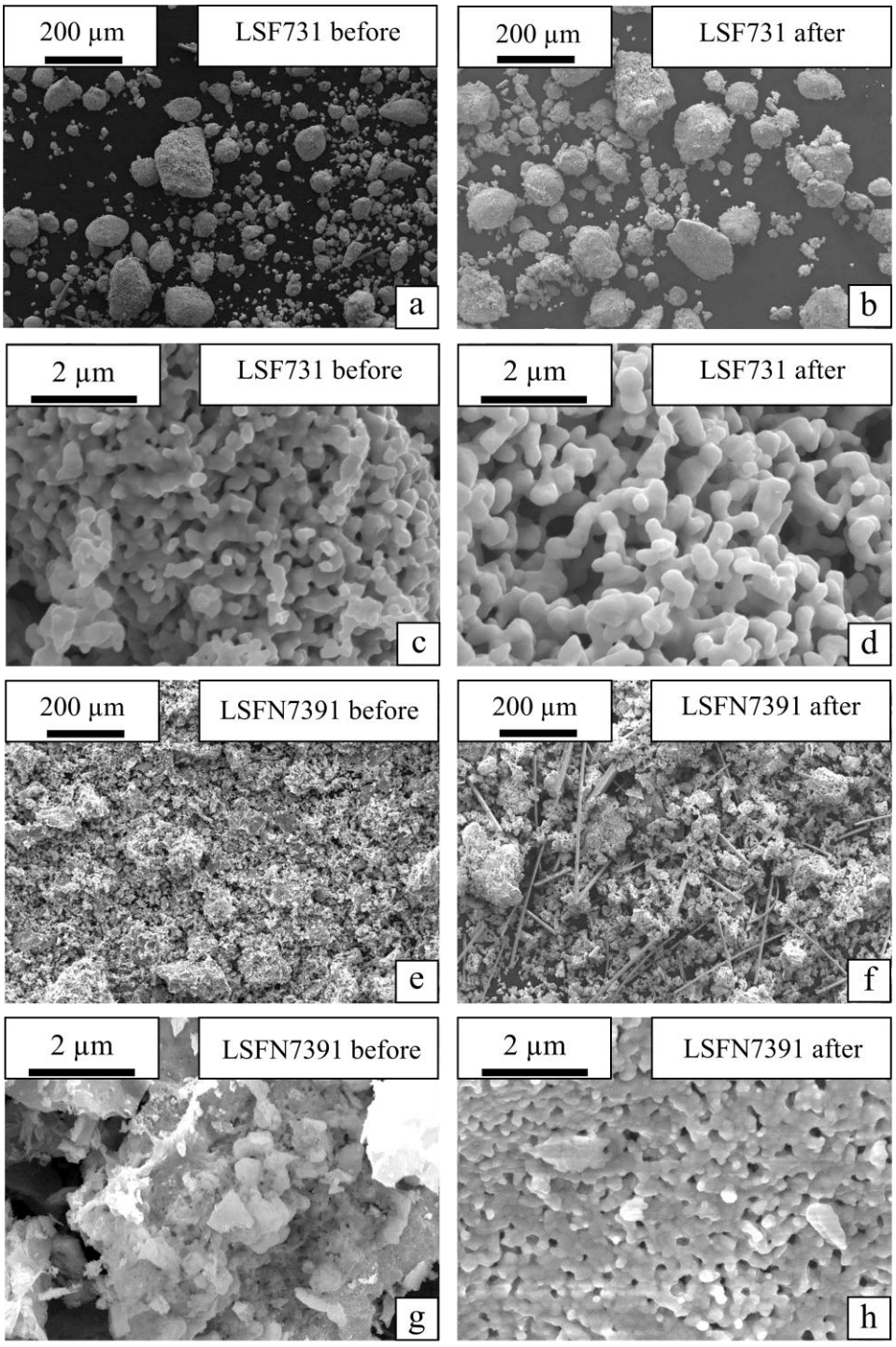

Figure 8.7 SEM images of (a) and (c) fresh LSF731, (e) and (g) fresh LSFN7391, (b) and (d) LSF731 following isothermal chemical looping WGS operation at 850^{o}C and (f) and (h) LSFN7391 following isothermal chemical looping WGS operation at 850^{o}C. Images (c), (d), (g) and (h) are magnified images of a typical particle surface.

XRD analysis of LSFN7391 following isothermal chemical looping WGS (as shown in Figure 8.6d) shows that the structure had remained in a perovskite form but that carbon and nickel were present (although the low height of the peaks associated to these reflections may indicate that a low number of crystallites existed in these phases). The formation of carbon on the LSFN7391 sample supports the theory that there was an accumulation of carbon forming during the reduction steps that may not have been oxidised during the subsequent water oxidation steps. XRD analysis of LSF731 following isothermal chemical looping WGS operation at 850^{o}C showed no indication of carbon deposition, and therefore it could be the presence of nickel in LSFN7391 which influences this.

The SEM image taken of LSFN7391 following operation (Figure 8.7h) shows that the material has similar (but not entirely the same) surface features as LSF731, whereas before operation the finger-like features were not present (Figure 8.7g). A comparison of the low magnification SEM images for LSFN7391 show no significant changes.

8.3 Summary

In a previous experiment performed for this thesis (Section 6), LSF731 was used to perform 150 cycles of isothermal chemical looping WGS operation at 850^{o}C involving reduction by carbon monoxide and oxidation by water. These results show that this OCM had great material stability and allowed steady hydrogen production during cycling. In this chapter, a similar material containing a small amount of nickel on the B-site of the perovskite was used (LSFN7391) to perform 65 of the same redox cycles in an attempt to improve reactivity compared to LSF731 (which may allow shorter reduction and oxidation cycles).

The presence of nickel caused higher carbon dioxide formation during the reduction steps, which according to carbon molar balances was due to the additional formation of solid carbon which was not removed during water oxidation steps. This theory is confirmed by the results presented in Section 5 of this thesis which involves an experiment utilising supported nickel oxide as an OCM for temperature

programmed chemical looping WGS operation. In that study, nickel oxide was found to be very susceptible to carbon deposition, and more so compared to iron oxide or the iron-containing perovskites (LSF731 and LSCF6428).

Compared to LSF731, a longer time was required to complete oxidation of the OCM for LSFN7391 during the water oxidation steps. The presence of nickel showed no improvement on reduction and oxidation rates of reactions and seemed to only generate detrimental effects such as lower rates of reaction and higher susceptibility to carbon deposition. As mentioned in Section 3.2.5, a study by Otsuka *et al.*[75] was performed to test the effects of adding 3 mol. % of different metals to iron oxide in a chemical looping water splitting process, which showed that the noble metals ruthenium, rhodium, palladium, silver, iridium and platinum enhanced water splitting. Therefore, in future work these metals could be used as additive metals instead of nickel which may show improved water splitting in an isothermal chemical looping WGS process using stable iron-containing perovskite OCMs.

Chapter 9

9. Conclusions

9.1 Summary

The main objective of this PhD project was to assess the feasibility of using oxygen deficient perovskites as oxygen carrier materials in chemical looping processes for hydrogen production by water splitting. The lanthanum and strontium containing perovskites, $La_{0.6}Sr_{0.4}Co_{0.2}Fe_{0.8}O_{3-\delta}$ and $La_{0.7}Sr_{0.3}FeO_{3-\delta}$ were selected as potential candidates for this, and they were compared against 60% Fe_2O_3/Al_2O_3 and 20% NiO/Al_2O_3 in a preliminary test using five cycles of temperature programmed reduction and oxidation up to 1000^oC using carbon monoxide as the reducing agent and water as the oxidising agent. $La_{0.7}Sr_{0.3}FeO_{3-\delta}$ generated steady hydrogen production over the five water oxidation steps performed and material characterisation indicated that the sample had not fragmented or agglomerated during operation and that the material had not formed secondary crystallite phases. $La_{0.6}Sr_{0.4}Co_{0.2}Fe_{0.8}O_{3-\delta}$ gave a similar performance to $La_{0.7}Sr_{0.3}FeO_{3-\delta}$ but material characterisation showed the formation of a secondary phase of La_2CoO_4, indicating material instability. Both perovskite materials appeared to produce high purity hydrogen during the water oxidation steps, which gave similar levels of hydrogen purity compared to 60% Fe_2O_3/Al_2O_3. However, the 60% Fe_2O_3/Al_2O_3 showed signs of material deactivation as the cycles progressed which was due to material agglomeration and the formation of iron aluminate. 20% NiO/Al_2O_3 appeared to give the worst results out of the four oxygen carrier materials tested, and this was due to the formation of solid carbon upon the surface of the metal oxide during the reduction step, which led to low purity hydrogen production during the water oxidation steps

As a result of this preliminary test, the best performing perovskite ($La_{0.7}Sr_{0.3}FeO_{3-\delta}$) and best performing metal oxide (60% Fe_2O_3/Al_2O_3) were selected for further testing by isothermal chemical looping operation involving hydrogen production by water splitting. 150 cycles of isothermal water-gas shift redox cycles (reduction by carbon monoxide and oxidation by water) were performed for $La_{0.7}Sr_{0.3}FeO_{3-\delta}$ and 60% Fe_2O_3/Al_2O_3 at 850^{o}C to assess the long-term material stability of these oxygen carrier materials. The results showed that during the first 10 redox cycles, $La_{0.7}Sr_{0.3}FeO_{3-\delta}$ gave a slight drop in hydrogen production as the cycles progressed, but following this hydrogen production was steady indicating good material stability (this result complemented post-operation material characterisation analysis which showed that there were no significant changes in phase or structure). 60% Fe_2O_3/Al_2O_3 maintained steady hydrogen production over the first 40 cycles, but following this there was a large drop over the subsequent cycles. Post-operation material characterisation indicated that iron aluminate had been formed and also that the material had agglomerated leading to larger sized particles. The results from this study prove that $La_{0.7}Sr_{0.3}FeO_{3-\delta}$ is a suitable oxygen carrier material for long-term isothermal chemical looping cycling involving water splitting for pure hydrogen production.

In a further test, $La_{0.7}Sr_{0.3}FeO_{3-\delta}$ and 60% Fe_2O_3/Al_2O_3 were utilised as oxygen carrier materials in a chemical looping process involving reduction by methane, and oxidation by water then air (all at 850^{o}C). The benefit of using this process in industry is the option of producing syngas (in a ratio of 2:1 of hydrogen-to-carbon monoxide) by the methane reduction step which could be used for further processing of useful products. Additionally, the air oxidation step produces heat which may allow the whole process to be operated autothermally. In this study, 60% Fe_2O_3/Al_2O_3 out-performed $La_{0.7}Sr_{0.3}FeO_{3-\delta}$ in terms of producing higher purity hydrogen during the water oxidation step. $La_{0.7}Sr_{0.3}FeO_{3-\delta}$ induced methane pyrolysis during the reduction step which led to large amounts of carbon monoxide being produced in the water oxidation step due to carbon carryover. However, $La_{0.7}Sr_{0.3}FeO_{3-\delta}$ showed much higher material stability compared to 60% Fe_2O_3/Al_2O_3. In additional tests, water was added to the methane reducing feed whilst using $La_{0.7}Sr_{0.3}FeO_{3-\delta}$ as the OCM in an attempt to prevent carbon deposition. This resulted in the production of high purity hydrogen. It was concluded that the

occurrence of carbon deposition during the three-step chemical looping process using perovskites as the oxygen carrier material could be suppressed by lowering operating temperature, adding water to the reducing feed or selecting a perovskite composition that is thermodynamically favourable for lowering carbon production.

In the literature, nickel doping on iron oxide has shown improved rates of reactions for chemical looping water splitting processes. In an attempt to improve rates of reactions involving $La_{0.7}Sr_{0.3}FeO_{3-\delta}$ as the oxygen carrier material (and therefore allow shorter cycling time), a small amount of nickel was added to the perovskite phase in place of iron on the B-sites to form a new perovskite structure, $La_{0.7}Sr_{0.3}Fe_{0.9}Ni_{0.1}O_{3-\delta}$. This material was subjected to 65 cycles of isothermal chemical water-gas shift operation at 850^{o}C, and directly compared to $La_{0.7}Sr_{0.3}FeO_{3-\delta}$. The results showed that $La_{0.7}Sr_{0.3}Fe_{0.9}Ni_{0.1}O_{3-\delta}$ gave slightly lower hydrogen purity compared to $La_{0.7}Sr_{0.3}FeO_{3-\delta}$, and it also appeared to give no improvement in terms of reaction rates (oxygen uptake of $La_{0.7}Sr_{0.3}Fe_{0.9}Ni_{0.1}O_{3-\delta}$ during water oxidation appeared to last longer compared to $La_{0.7}Sr_{0.3}FeO_{3-\delta}$, indicating that it gave a lower rate of oxidation). In terms of stability, both perovskites gave similar performances and showed no loss in activity as the cycles progressed.

In chemical looping processes, the oxygen carrier material undergoes continuous reduction and oxidation at high temperatures, which could lead to material stresses and sintering. It has been proven in this thesis that certain perovskite materials are potential oxygen carrier materials that can allow redox reactions involving water splitting to occur by oxygen uptake and release without undergoing a structural or phase change, even under high temperatures, very reducing conditions and over a high number of redox cycles. In an industrial chemical looping water splitting process, the use of stable iron-containing perovskites as oxygen carrier materials may reduce overall operational costs compared to conventional metal oxides as they could allow lower process down time and less frequent replacement of material. Also, following deactivation of iron-containing perovskite, a simple recalcination step involving a reaction with air at high temperature can be used to regenerate the material and remove carbon deposits, which would allow the material to be considered as a capital cost.

9.2 Suggested future work

$La_{0.7}Sr_{0.3}FeO_{3-\delta}$ was successfully used to perform a high number of redox cycles by isothermal water-gas shift operation at 850^{o}C. Although 150 cycles appear to be more than the highest number of redox cycles performed by chemical looping water splitting in the literature so far, $La_{0.7}Sr_{0.3}FeO_{3-\delta}$ could be used to perform a much higher number of redox cycles to further test long-term activity. This would assess the feasibility of using perovskite materials in industrial applications.

$La_{0.7}Sr_{0.3}FeO_{3-\delta}$ was used to perform a three-step chemical looping process involving reduction by methane, oxidation by water and oxidation by air at 850^{o}C. The results showed that when pure methane was used as the reducing feed, methane pyrolysis occurred which caused the production of low purity hydrogen during the water oxidation steps. The addition of water into the reducing feed did suppress carbon formation, but further investigations could be performed to test other compositions of perovskites (containing alternative A- and B-site metals) which may be able to suppress carbon formation whilst allowing pure methane to be used as the reducing feed. In particular, addition of the noble metals ruthenium, rhodium, palladium, silver, iridium and platinum may show enhanced water splitting according to the literature. In addition to using methane, other reducing feeds such as biomass and coal (either in solid form or gasified) could be used in chemical looping cycles using perovskites as the oxygen carrier material. Testing for the effects of contaminants such as sulphur, chlorine and tar would be essential for these processes.

The steam-iron process dates back to 1903, and since then iron oxide has been well studied in chemical looping water splitting processes, in as much detail that the oxidation states and phase changes that occur in a chemical looping system can be determined simply by performing thermodynamic analysis. There also appears to be certain oxidation states that relate to material deactivation (iron is more likely to deactivate in the presence of a reducing agent compared to haematite). To further optimise the use of $La_{0.7}Sr_{0.3}FeO_{3-\delta}$ (in a similar manner to iron oxide oxygen carrier materials), further experiments could be performed to assess whether only certain ranges of δ should be utilised during redox cycling to improve performance and reactivity rather than performing full reductions and oxidations.

In the chemical looping literature, oxygen carrier materials have been used in the form of either powders or pellets, but there is also the potential to form other structures. Perovskite materials in previous literature have been used as mixed ionic-electronic conducting membranes in the form of hollow fibres and this geometric structure could be used to form an oxygen carrier material capsule[206] comprising of a reactive metal oxide encapsulated in perovskite (Figure 9.1).

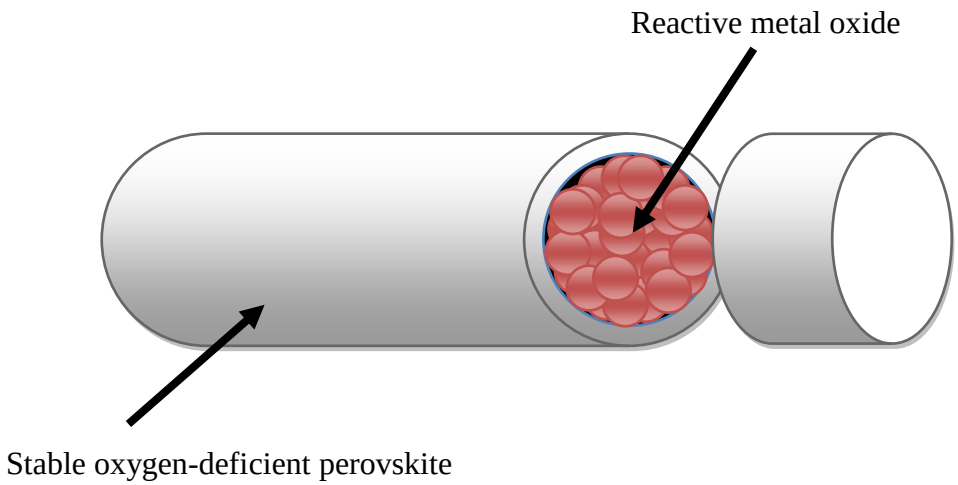

Figure 9.1 Concept of an oxygen carrier material capsule (cross-section)

To form this capsule, the perovskite material could be formed into a hollow fibre membrane by an inversion precipitation method. A reactive metal oxide in powdered form could be filled inside the perovskite hollow fibre membrane and the membrane could be capped or closed on both ends to form the capsule. Even if the reactive metal oxide is susceptible to carbon deposition or is vulnerable to material degradation, carbon would never reach the metal oxide and also fragmented metal oxide would remain contained with the perovskite capsule (therefore there would be no loss of reactive metal oxide material). In order for the capsule system to be effective, the perovskite material would need to give high oxygen permeation rates and also should not be susceptible to carbon deposition (as this would block oxygen permeation sites). This capsulated system could potentially allow the use of highly

reactive metal oxides in chemical looping systems which would normally be excluded due to susceptibility to carbon deposition or low material stability.

To perform continuous hydrogen production in a chemical looping process, a circulating fluidised bed reactor system could be used (where each reduction and oxidation step occurs in separate reactors and the solid oxygen carrier material is fluidised and circulated through each). However, it appears that in chemical looping water splitting processes involving these types of reactors, perovskite materials have not been used as the oxygen carrier material and therefore a study of this kind should be performed to investigate the benefits or impediments of using such a system.

The use of perovskites as oxygen carrier materials in a chemical looping water splitting process is a promising strategy for hydrogen production. If it can be proven that the perovskites can maintain hydrogen production over a very long operational time (so far there have not been any indications that this is not the case) and if a feasibility study can be performed to show that the process can be scaled up, this process would be very attractive for industrial application and could compete with conventional methods of hydrogen production such as steam methane reforming.

10. References

1. J. Irvine, "Overview of the state-of-the-art in hydrogen production", Progress in Hydrogen Safety Conference, Belfast, 2010.
2. A. T-Raissi and D. L. Block, *Power and Energy Magazine, IEEE*, 2004, **2**, 40-45.
3. B. Gaudernack and S. Lynum, *International Journal of Hydrogen Energy*, 1998, **23**, 1087-1093.
4. International Energy Agency, Hydrogen production and distribution, http://www.iea.org/textbase/nppdf/free/2005/hydrogen2005.pdf, Accessed 18th August 2011.
5. New York State Energy Research and Development Authority, Hydrogen Production - Steam Methane Reforming, http://www.getenergysmart.org/, Accessed 18th August 2011.
6. J. Stocker and M. Whysall, 30 years of PSA technology for hydrogen purification, http://www.uop.com/objects/30YrsPSATechHydPurif.pdf, Accessed 11th September 2011.
7. H.-J. Ryu and G.-T. Jin, *Korean Journal of Chemical Engineering*, 2007, **24**, 527-531.
8. N. Z. Muradov and T. N. Veziroglu, *International Journal of Hydrogen Energy*, 2008, **33**, 6804-6839.
9. S. Ahmed, A. Aitani, F. Rahman, A. Al-Dawood and F. Al-Muhaish, *Applied Catalysis A: General*, 2009, **359**, 1-24.
10. A. G. Mamalis, L. O. G. Vogtländer and A. Markopoulos, *Precision Engineering*, 2004, **28**, 16-30.
11. J. D. Holladay, J. Hu, D. L. King and Y. Wang, *Catalysis Today*, 2009, **139**, 244-260.
12. J. E. Funk, *International Journal of Hydrogen Energy*, 2001, **26**, 185-190.
13. P. B. Scott, *Fuel Cell Review*, 2005, **2**, 21-25.
14. C. Koroneos, A. Dompros, G. Roumbas and N. Moussiopoulos, *International Journal of Hydrogen Energy*, 2004, **29**, 1443-1450.
15. Hydrogen Solar Guildford, Hydrogen Solar, http://www.hydrogensolar.com/, Accessed 18th August 2011.
16. V. M. Aroutiounian, V. M. Arakelyan and G. E. Shahnazaryan, *Solar Energy*, 2005, **78**, 581-592.
17. K. Vijayaraghavan, R. Karthik and S. P. Kamala Nalini, *International Journal of Hydrogen Energy*, 2009, **34**, 7964-7970.
18. D. B. Levin, L. Pitt and M. Love, *International Journal of Hydrogen Energy*, 2004, **29**, 173-185.
19. P. Aldhous, in *"Growing hydrogen for the cars of tomorrow", New Scientist*, 2006.
20. H. Lane, in *"The Lane Hydrogen Producer", Flight*, Britain, 1909.
21. M. Ishida and H. Jin, *Energy Conversion and Management*, 1997, **38**, S187-S192.

22. S. J. Gasior, ed. "Production of Synthesis Gas and hydrogen by the Steam-Iron Process: Pilot Plant Study of Fluidized and Free-Falling Beds", Bureau of Mines, Washington, 1961.
23. International Energy Agency, Prospects for hydrogen and fuel cells, http://www.iea.org/textbase/nppdf/free/2005/hydrogen2005.pdf, Accessed 18th August 2011.
24. BP, BP statistical review of world energy June 2010, www.bp.com/statisticalreview, Accessed 18th August 2011.
25. S. D. Fraser, M. Monsberger and V. Hacker, *Journal of Power Sources*, 2006, **161**, 420-431.
26. P. Chiesa, G. Lozza, A. Malandrino, M. Romano and V. Piccolo, *International Journal of Hydrogen Energy*, 2008, **33**, 2233-2245.
27. P. L. Teed, *The Chemistry and Manufacture of Hydrogen*, New York, Longmans, Green and co.; London, Arnold, ISBN: 1146728093, 1919.
28. J. Langins, *Annals of Science*, 1983, **40**, 531 - 558.
29. Max Appl, *Ammonia*, Wiley-VCH Verlag GmbH & Co. KGaA, ISBN: 3527295933, 2000.
30. R. G. Minet and K. Desai, *International Journal of Hydrogen Energy*, 1983, **8**, 285-290.
31. P. W. Doughty, G. Harrison and G. J. Lawson, *Fuel*, 1989, **68**, 1257-1263.
32. M. R. Othman, Martunus, R. Zakaria and W. J. N. Fernando, *Energy Policy*, 2009, **37**, 1718-1735.
33. S. C. Page, A. G. Williamson and I. G. Mason, *Energy Policy*, 2009, **37**, 3314-3324.
34. H. Howard J, *Energy Economics*, 2011, **33**, 597-604.
35. UT-Battelle, *Oak Ridge National Laboratory Review*, 2000, **33**.
36. U.S. Department of Energy, Fuel Cell Technologies Program, http://www1.eere.energy.gov/hydrogenandfuelcells, Accessed 18th August 2011.
37. BMW, Hydrogen Combustion Engine, www.bmw.com, Accessed 18th August 2011.
38. A. J. Appleby, *Journal of Power Sources*, 1990, **29**, 3-11.
39. G. C. Congress, New On-Board Solid Oxide Fuel Cell Delivers 50% Efficiency, http://www.greencarcongress.com, Accessed 18th August 2011.
40. EG&G Technical Services Inc., *Fuel Cell Handbook (7th edition)*, ISBN: 1410219607, 2004.
41. L. Klebanoff, "Materials for hydrogen storage", Progress in Hydrogen Safety Conference, Belfast, 2010.
42. H. D. Ng and J. H. S. Lee, *Journal of Loss Prevention in the Process Industries*, 2008, **21**, 136-146.
43. D. Baraldi, A. Kotchourko, A. Lelyakin, J. Yanez, A. Gavrikov, A. Efimenko, F. Verbecke, D. Makarov, V. Molkov and A. Teodorczyk, *International Journal of Hydrogen Energy*, **35**, 12381-12390.
44. M. Raju, J. P. Ortmann and S. Kumar, *International Journal of Hydrogen Energy*, 2010, **35**, 8742-8754.
45. Y. H. P. Zhang, *International Journal of Hydrogen Energy*, **35**, 10334-10342.
46. Hydrogen Cars Now, European Union Hydrogen Highway, http://www.hydrogencarsnow.com/, Accessed 18th August 2011.

47. M. Mogensen, T. Armstrong, R. M. Gur and H. Yokokawa, *Ionic and Mixed Conduction Ceramics 6*, The Electrochemical Society, ISBN: 1615672850, 2008.
48. P. Heidebrecht and K. Sundmacher, *Chemical Engineering Science*, 2009, **64**, 5057-5065.
49. P. Heidebrecht, C. Hertel and K. Sundmacher, *International Journal of Chemical Reactor Engineering*, 2008, **6**.
50. P. Kolbitsch, T. Pröll, J. Bolhar-Nordenkampf and H. Hofbauer, *Energy Procedia*, 2009, **1**, 1465-1472.
51. S. Hurst, *"Production of hydrogen by the steam-iron method", Oil and Soap*, 1939.
52. S. Choi, J. Park, C. Han and E. S. Yoon, *Industrial & Engineering Chemistry Research*, 2007, **47**, 323-331.
53. *USA Pat.*, US Patent 1658939, 1928.
54. *USA Pat.*, US Patent 2182747, 1939.
55. *USA Pat.*, US Patent 2635947 1953.
56. *USA Pat.*, US Patent 3027238, 1962.
57. *USA Pat.*, US Patent 3421869, 1969.
58. *USA Pat.*, US Patent 3442619, 1969.
59. *USA Pat.*, US Patent 3619142, 1971.
60. Xiang and Chen, *Energy & Fuels*, 2007, **21**, 2272-2277.
61. J. P. E. Cleeton, C. D. Bohn, C. R. Müller, J. S. Dennis and S. A. Scott, *International Journal of Hydrogen Energy*, 2009, **34**, 1-12.
62. V. Hacker, R. Fankhauser, G. Faleschini, H. Fuchs, K. Friedrich, M. Muhr and K. Kordesch, *Journal of Power Sources*, 2000, **86**, 531-535.
63. F. Li, H. R. Kim, D. Sridhar, F. Wang, L. Zeng, J. Chen and L. S. Fan, *Energy & Fuels*, 2009.
64. N. V. Gnanapragasam, B. V. Reddy and M. A. Rosen, *International Journal of Hydrogen Energy*, 2009, **34**, 2606-2615.
65. J.-B. Yang, N.-S. Cai and Z.-S. Li, *Energy & Fuels*, 2008, **22**, 2570-2579.
66. N. Kobayashi and L.-S. Fan, *Biomass and Bioenergy*, 2011, **35**, 1252-1262.
67. M. F. Bleeker, S. R. A. Kersten and H. J. Veringa, *Catalysis Today*, 2007, **127**, 278-290.
68. M. F. Bleeker, H. J. Veringa and S. R. A. Kersten, *Industrial & Engineering Chemistry Research*, 2009, **49**, 53-64.
69. L. F. de Diego, M. Ortiz, F. García-Labiano, J. Adánez, A. Abad and P. Gayán, *Journal of Power Sources*, 2009, **192**, 27-34.
70. K. S. Go, S. R. Son, S. D. Kim, K. S. Kang and C. S. Park, *International Journal of Hydrogen Energy*, 2009, **34**, 1301-1309.
71. S. Fukase and T. Suzuka, *Applied Catalysis A: General*, 1993, **100**, 1-17.
72. C. Yang, Z. Ma, N. Zhao, W. Wei, T. Hu and Y. Sun, *Catalysis Today*, 2006, **115**, 222-227.
73. L. A. Pellegrini, G. Soave, S. Gamba and S. Lange, *Applied Energy*, 2011, **88**, 4891-4897.
74. K. Otsuka, C. Yamada, T. Kaburagi and S. Takenaka, *International Journal of Hydrogen Energy*, 2003, **28**, 335-342.
75. K. Otsuka, T. Kaburagi, C. Yamada and S. Takenaka, *Journal of Power Sources*, 2003, **122**, 111-121.
76. H. Imanishi, A. Maeda, T. Maegawa, S. Matsuno and T. Aida, *Chemical Engineering Science*, 2008, **63**, 4974-4980.

77. J. A. Peña, E. Lorente, E. Romero and J. Herguido, *Catalysis Today*, 2006, **116**, 439-444.
78. D. P. Harrison, *Industrial & Engineering Chemistry Research*, 2008, **47**, 6486-6501.
79. B. González, J. Blamey, M. McBride-Wright, N. Carter, D. Dugwell, P. Fennell and J. C. Abanades, *Energy Procedia*, **4**, 402-409.
80. V. Dupont, A. B. Ross, I. Hanley and M. V. Twigg, *International Journal of Hydrogen Energy*, 2007, **32**, 67-79.
81. J. Wolf and J. Yan, *International Journal of Energy Research*, 2005, **29**, 739-753.
82. P. Pimenidou, G. Rickett, V. Dupont and M. V. Twigg, *Bioresource Technology*, 2010, **101**, 9279-9286.
83. M. Rydén, A. Lyngfelt, T. Mattisson, D. Chen, A. Holmen and E. Bjørgum, *International Journal of Greenhouse Gas Control*, 2008, **2**, 21-36.
84. V. Hacker, G. Faleschini, H. Fuchs, R. Fankhauser, G. Simader, M. Ghaemi, B. Spreitz and K. Friedrich, *Journal of Power Sources*, 1998, **71**, 226-230.
85. K. Mondal, H. Lorethova, E. Hippo, T. Wiltowski and S. B. Lalvani, *Fuel Processing Technology*, 2004, **86**, 33-47.
86. R. D. Solunke and G. Veser, *Industrial & Engineering Chemistry Research*, 2010, **49**, 11037-11044.
87. Q. Zafar, T. Mattisson, M. Johansson and A. Lyngfelt, Chemical-Looping Combustion - A New CO_2 Management Technology, Carbon Management Symposium, Dhahran, 2006.
88. K. Svoboda, A. Siewiorek, D. Baxter, J. Rogut and M. Pohorelý, *Energy Conversion and Management*, 2008, **49**, 221-231.
89. K. Svoboda, A. Siewiorek, D. Baxter, J. Rogut and M. Punčochář, *Chemical Papers*, 2007, **61**, 110-120.
90. K. Svoboda, G. Slowinski, J. Rogut and D. Baxter, *Energy Conversion and Management*, 2007, **48**, 3063-3073.
91. A. Earnshaw and N. Greenwood, *Chemistry of the Elements, Second Edition*, Butterworth-Heinemann, ISBN: 0750633654, 1997.
92. A. Pineau, N. Kanari and I. Gaballah, *Thermochimica Acta*, 2006, **447**, 89-100.
93. H.-Y. Lin, Y.-W. Chen and C. Li, *Thermochimica Acta*, 2003, **400**, 61-67.
94. C. D. Bohn, C. R. Muller, J. P. Cleeton, A. N. Hayhurst, J. F. Davidson, S. A. Scott and J. S. Dennis, *Industrial & Engineering Chemistry Research*, 2008, **47**, 7623-7630.
95. B. Wang, R. Yan, D. H. Lee, D. T. Liang, Y. Zheng, H. Zhao and C. Zheng, *Energy & Fuels*, 2008, **22**, 1012-1020.
96. M. M. Hossain and H. I. de Lasa, *Chemical Engineering Science*, **65**, 98-106.
97. S. T. Bayu Alamsari, Azis Trianto, and Yazid Bindar, *ISRN Mechanical Engineering*, 2011, **2011**.
98. E. Lorente, J. A. Peña and J. Herguido, *International Journal of Hydrogen Energy*, 2008, **33**, 615-626.
99. C. D. Bohn, J. P. Cleeton, C. R. Müller, S. Y. Chuang, S. A. Scott and J. S. Dennis, *Energy & Fuels*, 2010, **24**, 4025-4033.
100. A. M. Kierzkowska, C. D. Bohn, S. A. Scott, J. P. Cleeton, J. S. Dennis and C. R. Müller, *Industrial & Engineering Chemistry Research*, 2010, **49**, 5383-5391.

101. A. Bandopadhyay, A. Ganguly, K. N. Gupta and H. S. Ray, *Thermochimica Acta*, 1996, **276**, 199-207.
102. M. A. Qayyum and D. A. Reeve, *Carbon*, 1976, **14**, 199-202.
103. M. Selan, J. Lehrhofer, K. Friedrich, K. Kordesch and G. Simader, *Journal of Power Sources*, 1999, **61**, 247-253.
104. H. Kindermann, M. Kornberger, J. Hierzer, J. O. Besenhard and V. Hacker, *Journal of Power Sources*, 2005, **145**, 697-701.
105. M. Thaler, V. Hacker, M. Anilkumar, J. Albering, J. O. Besenhard, H. Schröttner and M. Schmied, *International Journal of Hydrogen Energy*, 2006, **31**, 2025-2031.
106. V. Hacker, R. Vallant and M. Thaler, *Industrial & Engineering Chemistry Research*, 2007, **46**, 8993-8999.
107. V. Galvita and K. Sundmacher, *Journal of Materials Science*, 2007, **42**, 9300-9307.
108. V. Galvita and K. Sundmacher, *Applied Catalysis A: General*, 2005, **289**, 121-127.
109. V. Galvita, T. Schröder, B. Munder and K. Sundmacher, *International Journal of Hydrogen Energy*, 2008, **33**, 1354-1360.
110. V. Galvita, T. Hempel, H. Lorenz, L. K. Rihko-Struckmann and K. Sundmacher, *Industrial & Engineering Chemistry Research*, 2007, **47**, 303-310.
111. V. Galvita and K. Sundmacher, *Chemical Engineering Journal*, 2007, **134**, 168-174.
112. J. N. Armor, *Catalysis Today*, 2010, **163**, 3-9.
113. S. Takenaka, T. Kaburagi, C. Yamada, K. Nomura and K. Otsuka, *Journal of Catalysis*, 2004, **228**, 66-74.
114. K. Urasaki, N. Tanimoto, T. Hayashi, Y. Sekine, E. Kikuchi and M. Matsukata, *Applied Catalysis A: General*, 2005, **288**, 143-148.
115. T. Kodama, T. Shimizu, T. Satoh, M. Nakata and K. I. Shimizu, *Solar Energy*, 2002, **73**, 363-374.
116. K.-S. Kang, C.-H. Kim, W.-C. Cho, K.-K. Bae, S.-W. Woo and C.-S. Park, *International Journal of Hydrogen Energy*, 2008, **33**, 4560-4568.
117. K.-S. Kang, C.-H. Kim, K.-K. Bae, W.-C. Cho, W.-J. Kim, Y.-H. Kim, S.-H. Kim and C.-S. Park, *International Journal of Hydrogen Energy*, 2009, **35**, 568-576.
118. A. Miyamoto, M. Miura, K. Sakamoto, S. Kamitomai, Y. Kosaki and Y. Murakami, *Industrial & Engineering Chemistry Product Research and Development*, 1984, **23**, 467-470.
119. T. Kodama, H. Ohtake, S. Matsumoto, A. Aoki, T. Shimizu and Y. Kitayama, *Energy*, 2000, **25**, 411-425.
120. K. Otsuka, M. Hatano and A. Morikawa, *Journal of Catalysis*, 1983, **79**, 493-496.
121. A. S. Bhalla, R. Guo and R. Roy, *Materials Research Innovations*, 2000, **4**, 3-26.
122. Materials Research Centre, Perovskites, http://mrc.iisc.ernet.in, Accessed 18th August 2011.
123. N. Xu, H. Zhao, X. Zhou, W. Wei, X. Lu, W. Ding and F. Li, *International Journal of Hydrogen Energy*, **35**, 7295-7301.
124. D. M. Smyth, *Solid State Ionics*, 2000, **129**, 5-12.
125. P. Karen, *Journal of Solid State Chemistry*, 2006, **179**, 3167-3183.

126. H. R. L. Martijn, J. M. B. Henny and V. Henk, *Journal of the American Ceramic Society*, 1997, **80**, 2175-2198.
127. S. Stolen, E. Bakken and C. E. Mohn, *Physical Chemistry Chemical Physics*, 2006, **8**, 429-447.
128. V. V. Kharton, F. M. B. Marques and A. Atkinson, *Solid State Ionics*, 2004, **174**, 135-149.
129. M. Mogensen, D. Lybye, N. Bonanos, P. V. Hendriksen and F. W. Poulsen, *Solid State Ionics*, 2004, **174**, 279-286.
130. C. P. Flynn, *Surface Science*, 2007, **601**, 1648-1658.
131. I. Riess, *Solid State Ionics*, 2003, **157**, 1-17.
132. M. Oishi, K. Yashiro, K. Sato, J. Mizusaki and T. Kawada, *Journal of Solid State Chemistry*, 2008, **181**, 3177-3184.
133. U. Balachandran, T. H. Lee and S. E. Dorris, *International Journal of Hydrogen Energy*, 2007, **32**, 451-456.
134. U. Balachandran, T. H. Lee, S. Wang and S. E. Dorris, *International Journal of Hydrogen Energy*, 2004, **29**, 291-296.
135. B. Cales and J. F. Baumard, *Journal of Materials Science*, 1982, **17**, 3243-3248.
136. A. Evdou, L. Nalbandian and V. T. Zaspalis, *Journal of Membrane Science*, 2008, **325**, 704-711.
137. H. Jiang, Z. Cao, S. Schirrmeister, T. Schiestel and J. Caro, *Angewandte Chemie International Edition*, 2010, **49**, 5656-5660.
138. H. Jiang, F. Liang, O. Czuprat, K. Efimov, A. Feldhoff, S. Schirrmeister, T. Schiestel, H. Wang and J. Caro, *Chemistry - A European Journal*, 2010, **16**, 7898-7903.
139. H. Jiang, H. Wang, F. Liang, S. Werth, S. Schirrmeister, T. Schiestel and J. Caro, *Catalysis Today*, 2010, **156**, 187-190.
140. H. Jiang, H. Wang, S. Werth, T. Schiestel and J. Caro, *Angewandte Chemie - International Edition*, 2008, **47**, 9341-9344.
141. J. Lede, F. Lapicque, J. Villermaux, B. Cales, A. Ounalli, J. F. Baumard and A. M. Anthony, *International Journal of Hydrogen Energy*, 1982, **7**, 939-950.
142. T. H. Lee, C. Y. Park, S. E. Dorris and U. Balachandran, *ECS Transactions*, 2008, **13**, 379-384.
143. H. Naito and H. Arashi, *Solid State Ionics*, 1995, **79**, 366-370.
144. L. Nalbandian, A. Evdou and V. Zaspalis, *International Journal of Hydrogen Energy*, 2009, **34**, 7162-7172.
145. C. Y. Park, T. H. Lee, S. E. Dorris and U. Balachandran, *ECS Transactions*, 2008, **13**, 393-403.
146. C. Y. Park, T. H. Lee, S. E. Dorris and U. Balachandran, *International Journal of Hydrogen Energy*, 2010, **35**, 4103-4110.
147. C. Y. Park, T. H. Lee, S. E. Dorris, Y. Lu and U. Balachandran, *International Journal of Hydrogen Energy*, 2011, **36**, 9345-9354.
148. M. Martin, *The Journal of Chemical Thermodynamics*, 2003, **35**, 1291-1308.
149. Y. Teraoka, H. M. Zhang, K. Okamoto and N. Yamazoe, *Materials Research Bulletin*, 1988, **23**, 51-58.
150. J. W. Stevenson, T. R. Armstrong, R. D. Carneim, L. R. Pederson and W. J. Weber, *Journal of The Electrochemical Society*, 1996, **143**, 2722-2729.
151. L. W. Tai, M. M. Nasrallah, H. U. Anderson, D. M. Sparlin and S. R. Sehlin, *Solid State Ionics*, 1995, **76**, 259-271.

152. L. W. Tai, M. M. Nasrallah, H. U. Anderson, D. M. Sparlin and S. R. Sehlin, *Solid State Ionics*, 1995, **76**, 273-283.
153. S. J. Benson, D. Waller and J. A. Kilner, *Journal of The Electrochemical Society*, 1999, **146**, 1305-1309.
154. D. Mantzavinos, A. Hartley, I. S. Metcalfe and M. Sahibzada, *Solid State Ionics*, 2000, **134**, 103-109.
155. A. Esquirol, N. P. Brandon, J. A. Kilner and M. Mogensen, *Journal of The Electrochemical Society*, 2004, **151**, A1847-A1855.
156. S. Diethelm and J. Van herle, *Journal of the European Ceramic Society*, 2004, **24**, 1319-1323.
157. A. Mineshige, J. Izutsu, M. Nakamura, K. Nigaki, J. Abe, M. Kobune, S. Fujii and T. Yazawa, *Solid State Ionics*, 2005, **176**, 1145-1149.
158. K. K. Hansen and K. V. Hansen, *Solid State Ionics*, 2007, **178**, 1379-1384.
159. J. E. Readman, A. Olafsen, Y. Larring and R. Blom, *Journal of Materials Chemistry*, 2005, **15**, 1931-1937.
160. M. Junichiro, S. Tadashi, C. W. Roger and B. H. Kent, *Journal of the American Ceramic Society*, 1983, **66**, 247-252.
161. J. E. ten Elshof, H. J. M. Bouwmeester and H. Verweij, *Solid State Ionics*, 1995, **81**, 97-109.
162. J. E. ten Elshof, H. J. M. Bouwmeester and H. Verweij, *Solid State Ionics*, 1996, **89**, 81-92.
163. E. V. Tsipis, M. V. Patrakeev, V. V. Kharton, A. A. Yaremchenko, G. C. Mather, A. L. Shaula, I. A. Leonidov, V. L. Kozhevnikov and J. R. Frade, *Solid State Sciences*, 2005, **7**, 355-365.
164. M. V. Patrakeev, J. A. Bahteeva, E. B. Mitberg, I. A. Leonidov, V. L. Kozhevnikov and K. R. Poeppelmeier, *Journal of Solid State Chemistry*, 2003, **172**, 219-231.
165. X. Dai, C. Yu and Q. Wu, *Journal of Natural Gas Chemistry*, 2008, **17**, 415-418.
166. S. P. Scott, D. Mantzavinos, A. Hartley, M. Sahibzada and I. S. Metcalfe, *Solid State Ionics*, 2002, **152-153**, 777-781.
167. J. Mizusaki, M. Yoshihiro, S. Yamauchi and K. Fueki, *Journal of Solid State Chemistry*, 1985, **58**, 257-266.
168. M. Søgaard, P. Vang Hendriksen and M. Mogensen, *Journal of Solid State Chemistry*, 2007, **180**, 1489-1503.
169. B. T. Dalslet, M. Søgaard, H. J. M. Bouwmeester and P. V. Hendriksen, *Solid State Ionics*, 2009, **180**, 1173-1182.
170. B. A. van Hassel, T. Kawada, N. Sakai, H. Yokokawa, M. Dokiya and H. J. M. Bouwmeester, *Solid State Ionics*, 1993, **66**, 295-305.
171. M. Takano, T. Okita, N. Nakayama, Y. Bando, Y. Takeda, O. Yamamoto and J. B. Goodenough, *Journal of Solid State Chemistry*, 1988, **73**, 140-150.
172. J. L. G. Fierro, *Metal oxides: chemistry and applications*, CRC Press, ISBN: 0824723716, 2005.
173. University of Winsconsin-Madison, Defects, http://mrsec.wisc.edu, Accessed 18th August 2011.
174. J. E. Readman, A. Olafsen, Y. Larring and R. Blom, *Journal of Materials Chemistry*, 2005, **15**, 1931-1937.
175. J. Cheng, A. Navrotsky, X.-D. Zhou and H. U. Anderson, *Chemistry of Materials*, 2005, **17**, 2197-2207.
176. A. Evdou, V. Zaspalis and L. Nalbandian, *Fuel*, **89**, 1265-1273.

177. M. E. Rivas, J. L. G. Fierro, M. R. Goldwasser, E. Pietri, M. J. PÃ©rez-Zurita, A. Griboval-Constant and G. Leclercq, *Applied Catalysis A: General*, 2008, **344**, 10-19.
178. Grant Scientific, Grant Scientific: Refrigerated Thermostatic Baths and Circulators, www.grant.co.uk, Accessed 18th August 2011.
179. R. Battino and H. L. Clever, *Chemical Reviews*, 1966, **66**, 395-463.
180. Purdue University, Scanning Electron Microscope, http://www.purdue.edu/rem/rs/sem.htm, Accessed 18th August 2011.
181. J. Goldstein, D. E. Newbury, D. C. Joy, C. E. Lyman, C. E. Echlin, P. Lifshin, L. Sawyer and J. R. Michael, *Scanning Electron Microscopy and X-ray Microanalysis*, Kluwer Academic, ISBN: 0306472929, 2003.
182. LSM Analytical Services, Inductively Coupled Plasma - Optical Emission Spectrometry, http://www.lsmanalytical.com, Accessed 18th August 2011.
183. University College London, Bragg's Law, http://pd.chem.ucl.ac.uk/pdnn/powintro/braggs.htm, Accessed 18th August 2011.
184. S. Brunauer, P. H. Emmett and E. Teller, *Journal of the American Chemical Society*, 1938, **60**, 309-319.
185. A. Murugan, A. Thursfield and I. S. Metcalfe, *Energy & Environmental Science*, 2011, **4**, 4639-4649.
186. J. Wolf, M. Anheden and J. Yan, *Fuel*, 2005, **84**, 993-1006.
187. I. Chen, S. Y. Lin and D. W. Shiue, *Industrial & Engineering Chemistry Research*, 1988, **27**, 926-929.
188. K. P. Trumble, *Acta Metallurgica et Materialia*, 1992, **40**, S105-S110.
189. A. Tsvigunov, A. Apolenis, V. Annikov and V. Raikova, *Glass and Ceramics*, 2007, **64**, 429-436.
190. X.-G. Li, Y.-H. Dong, H. Xian, W. Y. Hernandez, M. Meng, H.-H. Zou, A.-J. Ma, T.-Y. Zhang, Z. Jiang, N. Tsubaki and P. Vernoux, *Energy & Environmental Science*, 2011, **4**, 3351-3354.
191. H. l. n. Provendier, C. Petit and A. Kiennemann, *Comptes Rendus de l'AcadÃ©mie des Sciences - Series IIC - Chemistry*, 2001, **4**, 57-66.
192. *USA Pat.*, US Patent 3027238, 1984.
193. V. C. Belessi, A. K. Ladavos and P. J. Pomonis, *Applied Catalysis B: Environmental*, 2001, **31**, 183-194.
194. J.-M. Kim, G.-J. Hwang, S.-H. Lee, C.-S. Park, J.-W. Kim and Y.-H. Kim, *Journal of Membrane Science*, 2005, **250**, 11-16.
195. Y. Zeng, S. Tamhankar, N. Ramprasad, F. Fitch, D. Acharya and R. Wolf, *Chemical Engineering Science*, **58**, 577-582.
196. C.-H. Wang, C.-L. Chen and H.-S. Weng, *Chemosphere*, 2004, **57**, 1131-1138.
197. C. J. Chen and M. H. Back, *Carbon*, 1979, **17**, 175-180.
198. F. Mudu, B. r. Arstad, E. Bakken, H. FjellvÃ¥g and U. Olsbye, *Journal of Catalysis*, **275**, 25-33.
199. Y. Cai, Y. Niu and Z. Chen, *Fuel Processing Technology*, 1997, **50**, 163-170.
200. J. F. Knifton, *Journal of Catalysis*, 1983, **79**, 147-155.
201. D. Salerno, H. Arellano-Garcia, G. Wozny, M. C. G. E.N. Pistikopoulos and A. C. Kokossis, *Computer Aided Chemical Engineering*, **29**, 1874-1878.
202. J. Zaman, *Fuel Processing Technology*, 1999, **58**, 61-81.
203. G. W. Coffey, J. S. Hardy, L. R. Pederson, P. C. Rieke and E. C. Thomsen, *Electrochemical and Solid-State Letters*, 2003, **6**, A121-A124.

204. V. V. Kharton, A. P. Viskup, E. N. Naumovich and V. N. Tikhonovich, *Materials Research Bulletin*, 1999, **34**, 1311-1317.
205. U. F. Vogt, J. Sfeir, J. Richter, C. Soltmann and P. Holtappels, *Pure and Applied Chemistry*, 2008, **80**, 2543-2552.
206. I. S. Metcalfe, personal communication.
207. E. R. Stobbe, B. A. de Boer and J. W. Geus, *Catalysis Today*, 1999, **47**, 161-167.
208. M. Fathi, E. Bjorgum, T. Viig and O. A. Rokstad, *Catalysis Today*, 2000, **63**, 489-497.
209. Y. Zeng, S. Tamhankar, N. Ramprasad, F. Fitch, D. Acharya and R. Wolf, *Chemical Engineering Science*, 2003, **58**, 577-582.
210. Q. Zafar, T. Mattisson and B. r. Gevert, *Industrial & Engineering Chemistry Research*, 2005, **44**, 3485-3496.
211. Q. Zafar, T. Mattisson and B. Gevert, *Energy & Fuels*, 2005, **20**, 34-44.
212. M. Rydén, A. Lyngfelt and T. Mattisson, *Fuel*, 2006, **85**, 1631-1641.
213. L. F. de Diego, M. Ortiz, J. Adánez, F. García-Labiano, A. Abad and P. Gayán, *Chemical Engineering Journal*, 2008, **144**, 289-298.
214. M. Johansson, T. Mattisson, A. Lyngfelt and A. Abad, *Fuel*, 2008, **87**, 988-1001.
215. M. Ryden, A. Lyngfelt and T. Mattisson, *Energy & Fuels*, 2008, **22**, 2585-2597.
216. J. Bolhàr-Nordenkampf, T. Pröll, P. Kolbitsch and H. Hofbauer, Chemical looping autothermal reforming at a 120 kW pilot rig, Proceedings of the 20th International Conference on Fluidized Bed Combustion, 2009.
217. J. Bolhàr-Nordenkampf, T. Pröll, P. Kolbitsch and H. Hofbauer, Performance of a NiO-based oxygen carrier for chemical looping combustion and reforming in a 120 kW unit, Proceedings of Energy Procedia Conference, 2009.
218. L. F. de Diego, M. Ortiz, F. García-Labiano, J. Adánez, A. Abad and P. Gayán, *Energy Procedia*, 2009, **1**, 3-10.
219. F. He, Y. Wei, H. Li and H. Wang, *Energy & Fuels*, 2009, **23**, 2095-2102.
220. O. Nakayama, N. Ikenaga, T. Miyake, E. Yagasaki and T. Suzuki, *Industrial & Engineering Chemistry Research*, 2009, **49**, 526-534.
221. M. Ortiz, L. F. de Diego, A. Abad, F. García-Labiano, P. Gayán and J. Adánez, *International Journal of Hydrogen Energy*, 2009, **35**, 151-160.
222. T. Pröll, J. Bolhàr-Nordenkampf, P. Kolbitsch and H. Hofbauer, *Fuel*, 2009, **89**, 1249-1256.
223. K. Li, H. Wang, Y. Wei and D. Yan, *International Journal of Hydrogen Energy*, 2010, **36**, 3471-3482.
224. O. Mihai, D. Chen and A. Holmen, *Industrial & Engineering Chemistry Research*, 2010, **50**, 2613-2621.
225. F. Mudu, B. Arstad, E. Bakken, H. Fjellvåg and U. Olsbye, *Journal of Catalysis*, 2010, **275**, 25-33.
226. P. Pimenidou, G. Rickett, V. Dupont and M. V. Twigg, *Bioresource Technology*, 2010, **101**, 6389-6397.
227. Y. Wei, H. Wang and K. Li, *Journal of Rare Earths*, 2010, **28**, 560-565.

Appendix A: Steam-Iron Process Patents

A1. US Patent 1658939

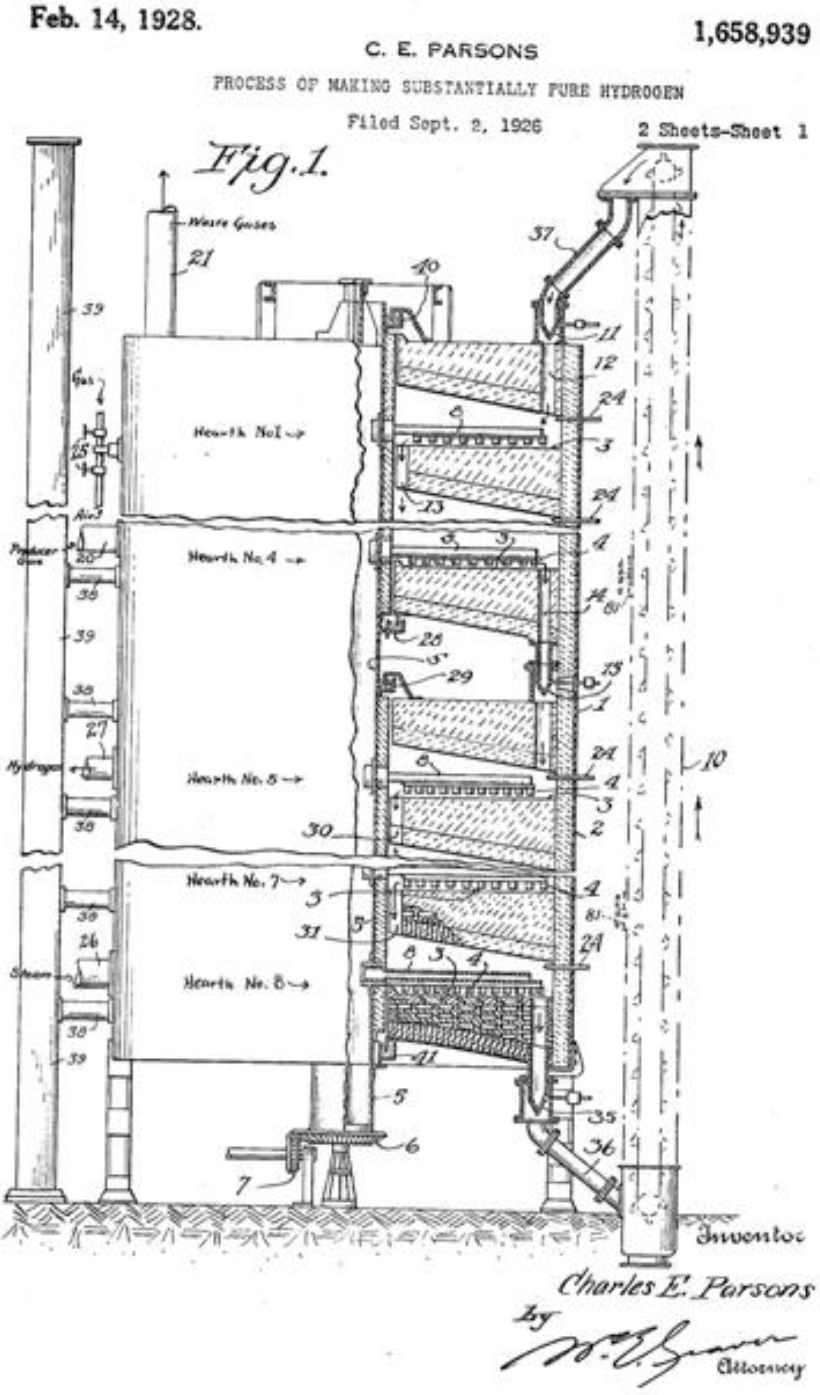

A2. US Patent 2182747

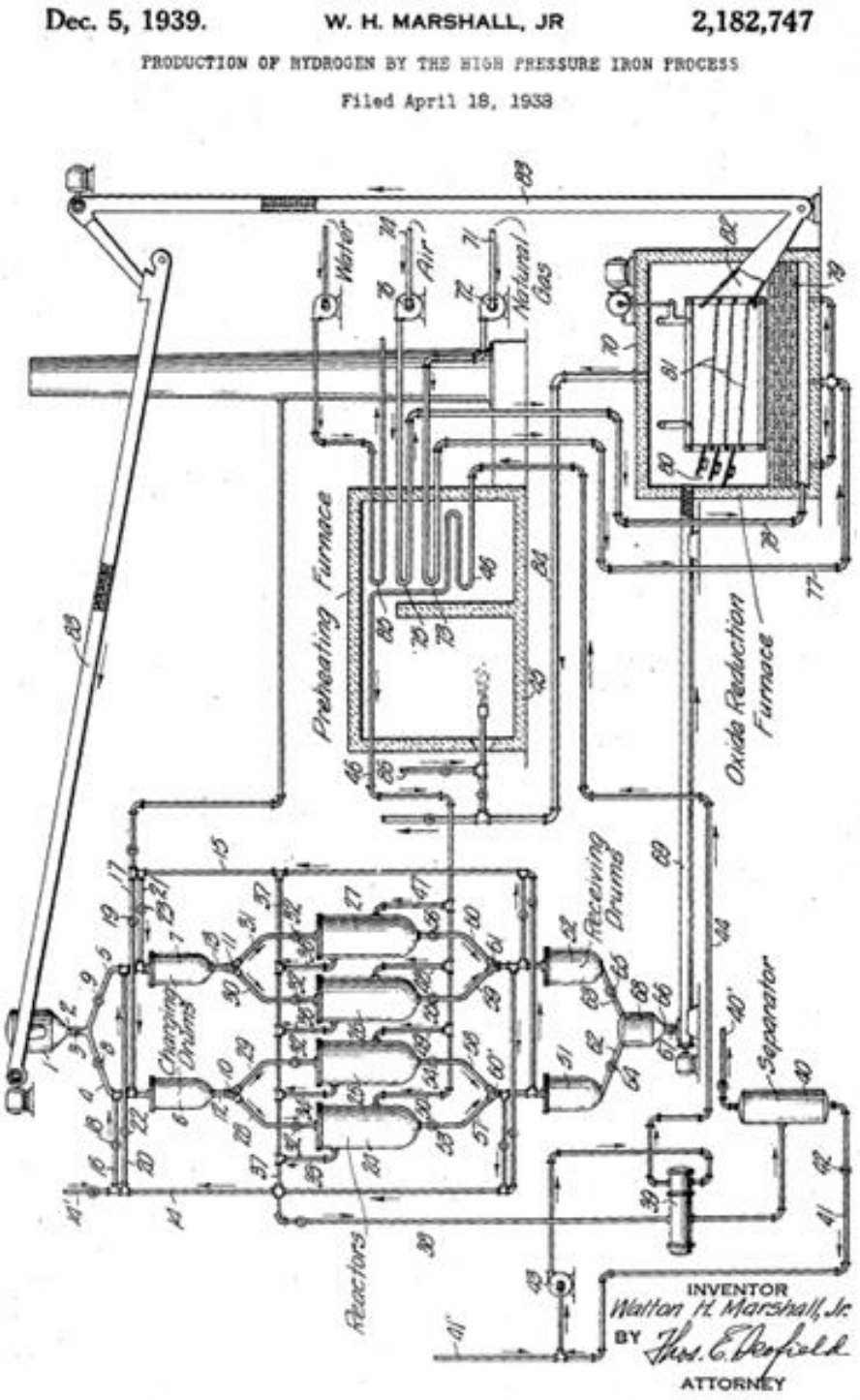

A3. US Patent 2635947

April 21, 1953 H. C. REED ET AL 2,635,947

HYDROGEN PROCESS

Filed July 2, 1948

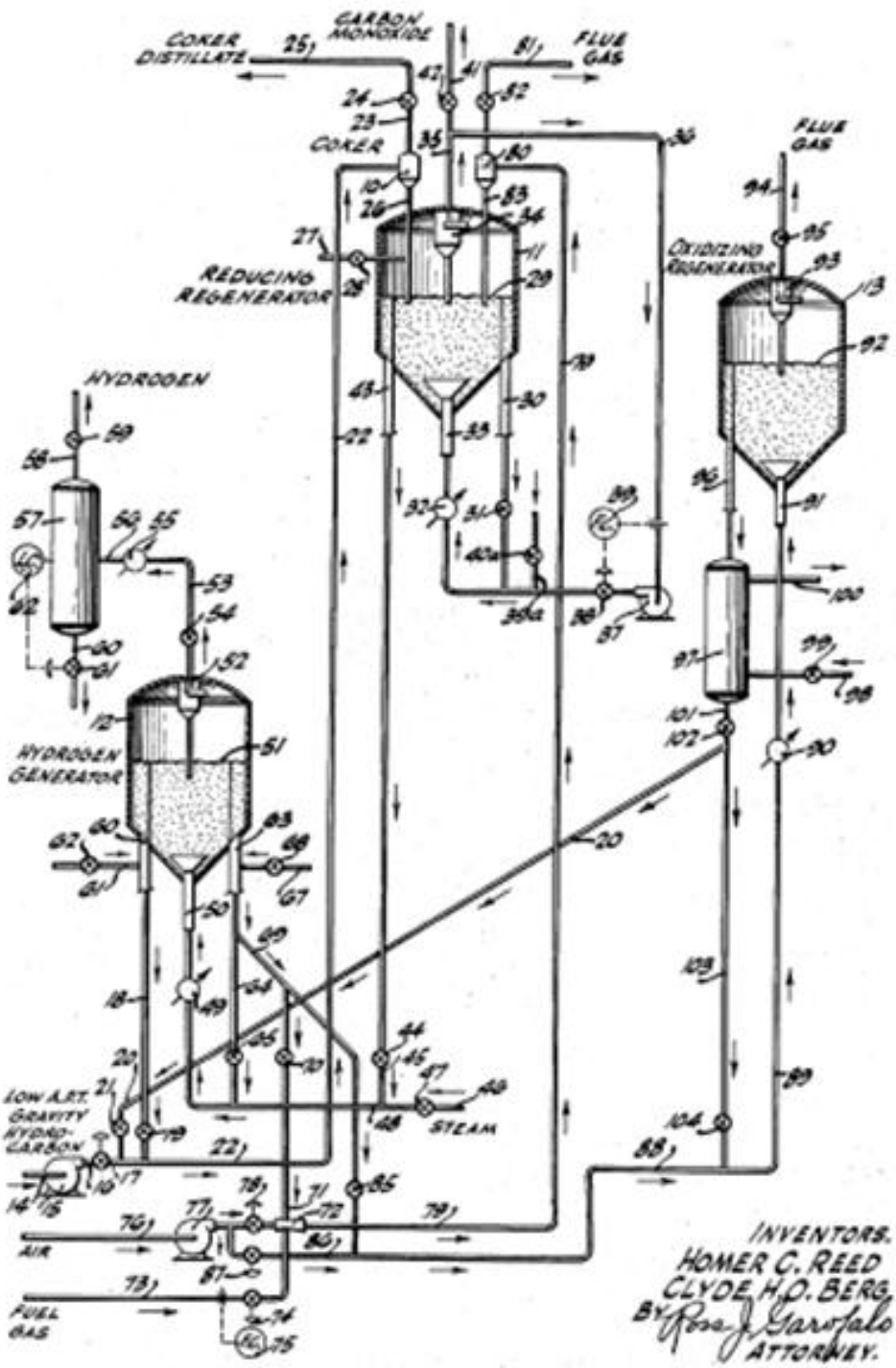

A4. US Patent 3027238

March 27, 1962 C. H. WATKINS 3,027,238

HYDROGEN MANUFACTURE

Filed Dec. 7, 1959

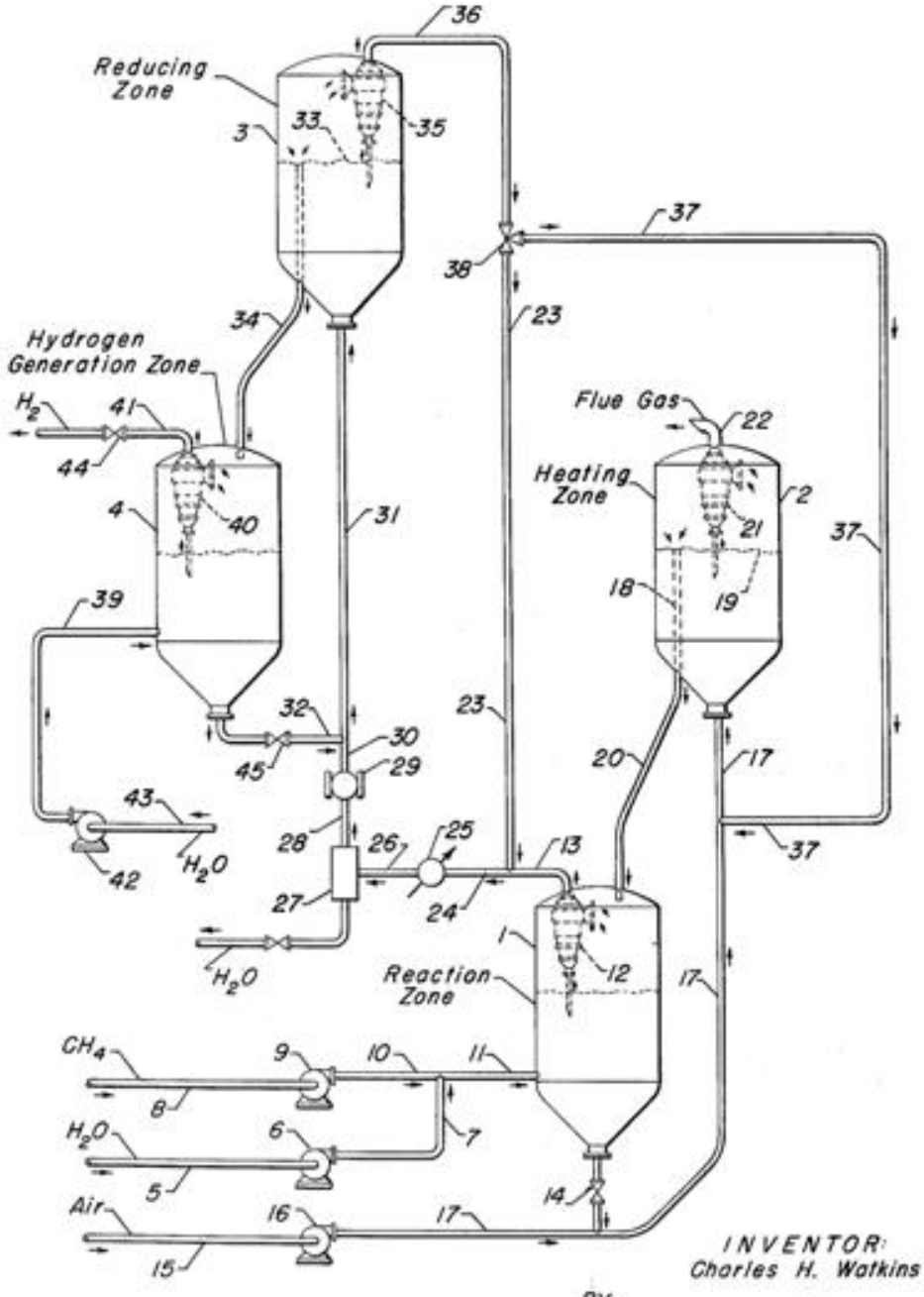

INVENTOR:
Charles H. Watkins

BY:
Chester J. Giuliani
Philip T. Liggett
ATTORNEYS

A5. US Patent 3421869

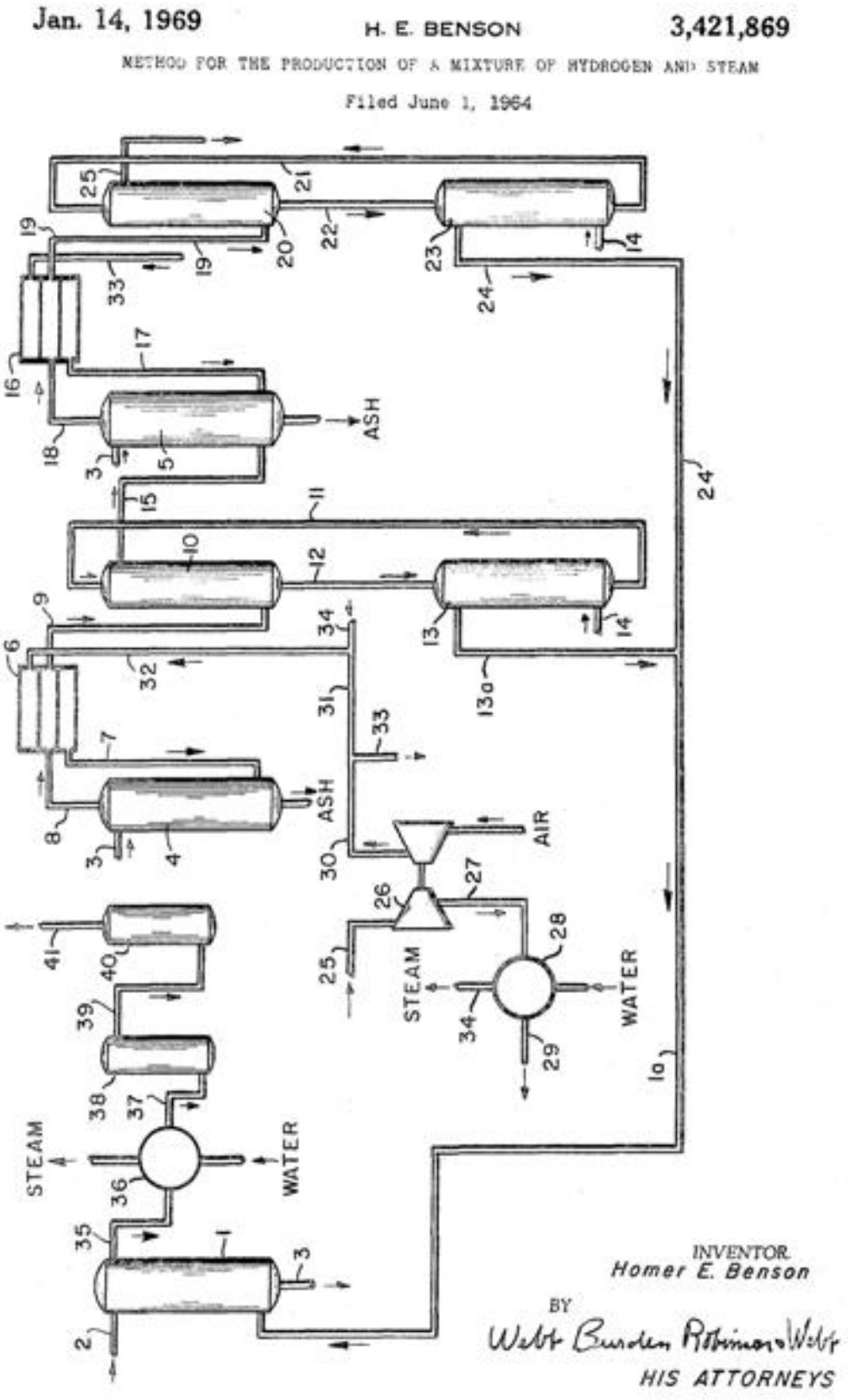

A6. US Patent 3442619

May 6 1969 J. HUEBLER ET AL 3,442,619

PRODUCTION OF HYDROGEN VIA THE STEAM-IRON PROCESS UTILIZING DUAL SOLIDS RECYCLE

Filed March 27, 1968

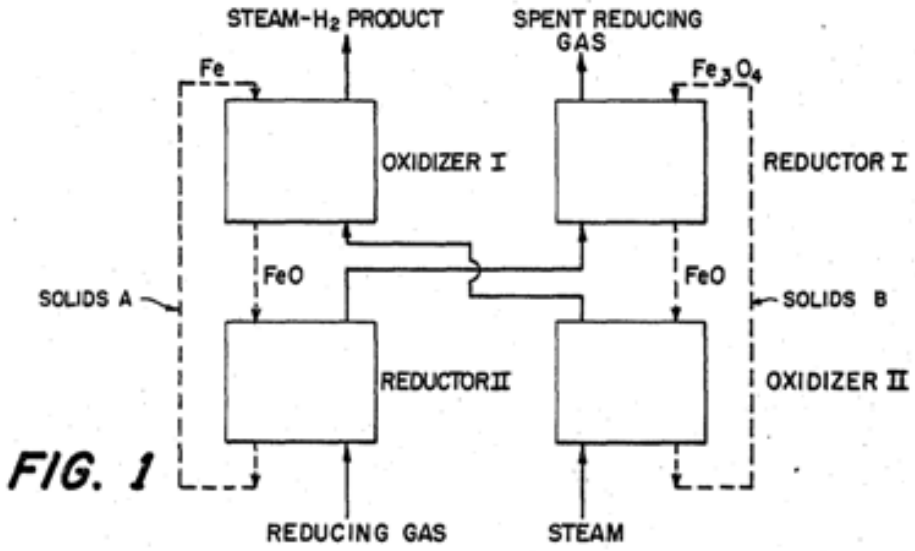

FIG. 1

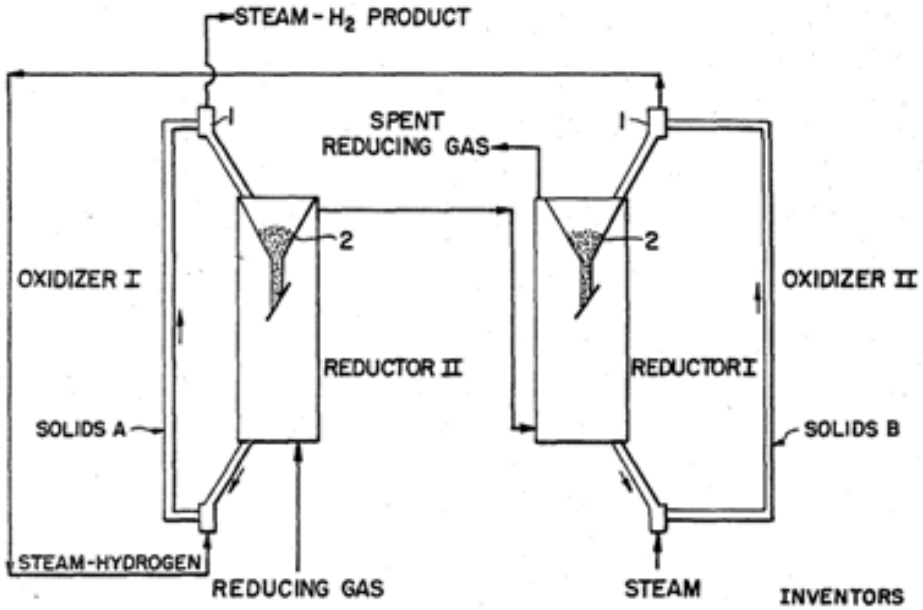

FIG. 2

INVENTORS
JACK HUEBLER
JAMES L. JOHNSON
FRANK C. SCHORA, JR.
PAUL B. TARMAN

A7. US Patent 3619142

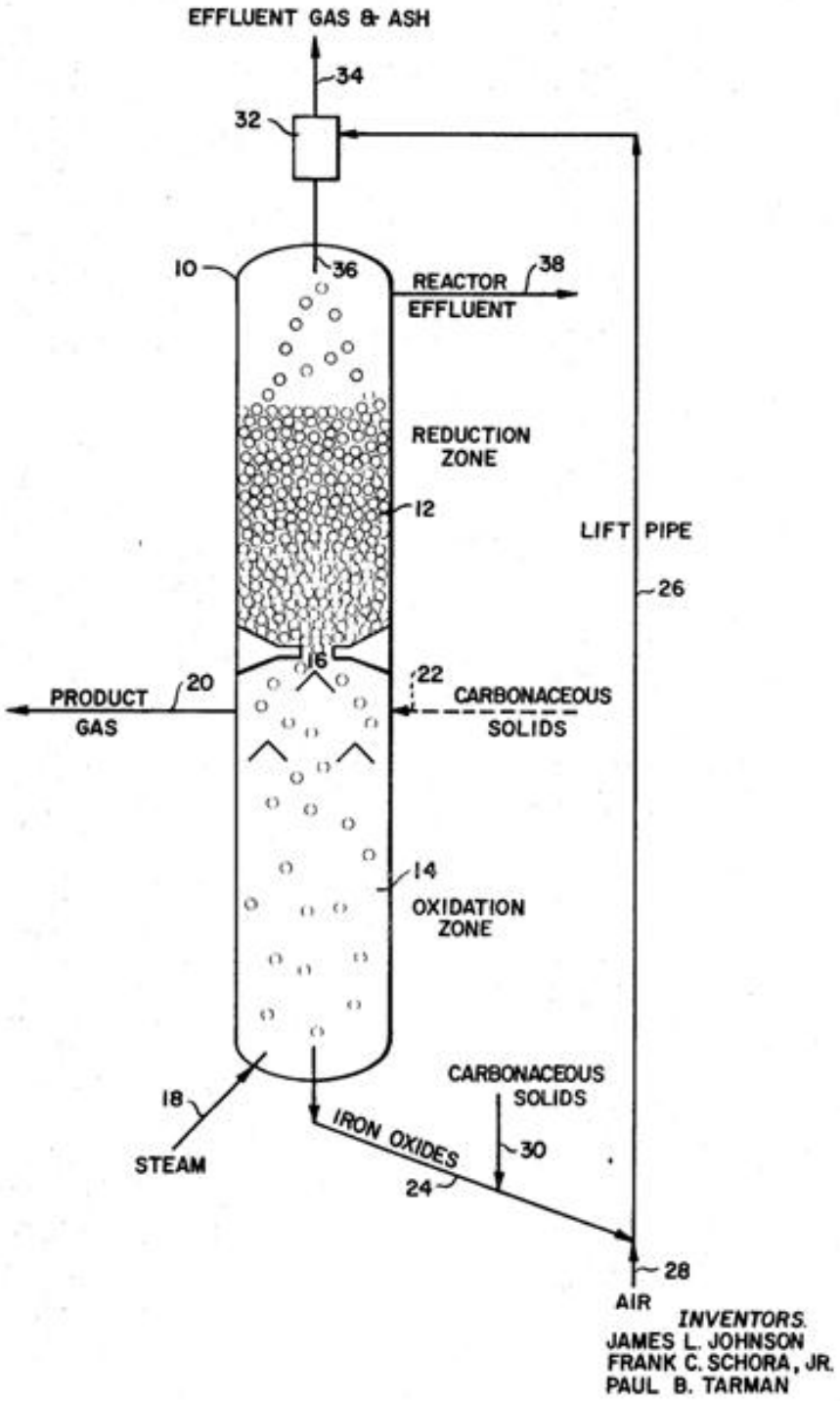

Appendix B: Summary of Chemical Looping Reforming Studies

OCM	Support	Agents		Sample weight	Temperature range	Reactor type[a]	Number of cycles	Cycle time	Post op' analysis [b]	Reference
		Reducer	Oxidiser	g	°C					
Mn_3O_4		CH_4	O_2	0.08	600-800	FB	4	4 hours	TEM	Stobbe[207]
Rh and Pt	CeO_2/Al_2O_3	CH_4	O_2 and CO_2	0.5	700	FB	1	20 pulses of 10 μmol (per step)	XRD	Fathi[208]
$La_{0:8}Sr_{0:2}Co_{0:5}Fe_{0:5}O_{3-\delta}$		CH_4	O_2	1.67	750-950	FB	1	---	---	Zeng[209]
Fe/Mn/Ni/Cu	SiO_2	CH_4/H_2O	O_2	10-15	700-950	FB	4-7	1100-4000s	SEM/XRD	Zafar[210]
Ni/Cu/Fe/Mn	SiO_2 or $MgAl_2O_4$	CH_4 with H_2O/CO_2	O_2	0.02	800-1000	TGA	4	600-1000s	BET	Zafar[211]
NiO	$MgAl_2O_4$	CH_4	O_2	350	824-925	CFB	(circulating)	(70-260 mins)	---	Ryden[212]
NiO	Al_2O_3	CH_4 with H_2O	O_2	300-400	800-950	BFB (and TGA)	1	400-1000s	---	de Diego[213]
NiO	$NiAl_2O_4$ or $MgAl_2O_4$	CH_4 with H_2O	O_2	15	800-950	FB	1	2000-3000s	---	Johansson[214]
NiO	Al_2O_3 or $MgAl_2O_4$	CH_4	O_2	170-250	950	CFB	(circulating)	(4-86 hrs)	SEM/XRD	Rydén[215]
LSCF, LSF, Ni, Fe_2O_3 and Mn_3O_4	$MgAl_2O_4$	CH_4	O_2	1	900	FB	5-10	~10 mins	XRD	Rydén[83]
NiO	$NiAl_2O_4$ or $MgAl_2O_4$	CH_4	O_2	---	750-900	CFB	(circulating)	---	---	Bolhàr-Nordenkampf[216]
NiO	$NiAl_2O_4$ or	CH_4	O_2	---	750-900	CFB	(circulating)	---	---	Bolhàr-

	$MgAl_2O_4$									Nordenkampf[217]
NiO	Al_2O_3	CH_4 with H_2O	O_2	1500	800-950	CFB (and TGA)	(circulating)	(over 50 hrs)	Density/Crushing strength/SEM/BET /XRD/Porosity	de Diego[69]
NiO	Al_2O_3	CH_4 with H_2O	O_2	1500	800-950	CFB (and TGA)	(circulating)	(over 50 hrs)	Density/Crushing strength/SEM/BET /XRD/Porosity	de Diego[218]
CeO_2 with Fe, Cu and Mn		CH_4	O_2	1.8	600-900	FB (and TGA)	20	~2000s	SEM/XRD	He[219]
NiO-Cr2O3-MgO and NiO-Cr_2O_3	SiO_2 or MgO	CH_4	O_2	0.5	500-800	FB	10	10-20 mins	XRD/XPS	Nakayama[220]
NiO	Al_2O_3	CH_4 with H_2O	O_2	---	800-950	SFB	(continuous)	(80-100 min)	Density/Crushing strength/SEM/BET /XRD/Porosity	Ortiz[221]
NiO	$NiAl_2O_4$ or $NiAl_2O_4$/$MgAl_2O_4$	CH_4	O_2	65 000	750-900	CFB	(circulating)	(5-6 hrs)	---	Pröll[222]
Ce-Fe-O		CH_4	O_2	1.8	850	FB	10	13-16 mins for reduction step	XRD/XPS	Li[223]
$LaFeO_3$		CH_4	O_2	0.1	780-900	FB	5	8 mins	SEM/XRD	Mihai[224]
$La_{0.8}Sr_{0.2}Fe_{0.8}Co_{0.2}O_{3-\delta}$, $La_{0.75}Sr_{0.25}Fe_{0.6}Co_{0.15}Al_{0.25}O_{3-\delta}$ and $La_{0.8}Sr_{0.2}Fe_{0.8}Co_{0.2}O_{3-\delta}$ with Rh or Pt	AlO(OH)	CH_4	O_2	0.1	600	FB (and TGA)	13	14 - 50 pulses of 0.25 μmol (per step)	In-situ XRD	Mudu[225]
NiO	Al_2O_3	Waste cooking oil with H_2O	O_2	40 or 80	600 or 700	FB (and TGA)	6	~80 mins	---	Pimenidou[226]
Ce-Fe-O		CH_4	O_2	1.8	850	FB (and TGA)	5	2130-2300 s	SEM/XRD/XPS	Wei[227]

Appendix C: Preliminary Experiments

C1. Measurement of water, hydrogen, nitrogen and oxygen partial pressures by the QMS at various water saturator set-point temperatures between 5-25^{o}C

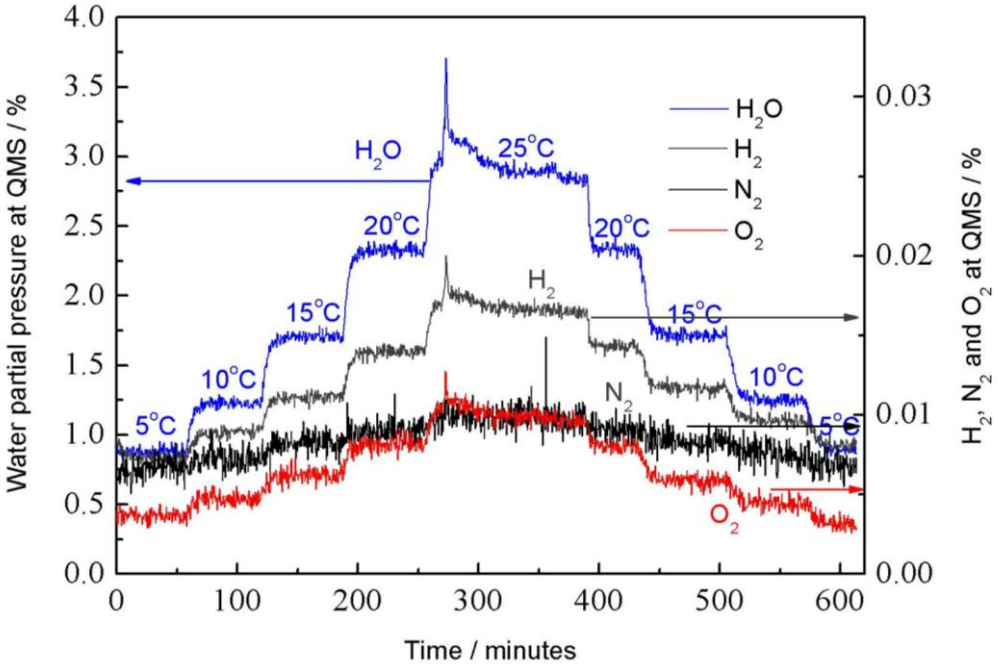

C2. The effects of changing heating temperature of the QMS inlet capillary line to the inlet flowrate taken by the QMS

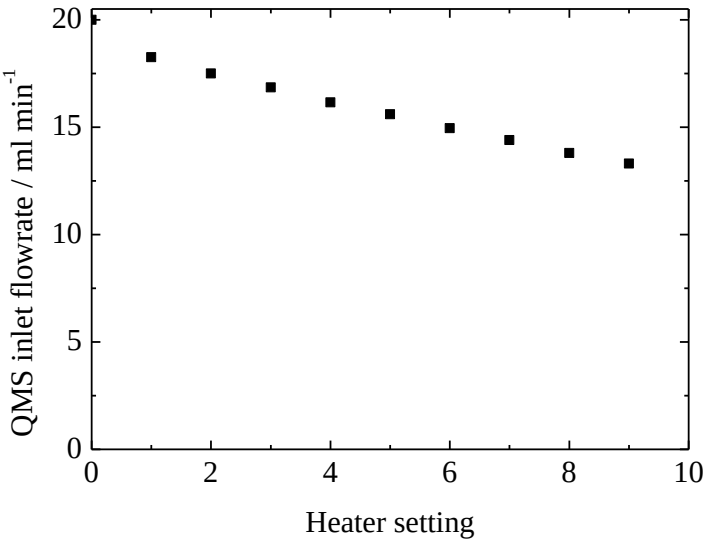

Appendix D: Calibration Tests

D1. QMS reading during 100% helium gas flow through the microreactor at room temperature

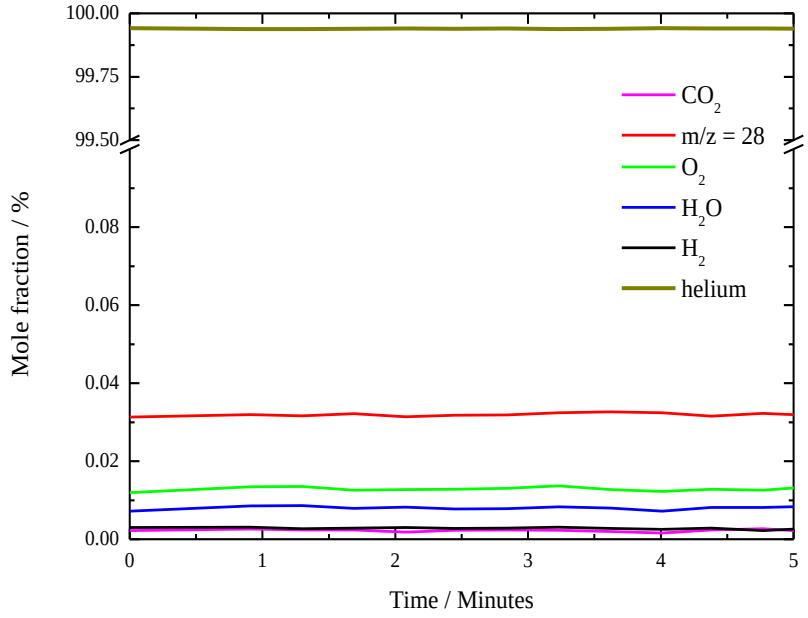

D2. QMS reading during 5% CO in helium gas flow through the microreactor at room temperature

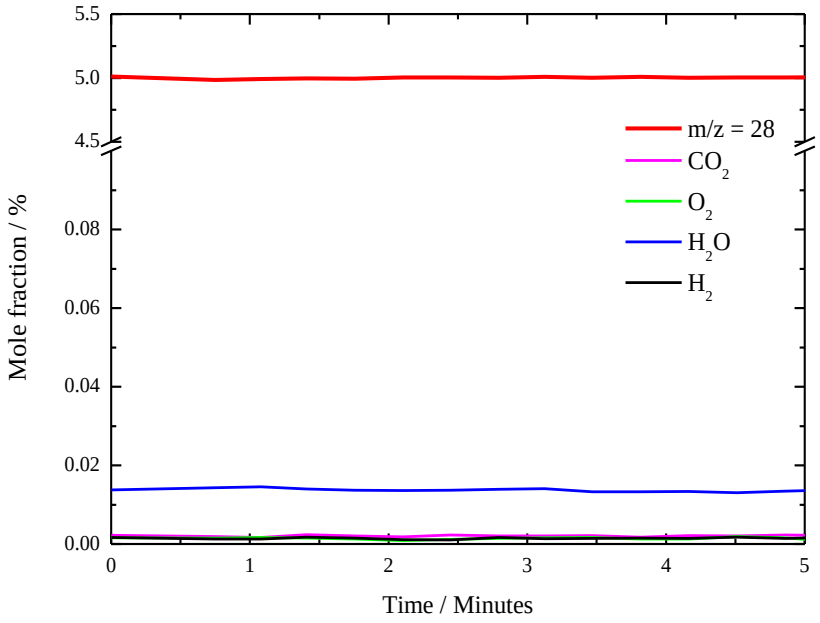

D3. QMS reading during 10% CH_4 in helium gas flow through the microreactor at room temperature

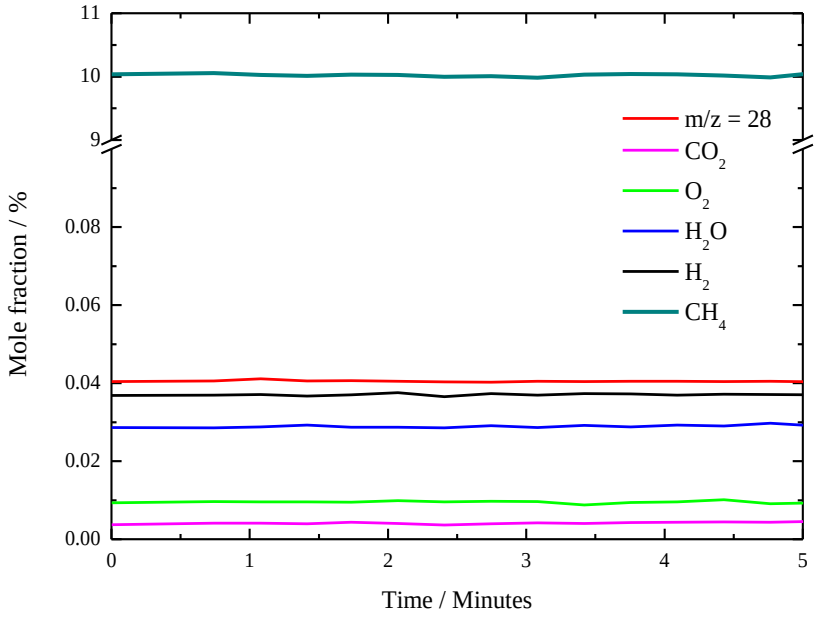

D4. QMS reading during 1% H_2O in helium gas flow through the microreactor at room temperature

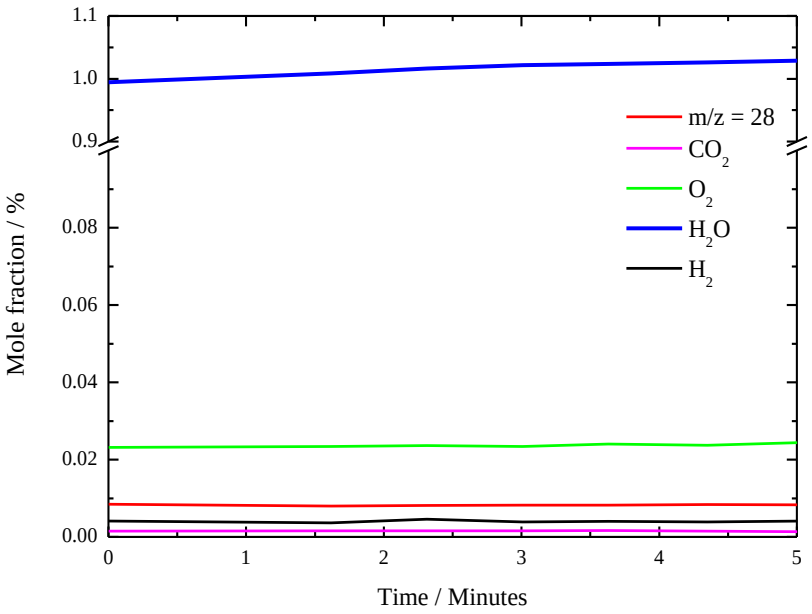

D5. QMS reading during 5% O_2 in helium gas flow through the microreactor at room temperature

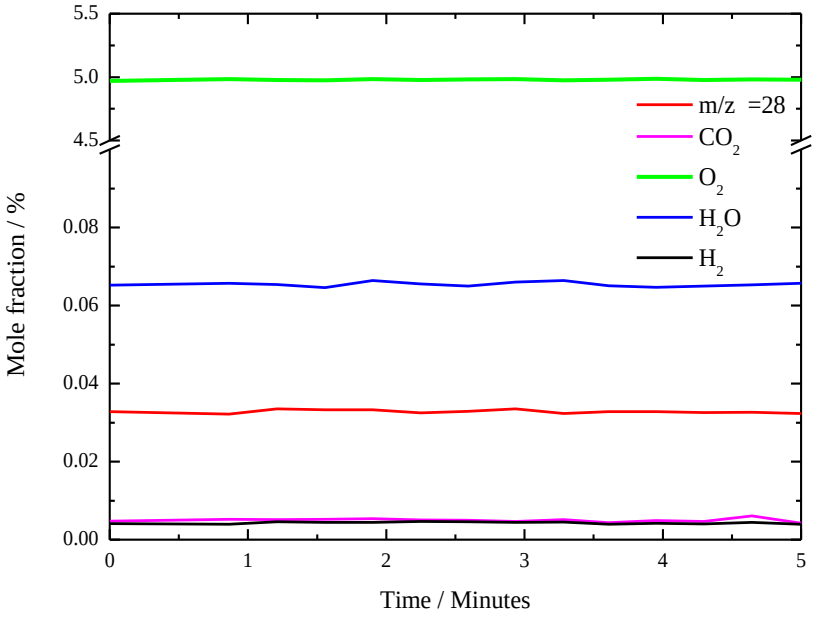

Appendix E: Molar balances

E1. Hydrogen molar balance for the 1st H_2O-TPO during the temperature programmed experiments performed using LSCF6428

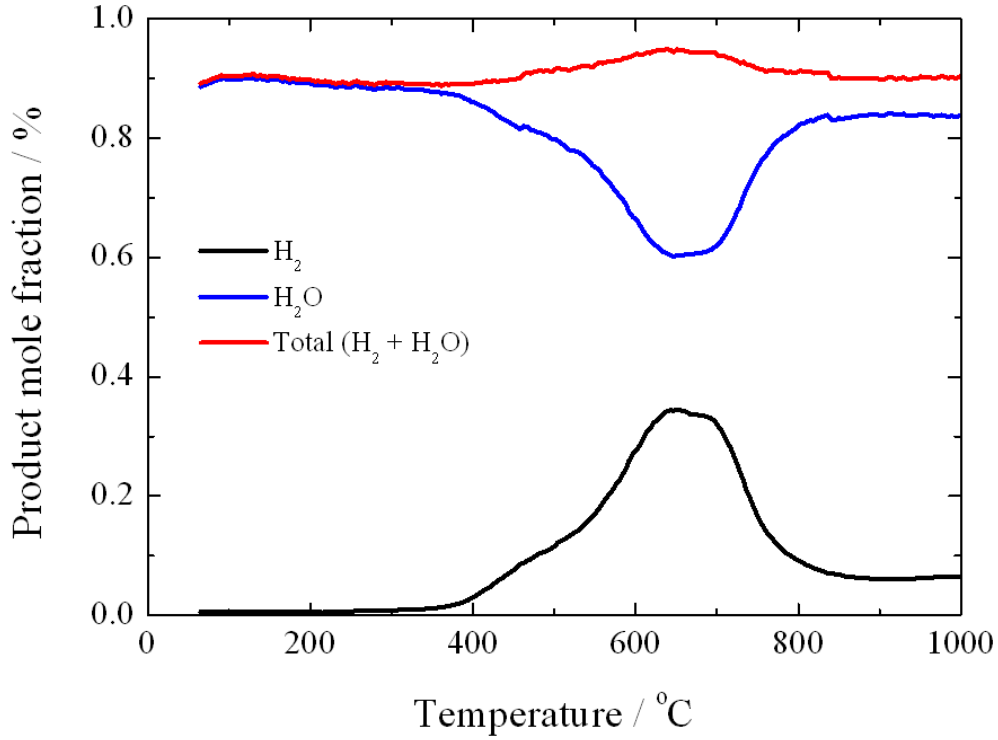

Appendix F: Autothermal chemical looping operation for hydrogen

F1. Molar products of hydrogen, water, carbon monoxide and carbon dioxide formed during the reduction steps of autothermal chemical looping redox cycling at 850^{o}C using Fe60 (using feeds of methane, water and air)

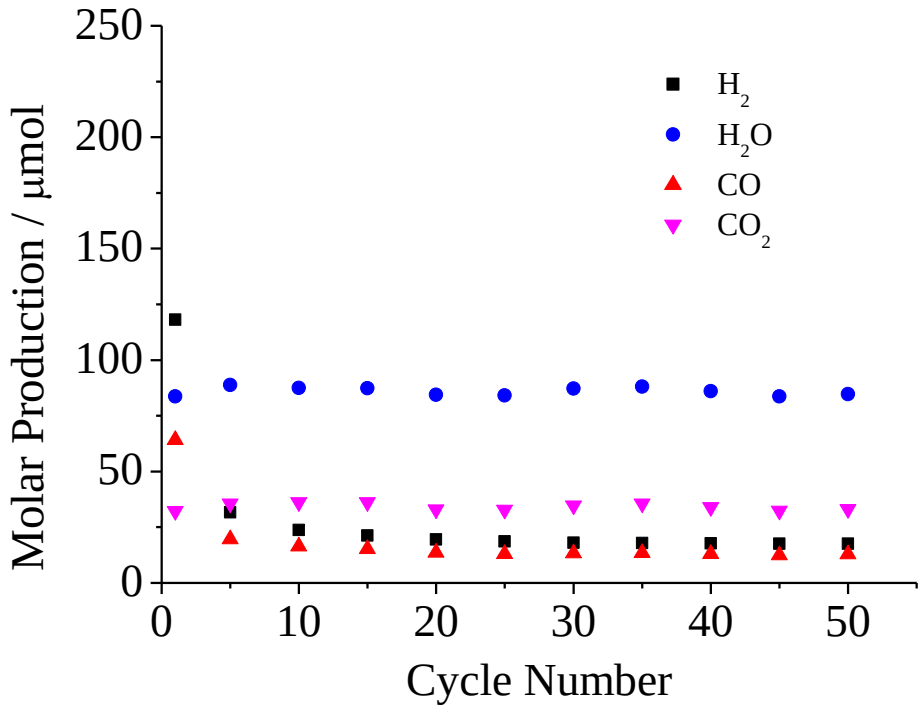

F2. Molar products of hydrogen, water, carbon monoxide and carbon dioxide formed during the reduction steps of autothermal chemical looping redox cycling at 850^{o}C using LSF731 (using feeds of methane, water and air)

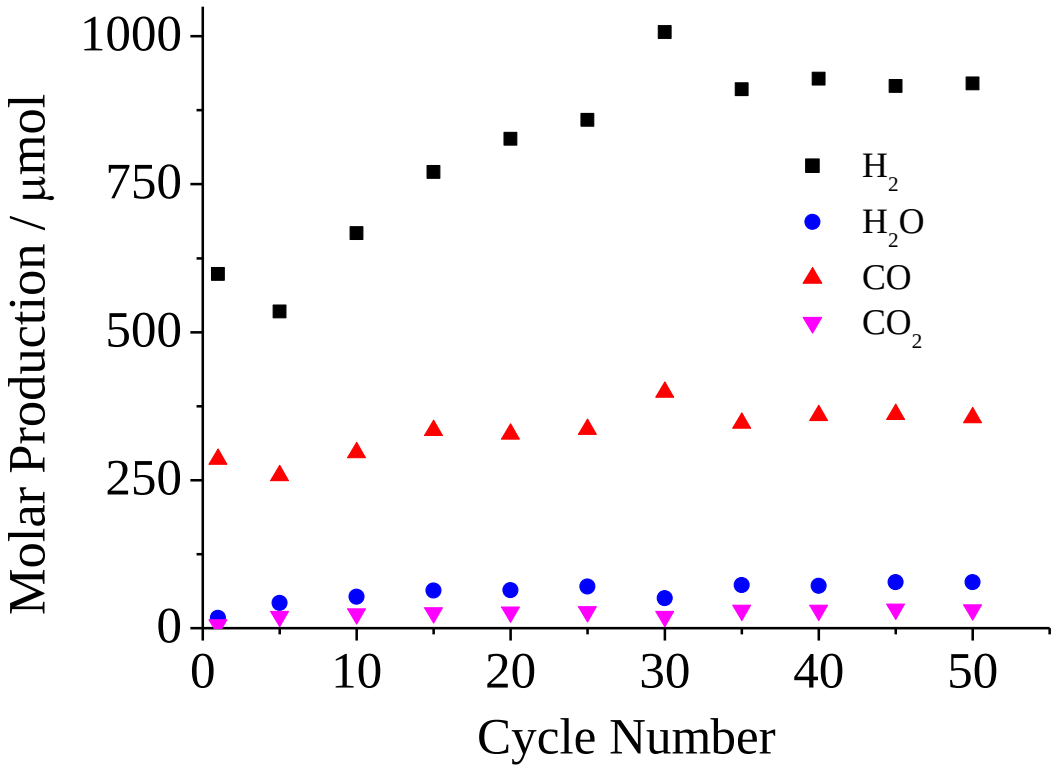

F3. Molar products of hydrogen, water, carbon monoxide and carbon dioxide formed during the reduction steps of autothermal chemical looping redox cycling at 850^{o}C using LSF731 (using feeds of 4.5:1 methane:water, water and air)

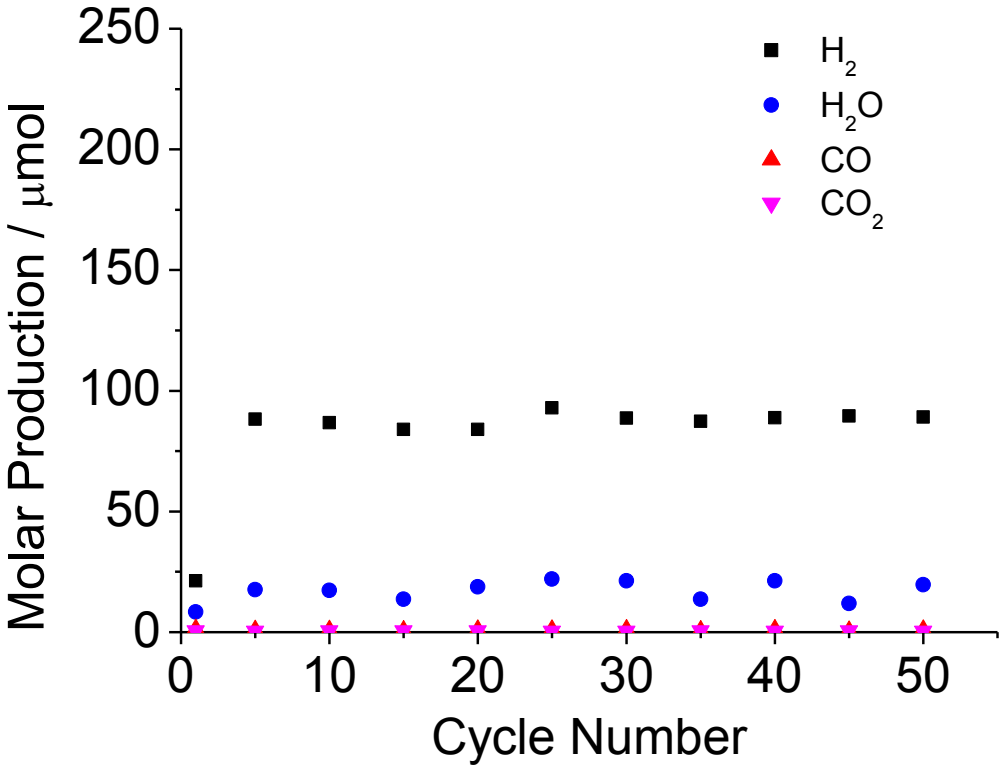

F4. Molar products of hydrogen, water, carbon monoxide and carbon dioxide formed during the reduction steps of autothermal chemical looping redox cycling at 850^{o}C using LSF731 (using feeds of 2.2:1 methane:water, water and air)

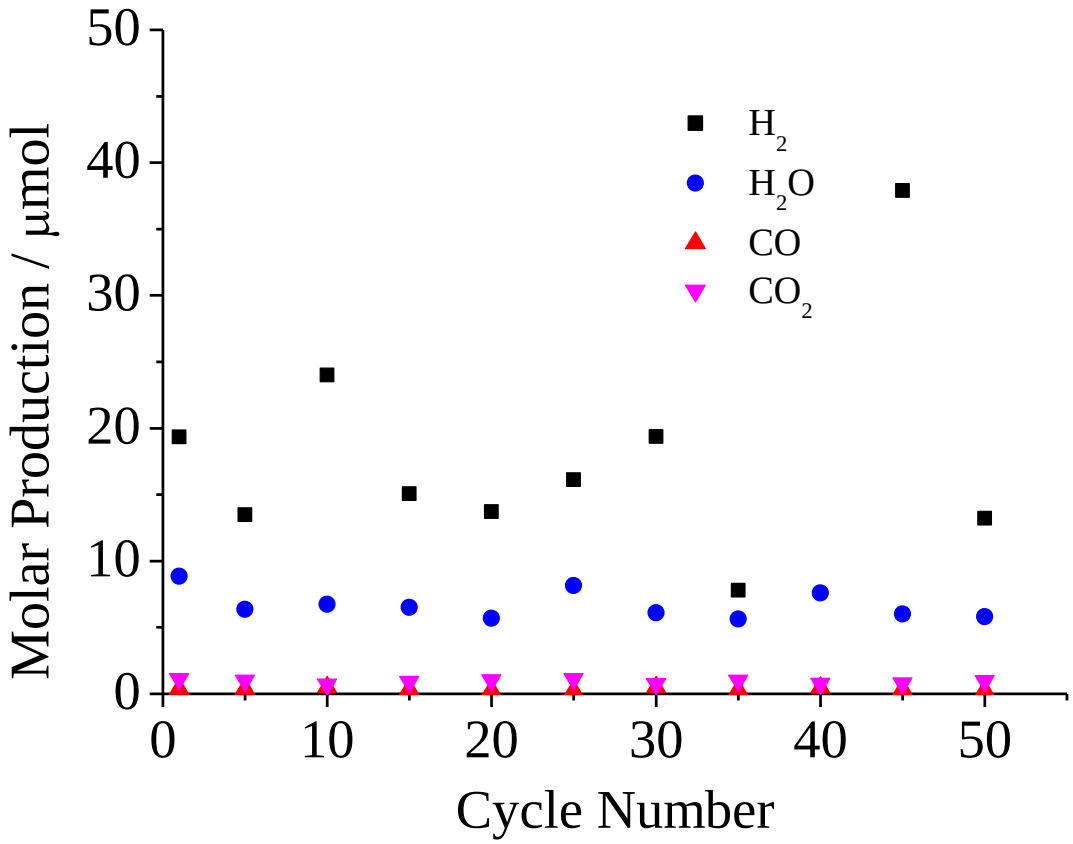

F5. Molar products of hydrogen, carbon monoxide, carbon dioxide and methane formed during the oxidation steps of autothermal chemical looping redox cycling at 850^{o}C using Fe60 (using feeds of methane, water and air)

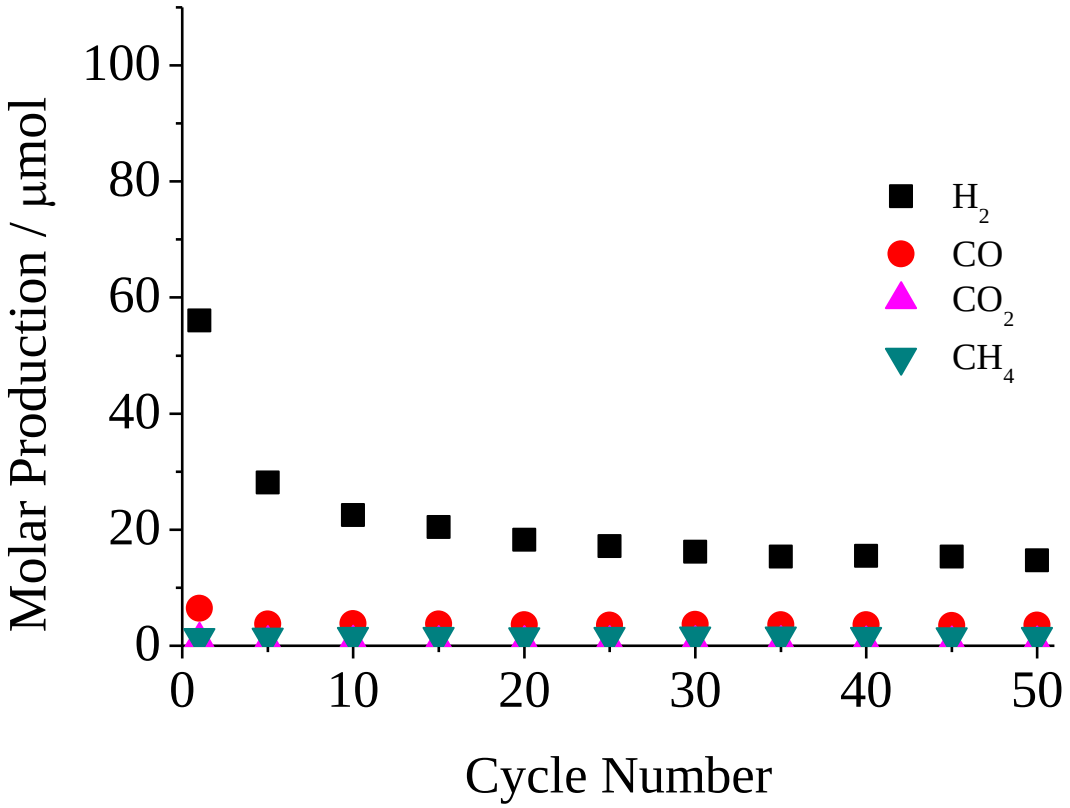

F6. Molar products of hydrogen, carbon monoxide, carbon dioxide and methane formed during the oxidation steps of autothermal chemical looping redox cycling at 850^{o}C using LSF731 (using feeds of methane, water and air)

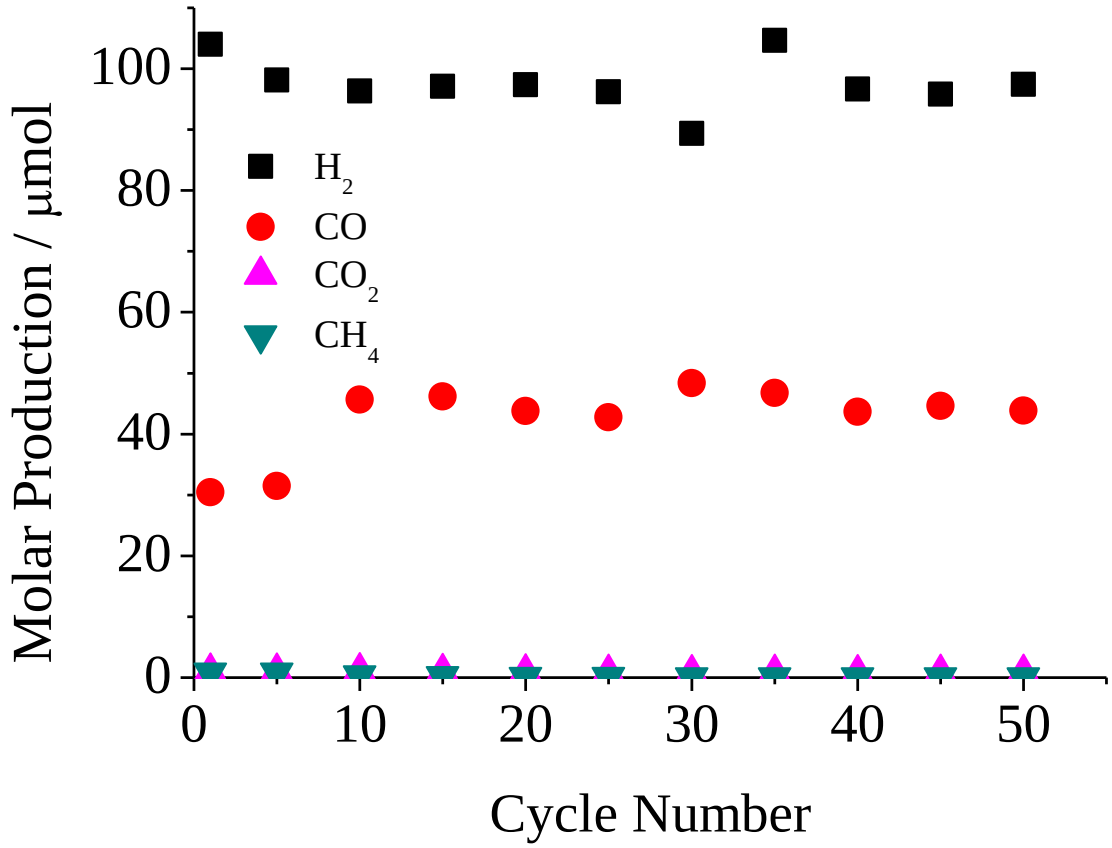

F7. Molar products of hydrogen, carbon monoxide, carbon dioxide and methane formed during the oxidation steps of autothermal chemical looping redox cycling at 850^{o}C using LSF731 (using feeds of 4.5:1 methane:water, water and air)

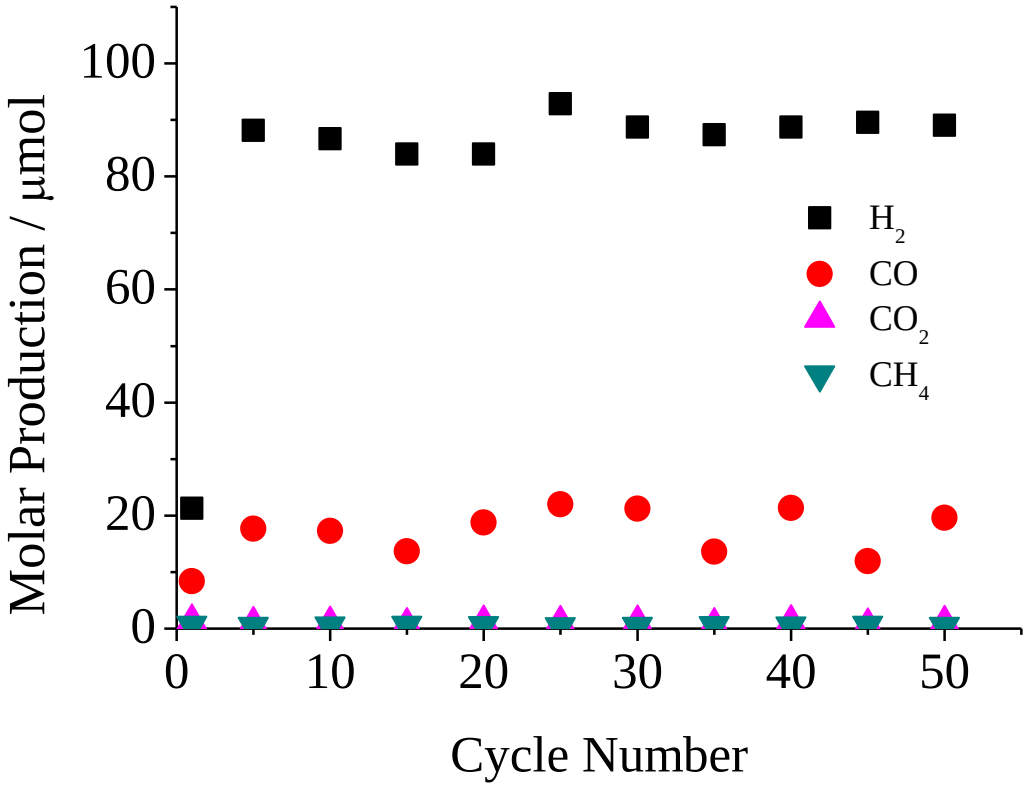

F8. Molar products of hydrogen, carbon monoxide, carbon dioxide and methane formed during the oxidation steps of autothermal chemical looping redox cycling at 850^{o}C using LSF731 (using feeds of 2.2:1 methane:water, water and air)